Volcanology from space: applications of infrared remote sensing

Thesis

Volcanology from space: applications of infrared remote sensing

A thesis presented for the degree of Doctor of Philosophy

Clive Oppenheimer BA Hons (Cantab)

1991

Department of Earth Sciences, The Open University

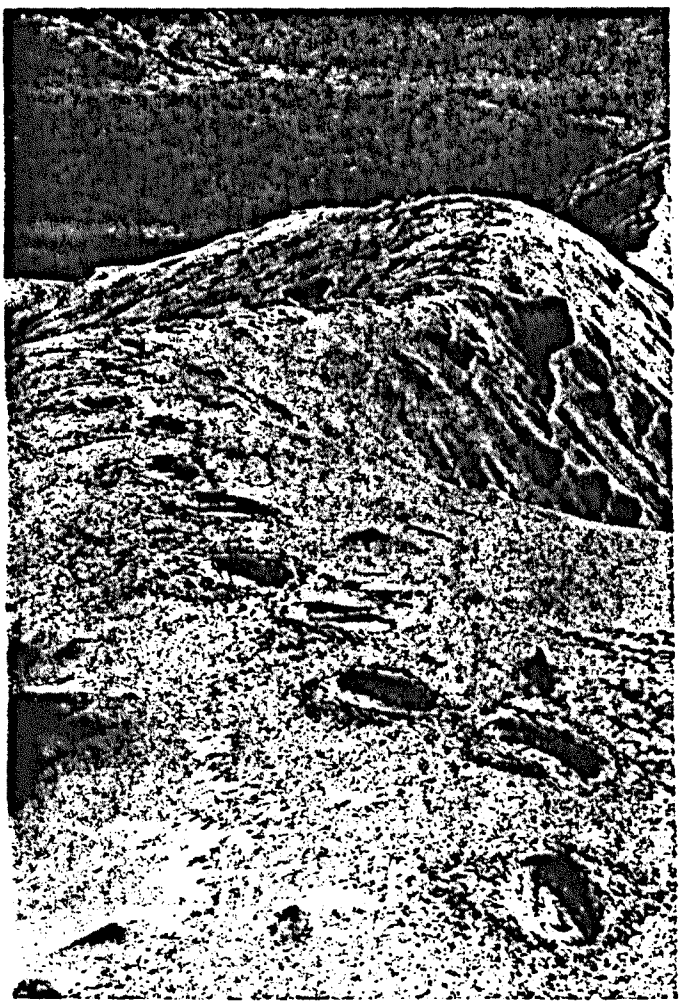

Abstract

Remote sensing techniques are being used increasingly to address volcanological problems. This thesis is concerned with the interpretation of multispectral infrared data of volcanic thermal features.

Data from the two short wavelength infrared (SWIR) bands of the Landsat Thematic Mapper (TM) are used to constrain sizes and temperatures of subpixel resolution hot spots. Analysis of a 1989 TM scene of Lonquimay volcano suggests a cooling from 250 to 170°C of the crust of an active lava flow down 1.5 km of its length. Estimates of the summed radiative and convective heat losses from the flow top fall from 6 to 3 MW per 30 x 30 m pixel downflow.

Thermal data were collected at volcanoes in Chile, Nicaragua and Italy to test assumptions explicit in such calculations. These surveys suggest that SWIR emission from fumarole fields is dominated by that from the interior walls of vents, and that surface temperatures around fumarole vents are lower than those of typical active lava bodies. The relative response of the two SWIR sensors of the TM is sensitive to such differences and therefore provides a basis for the interpretation of thermal anomalies known only from satellite data.

Abstract

Comparison of measurements in the two SWIR bands is performed with fourteen TM scenes recorded between 1984 and 1991, of a persistent hot spot at Láscar volcano, Chile. Evolution of the thermal source is charted by comparing the summed spectral radiance in each of the SWIR bands. Thus it appears that Láscar has experienced at least two periods of lava dome growth punctuated by the explosive eruptions of 1986 and 1990.

Infrared sensors to be deployed on forthcoming remote sensing platforms, including the Japanese Earth Resources Satellite and NASA's Earth Observing System, promise to constrain thermal emissions from volcanoes more effectively than possible with existing orbital systems. These investigations will improve understanding of the physical processes that influence the emplacement of lavas, as well as the potential for detecting eruption precursors and evaluating volcanic hazards.

Preface

This thesis was completed in September 1991 (three months since Pinatubo and Unzen, one month after Hudson). My whole-hearted thanks go to several people and institutes that have helped me over the last three years.

Peter Francis and David Rothery were world-class supervisors. I am indebted to them both for unfailing guidance, stimulation and badinage.

The Natural Environment Research Council funded the project generously (under NERC grant GT4/88/GS/87). It met costs of field trips to Italy and Latin America, attendance of conferences in the United States, Germany, United Kingdom and Italy, and purchase of satellite data. Angela Morrison arranged with EOSAT for the TM to be switched on over Nicaragua and Chile; Steve Groom unpacked AVHRR images.

The Landsat TM scene of Lonquimay volcano (Chapter 2) was bought with an Open University Research Grant awarded to David Rothery. NASA paid for several of the Láscar TM images through a grant held by Peter Francis. NASA also footed the bill for a visit to Hawaii.

On location, I enjoyed working with Geoff Brown, Steve Hallinan, Hazel Rymer and Gerardo Soto (Costa Rica), Ben van Wyk de Vries, Leonel Urbina, Odel Castellón and Helman Taleno (INETER, Nicaragua), José Naranjo, Hugo Moreno, Moyra Gardeweg, Steve Sparks, Mark Stasiuk and Steve Matthews (Chile), and Lori Glaze, David Pieri, John Murray, Vittorio Scribano, Massimo Pompilio and Mauro Coltelli (Italy). Especial thanks go to Lori, for hospitality in Los Angeles.

At the Open University, I benefitted from discussions with Helen Budgey, Ardemirio de Barros Silva, Jill Eyers, Liz Harper, Lottie Hosie, David Jackson, Jon Maynard, Fiona McGibbon and David Stevenson. John Taylor and Andy Lloyd assisted with artwork and photography but more than anyone, it was Dick Carlton who helped improve my image.

Several colleagues shared ideas or gave helpful comments on manuscripts: Sarah Stockwell (Chapters 1 and 6), Steve Blake, Joy Crisp, Lori Glaze, David Pieri, David Stevenson, Geoff Wadge and Lionel Wilson (Chapter 2), Angus Duncan (Chapter 3), and Claude Jaupart (Chapter 5). Steve Blake and Lionel Wilson examined the thesis.

I thank Sarah, Suzy and J.O. for encouraging me always. I acknowledge P. for a key rôle in implementation of my writing-up strategy.

Table of contents

List of figures

Figures

List of tables

Chapter 1. Infrared remote sensing of active volcanoes: prospects, principles and problems

1.1. Introduction

Five hundred and thirty volcanoes are known to have erupted in historic times; a further two thousand have been active during the last ten thousand years (C. Newhall, personal communication, 1990). Of these potentially dangerous volcanoes, only a tiny fraction is presently subjected to routine surveillance. At a time when significant advances are being made in the modelling of volcanic processes, it seems remarkable that the task of merely documenting the volcanoes of the world remains incomplete. Even less would be known about the geographic distribution of volcanic centres were it not for pioneering studies which have capitalised on the synoptic perspective afforded by satellite images (e.g., de Silva and Francis, 1991).

Few, if any, volcanoes erupt without monition. Nevertheless, the signals of unrest are often subtle or ambiguous. Eruption prediction - which remains based essentially on empiricism and pattern recognition - though sometimes successful, has rarely been attempted. Many of the most dangerous volcanoes are in countries where

increasingly large populations crowd fertile volcano flanks, and where the financial and scientific resources to conduct adequate monitoring are often lacking (Tilling, 1989). While the most rigourous investigations are conducted at persistently active volcanoes, like Mount Etna (Italy) and Kilauea (Hawaii), many devastating eruptions have taken place at sites that had been quiescent for centuries or millenia. In 1956, 3000 people in Papua New Guinea were killed by an eruption of Mount Lamington, which was not even known to be a volcano (Taylor, 1983). With the UN-endorsed International Decade of Natural Disaster Reduction (IDNDR) underway, remote sensing techniques, in consort with advances in geophysical and geochemical surveillance, are contributing increasingly towards both the operational needs of volcano monitoring and emergency response, and to a better understanding of the physical processes underlying volcanic behaviour.

The extension of the perceptual range of spaceborne sensors through many regions of the electromagnetic spectrum is the key to several inspired applications of remote sensing techniques to volcanological investigations. This thesis explores the potential of multispectral infrared data for observing hot volcanic manifestations such as fumarole fields and lava bodies.

1.2 Applications of satellite remote sensing in volcanology

The utility of satellite remote sensing systems for volcanology stems from four essential aspects: global coverage, synoptic perspective (from a safe distance), multispectral capability, and continuity of data acquisition. We shall see all of these attributes illustrated in the examples that follow.

1.2.1. Mapping

When Landsats 1 (1972), 2 (1975), and 3 (1978) were launched, volcanologists had 'access' for the first time to all the world's subaerial volcanoes. Important discoveries made with Multi-spectral Scanner (MSS) data included that of the previously unrecognised 2.2 Ma old Cerro Galan caldera in northwest Argentina, arguably the best exposed example of a large resurgent caldera on Earth (Francis *et al.*, 1983). When the

Thematic Mapper (TM) was deployed on Landsats 4 (1982) and 5 (1984), its enhanced spatial resolution and spectral capability enabled more subtle discrimination of geomorphic features and volcanogenic products. This has facilitated relative dating of lavas, pyroclastic and debris flows, and airfall deposits (e.g., Francis and de Silva, 1989; de Silva and Francis, 1990); Francis and Wells (1988) identified fifteen previously unknown debris avalanche deposits from TM images of the central Andes.

Other sensors have also proved useful. By combining spatially detailed SPOT-1 HRV images with Large Format Camera (LFC) photographs taken from the Space Shuttle, Munro and Mouginis-Mark (1990) mapped the distribution of cones, eruptive fissures and lava flows on Isla Fernandina (Galapagos Islands). Using low spatial resolution data recorded by the Advanced Very High Resolution Radiometer (AVHRR - carried on board the NOAA-series of polar-orbiting platforms) Tucker and Matson (1985) estimated the extent of ash deposition from the 1982 eruptions of El Chichón (Mexico).

Increasingly, digital elevation models (DEMs) are being integrated with satellite data within geographic information systems. With the extra dimension of surface topography, concerns such as slope stability, and the likely paths of lava, pyroclastic and debris flows can be addressed (e.g., Young and Wadge, 1990). Automated computer techniques are even available for obtaining DEMs directly from stereoscopic satellite image pairs (Otto and Chau, 1989). Methods such as these will be valuable for the construction of hazard zonation maps of active volcanoes.

1.2.2. Detecting and measuring thermal emission

Airborne and ground-based thermal infrared surveys have been carried out sporadically over the last twenty-five years at numerous active volcanoes and geothermal sites, for the purpose of detection, mapping and monitoring of thermal anomalies (e.g., Fischer *et al.* 1964, Moxham 1971, Kieffer *et al.*, 1980, Tabbagh *et al.* 1987, Bianchi *et al.* 1990). There are two levels of investigation of such data: the first is concerned simply with detection of new thermal features or changes in existing ones; the second attempts to use such radiometric observations to provide insight into the thermal physics

of volcanic processes. However, quantitative measurements from these kinds of data are not straightforward because of difficulties in calibrating the instruments, and correcting for the effects of solar heating and reflection. Airborne campaigns are costly to mount, pose many logistical problems, and have not therefore provided a routine source of infrared data for volcano monitoring (Francis, 1979) nor are they likely to in the future.

Orbital remote sensing from unmanned spacecraft does, however, offer a means of regular observation of subaerial volcanoes world-wide. The potential of spaceborne infrared sensors to detect thermal manifestations was demonstrated as long ago as 1966 when the High Resolution Infrared Radiometer (sensitive in the wavelength range 3.45-4.07 μm) on board the Nimbus II meteorological satellite picked up thermal radiation from lava flows erupted at Surtsey, Iceland (Williams and Friedman, 1970). Wiesnet and D'Aguanno (1982) and Rothery and Oppenheimer (in press) reported a similar phenomenon in thermal infrared imagery of Mount Erebus, Antarctica, recorded by the AVHRR. Bonneville *et al.* (1985) and Bonneville and Kerr (1987) also used AVHRR data to document thermal anomalies on Mount Etna. If such measurements can be calibrated, radiant temperatures may be estimated for the surface viewed, e.g., ground, sea, cloud, or ash plume, from Planck's distribution law which expresses radiated power output as a function of temperature and wavelength.

Planck's law also underpins a two-waveband algorithm for estimating temperatures and sizes of sub-pixel sized thermal features (section 1.3.1; Dozier, 1981; Matson and Dozier, 1981). Following on the discovery by Francis and Rothery (1987) of a small but pronounced thermal anomaly in the short wavelength infrared (SWIR) bands of TM images of the north Chilean volcano, Láscar, Rothery *et al.* (1988) adapted this technique to make thermal measurements at this and several other volcanoes, including Erta 'Ale (Ethiopia) and Erebus (Antarctica). Observations in the SWIR part of the spectrum are distinct from those at the longer wavelengths of the thermal infrared, because of their greater sensitivity to very high temperature (magmatic) phenomena. It is possible to detect ground at temperatures around 1000°C, that occupies just one-ten thousandth the nominal 30 x 30 m pixel area, in the two TM bands 5 and 7 (Rothery *et*

al., 1988). Early studies were extended to model changes in radiated power output at Láscar (Glaze *et al.*, 1989a), and to estimate heat losses from a lava flow at Etna (Pieri *et al.*, 1990). However, there are limitations to these techniques, and the aim of this thesis is to develop a fuller understanding of what can be learnt from remotely-sensed thermal anomalies on volcanoes. We shall return to this topic shortly.

1.2.3. Observations of volcanic ash clouds

The frequent coverage provided by geostationary weather satellites is particularly useful for near real-time surveillance of the ash clouds released by explosive volcanic eruptions. It is, in fact, extremely difficult to measure the extent of large volcanic plumes by any other method (e.g., Kienle and Shaw, 1979; Robock and Matson, 1983; Sparks *et al.*, 1986), and such data show promise for emergency management, notably in respect of advising the aviation community when ash has travelled into air corridors (Eos, 1989). Downwind transport of ash is mapped simply by examining contiguous satellite 'snapshots' (e.g., Malingreau and Kaswanda, 1986). However, it has not always been straightforward to discriminate between volcanic plumes and ordinary meteorological clouds on such images. Multispectral digital data such as AVHRR can be processed to enhance spectral differences between the two types (e.g., Prata, 1989; Kienle *et al.*, 1990; Holasek and Rose, 1991) but difficulties remain. The spatial resolution of the satellite data also places constraints on the size of clouds that can be detected. At present there are probably several eruptions of remote volcanoes each year which go wholly unnoticed.

Eruption plume heights have been estimated both by shadow techniques and by calibration of ash cloud-top temperatures, derived from thermal infrared images, against vertical atmospheric temperature profiles (e.g., Sawada, 1983; Glaze *et al.*, 1989b). Maximum column height is an important parameter since it is correlated with the rate of magma discharge (e.g., Wilson *et al.*, 1978). Satellite data can contribute to an appraisal of the energetics of eruptions, as well as lending support to physical models that predict the fallout of ash (Glaze and Self, 1991).

1.2.4. Observations of volcanic gas and aerosol clouds

In addition to silicate ash, major explosive eruptions inject large amounts of gases into the atmosphere. Even quiescent volcanoes are notable for their gas emissions (e.g., Casadevall *et al.*, 1984; Allard *et al.*, 1991), and large volume effusive eruptions have also been implicated in substantial release of volatiles (Rampino *et al.*, 1988). Sulphur dioxide expelled from volcanoes is known to influence the physical behaviour of the atmosphere, although the chemical processes responsible for converting SO_2 into sulphuric acid aerosols, capable of absorbing and backscattering solar irradiation, are not fully understood. Some eruptions are more sulphur-rich than others, reflecting variable sulphur contents in magmas, or possibly the assimilation of fumarolic sulphur deposits (Oppenheimer, 1991a). Against the background of concern about global climatic change, the possible effects of major volcanic eruptions on regional and global climate have been examined by numerous researchers (for a review see Rampino *et al.*, 1988).

Sulphur dioxide absorbs certain wavelengths of ultraviolet radiation between 0.30 and 0.33 μm, and it this which has enabled the Total Ozone Mapping Spectrometer (TOMS) carried by the Nimbus 7 satellite to detect and quantify volcanogenic releases. This is an inspired use of a sensor designed for a quite different purpose. Major eruptions from El Chichón in 1982 propelled eruption columns more than 20 km into the atmosphere. AVHRR sensors tracked the ash plume once around the entire globe (Robock and Matson, 1983), while TOMS measurements suggested that over 3 Mt of gaseous sulphur dioxide had been injected into the stratosphere (Krueger, 1983). TOMS data for the 1985 eruption of Nevado del Ruiz suggested a lesser release of 0.66 Mt of sulphur dioxide (Krueger *et al.*, 1990) but the June 1991 convulsions at Pinatubo, which rate among the largest eruptions of this century, are believed to have exceeded the El Chichón eruption, in terms of sulphur dioxide release, by a factor of two (Smithsonian Institution, 1991b).

1.2.5. Direction of future research

The present decade should see the deployment of a number of satellite platforms carrying many new sensors that show promise for volcanological lines of enquiry (Mouginis-Mark and Francis, *sub judice*). Notable among these is NASA's Earth Observing System (EOS), although its funding situation remains unstable (Eos, 1991). Mouginis-Mark *et al.* (1991) have reviewed the EOS instruments which show volcanological potential. Multinational working groups involved in remote sensing of volcanoes include the IAVCEI (International Association of Volcanology and Chemistry of the Earth's Interior) Commission on Satellite Volcano Applications (currently led by David Pieri at the Jet Propulsion Laboratory in Pasadena, California), and the Earth Observing System Volcanology Investigation team (headed by Peter Mouginis-Mark at the University of Hawaii). The scope of these investigations was expressed by Mouginis-Mark *et al.* (1989) as follows: "(1) to understand the eruption of lavas, gases and aerosols from volcanoes, the dispersal of these materials on the Earth's surface and through the atmosphere, and the effects of these eruptions on the climate and environment; and (2) to understand the physical processes that lead to the initiation of volcanic activity, that influence the styles of volcanic eruptions, and that dictate the morphology and evolution of volcanic landforms".

Ideally, it would be desirable to have access to a satellite dedicated to the surveillance of volcanoes. There are plans to design just such an instrument - an orbiting volcano observatory (OVO) - and launch it into low Earth orbit (section 6.2.3; Pieri and Glaze, 1989). Such an experimental mission could provide a consistent means of monitoring levels of activity at volcanoes across the globe and offer scope for hazard mitigation. Whether or not such systems as OVO get off the ground, existing and forthcoming environmental remote sensing satellites can and will observe volcanoes in a number of useful ways. The IAVCEI Task Group for the IDNDR has included satellite remote sensing as an important area for development in a package of major project

proposals (IAVCEI, 1990). They "support increased use of satellite monitoring where it offers cost and technical advantages over land-based monitoring".

Aside from the hazards they pose, volcanoes provide insight into the internal dynamics of planetary bodies. Remote sensing principles are also applied to the study of extra-terrestrial volcanoes. Images recorded by space probes have shown dramatically that volcanism has shaped, and in some cases continues to shape, other planets and moons (e.g., Viking at Mars [Carr, 1981], Voyager at Io [Carr *et al.*, 1979], and Magellan at Venus [Head and Crumpler, 1990]). Interpretations of the surface geological features of other planetary bodies, and therefore the deeper dynamic processes which they express, depend on an ability both to describe analogous phenomena on Earth, and to understand how surface characteristics determine the response of sensors in different parts of the electromagnetic spectrum. Knowledge of the internal dynamics of planets such as Venus (under on-going observation by the Magellan spacecraft, and the most Earth-like of our neighbours) promises, in turn, new insight into the Earth's own interior (see Head and Crumpler, 1990).

1.3 Satellite measurements of radiant heat from volcanoes

1.3.1. Principles

There are essentially two methods by which surface temperatures can be estimated from satellite infrared data. The first involves calibration of a given satellite sensor's response against "ground truth", i.e. surface temperatures measured simultaneously in the field (Lathrop and Lillesand, 1986). Although this empirical approach inherently accounts for atmospheric effects, it is generally impractical since simultaneous satellite and in situ measurements are required. The second method is theoretical, in that it exploits the Planck distribution law, according to which the spectral radiant emittance $H(\lambda,T)$ from a surface is a function of its blackbody absolute temperature T

$$H(\lambda,T) = 2hc^2\lambda^{-5}[\exp(hc / \lambda kT) - 1]^{-1} \qquad (1.1)$$

where λ is wavelength, h is Planck's constant, k is the Boltzmann constant, and c is the speed of light. This is often rewritten more simply as:

$$H(\lambda,T) = c_1\lambda^{-5}[\exp(c_2 / \lambda T) - 1]^{-1} \quad (1.2)$$

where the constants c_1 and c_2 have values 3.74127×10^{-16} W m^2 and 1.4388×10^{-2} m K, respectively. For isotropic radiation, $H(\lambda,T)$ is independent of direction, and the spectral radiance $L(\lambda,T)$ is given by

$$L(\lambda,T) = H(\lambda,T) / \pi \quad (1.3).$$

The infrared energy which falls on a satellite detector is composed of varying proportions of radiation emitted and reflected from the target surface, (partially transmitted by the atmospheric column), and upwelling radiation emitted or scattered by the constituents of the atmosphere itself (so-called "path radiance"). The spectral radiance, R_λ, reaching a satellite at wavelength λ may be written as:

$$R_\lambda = \tau_\lambda\varepsilon_\lambda L(\lambda,T) + \tau_\lambda\rho_\lambda R_{\lambda D} + R_{\lambda U} \quad (1.4)$$

where τ_λ is the wavelength-dependent atmospheric transmission coefficient, ε_λ and ρ_λ are, respectively, the spectral emissivity and spectral reflectivity of the surface, T its radiant temperature, and $R_{\lambda D}$ and $R_{\lambda U}$ are, respectively, the downwelling and upwelling atmospheric spectral radiances (Figure 5.3). R_λ is obtained from satellite infrared measurements by radiometric calibration of the sensor output voltage. This is usually in the form of:

$$R_\lambda = \alpha_\lambda DN_\lambda + \beta_\lambda \quad (1.5)$$

where α_λ and β_λ are known calibration coefficients, and DN_λ is the digital number in band λ for a given pixel of image data.

In order to use (1.4) to estimate surface temperatures, first, that part of the satellite response corresponding to the partially transmitted target thermal radiance, $R_{\lambda,thermal} = \tau_\lambda\varepsilon_\lambda L(\lambda,T)$, must be isolated. In simple cases, this can be achieved by subtracting a background non-thermal signal from the anomalous signal over a hot spot (Chapters 2 and 5). "Pixel-integrated temperatures" can then be derived by rearrangement of (1.3):

$$T = \frac{c_2}{\lambda \ln[1 + c_1 \tau_\lambda \varepsilon_\lambda / (10^7 \pi \lambda^5 R_{\lambda,thermal})]} \qquad (1.6)$$

where λ is in metres and $R_{\lambda,thermal}$ is in units of mW cm^{-2} sr^{-1} μm^{-1}. τ_λ can be estimated from radiation propagation models such as those incorporated in the widely used LOWTRAN computer code (Kneizys *et al.*, 1988). Estimates of spectral emissivity can be based on published data for appropriate surface materials (e.g., Pollack *et al.*, 1973).

If the atmosphere between target and sensor has been well-characterised, this approach can give accurate estimates of the surface temperature of large bodies of water (e.g., Bartolucci *et al.*, 1988). The spectral emissivity of water is well-known and close to unity in the TIR, and in most cases temperature distributions across sea or lake surfaces are reasonably homogeneous at pixel scales (e.g., 120 m for Landsat TM band 6, and 1.1 km at nadir for AVHRR data). Where independent data on the atmospheric path are lacking, multi-channel ("dual-band", "split window" and triple-band") algorithms have enabled the derivation of sea surface temperatures to high accuracies (e.g., McClain *et al.*, 1985).

On land, surface temperature measurement is far more complex (Wan and Dozier, 1989). It may be unrealistic to suppose that thermal distributions, or even terrain types (e.g., ice, snow, rock, vegetation, lava) are uniform across the instantaneous field of view (IFOV) of the satellite sensor. Volcanic thermal features represent an extreme case when surfaces at ambient and magmatic temperatures occur in very close proximity. Even at high spatial resolutions (for example the nominal 30 x 30 m pixel dimensions of TM bands 1-5 and 7), where a pixel falls across such a region, the derived temperature will lie somewhere between those of the hottest and coolest material present, the actual value being weighted according to the spectral radiance integrated across the whole IFOV of the sensor. In addition, since spectral radiance is a function of wavelength (equation 1.1), temperature derivations will vary according to the spectral bandpass of the sensor. This is the reason why Francis and Rothery (1987), using TM data to examine a lava body in the active crater of Láscar volcano (Chile), observed markedly different pixel-

integrated temperatures in the two short wavelength infrared (SWIR) bands 5 and 7 (at 1.55-1.72 μm and 2.08-2.35 μm, respectively).

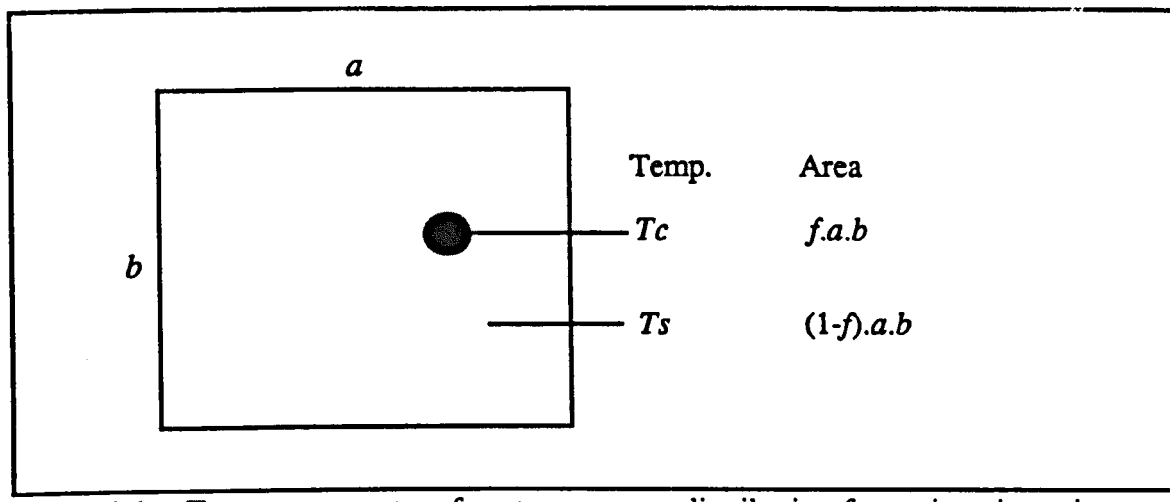

Figure 1.1. Two-component surface temperature distribution for an imaginary image pixel. Ground at the elevated temperature of T_c occupies a fraction f of the nominal pixel area, while cooler ground, at temperature T_s, occupies the remaining portion (1-f).

Dozier (1981) and Matson and Dozier (1981) recognised that such discrepancies (which they observed in AVHRR thermal infrared channels 3 and 4) were explained by the presence of sub-pixel sized hot sources. Dozier (*op. cit.*) stated this as follows: "If one part of a pixel is much warmer than the remainder... [it] will contribute proportionally more radiance to the signal in the shorter wavelengths in the thermal infrared than in longer wavelengths". Both of these papers demonstrated that this effect could be exploited in order to measure the temperatures of the sub-pixel thermal components of the scene. The starting point is a simplified model of the radiant surface which considers only two thermal components (Figure 1.1): a hot portion, at kinetic temperature T_c occupying a fraction f of the pixel, and a cooler part at kinetic temperature T_s occupying the remaining fraction (1 - f). If two channels, of differing central wavelengths λ_x and λ_y, of a remote sensing device detect a thermal anomaly (and neither is saturated) the isolated thermal radiance values, $R_{x,thermal}$ and $R_{y,thermal}$, in each spectral bandpass can be related to this idealised thermal model of the surface as follows:

$$R_{x,thermal} = \varepsilon_x \tau_x [f L(\lambda_x, T_c) + (1 - f) L(\lambda_x, T_s)] \qquad (1.7)$$

and

$$R_{y,thermal} = \varepsilon_y \tau_y [f L(\lambda_y, T_c) + (1 - f) L(\lambda_y, T_s)] \quad (1.8)$$

where ε_x, ε_y are the emissivities (assumed equal for each thermal component), τ_x, τ_y the atmospheric transmissivities in each channel, and $L(\lambda,T)$ the spectral radiance (equation 1.3). Any two of the parameters out of f, T_c and T_s can then be found by graphical or numerical solution of these simultaneous equations, if the third is assumed (choosing also appropriate values for spectral emissivities and transmissivities; see Appendix A2). The errors that arise from the approximation of a central wavelength for the sensor bandpass are small for channels of fine width. Matson and Dozier (*op. cit.*) estimated temperatures of various industrial hot spots, including gas flares, by this method. Notably, they chose to use night-time AVHRR data to obviate the problem of reflected sunlight to which channel 3 (3.55-3.93 μm) is sensitive.

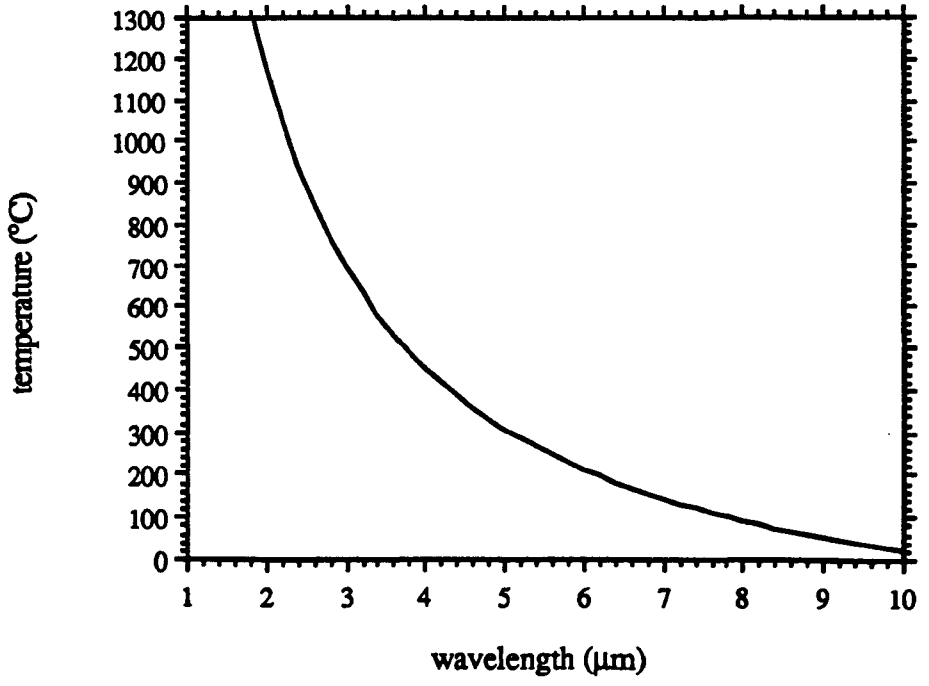

Figure 1.2. Wavelength of peak spectral radiance, λ_{max}, from Wien's displacement law (1.9), for a range of temperatures likely to be encountered on volcanoes.

Adapting this approach, Rothery *et al.* (1988) concentrated on the use of SWIR data, particularly from the TM, for estimating sub-pixel temperatures of magmatic phenomena. The importance of this part of the spectrum can be appreciated by inspection of Wien's displacement law (obtained by differentiating 1.1 with respect to λ),

according to which the wavelength, λ_{max}, of the peak spectral radiant emittance from a black-body source is inversely proportional to its absolute brightness temperature, T:

$$\lambda_{max} T = b \qquad (1.9)$$

where the constant b = 2.89782 x 10^{-3} m K. As surface temperature increases, so the peak in spectral radiance moves to shorter wavelengths. From this relationship, it can be shown that the peak spectral radiance from a surface at magmatic temperatures in the range 800-1250°C corresponds to wavelengths between about 2.7 and 1.9 μm (Figure 1.2). The position of atmospheric 'windows', through which electromagnetic radiation passes with relatively little attenuation (0.4-1.3 μm, 1.5-1.8 μm, 2.0-2.5 μm, 3-5 μm and 8-14 μm) further qualifies the parts of the spectrum favourable for observation of high-temperature volcanic phenomena.

Temperature estimates obtained from TM data have been used to model radiative heat outputs from high-temperature features (Glaze *et al.* 1989a, Pieri *et al.* 1990) using Stefan's law (which is derived by integrating equation 1.3 with respect to wavelength). The total radiant exitance, Q_{rad}, from a perfect black-body varies as the fourth power of its absolute temperature:

$$Q_{rad} = \sigma T^4 \qquad (1.10)$$

where the value of the Stefan-Boltzmann constant, σ, is 5.6687 x 10^{-3} W $m^{-2} K^{-4}$. Glaze *et al.* (1989a) suggested that, with sufficient base-line information for individual volcanoes, variations in radiant energy output could be interpreted in the context of eruption likelihood. In addition, they attempted intercomparisons of the levels of activity of different volcanoes.

1.3.2. Problems

Despite encouraging results from TM investigations of volcanic thermal features, several areas of uncertainty remain.

(i) Solution of the 'dual-band' equations (1.7) and (1.8) requires that the value of one of the parameters f, T_S, and T_C be predetermined in order to quantify the other two.

Rothery *et al.* (1988) assumed the simplest case prevailed in which T_s was sufficiently low that it contributed negligible radiance in the SWIR. Because they wanted to estimate radiated power outputs (1.7) from TM data, Glaze *et al.* (1989a) and Pieri *et al.* (1990) *were* concerned about neglecting background temperatures in this way. They tackled the problem by choosing reasonable values for T_s determined by the operating limits of bands 5 and 7. However, even this procedure is likely to yield rather arbitrary values of Q_{rad}, particularly when the hotter thermal component occupies very small areas.

(ii) The limited number of spectral channels on instruments such as the TM dictates the choice of very simple thermal models in order to make sub-pixel thermal measurements. Field observations (e.g., Flynn *et al.*, 1989; Pieri *et al.*, 1985), support two-temperature models for some basaltic lava bodies but these represent a very small sample of the range of volcanic thermal phenomena. For example, no comparable investigations have been made hitherto for fumarole fields, which are almost ubiquitous on active but often non-erupting volcanoes. Where very shallow magmas are present, fumarole temperatures can be sufficient to cause incandescence of the rock walls of vents and therefore fierce SWIR emission, which can be detected by satellite sensors.

(iii) The radiation which reaches a satellite is a mixture of thermal radiance from any hot features on the ground, and, by day, reflected and backscattered sunlight, *after* interaction with the atmospheric column. The correcting factors for atmospheric transmittance, which appear in the terms τ_x and τ_y in equations (1.7) and (1.8), can be estimated from a variety of standard or user-defined atmospheres provided by codes such as LOWTRAN 7 (Kneizys *et al.*, 1988). However, sensors aimed at hot volcanic features inevitably view through an atmospheric column modified by volcanic effluent.

Concentrations of different volcanogenic gas and aerosol species along the atmospheric path during the instant of observation cannot be constrained by measurements at just a few wavelengths, and their potential effects have barely been considered in previous investigations. Furthermore, since amounts of fumes between ground and satellite sensor are likely to vary over short timescales, if they cause

significant attenuation of ground-emitted SWIR radiation, then comparisons of satellite 'snapshots' acquired at different times may not be meaningful.

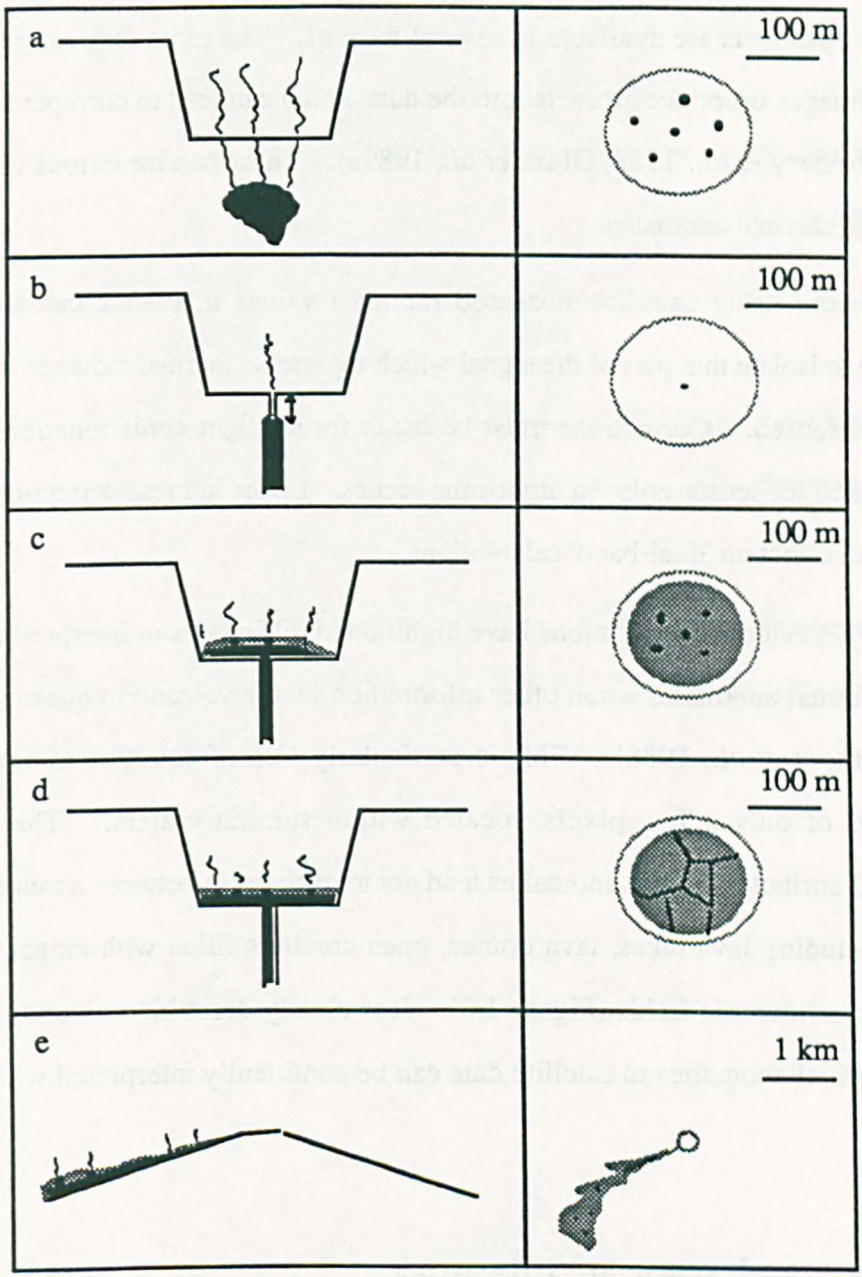

Figure 1.3. Assorted high-temperature volcanic phenomena: (a) fumaroles, (b) an open vent containing magma whose level varies with time, (c) an active lava dome with a cooling carapace, (d) an active lava lake with 'rifting' centres, and (d) an active lava flow. Solid shading indicates material at close to magmatic temperatures. Stipple represents cooler, crusted lava.

(iv) Uncertainties arise in the satellite measurements themselves from characteristics and registration of the spatial responses of sensors, resampling of raw data, and contamination with reflected sunlight. Rothery *et al.* (1988) drew attention to the effects of possible spatial misregistration between the TM bands 5 and 7, hysteresis in

sensor response, and approximation of the sensor wavelengths by the midpoints of their spectral bandpasses. A further concern arises from preprocessing of image data; Landsat TM digital products are available in several formats. The more familiar geometrically rectified images introduce artifacts into the data which can lead to corrupted radiometric results (Rothery *et al.*, 1988, Glaze *et al.*, 1989a). These can be serious in the case of small-sized thermal anomalies.

Before using satellite-measured radiance values in Planck calculations, it is necessary to isolate that part of the signal which represents thermal radiance from the area of ground sensed. Corrections must be made for sunlight contamination in daylight imagery, and for sensor noise in night-time scenes. Errors in these corrections may have a profound effect on 'dual-band' calculations.

(v) Previous investigations have highlighted difficulties in interpreting remotely-sensed thermal anomalies when other information on the volcano in question is lacking (e.g., Rothery *et al.*, 1988). This is particularly true of equidimensional hot spots composed of only a few pixels, located within summit craters. The spatial and contextual attributes of such anomalies tend not to distinguish between a range of possible causes including lava lakes, lava domes, open conduits filled with magma, and high-temperature fumarole fields (Figure 1.3). It is clearly desirable to know the extent to which thermal anomalies in satellite data can be confidently interpreted without ground truth.

1.4. Aims and scope of this work

Several of the grey areas outlined above will be addressed in the chapters which follow. Four primary aims of this work are:

(i) To consider means for obtaining the most useful information from radiometric data of known thermal features. Assuming a value for T_s may not be the best approach to solving the 'dual-band' equations (1.7 and 1.8) and Chapter 2 considers the benefits of predetermining T_c instead, enabling estimation of T_s and f. This method is applied in

analysing a TM image of an active andesitic lava flow at Lonquimay volcano, Chile, recorded in 1989.

(ii) To appraise the reliability of any temperature distribution calculations made using 'dual-band' techniques, given all the assumptions that must be made (1.3.2). Chapters 3 and 4 report the results of surveys of surface temperature distributions at fumarole fields and consider whether representations by two temperature components are appropriate. Radiant temperature measurements were also repeated over intervals from seconds to months in order to document their variability.

(iii) To consider, where spatial clues as to the nature of a thermal anomaly are ambiguous, if multichannel SWIR data can provide *spectral* clues that would assist in identification of anomalies (Chapters 4 and 5).

(iv) To assess the potential of several forthcoming remote sensing instruments equipped with short wavelength infrared sensors for making thermal measurements of volcanic phenomena (Chapter 6).

Chapter 2. Lava flow cooling estimated from Landsat Thematic Mapper infrared data: the Lonquimay eruption, Chile, 1989

Paper in press for *Journal of Geophysical Research*

2.1. Abstract

Surface temperatures of a 1989 andesite lava flow at Volcán Lonquimay, Chile, derived from an analysis of Landsat Thematic Mapper (TM) infrared data, show a progressive cooling of crusted lava from 250°C to 170°C down a 1.5 km segment of the flow. These results are obtained by solving 'dual-band' equations for the two short-wavelength infrared TM bands, assuming that the lava surface can be represented by two thermal components - exposed core and chilled crust - and in contrast to what was done in previous investigations, by predetermining the temperature of the hot component rather than the cool component. This approach is consistent with both observational data and theoretical models, and shows that any exposed core of the flow occupies tiny fractions - possibly less than 0.03% - of the surface area. As a result, the crust made by far the

greatest contribution to radiative heat losses - estimated at between 1 and 3 MW per 30 x 30 m pixel - along most of the flow's length. Convective heat transfer into the air above the flow is about two-thirds the corresponding radiative flux. These estimated surface heat losses suggest thicknesses of less than 1 m for a conductive thermal boundary layer component of the crust. Radiance values in the thermal infrared band 6 of the TM image are consistent with temperatures derived from the short-wavelength infrared data, and reveal the thermal manifestation of a topographic step beneath the flow.

2.2. Introduction

The sensitivity of the infrared channels of several operational remote sensing satellites to high-temperature, subpixel resolution thermal sources is well established. In a volcanic context, the thermal signatures of lava bodies (including open vents/ lakes, flows and domes), hot tephra and high-temperature fumarole fields have been identified in satellite data (Williams and Friedman, 1970; Wiesnet and D'Aguanno, 1982; Scorer, 1986; Francis and Rothery, 1987; Glaze *et al.*, 1989a,b; Oppenheimer, 1989). Because the temperature distributions of such features are typically inhomogeneous at the scale of image pixels of orbital remote sensing data, calculation of single-channel, 'pixel-integrated' temperatures is rather uninformative. For example, even an elementary description of active lava surfaces would consider two end-member temperature components: one representing incandescent regions such as cracks or shear margins, T_c, the other the surrounding, cooler crust, T_s. A pixel-integrated temperature measurement of such a surface would fall somewhere between T_c and T_s and could not be used to derive a meaningful estimate of the radiant energy flux (Rothery *et al.*, 1988).

Numerous physical processes, including degassing, crystallization, solidification and radiative cooling, influence the rheology of lava during its emplacement and hence the eventual dimensions and morphologies of flows. Consequently, many physical models have been proposed to describe lava flow behaviour, which give different weight to the importance of factors such as radiative cooling, viscosity, yield strength and effusion rates. A recent model is that of Crisp and Baloga (1990a) who assert that the rate of heat

loss by radiation from the top of surface-fed, single-lobed flows can exert significant control over a flow's cooling history. Their treatment is attractive from a remote sensing standpoint because it considers the flow surface to consist of two end-member thermal components, namely an exposed inner core, and a cooler crustal boundary layer, at temperatures T_c and T_s, respectively. A third important parameter is the fractional area of the high-temperature component, f, (the fractional area of the crust then being given by [1-f]). Together with spectral emissivities, these quantities define an idealized model of the radiative properties of the lava surface.

I attempt here to use Landsat Thematic Mapper (TM) data to measure T_s and f for an active lava flow. Although this characterization undoubtedly oversimplifies true thermal distributions, it is certainly more realistic than previous models of radiative losses which supposed flows to be isothermal in cross-section perpendicular to the flow direction (e.g. Daneš, 1972; Hulme and Fielder, 1977; Park and Iversen, 1984; Dragoni *et al.*, 1986; Dragoni, 1989). Some evidence for the inadequacy of the 'thermally mixed' case to describe real observations was presented by Pieri and Baloga (1986), whose favoured model considered surfaces of flows to radiate at temperatures substantially below those of their interiors.

2.3. Dual-band calculations

The underlying principle for deriving surface temperatures from remotely sensed data is the Planck distribution law, according to which spectral radiant intensity emittance $H(\lambda,T)$ is a function of black-body absolute temperature, T, and wavelength, λ :

$$H(\lambda,T) = c_1\lambda^{-5}[\exp(c_2 / \lambda T) - 1]^{-1} \qquad (2.1)$$

where the constants c_1 and c_2 have the values 3.74127×10^{-16} W m^2 and 1.4388×10^{-2} m K respectively. For isotropic radiation, $H(\lambda,T)$ is independent of direction, and the spectral radiance, $L(\lambda,T)$ is given by:

$$L(\lambda,T) = H(\lambda,T) / \pi \qquad (2.2).$$

To estimate brightness temperatures, pixel-by-pixel, from satellite data simply requires calibration of the raw radiance signal measured at the satellite, and selection of a central wavelength for the sensor in question (an approximation which is generally good for channel bandpasses of fine spectral-width). Corrections for sky radiance, solar reflection, sensor noise and atmospheric atennuation can be made as necessary.

However, if a pixel contains two (or more) thermal components, such pixel-integrated temperatures measured at distinct wavelengths should differ because of the relationship expressed in (2.1). This observation underlies the investigation of subpixel-sized thermal sources. In the case of our idealized lava flow with just two thermal components, detected by two sensors of unequal central wavelengths λ_x and λ_y, any two of the parameters f, T_c and T_s may be obtained if the third is assumed. Adapting the method of Matson and Dozier (1981), this is achieved by numerical or graphical solution of the 'dual-band' equations:

$$R_x = \varepsilon_x \tau_x [f\mathrm{L}(\lambda_x, T_c) + (1 - f)\mathrm{L}(\lambda_x, T_s)] \tag{2.3}$$

and

$$R_y = \varepsilon_y \tau_y [f\mathrm{L}(\lambda_y, T_c) + (1 - f)\mathrm{L}(\lambda_y, T_s)] \tag{2.4}$$

where R_x and R_y are the spectral radiances of thermal origin measured in bands x and y respectively, and ε_x, ε_y are the emissivities of the lava surface (assumed equal for each thermal component) and τ_x, τ_y the atmospheric transmissivities in each channel. Clearly, appropriate values for ε_x, ε_y, τ_x and τ_y must also be decided upon.

Using this method, Rothery *et. al.* (1988) demonstrated the value of short-wavelength infrared (SWIR) data, particularly from Landsat TM sensors 5 and 7, for radiometric measurements of high-temperature volcanic features. They solved the dual-band equations (2.3) and (2.4) to estimate f and T_c for several eruptive phenomena, by ignoring the component T_s on the grounds that it would be too cool to make a significant contribution to the total SWIR radiance. The range of thermal distributions that can be measured by the TM instrument depends on the sensors' dynamic ranges, and is illustrated in Figure 2.1 as a function of fractional area of a single, significant temperature

component, for Landsat TM bands 3 (0.63-0.69 μm), 4 (0.76-0.90 μm), 5 (1.55-1.72 μm) and 7 (2.08-2.35 μm).

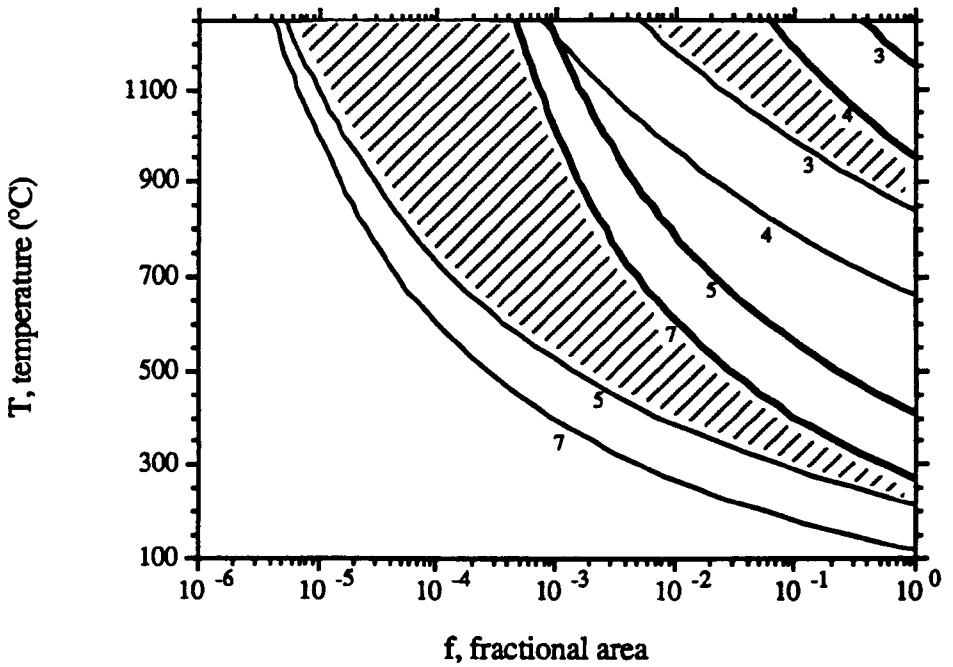

Figure 2.1. TM band 7, 5, 4 and 3 sensitivities to sub-pixel sized high-temperature sources, calculated for unit emissivities and atmospheric transmissivities. In this two thermal component model, the background is assumed to be sufficiently cool so as not to contribute significantly to the radiance at the wavelengths represented. The thin curves show the lower sensitivity limits of each sensor (calculated using a DN of 5 as a realistic minimum detectable anomaly - easily achievable in low-noise night-time data) and the bold curves represent sensor saturation. Shaded fields signify where dual-band calculations are feasible - note that not all possible situations are measurable in this way. Curves were computed using spectral dynamic ranges of TM sensors presented by Markham and Barker (1987).

Having estimated f and T_c, the next logical step is to attempt to measure the radiated component of the power output of the hot feature, the radiant exitance, Q_{rad}. This may facilitate multi-temporal monitoring of the same volcano as well as gross intercomparisons between the power outputs of different volcanoes (Glaze *et al.*, 1989a). However, in doing this it is unreasonable to ignore background temperatures, as can be seen by inspection of Stefan's law:

$$Q_{rad} = \sigma\varepsilon S[fT_c^4 + (1-f)T_s^4] \qquad (2.5)$$

where σ is the Stefan-Boltzmann constant (5.67×10^{-8} W m^{-2} K^{-4}), ε is emissivity and S is surface area (nominally 900 m^2 for TM pixels excepting the 10.4-12.5 μm [thermal infrared] band 6 which has 120 x 120 m pixels). High values of T_c^4 are offset by low

values of f, and the background can potentially make a significant, or even dominant, contribution to the total power output. Glaze *et al.* (1989a) and Pieri *et al.* (1990) tackled this problem by choosing reasonable values for T_s within the ranges bracketed approximately by band 5 and 7 minimum and maximum sensitivities (360°C for pixels where both bands 5 and 7 were saturated, 230°C if only band 7 was saturated, otherwise 125°C). Nevertheless, even this is likely to lead to somewhat arbitrary determinations of Q_{rad}. Furthermore, the values for T_c derived in this way tend to vary widely and, in the case of lava flows, in an inconsistent fashion downflow (Pieri *et al.*, 1990). Although these latter points are not necessarily unrealistic, it is possible that the assumption of only two thermal components is invalid, or the values chosen for T_s are inappropriate. For these reasons I propose an alternative approach to the 'dual-band' problem: rather than assume T_s, I pick a suitable value for T_c, based in this case on field measurements, and then calculate T_s and f. Solution of the 'dual-band' equations was performed numerically, making T_s the subject of equations (2.3) and (2.4), and iterating f from an initial value until T_s was approximately equal in both TM bands 5 and 7. To examine this method, I have studied a TM image, acquired on 8th August 1989, of an active flow at Lonquimay volcano in the southern Andes of central Chile.

2.4. Thermal measurements

The Lonquimay eruption, which began on 25 December 1988, was sited along a fissure previously active in 1887-9, on the northeast flank of the 2 865 m high Volcán Lonquimay (Moreno and Gardeweg, 1989). A pyroclastic cone, named Navidad, grew to an eventual height of over 200 m, while andesitic lava (approximately 58 wt% SiO_2) was erupted from its base until January 1990, by which time the total length of the main flow lobe exceeded 10 km (Figure 2.2). The surface of the flow generally had a black, rather coarse aa crust (Moreno and Gardeweg, 1989), but was sometimes more blocky. Observations by the author and others in March 1990 of the then-inactive flow suggested mean flow thicknesses in the region of 10 m but up to 60 m at the most distant flow front (near Lolco).

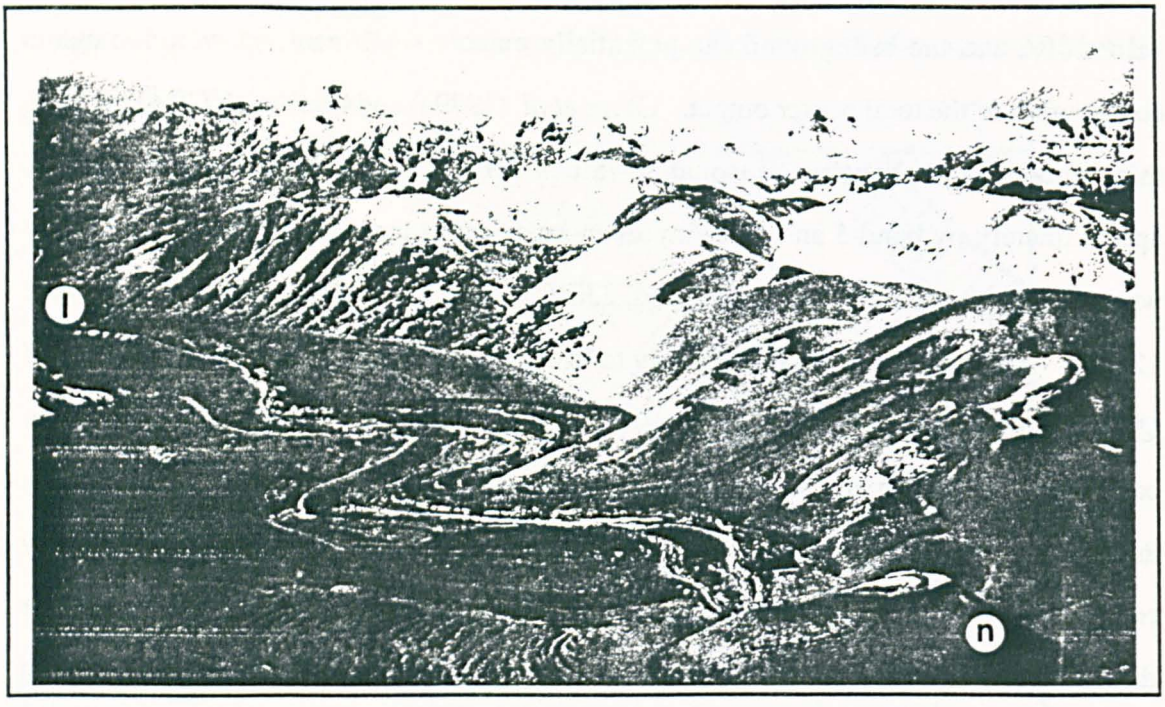

Figure 2.2. Photograph of most of the 1988-90 Lonquimay flow taken from the summit of Volcán Lonquimay (2 865 m above sea-level), looking approximately north. Navidad cone is denoted *n*; the flow front at Lolco is seen at *l*. The 1.5 km long segment of the lava flow studied in detail with the TM data is between the arrows.

The levées were typically composed of a poorly-sorted lower pink-red coloured zone, packed with rounded clasts in a fines-rich matrix, welded in places but elsewhere wholly unconsolidated, overlain by 1-3 m of well-sorted, black, rubbly aa consisting of rounded fragments and lacking matrix. Many bombs had been incorporated in the flow top. An additional surface morphology discovered was of more blocky to unfragmented lava composed of spiny or platy protrusions, up to 3 m high, with deeply recessed fissures in which incandescence was still visible. Unfortunately, there were few field observations of the flow during the (southern hemisphere) winter when the TM image was acquired, so that the surface texture of the flow prevailing at the time is uncertain.

In addition, actual flow widths during this period are not well constrained; reports vary from average widths of 300-400 m in January 1989 (Smithsonian Institution, 1989a) to near-source widths of only 7-12 m in January 1990 (Smithsonian Institution, 1990c). The flow width is important because, strictly, it should be sufficiently great for 30 x 30 m TM pixels to fall wholly within the active flow, for the two thermal component model to be reasonable - otherwise three, or more, components may be necessary.

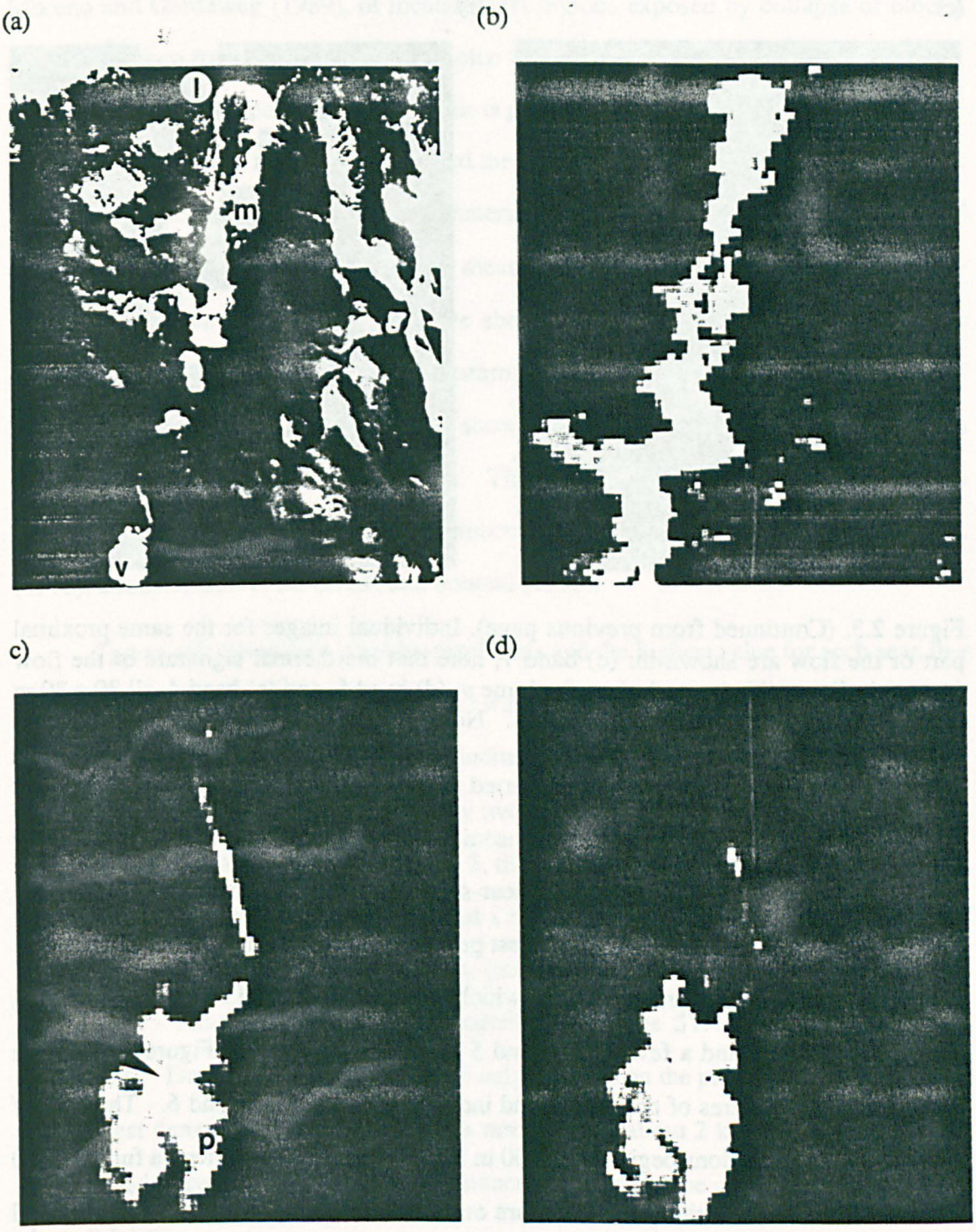

Figure 2.3. TM images of the Lonquimay lava flow on 8 August 1989, constructed from A-format, computer-compatible tape (CCT) data which preserve radiometric fidelity (scene ID number - Y4258014082X0, TM path / row - 233 / 086, quad - 4): (a) band 7, 5, 4 composite and (b) band 6 images of the whole flow. The vent is at *v*; fume or smoke from burning vegetation can be seen along the flow margins, e.g. at *m*; the active flow front at Lolco is denoted *l*. The bulk of the thermal observations presented here span the portion of the flow between the arrows. (Continued overleaf).

(e) (f)

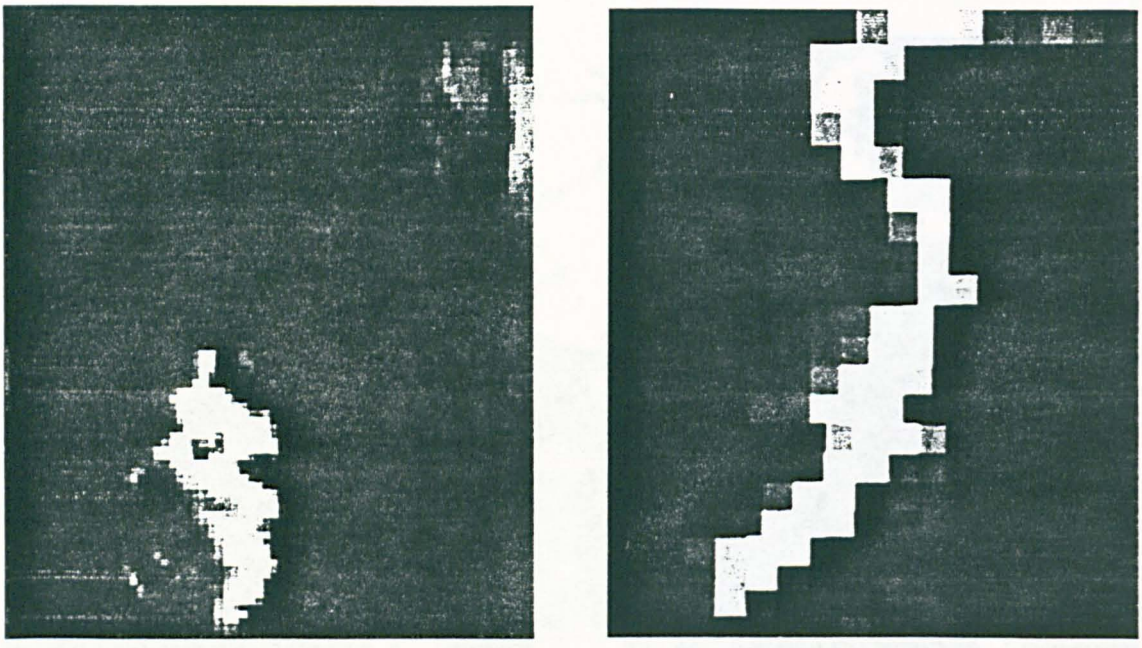

Figure 2.3. (Continued from previous page). Individual images for the same proximal part of the flow are shown in: (c) band 7, note that the thermal signature of the flow (arrow) is discernible beneath the ash plume *p*, (d) band 5, and (e) band 4, all 30 x 30 m pixels, and (f) band 6, 120 x 120 m pixels. North is up in all scenes.

In July 1989, a new vent was reported to have opened 80 m below an active lava pond which subsequently drained (Smithsonian Institution, 1989e) and, by November 1989, lava was still being erupted with near-source velocities estimated at 50-55 m h^{-1} (Smithsonian Institution, 1989f). The most proximal part of the flow in the TM scene is partly obscured by an ash and gas plume which appears bright in all reflective bands, and many of the band 7 and a few of the band 5 pixels are saturated. Figures 2.3 a-f are black and white pictures of composite and individual bands 7, 5, 4 and 6. The bulk of the dual-band calculations begin about 500 m from the source, and extend a further 1500 m downflow. Beyond this point there are only isolated band 7 thermal anomalies and little or no detectable thermal radiance in band 5, although the whole of the flow is warm in band 6 (Figure 2.3b).

2.4.1. Crust temperatures

In solving the dual-band equations, a kinetic temperature of 1040°C was assumed for the incandescent cracks, based on optical pyrometer measurements, reported by

Moreno and Gardeweg (1989), of incandescent regions exposed by collapse of blocks and within deep fractures at the distant Lolco flow front (over 9 km from the vent). In reality, the isothermal part of a flow interior is probably almost never truly exposed for aa lavas except, perhaps, right at the vent, and therefore any such temperature measurement is more likely to represent incandescent material radiating at a temperature below that of the core. Indeed, radiative temperature measurements of incandescent parts of active basaltic pahoehoe flows in Hawaii have shown rapid and substantial drops in skin temperature (A. Jones, personal communication, 1991; D. Pieri, personal communication, 1991). However, as is shown later, the determination of T_s is, in this case, quite insensitive to the choice of T_c. The value chosen for emissivity was 0.95 in both bands 5 and 7, based on reflectance spectra for andesites measured by Pollack *et al.* (1973), Bartholemew *et al.* (1989) and Pontual (1990).

T_s was calculated on a pixel-by-pixel basis and the highest value for each scan line (usually in the centre of the flow anomaly) was taken as most representative because the edges of the anomaly are more likely to include cold regions beyond the flow margins, and so not be adequately modelled by only two thermal components (Table 2.1). Where there was no anomalous radiance in band 5, the band 7 pixel-integrated temperature was calculated, and where band 7 was saturated a minimum estimate of T_s and maximum of f were made using the dual-band equations; (unless band 5 is saturated, T_s should be less than 410°C - considerably less if the contribution to the SWIR radiance from T_c is significant). Dual-band calculations were only possible on the proximal part of the flow; the greatest density of measurements was made within about 2 km of the vent. At the time of the image acquisition, the total distance to the active toe of the flow at Lolco was about 9.5 km.

Figures 2.4a and b show the dual-band derived, crust-surface temperatures, T_s plotted against distance downflow. They reveal an overall cooling trend - from about 250°C at 0.5 km to 170°C at 2.0 km from source - on which are superimposed at least two pronounced departures, one to lower temperatures at 0.8 km, the other to higher temperatures at 1.3 km. In the absence of turbulent mixing of the flow or steady-state

tubeflow, the crustal boundary layer is expected to thicken with time. Since lavas have low thermal conductivities, heat cannot be transferred rapidly enough by thermal conduction from the core to balance thermal losses at the surface. The crust surface of a given parcel of lava therefore cools with time, and hence distance from the source because this is a function of time spent in transit.

This effect is predicted by a conductive crust model presented by Crisp and Baloga (1990a, see their Figures 7 and 10), although direct comparison of their model with the TM results has not been attempted here due to the lack of flow-velocity measurements for the Lonquimay lava. The cooling is also consistent with field observations such as those of Pieri *et al.* (1985) who used a thermal infrared television camera to image basaltic flows during the 1984 Mauna Loa (Hawaii) eruption, and Jones *et al.* (1990) who used hand-held infrared thermometers to measure radiant temperatures of the 1990 Kilauea (Hawaii) lavas.

The anomalous points on Figure 2.4a are suggestive of transient phenomena since they do not perturb the cooling trend for more than a few pixels downflow, although it may be significant that the group of about four comparatively 'cool' pixels (equivalent to around 120 m, none of them radiant in band 5) at 0.8 km from source, coincides with a 90° change in direction of the flow (Figure 2.3c). Changes of slope or channel geometry are likely to influence the state of stress in the flow crust. Alternatively, this cool segment may have resulted from slumping of debris from Navidad cone onto the surface of the moving flow. Such a carpet of debris, 1-3 m thick, was observed during fieldwork on the then inactive flow in March 1990 (Smithsonian Institution, 1990c). I measured surface temperatures of up to 207°C with a Minolta / Land Cyclops 33 infrared thermometer (8-14 μm bandpass) on parts of the debris, though such high temperatures were by no means uniform, and may only have been associated with rootless fumaroles. Inward slumping of part of the wall of the active crater was also observed on August 10 (Smithsonian Institution, 1989e), only two days after the TM image was recorded. The hot region at 1.3 km suggests either that enhanced thermal renewal of the surface (exposure of core) took place on this flow segment during transit (see Figure 1 in Crisp

and Baloga, 1990a), or that some change in conditions took place at the vent during the eruption of this parcel of lava.

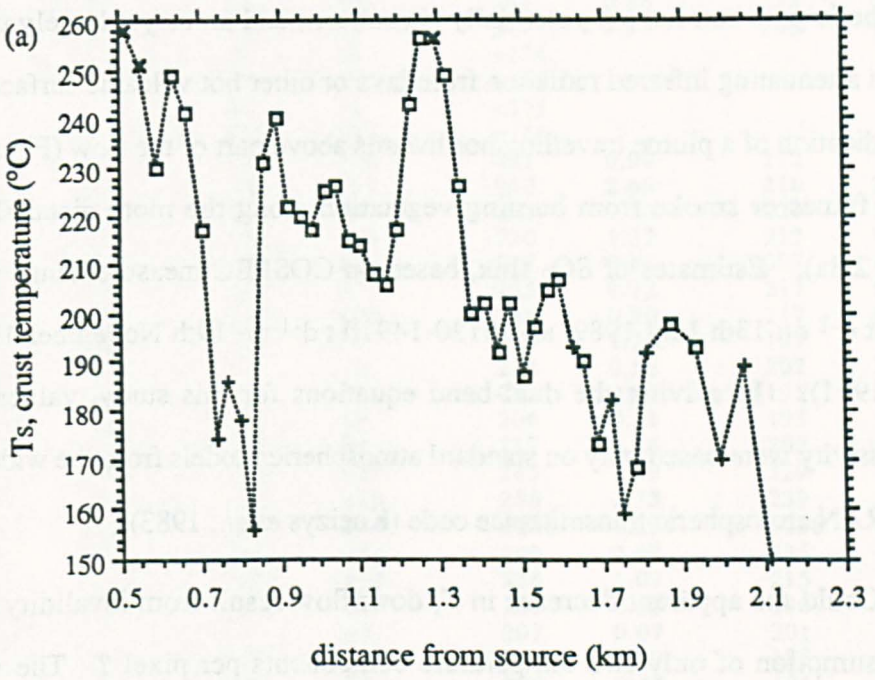

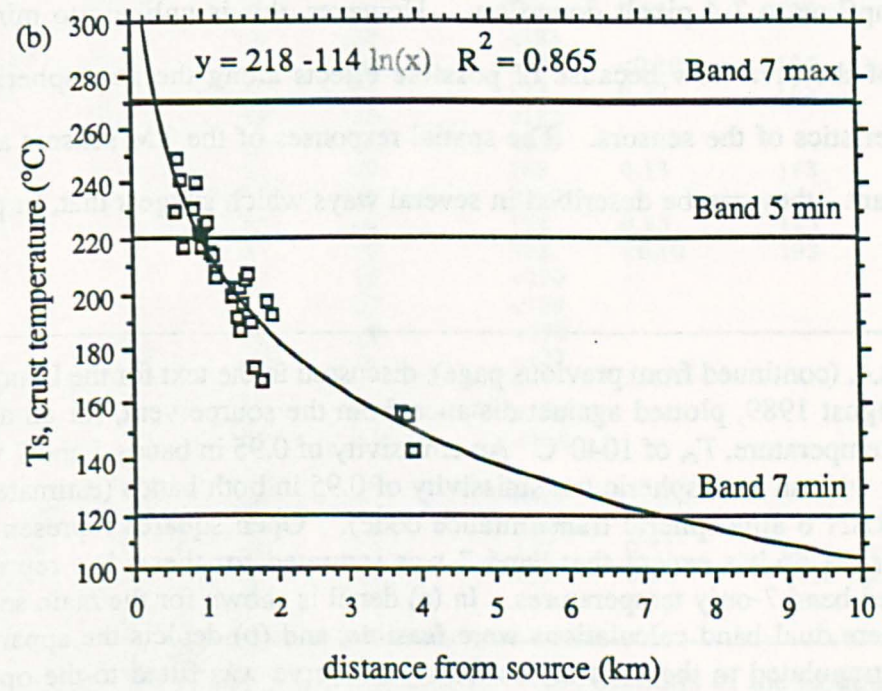

Figure 2.4. Crust temperature derived by the dual-band method (continued overleaf)

A concise treatment of some of the errors in remote sensing measurements of subpixel temperatures, due to effects of the atmosphere and sensor optics, is given by Rothery *et al.* (1988). It should be emphasised that volcanogenic fumes in the atmospheric path can have a potentially significant, and an as yet largely unquantified, effect in attenuating infrared radiation from lava or other hot volcanic surfaces. There is clear indication of a plume travelling northwards above part of the flow (Figure 2.3c-e) as well as fumes or smoke from burning vegetation along the more distal flow margins (Figure 2.3a). Estimates of SO_2 flux, based on COSPEC measurements, ranged from 80-300 t d^{-1} on 13th July 1989, and 5130-14910 t d^{-1} on 19th November 1989 (Andres *et al.*, 1991). In solving the dual-band equations for this study, values chosen for transmissivity were based only on standard atmospheric models from the widely available LOWTRAN atmospheric transmittance code (Kneizys *et al.*, 1983).

Could the apparent decrease in T_s downflow result from invalidity of the dual-band assumption of only two temperature components per pixel ? The width of the thermal signature in band 7 perpendicular to the flow direction ranges between about 3-6 pixels upflow to 2-4 pixels downflow. However, this is unlikely to mirror the true width of the lava flow because of possible effects along the atmospheric path, and characteristics of the sensors. The spatial responses of the TM sensors are probably significant - they can be described in several ways which suggest that, in practice, the

---

Figure 2.4. (continued from previous page). discussed in the text for the Lonquimay flow on 8 August 1989, plotted against distance from the source vent, for an assumed hot 'crack' temperature, T_c, of 1040°C An emissivity of 0.95 in bands 5 and 7 was chosen, together with an atmospheric transmissivity of 0.95 in both bands (estimated using the LOWTRAN 6 atmospheric transmittance code). Open squares represent dual-band solutions, as do 'x's except that band 7 was saturated for these; '+'s represent pixel-integrated band 7-only temperatures. In (a) detail is shown for the main section of the flow where dual-band calculations were feasible, and (b) depicts the apparent cooling trend extrapolated to the ends of the flow - the curve was fitted to the open squares, excluding the four at about 1.3 km. The TM instrument can provide thermal data for a small section of the flow only. Operating limits of bands 7 and 5 are represented by horizontal lines.

Line no.	Band 5 DN		Band 7 DN		T_c = 1040°C		T_c = 740°C	
	raw	corrected	raw	corrected	T_s (°C)	f (x 1e-4)	T_s (°C)	f (x 1e-4)
2942	55	28	255	221	>258	<1.76	>249	<13.68
2941	61	41	255	228	>251	<3.11	>230	<23.91
2940	36	18	144	120	230	1.15	219	8.78
2939	42	22	193	175	249	1.34	240	10.36
2938	32	16	161	141	241	0.86	235	6.61
2937	29	15	107	89	217	0.95	205	7.21
2936			34	20	<174			
2935			42	28	<186			
2934			34	22	<178			
2933			27	12	<156			
2932	30	16	129	116	231	0.96	222	7.32
2931	47	35	195	182	240	2.68	216	20.44
2930	23	8	93	81	222	0.26	220	1.99
2929	32	19	115	113	220	1.32	212	9.73
2928	28	14	101	87	217	0.86	207	6.48
2927	25	13	108	97	225	0.72	217	5.47
2926	32	15	114	104	226	0.90	217	6.85
2925	33	18	107	93	215	1.25	197	9.40
2924	28	10	87	72	214	0.50	207	3.75
2923	29	13	86	71	208	0.80	195	6.06
2922	28	13	84	69	206	0.81	193	6.10
2921	32	17	109	94	217	1.14	202	8.62
2920	43	26	182	168	243	1.79	229	13.76
2919	57	38	251	236	256	2.75	239	21.28
2918	58	40	255	241	>256	<2.94	>238	<22.72
2917	50	30	211	196	249	2.09	235	16.11
2916	33	17	127	109	226	1.09	215	8.28
2915	26	10	70	55	200	0.55	190	4.11
2914	23	5	60	45	202	0.07	201	0.52
2913	22	6	52	38	192	0.19	188	1.41
2912	24	9	68	55	202	0.45	195	3.35
2911	21	7	50	36	187	0.30	179	2.20
2910	21	6	57	42	197	0.18	193	1.34
2909	21	8	68	56	205	0.34	200	2.57
2908	22	10	73	63	207	0.53	199	3.95
2907			44	34	<193			
2906	18	5	44	34	190	<0.10	188	7.35
2905	19	6	37	25	173	0.22	165	1.62
2904			40	25	<182			
2903			26	13	<159			
2902	14	5	29	20	168	0.13	163	0.96
2901			43	33	<192			
2900	23	11	65	55	198	0.65	185	4.85
2899	16	4	47	35	193	<0.10	193	<0.10
2898			29	18	<170			
2897			42	30	<189			
2896			26	10	<150			
2895			20	5	<122			
2887			23	10	<150			
2886			27	15	<164			
2878			19	10	<150			
2877			25	10	<150			
2876	26	11	45	30	157	0.71	does not converge	
2875	29	12	47	32	156	0.80	does not converge	
2874	24	5	23	12	143	0.14	129	1.05

Table 2.1. Raw DN values in bands 5 and 7 for the sections of the Lonquimay flow studied. The scan-lines are listed in the downflow direction, that is approximately south to north. Corrections for reflective DN are also shown, with the results of temperature calculations given for two cases, T_c = 1040°C, and T_c = 740°C.

area of terrain sensed by the TM bands 1-5 and 7 somewhat exceeds the nominal 30 x 30 m pixel dimensions (e.g. Markham, 1985). Consequently, thermal anomalies are likely to be smeared out in both the along- and across-track directions, and indeed this is evident in a TM image (recorded in 1986) of a basaltic andesite flow on Arenal volcano, Costa Rica, described by Rothery *et al.* (1990). By coincidence, shortly before this TM scene was acquired, a high resolution panchromatic air photograph had been taken. Geographic co-registration of the two images, showed that although the active flow was less than 15 m in width, up to three TM pixels perpendicular to the flow direction were 'hot'. Scattering of infrared radiation by aerosols may also be responsible for blurring thermal anomalies (Rothery *et al.*, 1988). SWIR images acquired from aircraft over lava flows and ponds in Hawaii have shown broad haloes around the hot features in the channel equivalent to TM band 7, an effect thought to be the result of scattering by aerosols (L. Glaze, personal communication, 1990).

Regarding the Lonquimay TM image, the decrease in the number of radiant pixels per scan-line downflow could simply be a consequence of such blurring effects being more prominent closer to the source where the lava surface is hotter. It may also reflect a real progressive narrowing of the channel width (in response, for example, to debris-shedding to form levées). If pixels do contain significant portions of much cooler ground because they straddle the flow margin, then the dual-band calculations will underestimate the true crust temperature of the active flow. This possible effect was examined by allowing for up to half of pixel areas to be at an essentially non-radiant temperature (in the SWIR); simplistically, this would be representative of a flow of width between 15 and 30 m depending on where the flow falls within a given pixel. Recalculating the dual-band crustal temperatures in this fashion produces increases of between 23° and 27°C beyond about 1.5 km downflow, and I suggest that such potential errors are insufficient to account for the apparent decay in crustal temperatures downflow. Furthermore, it is as plausible that the channel widened downflow, in which case, if near-vent pixels were only half occupied by active flow, then upflow crust-surface

temperatures would be increased by about 28° and 31°C, augmenting the apparent downflow cooling trend.

A bonus of this TM image is that generally the 'cool' pixels next to the active flow are quite dark: band 7 and 5 digital numbers (DN) fall mostly in the range 10-15 for the studied length of flow; (digitization of the TM radiometric measurements results in a single number between 0 and 255 assigned to each individual pixel). Correction for the contribution of reflected sunlight to the DN of the thermally radiant flow pixels (accomplished on a line-by-line basis by interpolating the DN in adjacent pixels of bands 5 and 7, and by inspection of the wholly reflective response in band 4) was, therefore, comparatively accurate. Uncertainty of ± 5 DN in the determination of radiance for bands 5 and 7 produces errors in crust temperature of only about ± 5°C in most cases but this error increases to ± 15°C where DN are very low (further away from the vent). For most of the pixels examined here, T_s is quite unresponsive to changes in T_c. The value of 1040°C chosen may be open to question, and indeed, lower temperatures of 934°C and 948°C, were measured by thermocouple within 2 km of the vent (Smithsonian Institution, 1989e, 1990c), although this latter value was obtained some weeks after the effusion of lava had ceased. Nevertheless, decreasing T_c by 100°C from 1040°C results, in most cases, in less than 5°C decrease in the solution of T_s. This effect works in favour of enhancing the apparent cooling, since allowing T_c to decrease systematically downflow would lower T_s (while increasing f). Even recalculating T_s when T_c is taken as only 740°C has a fairly limited effect (Table 2.1).

2.4.2. Fractional area of exposed core, f

Figure 2.5 depicts the fractional area, f, of incandescent 'cracks', assumed to be exposed core, simultaneously derived with T_s by the dual-band method, plotted as a function of distance along the flow. For pixels where the dual-band calculation was not possible because of lack of anomalous radiance in band 5, f was set to 10^{-5}, consistent with the channel's lower sensitivity limit at the chosen T_c of 1040°C (Figure 2.1). In their two-thermal component flow model, Crisp and Baloga (1990a) picked, for

mathematical convenience, a constant value of f as a function of time (and therefore distance) while acknowledging that this was an over-simplification. Inspection of Figure 2.5 suggests at least an order of magnitude variation in f, the trend being towards lower values downflow. This indicates a general lack of thermal renewal of the flow surface and is also clearly consistent with the observations of band 5 and 7 saturation closer to the source vent, and very little thermal radiance in the SWIR bands beyond about 2 km downflow (Figure 2.4b). This apparent decrease in f for an andesitic aa flow probably contrasts with the distribution of cracks on some pahoehoe flows which rapidly develop a thin skin or tubes (e.g. Rowland and Walker, 1990) while budding and exposing magmatic core at their advancing flow fronts. Note that the peak in crustal temperatures at 1.3 km from the flow source in Figure 2.4a corresponds also to a peak in f. The correlation between f and T_s for the portion of flow studied is displayed in Figure 2.6.

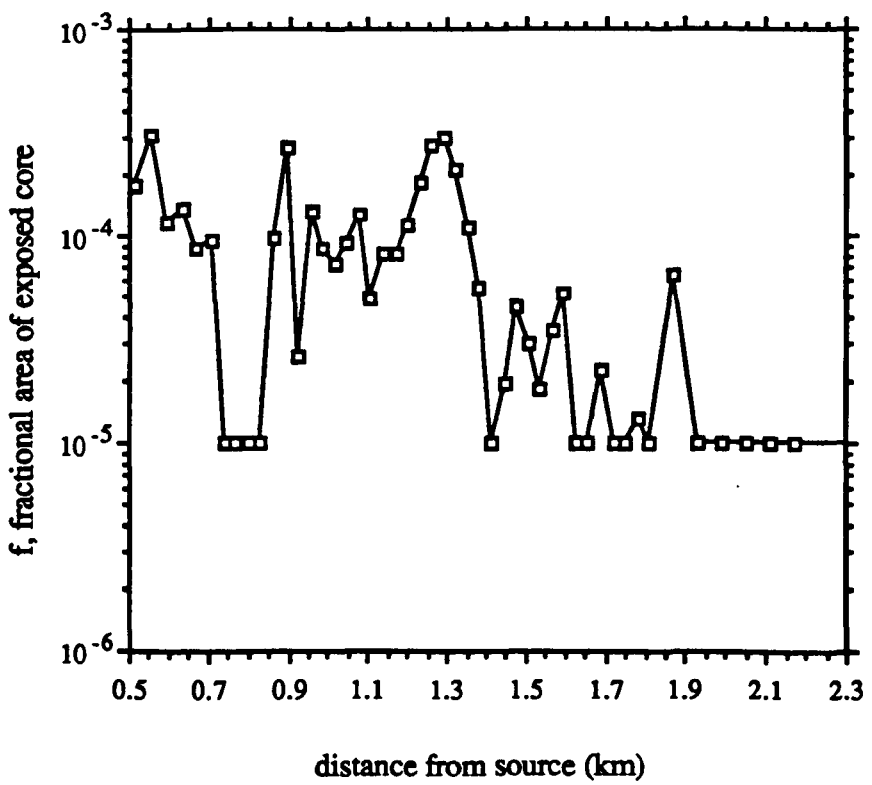

Figure 2.5. The fractional area of 1040°C material exposed at the flow top plotted against distance along the flow. Where there was no thermal radiance resolvable in band 5, f was set to 10^{-5}.

The values calculated for f are small (most are less than 0.03% for the length of flow examined, which, assuming a pixel area of 900 m^2, is equivalent to only about 0.3 m^2 per 30 x 30 m pixel), compared with values predicted by Crisp and Baloga (1990a), which range between 0.1 and 10 %, and used by them to estimate flow rates of planetary lavas (Crisp and Baloga, 1990b). The reason for this may reflect the slower advance rate of the Lonquimay flow and the different physical processes creating crust and exposing core involved in the emplacement of an andesitic aa or blocky flow, compared with the basaltic flows studied in Crisp and Baloga (1990a, b), although Pieri *et al.* (1990) also found f fractions between 0.01 and 0.1% from analysis of a TM image of the 1984 Mount Etna (Italy) basaltic flow. However, and this is one of the limitations of the TM data, if f were to exceed approximately 0.1% for lava at around 1000°C, band 7 would saturate and dual-band calculations would no longer be strictly applicable.

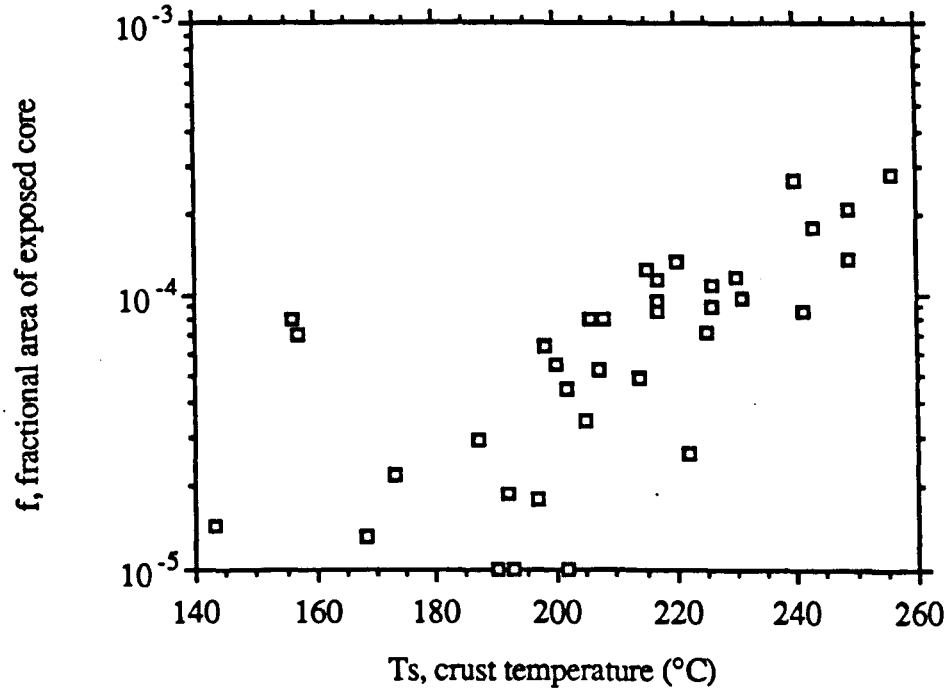

Figure 2.6. Correlation between f and T_s for pixels along studied length of flow for which the dual-band calculation was possible.

Most of the upflow part of the 1984 Mount Etna aa flow in the TM image used by Pieri *et al.* (1990) was saturated in band 7 and, to a lesser extent, band 5, indicating higher values of f. Likewise, the Arenal TM image described by Rothery *et al.* (1990)

exhibits this problem; many of the pixels along the 700 m long flow are saturated in band 7 suggesting values of f between 0.1-0.2% where band 5 is not saturated, and/or higher crust-surface temperatures (all the more so given that the active flow was significantly narrower than a single 30 x 30 m pixel). It must also be noted that proportional errors in the derivation of f are likely to be considerably more substantial than for T_s. Uncertainty of ± 5 DN in the correction for reflected sunlight produces variation of up to 35-80% in f. Also, if T_c has been chosen too high, then f will be underestimated. Decreasing T_c to 940°C typically doubles the value of f; decreasing T_c further to 740°C produces an approximately eight-fold increase over the value of f calculated for T_c = 1040°C (Table 2.1).

Unfortunately, there appear to be no comparable field observational data on f for lava flows. However, some estimates have been made for lava lakes, and it is instructive to consider these because they relate to potential TM measurements. Among them are those of Flynn *et al.* (1989) who used an infrared field spectrometer to characterize emittance spectra of the Kupaianaha lava lake (Hawaii). The instrumental field of view covered 1-3 m^2 portions of the lake surface. During quiescent phases, crust temperatures of 225-425°C were estimated; incandescent material was at temperatures of 725-1025°C for fractions of 0.05-0.1% of the surface. Much of this range would produce radiance within the dynamic ranges of TM bands 5 and 7 (Figure 2.1) and hence dual-band calculations should be feasible. However, during the (rarer) periods of rifting of the lake surface, crust temperatures increased to 525-725°C and the fractional area of the hottest material at 825-1175°C to 1-3 %. Infrared thermometer measurements of flows draining the Kupaianaha lava lake, by Jones *et al.* (1990), revealed similar temperature ranges. Such conditions would easily produce saturation in TM bands 5 and 7, and the higher temperatures and f values in this range should even produce measurable radiance in band 4. (From Figure 2.1, radiance from 1% of a pixel at 1000°C should just be detectable in band 4 and as f increases to 10% the thermal radiance will be at the lower sensitivity limit of band 3). Likewise, the 1984 Mauna Loa eruption produced flows

that, on the basis of thermal infrared data presented by Pieri *et al.* (1985), would also saturate TM bands 5 and 7 for much of the flow length.

To date, no volcanic thermal anomalies have been detected in TM bands at shorter wavelengths than band 5, although the 1979 basaltic lava flow at Sierra Negra (Galápagos) did produce detectable thermal radiance in Landsat Multispectral Scanner (MSS) channels 5 (0.7-0.8 μm), 6 (0.7-0.8 μm) and 7 (0.8-1.1 μm) despite its larger nominal pixel size of 79 m (Rothery *et al.*, 1988). As Crisp and Baloga (1990a) point out, f is a parameter which deserves more attention in future - large values of f, typical of upper reaches of active flows, or perhaps induced downflow by sudden breaks in slope, changes in channel width, levée breaching, etc., could induce very rapid cooling of a flow. An effective way of making ground measurements of spatial temperature distributions would be to adopt the field spectrometry methods of Flynn *et al.* (1989), or the use of thermal infrared scanning television systems (Pieri *et al.*, 1985).

2.4.3. Thermal infrared band 6: estimation of active flow width

The thermal infrared (TIR) band 6 is generally unsuitable for simultaneous measurement of thermal distributions in conjunction with the SWIR bands because of its greater pixel dimensions. One band 6 pixel is equivalent in nominal area to sixteen of any of band 1-5 and 7 pixels. Nevertheless, it is instructive to examine the information provided in the TIR channel (Figure 2.3f), to check for consistency with the SWIR results. Band 6 saturates at a pixel-integrated brightness temperature of around 70°C. The observation that only one band 6 pixel over the flow in the Lonquimay Landsat image is saturated indicates that the high crust temperatures, T_s, (Figures 2.4a and b) do not prevail over whole 120 x 120 m pixels (Table 2.2). Radiance values in band 6 were used to derive pixel-integrated temperatures for the whole length of the flow (Figure 2.7), adopting the algorithm of Singh (1988); temperatures lie between about 10 and 60°C, so clearly quite substantial parts of the pixel must be at prevailing ambient temperatures (close to 0°C). Note also, at 7 km from the source, the jump and subsequent decay in temperature which is probably an expression of a step in the sub-flow topography (at the

front of a former flow); the further increase at 9.3 km coincides with the active flow toe. I have therefore chosen to equate the radiance in band 6 to the sum of three thermal components (Figure 2.8), namely T_s, T_c, and T_b, the temperature of ground beyond the active flow. Assuming that the flow runs approximately north-south (parallel to the nominal pixel edges), we have:

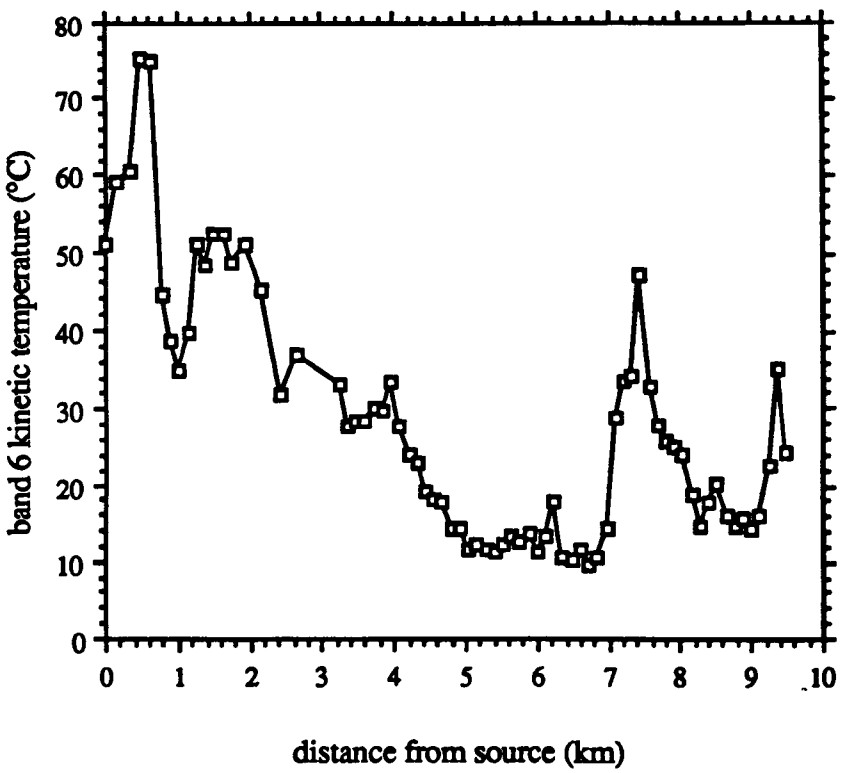

Figure 2.7. Pixel-integrated band 6 temperatures for the whole flow, calculated using the method of Singh (1988) and assuming an emissivity of 0.9, based on measurements by Walter and Salisbury (1989). The pixel with the highest DN in each scan line was chosen.

$$R_6 = \varepsilon_6\tau_6[f'L(\lambda_6,T_c) + f_1L(\lambda_6,T_s) + (1-f'-f_1)L(\lambda_6,T_b)] \qquad (2.6)$$

where f_1 is the fraction of a TM band 6 pixel occupied by lava surface at temperature T_s, and f' the fractional area of surface at temperature T_c. Since f' is very small, it makes little contribution in (2.6), and we can approximate f_1 by:

$$f_1 = [(R_6 / \varepsilon_6\tau_6) - R_0] / [L(\lambda_6,T_s) - R_0] \qquad (2.7)$$

where R_0 is the background radiance in band 6 for pixels away from the active flow. The values for T_s were first adjusted to brightness temperatures, and R_6 was calculated from the band 6 data for the highest DN pixel in each scan-line across the flow, using calibration coefficients from the TM tape header information. The results for f_1 are plotted in Figure 2.9, for a range of possible values of τ_6 between 0.6 and 0.933 (the latter figure being the transmissivity modelled by LOWTRAN).

Considering first the case where $\tau_6 = 0.933$, the corresponding flow widths can be bracketed assuming that at least half of a parallel-sided flow segment for each line of band 6 data occupies the 'hottest' band 6 pixel in that line, and giving consideration to the flow and pixel geometries. Taking the band 6 pixel area as 14400 m^2, and examining the bulk of the measurements beyond about 0.8 km from source (where the flow direction is at an angle of about 15° to the satellite along-track direction) the range of f_1 of between about 0.13 and 0.25 corresponds to theoretical flow widths of only about 16-30 m, assuming that the flow segment in each scan-line of band 6 data falls wholly within a single 120 x 120 m pixel. For this flow bearing, the flow width would have to be at least 66 m to guarantee that one 30 x 30 m SWIR pixel per scan-line fell entirely within it. These low values of f_1 suggest, therefore, that the assumption of only two thermal components in the SWIR pixels is not wholly accurate. However, this does not imply that the assumption is inappropriate, when it is recalled that even if half of a SWIR pixel is allowed to be at temperature T_b, the derivation of T_s is not greatly affected. It can easily be shown that, for a flow segment trending at 15° from the along-track direction, even the smallest derived value of f_1 in Figure 2.9 can correspond to a flow whose width is sufficient to fill almost half of a SWIR pixel. The low values of f_1 need not, therefore, undermine confidence in the dual-band calculations of T_s and f. They are nevertheless surprising in the light of field measurements of inter-levée distances in March 1990 which suggested minimum channel widths of about 85 m, 1 km from the bocca (M. Stasiuk, personal communication, 1990).

Distance from source (km)	Band 6 DN	Temperature (°C)
0.01	185	50.9
0.17	207	59.0
0.32	211	60.4
0.48	255	75.4
0.63	253	74.7
0.77	168	44.3
0.89	154	38.7
1.02	145	34.9
1.14	156	39.5
1.26	185	50.9
1.38	178	48.2
1.51	189	52.4
1.63	189	52.4
1.75	179	48.6
1.93	185	50.9
2.17	170	45.1
2.41	138	31.9
2.66	150	37.0
3.24	141	33.2
3.36	128	27.5
3.48	130	28.4
3.60	130	28.4
3.72	134	30.2
3.84	133	29.7
3.96	142	33.7
4.08	128	27.5
4.20	120	23.9
4.32	118	23.0
4.44	110	19.2
4.56	108	18.2
4.68	107	17.7
4.80	100	14.2
4.92	100	14.2
5.04	95	11.7
5.16	96	12.2
5.28	95	11.7
5.40	94	11.2
5.52	96	12.2
5.64	98	13.2
5.76	97	12.7
5.88	99	13.7
6.00	94	11.2
6.12	98	13.2
6.24	107	17.7
6.36	93	10.6
6.48	92	10.1
6.60	95	11.7
6.72	91	9.6
6.84	93	10.6
6.96	100	14.2
7.08	131	28.9
7.20	142	33.7
7.32	143	34.1
7.44	175	47.1
7.56	140	32.8
7.68	128	27.5
7.80	124	25.7
7.92	122	24.8
8.04	120	23.9
8.16	109	18.7
8.28	101	14.7
8.40	107	17.7
8.52	112	20.1
8.64	104	16.2
8.76	101	14.7
8.88	103	15.7
9.00	100	14.2
9.12	104	16.2
9.24	117	22.5
9.36	146	35.3
9.48	121	24.3

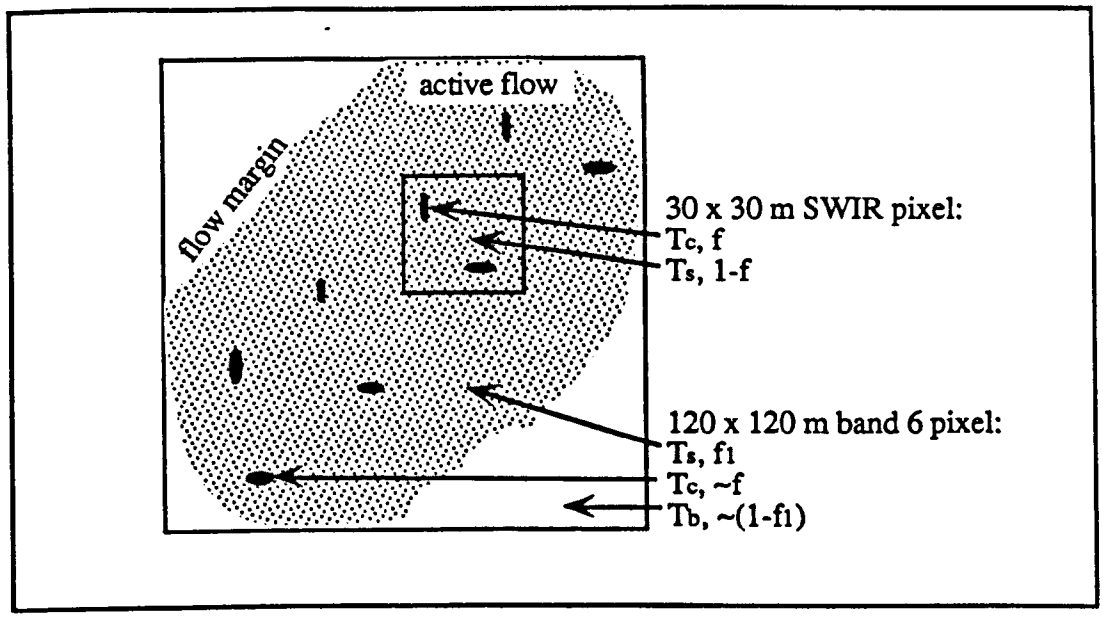

Figure 2.8. Thermal distribution models for TM infrared bands. The larger box represents a band 6 thermal infrared pixel containing three temperature components. The single SWIR pixel (ie. band 5 or 7) sits within the active flow and consists of only two thermal components.

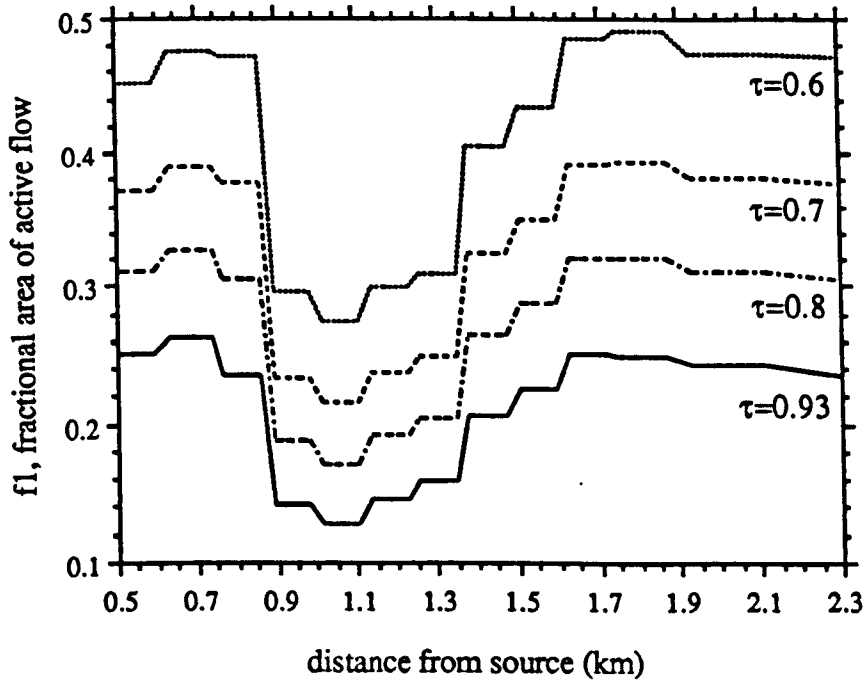

Figure 2.9. The fractional area of the active lava flow per TM band 6 pixel (120 x 120 m) calculated using equation 7, for different values of atmospheric transmissivity, τ.

Table 2.2 (on previous page). Raw DN values in the thermal infrared band 6 listed according to distance from the vent. Temperatures were calculated for an emissivity of 0.9, using the algorithm of Singh (1988).

It will be appreciated that there is something of a circular argument involved in the preceding discussion: if the band 6 data do suggest that a third thermal component is appropriate for the SWIR dual-band calculations, then the value of T_s used in the calculation of f_1 (2.7) was too small in the first place. Ideally, three equations should be written for the measured radiances in bands 5, 6 and 7 respectively, in terms of three thermal components, and solved simultaneously for f, T_s and the flow width. However, because of the unknown relationships between flow and pixel geometry, it would be an unsuitable approach in this case.

All of the foregoing qualifications and uncertainties may be unnecessary, however. Inspection of (2.6) shows that choosing lower values of any of ε_6, τ_6, T_b, or T_s, would increase f_1. Because the air above the flow is inevitably augmented by volcanogenic fumes, the value of τ_6 is particularly uncertain - that calculated by LOWTRAN was simply for a standard atmospheric model without any consideration of volcanic contributions. Naughton *et al.* (1969) recognised the absorption features of several volcanic gas species in 2.5-14.5 μm spectra of lava fountains recorded at Kilauea. My own measurements of lava surface temperatures with the 8-14 μm thermometer have indicated attenuation of emitted infrared radiation of the order of 50% over distances of 100-300 m. For this reason, I have derived f_1 for a range of τ_6 below that modelled by LOWTRAN (Figure 2.9). These can substantially increase the values of f_1 to the point where they are far more consistent with the assumption of only two thermal components in the SWIR pixels.

2.4.4. Power outputs

From (2.5) the radiant exitance from the 'cracks' and the crust can be calculated. The total flux, Q_{rad}, for each of the pixels chosen along the flow is plotted in Figure 2.10. Q_{rad} varies between about 3.8 MW per pixel upflow to 1.5 MW per pixel downflow. The proportion of the total flux that is contributed by the crust alone, Q_{crust} is shown in Figure 2.11. For the entire length of flow studied, the power radiated by the much hotter 'cracks' seldom exceeds 1% of the total radiative power output because of their low

proportional area. These results are comparable to average Q_{rad} values of about 1.4 MW per pixel that were estimated by Pieri *et al.* (1990) for the measurable part of the Etna 1984 flow. However, by choosing the background temperatures in advance, they had effectively predetermined the radiant flux because the hotter 'cracks', while at much higher temperatures, are so small that they contribute little to the total radiative power. This, in turn, is an expression of the measurable range of temperatures and f values constrained by the dynamic ranges of the TM SWIR sensors. In addition, the 'effective radiation temperatures' T_e, as defined by Pieri *et al.* (1990):

$$T_e = [(fT_c^4 + (1-f)T_s^4)]^{0.25} \tag{2.8}$$

will also be almost the same as T_s because of the smallness of f.

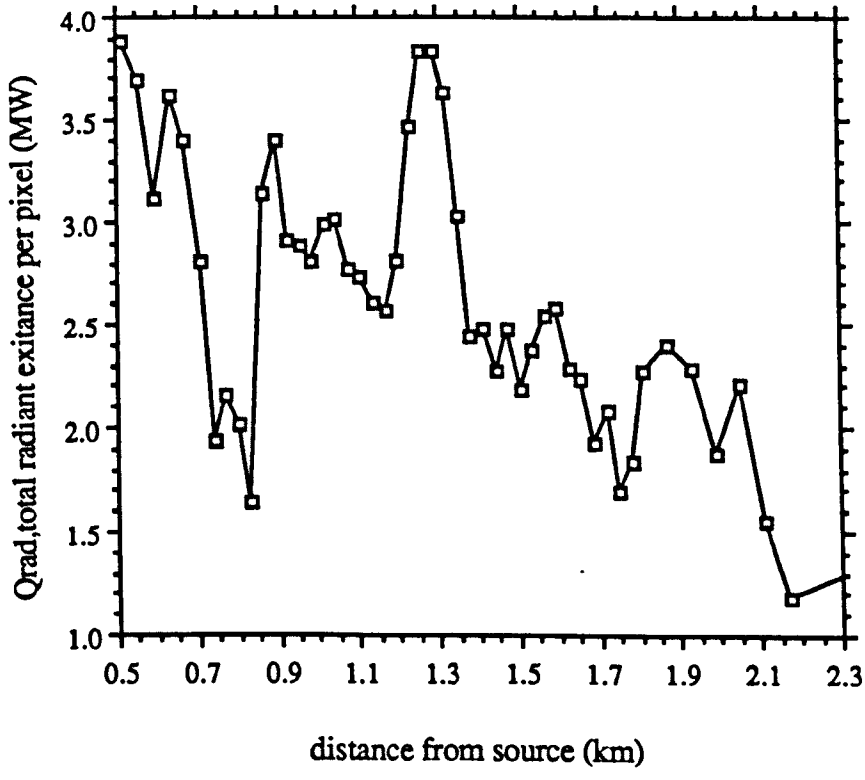

Figure 2.10. Total radiant exitance per 30 x 30 m pixel calculated from equation (2.5) for the longitudinal profile presented in Figures 2.4a and 2.5. For comparison, the flux from an equivalent area of background at a surface kinetic temperature of 0°C is about 0.26 MW.

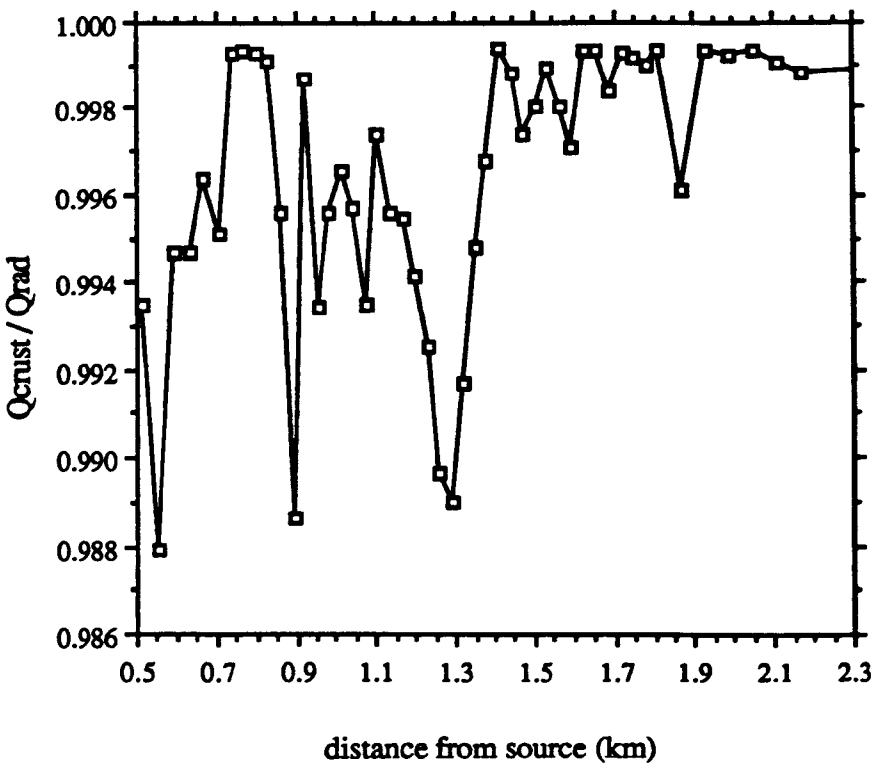

Figure 2.11. The fraction of total radiant exitance per 30 x 30 m pixel contributed by the crust .

In order to assess the importance of radiative cooling for the whole flow, it is crucial in this instance to examine the most proximal part of the flow up to its source. For aa flows, this is generally the region where core material is most exposed and hence radiative cooling most likely to dominate. Close inspection of the band 7 data in the TM image close to the source region clearly reveals the thermal signature of the lava flow beneath the eruption plume (Figure 2.3a, c). The flow starts abruptly, presumably at its bocca about 3 pixels (90 m) beyond the edge of a 3 x 4 pixel region saturated in band 7 which may represent an active strombolian vent. However, the flow cannot be distinguished beneath the plume in band 5 (Figure 2.3d) except in two places (which may correspond with thinner airborne ash or portions shadowed from the sun). In these 'windows', the radiance is of similar magnitude to the region studied downflow, suggesting that exposed core fractions are not appreciably different. For radiative losses from the core to exceed those from the crust, the relation $fT_c^4 > (1\text{-}f)T_s^4$ must hold (see Figure 2 in Crisp and Baloga, 1990a). The implications are that for substantially the

entire length of this flow, radiative losses from the exposed core are negligible with respect to those from the crust, although it is possible that attenuation of the emitted infrared through the plume is significantly greater over the spectral response of band 5, resulting in underestimation of the true radiance.

So far, only radiative losses from the flow surface have been considered. There are virtually no studies that consider all components of the thermal budgets of lava flows, although Le Guern (1987) and Le Guern *et al.* (1979) attempted crude estimations of the different heat transfers from lava lakes. Conductive losses through the bases of flows have generally been considered negligible (e.g. Daneš, 1972), and are not estimated here. However, it is likely that for this well-insulated flow, convective losses from the surface will be comparable, especially towards distal parts of the flow, to the radiative heat transfer. Neglecting the heat advected by degassing volatiles, free convection losses per 30 x 30 m pixel, Q_{conv}, can be estimated from the following relationships derived for turbulent circulation of air above a heated plate facing upwards (after Holman, 1972; Head and Wilson, 1986):

$$Nu = 0.14\ \sqrt[3]{(GrPr)} \tag{2.9}$$

where

$$Nu = LQ_{conv}/Sk\Delta T \tag{2.10},$$

$$Pr = \eta c_p/k \tag{2.11},$$

and

$$Gr = g\alpha\Delta TL^3\rho^2/\eta^2 \tag{2.12}$$

where L is a length scale (although for the temperatures involved in this case in which turbulent flow prevails, it can be seen from [2.9] -[2.12] that Q_{conv} is independent of L), S is area, $\Delta T = T_s - T_{air}$, and the properties η, dynamic viscosity, k, thermal conductivity, c_p, specific heat capacity at constant pressure, α, cubic expansivity, and ρ, density, are for air at the mean temperature, $T_{air} + \Delta T/2$ (values were taken for air at 373 K from tables in Kays and Crawford, 1980; the effect of decreased atmospheric pressure

at the < 1700 m altitude of the flow was, for simplicity, ignored). Because of the smallness of f, the convective component due to exposed core was also neglected. Taking S as 900 m^2 and T_{air} as 0°C, the solutions for Q_{conv} along the flow are represented in Figure 2.12. Q_{conv} drops from about 2.2 to 1.2 MW per pixel, between 0.5 and 2.0 km downflow from the vent. These power outputs are between 56 and 68% of the corresponding values for the radiative flux.

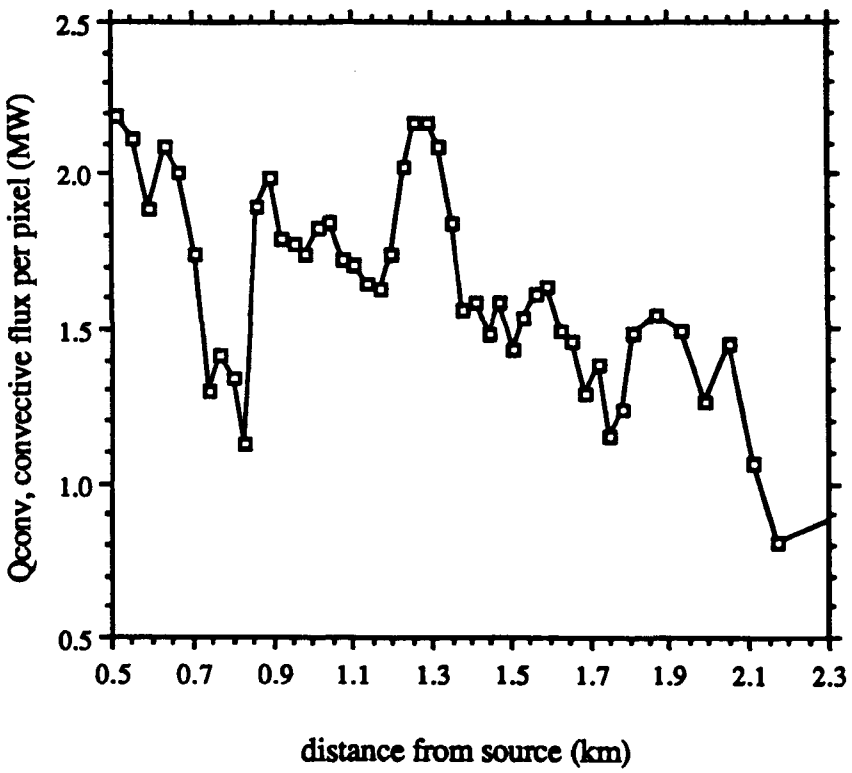

Figure 2.12. Natural convective heat flux per 30 x 30 m pixel calculated from equations (2.9)-(2.12) in the text.

All the derived components of the heat loss are shown in Figure 2.13, and the proportion of the total modelled surface heat losses that is contributed by convection is seen in Figure 2.14. Although only the case of natural convection has been investigated, forced convection heat loss fluxes should not differ significantly over the range of crust temperatures involved here (210 ± 40°C) and for moderate wind speeds (see Table 1 in Head and Wilson, 1986). Since the radiative and convective losses are comparable in magnitude they should, strictly, be calculated simultaneously, taking into account the

coupling between radiation and convection that takes place through the thermal boundary condition in the convection problem. However, because the air above the flow approximates a non-participating medium in that it is effectively transparent to radiation, the correction would be small compared with other sources of error and has not been calculated here.

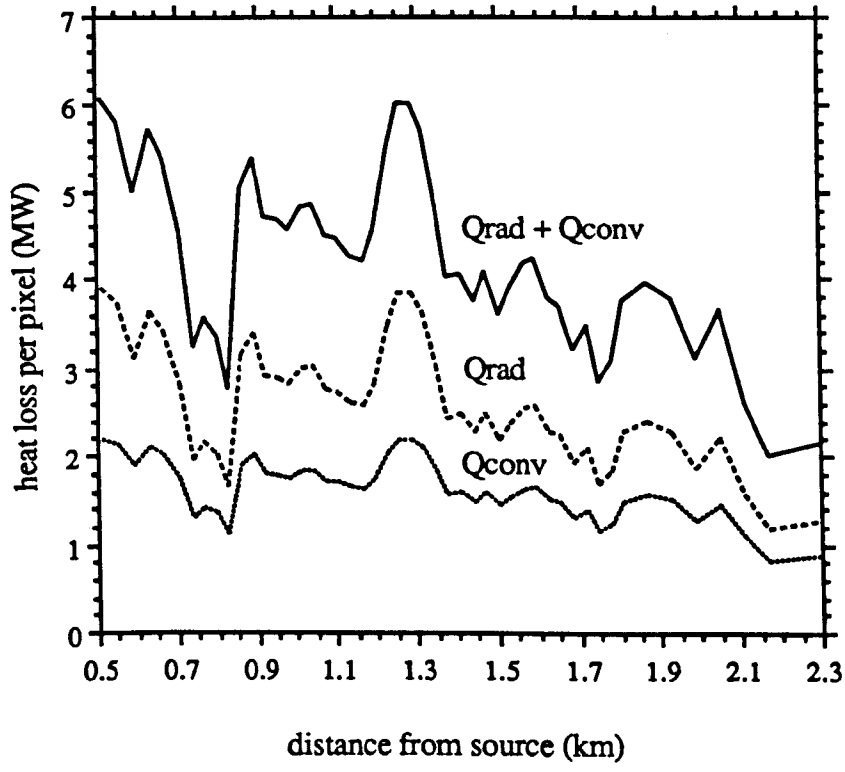

Figure 2.13. Components of the heat loss per 30 x 30 m pixel: Q_{rad} is the radiative flux, Q_{conv} the convective flux, and $Q_{rad} + Q_{conv}$ their sum.

A potentially more significant source of error is the assumption of the value of S. This is because (i) the actual spatial response of the TM sensors does not match the nominal pixel dimensions, and (ii) the actual surface area of the flow within the instantaneous field of view of the TM sensors is increased because of topography of the flow surface. In respect of this latter point, it may be mentioned that Gaddis *et al.* (1990) observed surface roughness of up to 1 m on basaltic aa flows in Hawaii.

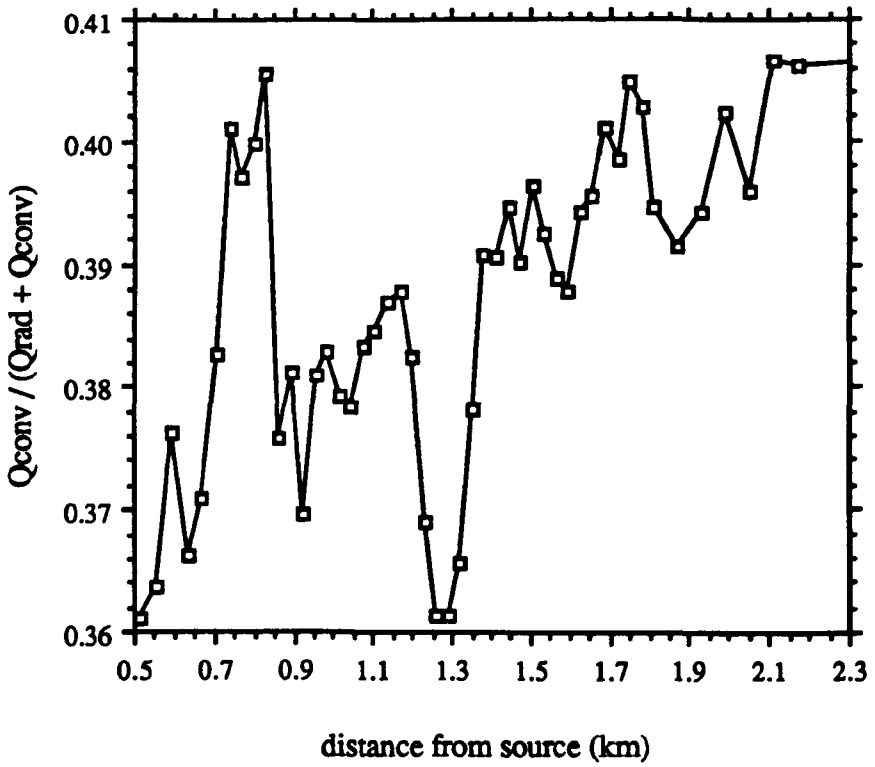

Figure 2.14. Proportion of the total modelled heat losses contributed by convection into the air above the flow.

2.4.5. Crustal boundary layer thickness

The complexities of surface roughness of the flow, thermal mixing or otherwise of the rubble and the magnitude of uncertainties in derivation of crust temperatures, etc., do not justify detailed modelling of the growth in thickness of the crust. Instead, I envisage a simple model in which a parcel of crust at some point along the flow, which consists of a conductive boundary layer sandwiched between isothermal core (at 1040°C), and thermally mixed rubble produced by disruption of the underlying solid boundary layer (Figure 2.15). The conductive boundary layer, which thickens with distance x from the vent, has a temperature at its upper interface equal to $T_s(x)$, the temperature of the rubbly top. The heat transfer through the conductive boundary layer, Q_{cond}, is approximated by the simple linear conduction equation:

$$Q_{cond} = kS\Delta T/\delta(x) \qquad (2.13)$$

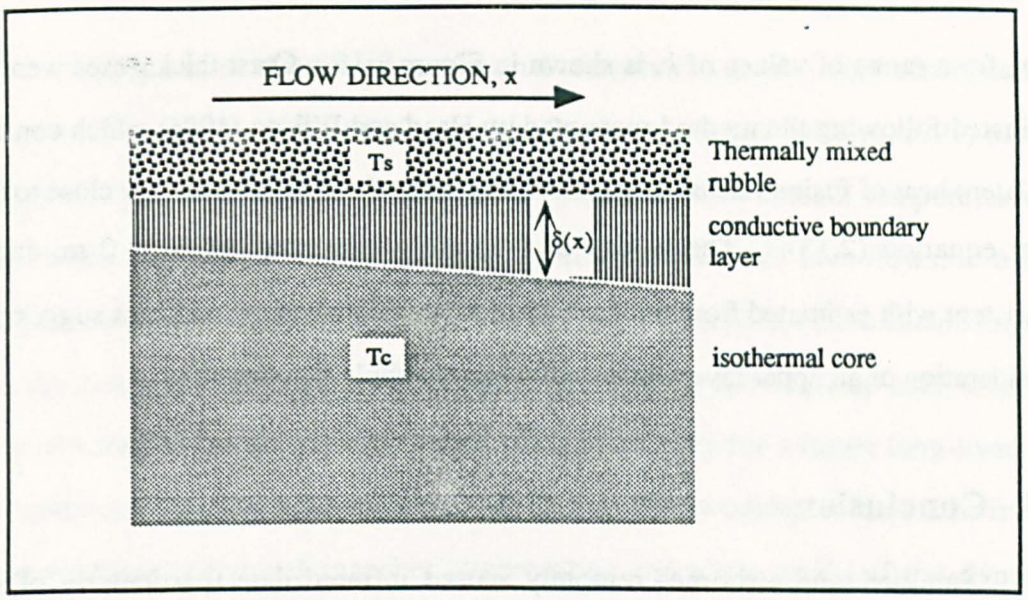

Figure 2.15. Schematic vertical profile through the lava flow showing a thermally mixed aa top overlying a conductive boundary layer which, in turn, overlies isothermal core.

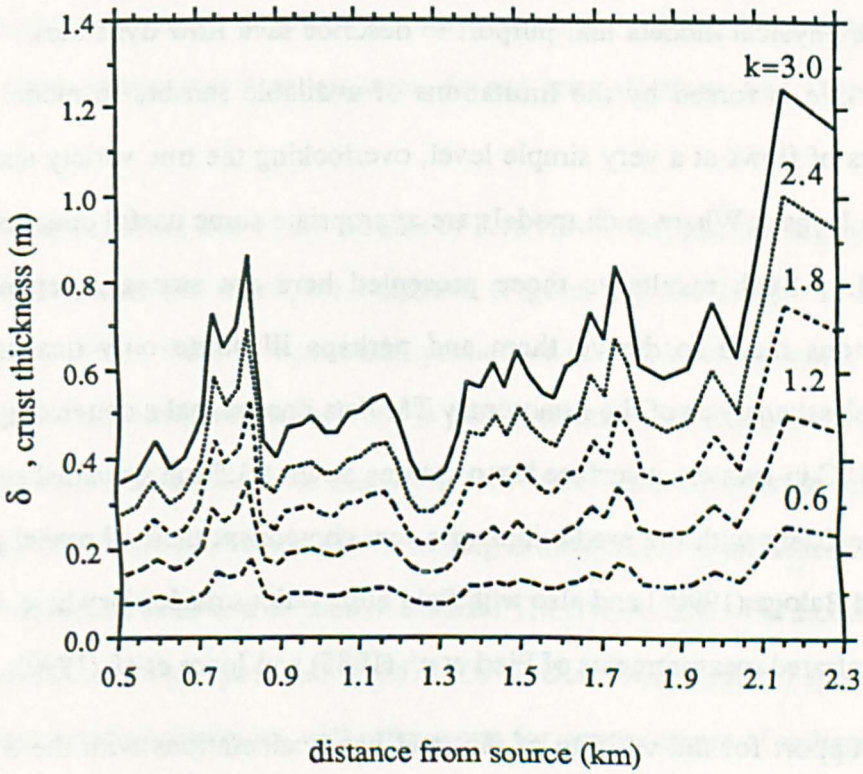

Figure 2.16. Thickness of the conductive boundary layer estimated for various values of thermal conductivity, k (W m^{-1} K^{-1}), from equation (2.13) in the text.

where k is thermal conductivity, ΔT is given by $T_c - T_s(x)$, and $\delta(x)$ is the thickness of the boundary layer at distance x from the source. Q_{cond} is taken to be equal to the total surface heat flux per pixel, $Q_{rad} + Q_{conv}$ (Figure 2.13). The solution of $\delta(x)$ along the

flow, for a range of values of k, is shown in Figure 2.16. Crust thicknesses were also evaluated following the method recounted by Head and Wilson (1986) which considers the latent heat of fusion released by solidifying lava - the results were very close to those from equation (2.13). The values of $\delta(x)$ are of the order of 0.1-1.0 m, and are consistent with estimated flow thicknesses of around 10 m; their smallness suggests that consideration of an upper layer of thermally mixed rubble is appropriate.

2.5. Conclusions

Satellite (and airborne) remotely sensed infrared data (particularly of short wavelengths) can provide basic information applicable to the understanding of the cooling of lava flows, which would be difficult to obtain at erupting volcanoes by any other method. Such techniques promise to provide data sets with which to test the numerous disparate physical models that purport to describe lava flow dynamics. However, at present, one is forced by the limitations of available sensors to model the thermal dynamics of flows at a very simple level, overlooking the true variety and complexity found in lavas. Where such models are appropriate some useful conclusions may be obtained. Such results as those presented here are strongly dependent on the assumptions made to derive them and perhaps illustrate only qualitative trends. Nevertheless, analysis of the Lonquimay TM data does reveal a convincing decrease of about 80 °C in lava crust surface temperatures down a 1.5 km proximal segment of the flow, consistent with the predictions of a two-component thermal model presented by Crisp and Baloga (1990a) and also with field observations made elsewhere, including the thermal infrared measurements of Pieri *et al.* (1985) and Jones *et al.* (1990).

Support for the validity of the dual-band calculations with the SWIR data is provided by indirect estimates of the active flow width, made by use of the thermal infrared band 6 data. The areal proportions of incandescent cracks on the flow top are very small for substantially the entire length of the flow and, as a consequence of this, the partly chilled crust dominates the cooling of the flow. Convective heat losses are comparable to, (about two-thirds of), the radiative losses.

Although some classification of spatial temperature distributions associated with lava lakes (Flynn *et al.*, 1989) and fumaroles (Oppenheimer and Rothery, 1991) has been attempted, there is a need for further field observations of radiant temperatures and proportional areas of thermal components on different kinds of lava flows, in order to verify the validity of the dual-band (or any other) approximations, and to enable improved interpretation of image data. It would be worthwhile to follow up such work with study of a time-series of remotely-sensed infrared imagery for a future long-lived flow, preferably one that does not form extensive tubes. This would provide a time frame in which to place individual snapshot observations and allow study of the dynamical evolution of the flow. Ideally, one would like contemporary ground-based observations of flow discharge rates, velocity profiles, surface and core temperatures and so on. Improvement of the radiometric accuracy of the remotely-sensed data can be achieved by acquiring night-time scenes in which 'contamination' by reflected sunlight, and the sometimes large corrections it necessitates, do not arise (Rothery and Oppenheimer, 1991).

It is also desirable that entire lengths of lava flows, not just the segments where TM sensor dynamic ranges allow, are examined (Figures 2.1 and 2.4b). In the case of the Lonquimay image there is a proximal portion of the flow where some pixels are saturated and consequently the radiant flux is poorly constrained, and a distal part where thermal radiance is below the SWIR channel sensitivities. It is unfortunate that the most radiant segments of flows, where radiative cooling is most likely to influence rheology of the lava, are typically saturated in present Landsat TM SWIR data. Forthcoming sensor packages scheduled for the payloads of EOS (Earth Observing System) spacecraft, and on other polar orbiting platforms, will offer scope for measurement of radiance through greater parts of the spectrum, and a host of exciting applications in volcanology. For example, the Optical Sensor (OPS) to be carried by the Japanese Earth Resources Satellite (JERS-1), due for launch in February 1992, is equipped with four bands in the SWIR (with central wavelengths of 1.655, 2.065, 2.190 and 2.335 μm) which will have an instantaneous field of view (IFOV) corresponding to approximately 20 m (NASDA,

1990). Looking further ahead, the EOS mission should include deployment of the Advanced Spaceborne Thermal Emission and reflection Radiometer (ASTER) which will be equipped with six channels between 1.6 and 2.43 μm with a nominal IFOV of 30 m, three channels between 0.52 and 0.86 μm with 15 m IFOV, and five channels between 7.95 and 12.0 μm with 90 m IFOV (A. Kahle, personal communication, 1991; Mouginis-Mark *et al.*, 1991), and eventually, perhaps, the High Resolution Imaging Spectrometer (HIRIS) which has 192 narrow spectral channels between 0.40-2.45 μm (Dozier and Goetz, 1989). The greater numbers of available channels on such instruments might enable more realistic thermal models to be chosen, and hence greater numbers of thermal components to be solved (Oppenheimer and Rothery, 1991), and with luck it will be possible to measure thermal radiation from lava flows from their boccas to their toes.

Chapter 3. Infrared monitoring of volcanoes by satellite

C.M.M. Oppenheimer and D.A. Rothery

Published in the Journal of the Geological Society of London, 148, 563-568, 1991.

3.1. Abstract

Sensors on future satellite platforms will be used routinely for volcano monitoring. In particular, infrared channels offer the potential to detect and measure temperatures of features such as lava bodies and fumarole fields. This is possible even though the surface temperature distributions associated with such phenomena are typically inhomogeneous at the pixel scale, so long as simplifying assumptions can be made. To test the applicability of the technique, we have carried out field studies of a range of volcanic thermal manifestations using portable infrared thermometers. Rock surface temperatures around fumarolic vents exhibit greater stability with time than those associated with actively degassing lava bodies but in both cases volcanogenic fumes can significantly attenuate the emitted infrared radiation. The scale of the temporal variability, at a given wavelength, dictates the quantitative value of isolated satellite

'snapshots'. If more spectral channels in the infrared were available on remote sensing platforms then more components of the surface temperature distribution could be extracted from the data. Imaging spectrometry offers the greatest flexibility, although data processing, including correction for atmospheric effects, would present difficulties.

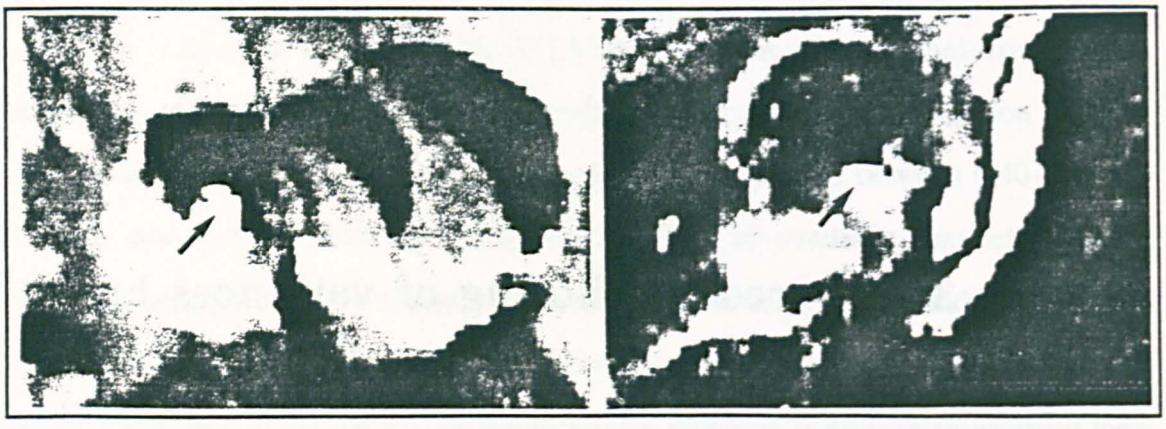

Figure 3.1. Landsat TM band 7 images showing thermal anomalies (arrowed) at: (left) a summit crater of Láscar volcano, Chile (17 July 1985). In this case the anomaly is obvious because it is located in a shadowed area; (right) the fumarole field on the 1953-5 intracrater cone at Poas volcano, Costa Rica (6 March 1986). Here the anomaly is less clear (because the pixels are in full sunlight) but has been verified by comparison with the shorter wavelength bands.

3.2. Introduction

Active volcano environments are usually unsympathetic to routine close-range monitoring. In many cases, access is difficult and/or hazardous, and equipment deployed close to active sites is prone to corrosion or physical destruction within a short period. Frequent visual observations, gas sampling, temperature measurements, and so on, are often impractical. Volcanoes in eruption present even greater difficulties, although it is at such times that information is most sought after. Furthermore, most of the world's active and potentially active volcanoes are in densely populated developing countries that lack the financial and scientific resources, and often political will, to conduct adequate monitoring (Tilling, 1989). Remote sensing may provide some solutions to these problems, and a future dedicated volcano-observing satellite is a real possibility (Pieri and Glaze, 1989). Such a system would provide a consistent means of monitoring levels of activity at volcanoes across the globe and offer scope for hazard

warning. Even in countries with sophisticated geophysical, geochemical and geodetic monitoring networks in place, satellite remote sensing can be a powerful additional tool for observing the whole of a volcano virtually instantaneously, in different parts of the electromagnetic spectrum, and on a systematic multitemporal basis. In the meantime, existing and forthcoming environmental remote sensing satellites provide very useful data for a number of volcanological applications.

Compared with other geophysical monitoring equipment, the relative costs of image processing facilities are not necessarily high. Moreover, one image processing system can be used to study data from many volcanoes. There are several ways in which orbital remote sensing can contribute directly to volcano monitoring (see Mouginis-Mark *et al.*, 1989): by (i) detecting hot sources and measuring their radiant energy (the topic of this paper); (ii) detecting and tracking the dispersal of erupted ash clouds; (iii) locating new volcanogenic products on the ground, (e.g.,. lava, pyroclastic and debris flows, airfall deposits); (iv) determining the composition and quantity of emitted gases (e.g., SO_2 by ultraviolet spectrometry); (v) by microwave- or laser-ranging to monitor ground deformation or the development of lava flow fields.

3.3. Measuring radiant heat from volcanoes

Remote sensing studies of the Earth's surface are restricted to a few atmospheric 'windows' where the transmission of radiation is high (0.4-1.3 μm, 1.5-1.8 μm, 2.0-2.5 μm, 3-5 μm and 8-14 μm). The spectral distribution of the energy radiated by a surface depends on its temperature, and is described by the familiar curves of Planck's formula (see Rothery *et al.*, 1988). As a consequence, the spectral radiance measured at a satellite depends on the proportions of the ground surface, in the sensor's field of view, at different temperatures (modified by atmospheric and instrumental effects and the surface spectral emissivity). The upper range of surface temperatures encountered on volcanoes is in the region of 850-1250°C, corresponding to active lava. However, the surface area of such hot material is usually subordinate to that of chilled crust. Another class of thermal manifestations considered here are fumarole fields, which develop where

magmatic gases reach the ground. Gas temperatures have been known to exceed 900°C, more than sufficient to cause incandescence of the rock surfaces surrounding the vents.

Most studies of thermal radiation from volcanoes have used the traditional thermal infrared (TIR) part of the spectrum, that is wavelengths greater than about 3 μm. TIR data from the Advanced Very High Resolution Radiometer (AVHRR) carried by NOAA polar orbiting platforms, have been shown to be capable of detecting lava bodies, particularly in channel 3, (3.55 - 3.93 μm, e.g., Wiesnet and D'Aguanno, 1982), as well as forest fires and gas flares (e.g., Matson and Dozier, 1981; Matson *et al.*, 1987). However, the use of AVHRR for quantitative measurements of such sub-pixel phenomena is limited by its coarse spatial resolution of about 1 km (Oppenheimer, 1989). This creates difficulties in correcting for topographic and atmospheric influences on ground temperature, as Bonneville and Kerr (1987) demonstrated in an attempt to map a thermal precursor to the 1983 flank eruption of Mt Etna, using data from channels 4 and 5 (10.3-11.3 μm and 11.5-12.5 μm). Landsat TM band 6 (10.3-12.5 μm) has nominal 120 m resolution but cannot by itself resolve sub-pixel detail of thermal structure.

Other work has illustrated the value of short wavelength infrared (SWIR) satellite data in detection and measurement of thermal radiation from hot volcanic sources, particularly Landsat Thematic Mapper (TM) bands 5 and 7, at 1.55-1.75 μm and 2.08-2.35 μm, respectively (Francis and Rothery, 1987). Examples of thermal anomalies detected in such images are shown in Figure 3.1. Rothery *et al.* (1988) demonstrated that the use of two SWIR wavebands enables sizes and temperatures of sub-pixel radiant areas to be constrained by a 'dual-band technique' devised by Matson and Dozier (1981), if it can be assumed that the surface temperature distribution in each pixel has only two significant components, namely the hot target and the cooler background. This technique was extended by Glaze *et al.* (1989) to measure the radiant energy flux of volcano hotspots. They noted systematic changes in radiant flux, in a time-series of Landsat TM images of Láscar volcano (Chile), before and after its September 1986 eruption, and speculated that the technique could be more widely applicable for predicting volcano behaviour. Satellite data are also being used to support theoretical models of lava flow

thermodynamics. For example, Pieri *et al.* (1990) have examined a Landsat TM image of the June 1984 Etna flow. They calculated hot crack temperatures and fractional areas using the dual-band method and, expanding on equations presented by Crisp and Baloga (1990a), modelled internal temperatures of the flow.

There are several drawbacks in trying to use presently available satellite data for monitoring volcano hotspots. Among these are the high cost of, and time delays in obtaining, SWIR data, and the coarse spatial resolution of the cheaper thermal infrared data from meteorological/ environmental satellites. Moreover, for many kinds of activity that produce rapid changes in surface temperature distribution, an occasional snapshot view from orbit may not be very meaningful. One of our chief aims has been to obtain the ground truth necessary for a better understanding of the remotely-sensed data, by field-based investigation of the surface temperature distributions associated with a range of volcanic thermal manifestations.

3.4. Thermal measurements in the field

Traditional thermal monitoring of volcanoes involves measurements of the temperature of fumarole gases, crater lakes, hotsprings and molten lava, typically using a thermocouple. However, to make comparisons with satellite data, we need to know the distribution of *surface* temperature at such sites. To date, there are few published data other than our own that document this.

We have used a range of thermometers including bimetallic and thermocouple devices but most importantly, two Minolta/Land 'Cyclops' infrared thermometers, whose specifications are outlined in Table 3.1. In most cases, the instruments were mounted on tripods and viewed the ground obliquely. The target size of each thermometer is a function of its angular field of view, and the viewing geometry. For the 8-14 μm thermometer, looking perpendicularly at level ground, the target diameter is approximately 2.6 cm at 1.5 m, and 87 cm at 50 m, or at an angle of 45°, 5.2 cm and 174 cm, respectively. The target diameters of the 0.8-1.1 μm instrument are one-third of

these values. Temperatures are automatically calculated from the integrated flux measured over the whole field of view and so do not necessarily equate with the temperature of the hottest material present. We have made no attempt here to correct our radiant temperature measurements for spectral emissivity, so they are quoted as brightness temperatures; nor have corrections been made for path attenuation as this is one of the effects we wish to demonstrate.

instrument	field of view	spectral response (μm)	temperature range (°C)	response time (s)
Cyclops 33	1°	8 to 14	-50° to 1000°	0.5 / 1.0
Cyclops 52	0.33°	0.8 to 1.1	600° to 3000°	0.03

Table 3.1. Specifications of Minolta/Land infrared thermometers

3.4.1. Active lava lakes and strombolian eruptions

We consider first the case of Stromboli volcano (Italy), which we visited during October/November 1988, and October 1989, as an example of the extreme short time-scale over which temperature distributions can change. The eruptive style was characterised by episodic and brief emissions of incandescent scoria from several small intracrater boccas. These mildly explosive eruptions took place at intervals of seconds to a few tens of minutes while the configuration, activity and dimensions of the discharging vents evolved more gradually; new incandescent vents appeared where high temperature gases broke the surface while the magma level in other conduits dropped.

With the 8-14 μm thermometer stationed at various sites around the crater rims, we recorded the temporal variability of radiant temperatures of different areas inside the craters, at viewing distances of approximately 50 m. Figure 3.2 (bottom) shows the temperature-time curve for an open conduit filled with magma. The magma degassed vigorously, constantly renewing the surface and frequently ejecting spatter in mild bursts to heights of several metres. The rapid fluctuation of recorded temperature correlated visually with (i) the passage of fumes between the thermometer and the hot target, and (ii) the activity of magma in the vent. These temperature changes must be seen in the context

of the 8-14 μm bandpass of the thermometer, because the transmission of radiation through the atmosphere (locally enriched by volcanic effluent) is wavelength-dependent. Using the 0.8-1.1 μm thermometer, we observed a more restricted, and higher, range of apparent temperatures for the active lava lake at Masaya volcano (Nicaragua), during February-March, 1989 (upper curve in Figure 3.2), consistent with less water vapour attenuation in this bandpass.

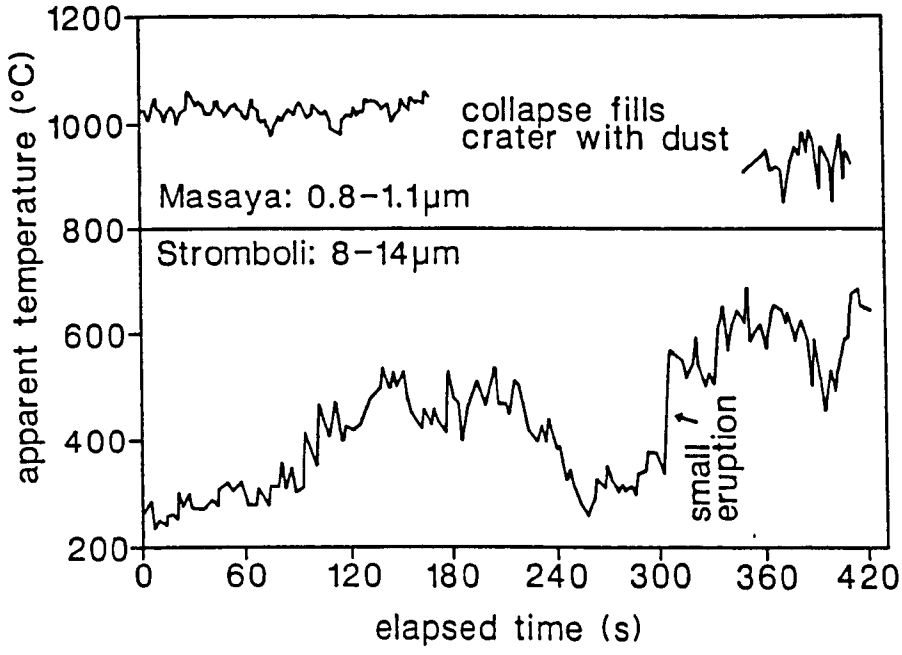

Figure 3.2. Temperature readings of magmatic features at Masaya, measured at 0.8-1.1 μm, and Stromboli, measured at 8-14 μm. The radiometer target circle fell within the perimeter of the magma body in both cases. Variable attenuation by fumes and activity of the magma account for much of the fluctuation which is greatest for the TIR thermometer.

An additional consideration results from the nature of strombolian activity: the frequent, mildly explosive eruptions deposit incandescent lava beyond the vent, effectively increasing the area of hot ground. The material cools at exponential rates but is typically, (after dark), seen to glow for several minutes after eruption. Rothery *et al.* (1988) suggest that the anomalously large apparent size of the lava lake at Mount Erebus (Antarctica) on a 1985 Landsat TM image may be explained by its acquisition shortly after a strombolian eruption. Our results show that quantitative measurements of radiant flux from isolated satellite 'snapshots' of these kinds of phenomena may not be especially

meaningful, although the value of satellite data simply for detection of such hot sources remains.

3.4.2. Moderate-temperature fumarole fields

Since its last eruption in 1888-90, Vulcano (Italy) has been in a state of variably intense fumarolic activity, now concentrated on the north rim of the main cone, Gran Cratere. During our field investigations in October/November 1988 and September/October 1989 gas temperatures were very stable; the highest recorded were 396°C in 1988, and 407°C in 1989 (at the same vent), though most temperatures were in the range 100-300°C. Rock surface temperatures around fumaroles reflected this stability, with slight fluctuations only, resulting from changes in wind velocity (Fig. 3a).

One of our aims in the field was to quantify the areas of ground within different temperature ranges. It was not practical to assess this for the crater as a whole so we concentrated on a continuous 40 m long fumarole fissure on the northern rim of the crater. The 8-14 μm thermometer was used to measure temperature profiles transverse to the fissure at several points. Although there were slight changes in the dimensions, particularly the depth, of some parts of the active fumarole fissure between 1988 and 1989, the temperature distribution across our repeated traverse was not greatly different (Figure 3.3b). The profiles are generally symmetrical about the fumarole axis, with steep gradients between about 80°C to 220 °C flanking a plateau of variable width at around 240°C.

Taking a representative temperature distribution across the fissure, we converted length to area simply by multiplying by the total length of the fissure (Oppenheimer and Rothery, 1989). It was then straightforward to make a crude estimate of its radiant flux and emittance using the Stefan-Boltzmann relationship. Placing the 40 m long fissure inside a 40 x 40 m square, equivalent to the ground cell of a blurred TM pixel (Rothery *et al.*, 1988), the integrated radiant flux and emittance (above background) were about 37 kW and 23 W m^{-2} , respectively (errors unconstrained but large). These are orders of magnitude lower than values calculated by Glaze *et al.*, (1989a) from TM SWIR data for

radiant anomalies on Lascar, Erta 'Ale and Erebus volcanoes, equivalent to fluxes of about 1 MW per pixel and emittances of 700-2300 W m^{-2}.

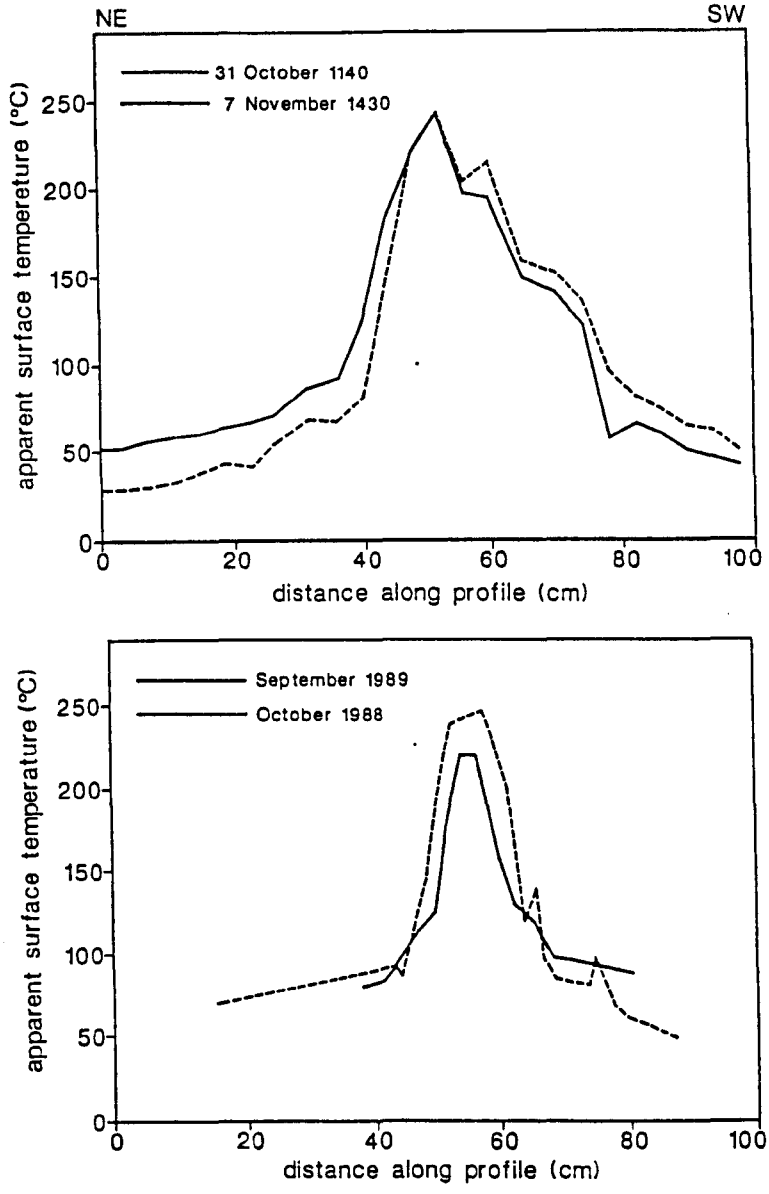

Figure 3.3. Surface temperatures (recorded at 8-14 μm) measured across a linear zone of fumarolic discharge at Vulcano: (a) the same profile measured on two days a week apart in 1988 when the wind blew in opposite directions. Wind chill of the upwind side and warming of the downwind side of the fumarole are evident; (b) the same profile measured 11 months apart. The hot zone at this site was somewhat cooler and narrower in 1989 than in 1988. (It is not suggested that this is representative of the whole fissure).

We have also estimated the at-sensor spectral radiances due to hot areas on Vulcano, by inserting our temperature-area model into the Planck equation for arbitrarily positioned pixels of Landsat TM and AVHRR infrared channels. We concluded that

Vulcano would not look hot on the satellite imagery - radiance in the SWIR is below the sensitivity of TM bands 5 and 7, and the response of the TIR channels would be swamped by background. We have examined four AVHRR scenes of Vulcano from October 1988, none of which shows thermal radiance attributable to the fumarole field (Oppenheimer, 1989). TIR imaging with high spatial resolution (of the order of 30 m in the 3-5 μm bandpass) would be necessary to measure ground surface temperatures around moderately hot fumaroles, such as those at Vulcano, unless the areas of hot ground were significantly greater, or the background temperature were much lower, for example on a high-altitude volcano.

3.4.3. High-temperature fumarole fields

Fumarole temperatures at Momotombo volcano (Nicaragua) are sufficient to cause bright orange incandescence of the inner walls of the vents. The gases burn with pale orange flames tens of cm long. During field study in March-April 1989, we recorded a maximum gas temperature of 880°C (by thermocouple), and surface temperature of 888°C (by 0.8-1.1 μm radiometer). As at Vulcano, both gas and surface temperatures were very stable, over a period of 5 weeks monitoring. However, repeat measurements in April 1990 revealed gas temperature decreases of 50-150°C at many fumaroles, the highest recorded during this time being 772°C.

There were several clusters of hot fumaroles within the summit crater but gas temperatures varied quite widely between individual vents, even those in close proximity. The vents were typically surrounded by areas of 10-100 m^2 where the surface temperature exceeded 100°C. However, much of this hot ground formed steeply inclined surfaces (45° or more) and many of the incandescent vents (some of them fissures up to a metre long) were recessed and overhung by fumarolic deposits. The temperature dropped abruptly across the lips of vents (Figure 3.4) and only the inner walls glowed visibly. Thus, a downward-looking satellite might well see nothing of the hotter interior of vents, and at best, only a small portion of the cooler inner walls near the mouths of the vents. We note that much of the high-temperature fumarolic field located on the lava

dome at Merapi volcano (Indonesia) is also developed on steep ground (T. Casadevall, personal communication, 1989). Unfortunately, the two Landsat TM images of Momotombo that we have examined (recorded on 20 February and 8 March 1989), show considerable reflected sunlight in channels 5 and 7, with the result that thermal radiance from the fumarole field is not apparent. We are now awaiting receipt of a night-time image scheduled for March-April 1990.

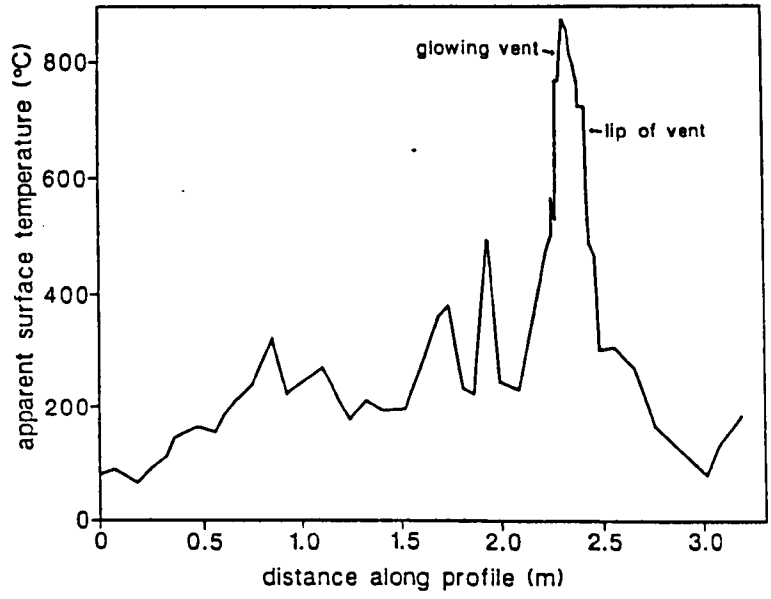

Figure 3.4. Surface temperature profile across high temperature fumaroles at Momotombo. Temperatures above 450°C around the hottest vent were measured at 0.8-1.1 μm, the remainder at 8-14 μm. The shorter peaks in the data correspond to vents smaller than the target area of the thermometer, so that the integrated temperatures are significantly lower.

3.5. Sensor requirements for remote sensing of hot volcanoes

Having shown examples of the thermal characteristics of hot volcanic features, we turn to a discussion of the sensors desirable for future volcanological remote sensing by satellite. We shall consider firstly situations in which there are only two different ground-surface temperatures within a pixel (for example glowing cracks and cool crust on a lava lake). Figure 3.5 shows spectral radiance measured at various wavelengths for a pixel in which only two surface temperatures occur, plotted for a range of fractional area occupied by the hot component. The horizontal part of each curve represents values

where the spectral radiance from the hot fraction is so small that the total spectral radiance is completely dominated by that from the 'cold' background. Conversely, the sloping straight-line part of each curve represents values where the spectral radiance from the hot fraction is so large that it completely dominates that from the background. The gradients are non-uniform where there is a significant contribution to the total spectral radiance from both the hot and the cold components of the pixel. The temperature of the hot area and the fraction of the area covered by it can be calculated by measuring the spectral radiances at two wavelengths if both these values can be assumed to be on the straight-line sloping parts of the curves, or if we know the temperature of the cold component and the values are in the range where the gradient of the curve is changing.

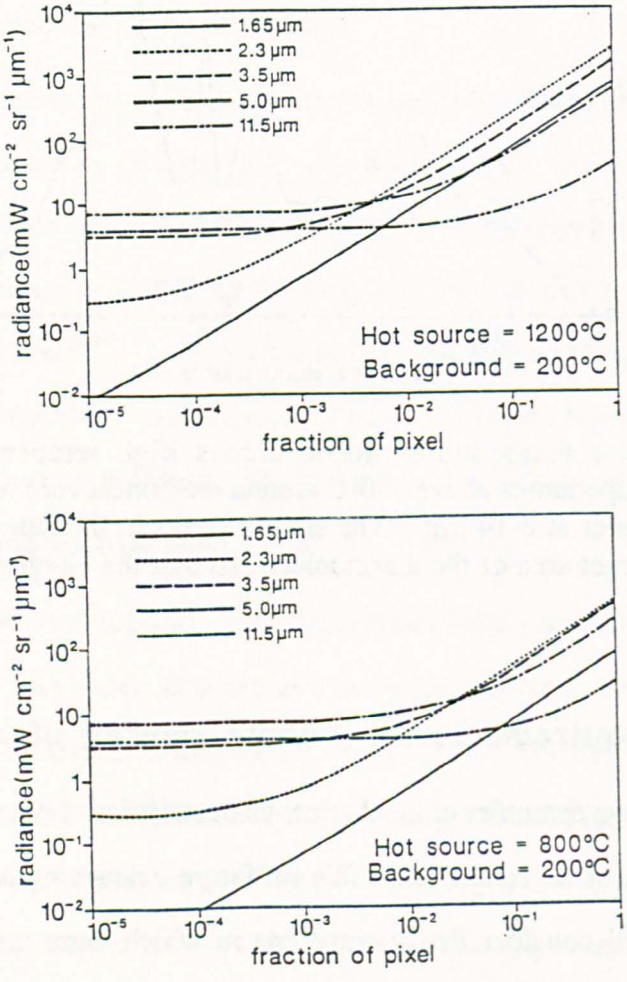

Figure 3.5. Spectral radiance at selected wavelengths within atmospheric windows in a pixel with only two surface temperatures, (top: 1200°C and 200°C; bottom: 800°C and 200°C) plotted against the fraction of the pixel at the hotter temperature.

Bearing this in mind, Figure 3.5 shows that a wide variety of commonly occuring volcanic surface conditions could be determined using two bands from adjacent atmospheric windows, provided the sensors had appropriate upper and lower sensitivity limits. The practical lower limit would be governed by instrumental, atmospheric and surface constraints, and the channel wavelength. A bandpass sensor system suitable for general purpose thermal volcanology should record spectral radiance up to around 100 mW cm^{-2} sr^{-1} μm^{-1}, ideally on a logarithmic scale; (we assume that a temperature of 1200°C is unlikely to occupy more than about a tenth of a pixel). Using an 8-bit range, it would be possible to determine temperatures with a precision of about 10 °C but only in situations where the dual-band assumptions are valid. In order to cover the full range of conditions, it should have a sensor in each of the SWIR and TIR atmospheric windows, preferably with two in the 3-5 μm window. Errors could be reduced by comparing spectral radiance from several pairs of channels, and (for SWIR data) by recording the images by night, thus avoiding the need to make a correction for reflected solar radiance.

To use this principal in cases where n surface temperatures are significant, it would be necessary to have measurements in $(2n - 1)$ spectral bands. However, solving multi-band equations simultaneously becomes a formidable obstacle, particularly so since even the two-wavelength equations have no analytical solution (Matson and Dozier, 1981). An alternative approach would be to use the data from imaging spectrometry, which records radiance in large numbers of closely-spaced, narrow-width spectral channels.

3.5.1. Imaging spectrometer data

For a surface at a uniform temperature, it is possible to use imaging spectrometer data to measure the temperature either by fitting a Planck curve to them, or simply by locating the wavelength of the maximum spectral radiance and using Wien's displacement law (which states that the wavelength at peak spectral radiance is inversely proportional to temperature). However, for likely mixtures of two or more temperatures on volcanoes it is uncommon for the sum of the spectral radiances from each temperature component to

result in separate maxima on the total spectral radiance curve, so Wien's displacement law cannot often be used. Thus to determine the temperatures and sizes of each component one must find a sum of an appropriate number of Planck curves (one for each component, weighted according to the fractional area of each, e.g., Flynn *et al.*, 1989) to match the resultant (total spectral radiance) curve determined by the spectrometer. We have not developed a means of doing this, but are encouraged by the fact that the *shape* of the Planck curve is unique for each temperature. If we want just to measure the radiant energy (which in some cases may be more meaningful than temperatures alone; see Glaze *et al.*, 1989a), then there is much less of a problem, because this energy is given directly by the area below the curve, although some extrapolation will still be necessary to wavelengths not covered by the spectrometer.

Figure 3.6 illustrates some of the difficulties in determining temperatures from imaging spectrometer data. We assume that reflected solar radiance has been estimated and removed, or has been avoided by use of night-time data. Figure 3.6a shows the spectral radiance curves for a three-component surface: 0.0005 of the surface occupied by 1200 °C ground, 0.02 of the surface occupied by 500 °C ground and the remainder occupied by 100 °C ground, together with the total radiance curve obtained by summing these components. In this case neither the 1200 °C nor the 500 °C maxima are preserved. In practice, we could never observe the total spectral radiance curve shown in Figure 3.6a, because of atmospheric absorption of the upwelling radiance. The observed spectral radiance would be more like the upper curve in Figure 3.6b, which shows the same curves but multiplied by atmospheric transmission coefficients calculated using a LOWTRAN 6 model (Kneizys *et al.*, 1983). Further refinements that would be necessary for an ideal system include correcting for local, volcanogenic, contributions to the atmosphere and allowing for spectral emissivity variations. Thus we would have to start with data resembling the top curve in Figure 3.6b, carry out all the corrections to produce a curve like the top one in Figure 3.6a, and then calculate the fractional areas and temperatures of the components responsible.

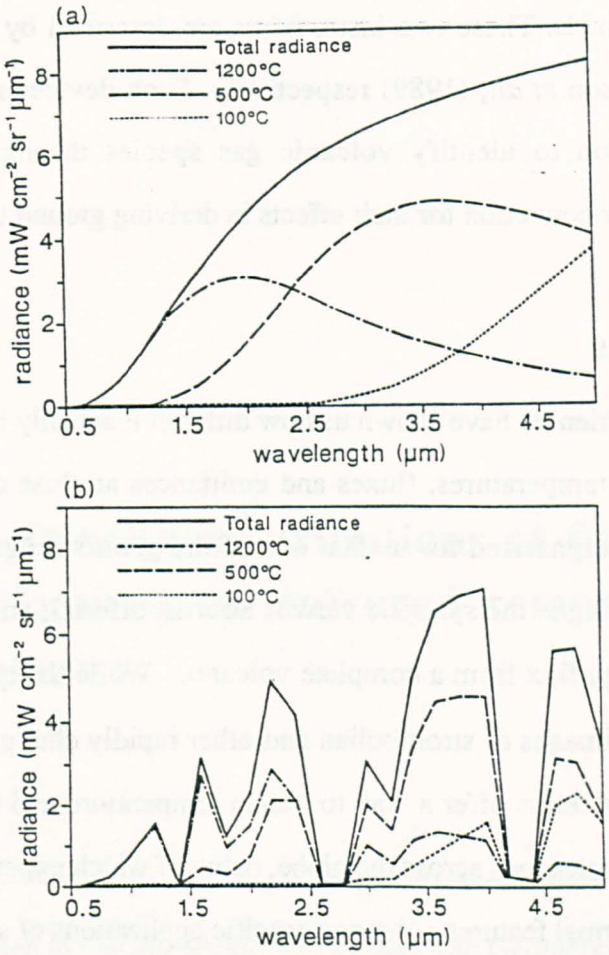

Figure 3.6. (a) Spectral radiance from surface components at three different temperatures and the total spectral radiance calculated from these, in the absence of atmospheric effects. (b) The same spectral radiance curves after correction for atmospheric transmission, derived from a LOWTRAN 6 model (mid-latitude, summer, 3000 m altitude). A surface emissivity of 0.8 is assumed.

At present, data of this sort covering volcanoes do not exist, but they should become available once the Earth Observing System (EOS) is deployed, beginning in the late 1990s, with major contributions from NASA, ESA, Japan and Canada. EOS will consist of several polar-orbiting satellites with a wide variety of remote sensing instruments. The two most appropriate instruments for measuring volcanic thermal radiance would appear to be the High Resolution Imaging Spectrometer (HIRIS), which will have about 200 narrow spectral channels extending from 0.4 μm to 2.5 μm with a 30 m instantaneous field of view, and the Moderate Resolution Imaging Spectrometer (MODIS), which will have 40 narrow spectral channels distributed between 0.4 μm and 14.2 μm (mostly in atmospheric windows) with an instantaneous field of view of

1000 m in most channels. These two instruments are described by Goetz and Herring (1989) and Salomonson *et al.*, (1989) respectively. Such devices may give sufficient additional information to identify volcanic gas species through their distinctive absorptions, and allow correction for their effects in deriving ground temperatures.

3.6. Conclusions

Our field experiences have shown us how difficult it actually is to obtain volcano-wide data on radiant temperatures, fluxes and emittances at close range using manual techniques. It has emphasised for us that one of the great strengths of satellite, and airborne, remote sensing is the synoptic view it affords, offering an excellent means to measure radiant energy flux from a complete volcano. While the quantitative value of occasional 'snapshot' images of strombolian and other rapidly changing activity may be limited, they do nevertheless offer a way to obtain temperature and radiant flux data of consistent quality for volcanoes across the globe, many of which experience more gradual changes of surface thermal features. Among specific applications of such data will be the acquisition of time-series infrared imagery of active lava flows to provide the much needed real data for understanding their behaviour (Pieri *et al.*, 1990).

Daytime imagery has given us some problems: in the SWIR, reflected sunlight may swamp lesser radiant anomalies, while at TIR wavelengths, the background radiates significantly and is difficult to model because surface temperatures vary as a result of solar heating, evaporative cooling, surface cover, etc. The difficulties in 'navigation' on night-time data may be outweighed by the increased likelihood of conclusive identification of hot sources and reduced errors in determining thermal radiant fluxes. (At the time of writing we are awaiting night-time Landsat TM images for Momotombo and Lascar volcanoes). Even at their simplest level, however, remote sensing techniques could provide a world-wide monitoring and warning system provided that data can be distributed quickly and affordably. We look forward to the data from forthcoming remote sensing platforms with great enthusiasm.

Chapter 4. Thermal distributions at fumarole fields: implications for infrared remote sensing of active volcanoes

---

Paper to be submitted to the *Journal of Volcanology and Geothermal Research.*

4.1. Abstract

Multi-channel short wavelength infrared (SWIR) data recorded by the Landsat Thematic Mapper (TM) have been used to estimate sub-pixel resolution temperatures of hot volcanic features. To do this requires simplifying assumptions to be made concerning the distribution of temperatures across the surface in question. The validity of these preconditions is investigated here for fumarole fields, an important class of thermal phenomena. Thermometric surveys, conducted at Momotombo (Nicaragua) and Vulcano (Italy), suggest that SWIR emission from the interiors of high-temperature fumarole vents far exceeds that from their surrounds. In contrast, cooling crust on active lava bodies can contribute more SWIR radiation than the small areas of exposed incandescent core which are often present. Such differences should be discernible in the relative response between the two TM SWIR bands, providing a basis for the

identification of unknown thermal anomalies in TM or similar data. However, estimates of sub-pixel temperatures and heat flux, made from such satellite data, remain unreliable.

4.2. Introduction

In the near future, a wealth of remotely sensed data of volcanoes will be provided by satellite remote sensing missions, notably NASA's Earth Observing System (EOS), whose first platform of instruments is scheduled for deployment in 1998 (Mouginis-Mark *et al.*, 1991). It is desirable that the knowledge necessary to understand and interpret this information is established before any data are actually recorded. The volcanic hazards community in particular will require, in addition to rapid dissemination of data, the availability of appropriate algorithms to analyse them. Mouginis-Mark *et al.* (1991) attached particular importance to the use of infrared sensors for detection of volcanic thermal anomalies. Several papers have already illustrated the sensitivity of Landsat TM SWIR channels to thermal radiance from lava domes and flows (e.g. Francis and Rothery, 1987; Rothery *et al.*, 1988), and fumarole fields (Oppenheimer and Rothery, 1991). In this paper I investigate some key problems made apparent by these existing studies.

4.2.1. The dual-band technique

The TM has two spectral channels in the SWIR region, band 5 at 1.55-1.75 μm, and band 7 at 2.08-2.35 μm, allowing the adaptation of a two-waveband technique, first proposed by Dozier (1981) and Matson and Dozier (1981), for estimating temperatures of very small fractions of TM image pixels (which nominally represent 30 x 30 m areas of ground). This was introduced as the 'dual-band technique' by Rothery *et al.* (1988).

Radiation thermometry relies on the Planck distribution law which expresses the spectral radiant intensity emittance, $H(\lambda,T)$, from a black-body at absolute temperature, T, as a function of wavelength, λ:

$$H(\lambda,T) = c_1\lambda^{-5}[\exp(c_2 / \lambda T) - 1]^{-1} \qquad (4.1)$$

where the constants c_1 and c_2 have the values 3.74127×10^{-16} W m^2 and 1.4388×10^{-2} m K respectively. For isotropic radiation, $H(\lambda,T)$ is independent of direction, and the spectral radiance, $L(\lambda,T)$ is given by:

$$L(\lambda,T) = H(\lambda,T) / \pi \qquad (4.2).$$

The dual-band technique requires the assumption that the thermal distribution of the area sensed in a given pixel is represented by only two components. In the case of a lava body, these might correspond to a hot portion, at kinetic temperature T_C occupying a fraction f of a pixel, and a cooler part at kinetic temperature T_S occupying the remaining fraction $(1 - f)$. If the two SWIR channels, which have central wavelengths λ_5 and λ_7, record spectral radiances of thermal origin, $R_{5,thermal}$ and $R_{7,thermal}$, then one may write:

$$R_{5,thermal} = \varepsilon_5 \tau_5 [f L(\lambda_5,T_c) + (1 - f) L(\lambda_5,T_s)] \qquad (4.3)$$

and

$$R_{7,thermal} = \varepsilon_7 \tau_7 [f L(\lambda_7,T_c) + (1 - f) L(\lambda_7,T_s)] \qquad (4.4)$$

where ε_5, ε_7 are spectral emissivities of the surface (assumed equal for each thermal component), and τ_5, τ_7 the atmospheric transmission coefficients in each channel. Any two of the parameters out of f, T_C and T_S can then be found by graphical or numerical solution of these simultaneous equations, if the third is assumed (choosing also appropriate values for spectral emissivities and transmissivities).

Having derived surface temperatures, it is possible to estimate radiative and convective heat losses from the surfaces in question. Such measurements are potentially useful for volcano monitoring (e.g. Glaze *et al.*, 1989a), and can also be used to parameterise physical models of aspects of active volcanism such as the dynamics of lava flows (Pieri *et al.*, 1990; Oppenheimer, 1991b). Two important questions arise from this work: (i) how can one identify the nature of a thermal anomaly discovered in an infrared image of a volcano, and (ii) how reliable are estimates of temperatures and heat fluxes derived from SWIR data ?

4.2.2. Identification of thermal anomalies

In several cases - usually where ground observations of the relevant volcano were lacking - it has proved difficult to identify confidently from TM images the nature of thermal features whose infrared signatures are so clearly written in the data. In particular, discrimination between lava bodies and high-temperature fumarole fields has been problematic in instances of intra-crater TM SWIR anomalies composed of only a few pixels (see Rothery *et al.* [1988] and Glaze *et al.* [1989a] on Láscar volcano). The inability, at times, to make even such general distinctions as whether or not lava has reached the surface obviously limits the value of the satellite data.

How does one identify the cause of a volcanic thermal anomaly in satellite data ? Knowledge of the site in question clearly aids interpretation (for example, in the case of a volcano with a known history of lava lake activity) but there are also clues in the remotely sensed data themselves. All of the following should be taken into account.

(i) Spatial attributes. Size, shape and distribution of thermal anomalies naturally reflect the coarse-scale disposition of hot sites on the ground. For example, long, narrow groupings of radiant pixels are suggestive of either lava or pyroclastic flows. Smaller groupings of pixels can be more difficult to identify, although scattered clusters have been interpreted as fumarole fields and nucleated groups as lava lakes (Rothery *et al.*, 1988); an annular thermal anomaly on a TM image of Láscar was interpreted as a lava dome (Chapter 5). Variation in measured intensity within an anomaly can also be significant: an anomaly may appear 'hotter' at the margins, or in its centre.

(ii) Context. In daytime images, the location of an anomaly with respect to the topography and other features of the volcano can be appraised. An anomaly may be sited within a crater, or on the flank or foot of a volcano. It may extend downslope, as would be expected of a flow. It may be associated with fumarole or ash plumes.

(iii) Spectral attributes. Where satellite observations are available in more than one spectral band, the distribution of thermal radiance between different wavelengths

depends on the surface temperatures of materials sensed, and their relative areas in a given pixel. These are important clues as to the nature of the thermal anomaly. For instance, a broad expanse of ground at 100°C will radiate negligibly in the SWIR region, yet may overwhelm the response of sensors in the thermal infrared (TIR). Conversely, a very small feature (compared with the spatial response of a given satellite sensor) but at close-to magmatic temperature, could saturate SWIR channels while being undetected in the TIR. Apparent temperatures can be misleading, however; hot surfaces lose heat and become cooler. It might, for instance, be impossible to distinguish between a recently deposited pyroclastic flow and a substantially cooled lava flow, using satellite data alone.

(iv) Comparison of time-series of satellite data. Temporal changes in spatial and/ or spectral attributes of an anomaly can also provide a context for interpretation. For example, radiant temperatures at the surface evolve more gradually for a fumarole field than for a lava-filled strombolian vent (Oppenheimer and Rothery, 1991).

Point (iii) above raises the need for characterisation of temperature distributions associated with different volcanic thermal manifestations. Hitherto, this has only been attempted for lava lakes; using a field spectrometer, Flynn *et al.* (1989) showed that the surface of the Kupaianaha lava lake (Hawaii) was dominated by 2 or 3 thermal components. In this paper, I report the results of infrared surveys made at fumarole fields. The aims are to establish thermal distributions associated with fumarolic surfaces, and to see if such descriptions distinguish them from other high-temperature phenomena. In addition to thermal mapping, fluctuations of temperature with time are also examined, since the value of regularly acquired satellite 'snapshots' for routine monitoring depends to a large extent on the timescale and magnitude of any changes in surface temperatures.

4.2.3. Fumaroles and field thermometry

Fumarole emissions are monitored at many volcanoes, the simplest level of such efforts being the routine measurement of temperatures of gases, crater lake waters, hot springs and ground test-sites, using thermoelectric, bimetallic or liquid-in-glass thermometers. Data of this kind have long been collected by personnel visiting active

sites but there are increasing opportunities for using telemetry, notably by satellite communication, to relay automatically recorded temperature, and other, measurements to distant observatories (e.g., Sabroux *et al.*, 1990). Such measurements represent *contact* temperatures of the media concerned. In order to provide information compatible with remotely sensed infrared data, *surface* temperature distributions are required, hence the rationale behind an independent programme of field measurements. Even where optical pyrometers and infrared thermometers have been used in the field - usually for recording lava temperatures - data are, for obvious reasons, rarely collected in a spatially consistent fashion, the goal often being merely to record a maximum temperature (see Archambault and Tanguy, 1976). Such surveys have provided little more than instantaneous readings at a few localities.

Airborne and previous ground-based single-band, infrared radiometric surveys have not provided suitable data either. Typically, these have involved observations in the TIR part of the spectrum (particularly in the 8-14 μm atmospheric window), of relatively low temperature ground heating associated with weak to moderate fumarolic/ hydrothermal activity (e.g. Moxham, 1970; Birnie, 1973; Tabbagh *et al.*, 1987; Bianchi *et al.*, 1990). There appear to be no well-calibrated data for high temperature fumaroles or lava bodies. In any case, such surveys have not, in general, been of sufficiently high spatial resolution to discriminate fine thermal structure. What they may provide is a link, in terms of spatial continuity, between satellite observations and close-range field radiometry of the nature undertaken in this study.

In order to document surface temperature distributions, I have used a range of thermometers including bimetallic and thermocouple devices, and two Minolta/Land 'Cyclops' infrared thermometers, one operating at 8-14 μm, the other at 0.8-1.1 μm (Table 4.1; Figure 4.1). Both work on the same principle: radiation from a well-defined portion of the target is focussed optically onto a detector, whose resulting analogue electrical signal is amplified, digitised, processed and displayed within the viewfinder. Target sizes of each thermometer are a function of the respective angular fields of view of their sensors (Table 4.1), and the viewing angle with respect to the surface being

measured. In the field, the instruments were tripod mounted, so as to view the ground approximately perpendicularly over distances of about 1-2 m. Where the aim was to map thermal distributions spatially, temperature readings were either annotated on Polaroid photographs taken on site, or recorded as a function of distance along linear profiles. To take readings in rapid succession, the temperature display in the viewfinder was called out, and recorded on audio cassette.

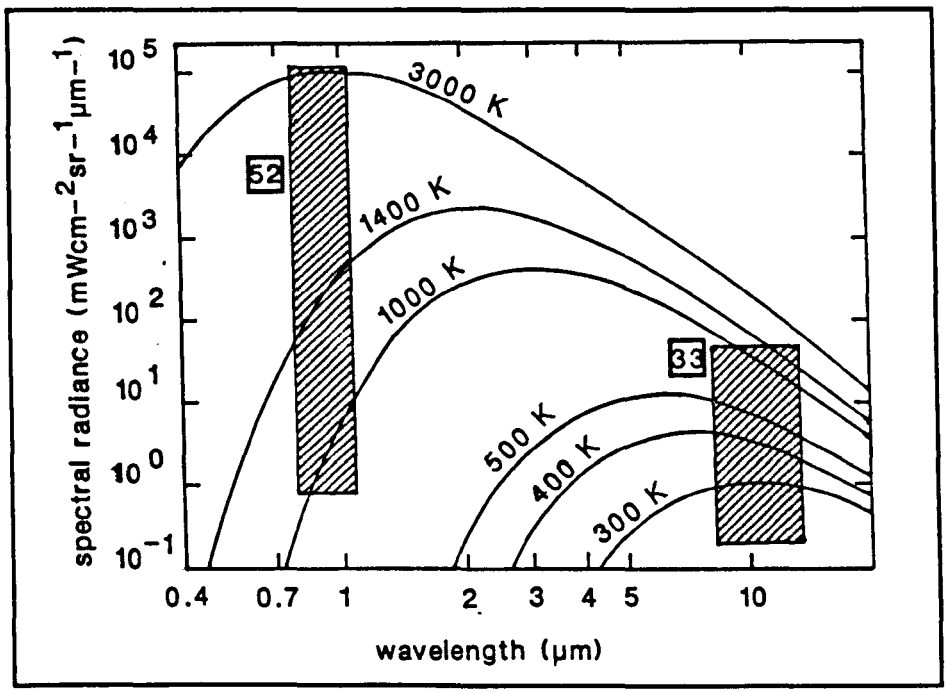

Figure 4.1. Spectral responses and dynamic ranges of the two infrared thermometers superimposed on Planck distribution curves of spectral radiance for a range of temperatures.

Several points concerning the operation of the thermometers should be borne in mind when interpreting their measurements:

(i) The readout from each instrument represents a temperature calculated from the spectral radiance within the sensor bandpass, integrated over the whole target field of view. If the target is not at a uniform surface temperature, then the Planck distribution law (4.1) results in a reading weighted according to each thermal component and its corresponding proportional area within the field of view. In other words, the readout represents a temperature somewhere between those of the highest and lowest sensed.

(ii) For consistency, and since surface emissivities were not measured, brightness (black-body) temperatures only were recorded.

(iii) The spectral bandpasses of the two thermometers (Figure 4.1) do not correspond favourably to the wavelengths of the most useful spaceborne sensors (unfortunately, there is no overlap with TM bands 5 and 7).

(iv) Because of the spatial detail of the thermal measurements, it was not feasible to map areas of ground comparable to the scale of 30 x 30 m TM pixels.

Instrument	Cyclops 33	Cyclops 52
Detector	lithium tantalate	silicon photocell
Bandpass (μm)	8 to 14	0.8 to 1.1
Temperature range (°C)	-50° to 1000°	600° to 3000°
Field of view	1°	0.33°
Target diameter	13 mm @ 75 cm	4.8 mm @ 101.4 cm
Response time (s)	0.5	0.03

Table 4.1. Specifications of Minolta/Land infrared thermometers.

4.3. Field observations

Two volcanoes were targeted for study on account of their persistent fumarole emissions, and ease of access to active sites: Volcán Momotombo, Nicaragua, and Vulcano, Italy.

Momotombo's last eruption in 1905 produced basaltic andesite lava flows from the summit crater. Since then, fumarolic activity has been intermittent, though temperatures rose markedly some time between July 1973 and February 1978 from 250°C to 750°C (Benhamou *et al.*, 1988). Allard and Sabroux (1980) suggested that the elevated temperatures indicated the presence of a large, convecting, very shallow magma intrusion, and Menyailov *et al.* (1986) claimed that the disposition of the fumaroles was controlled by concentric fissures related to subsidence of the crater floor.

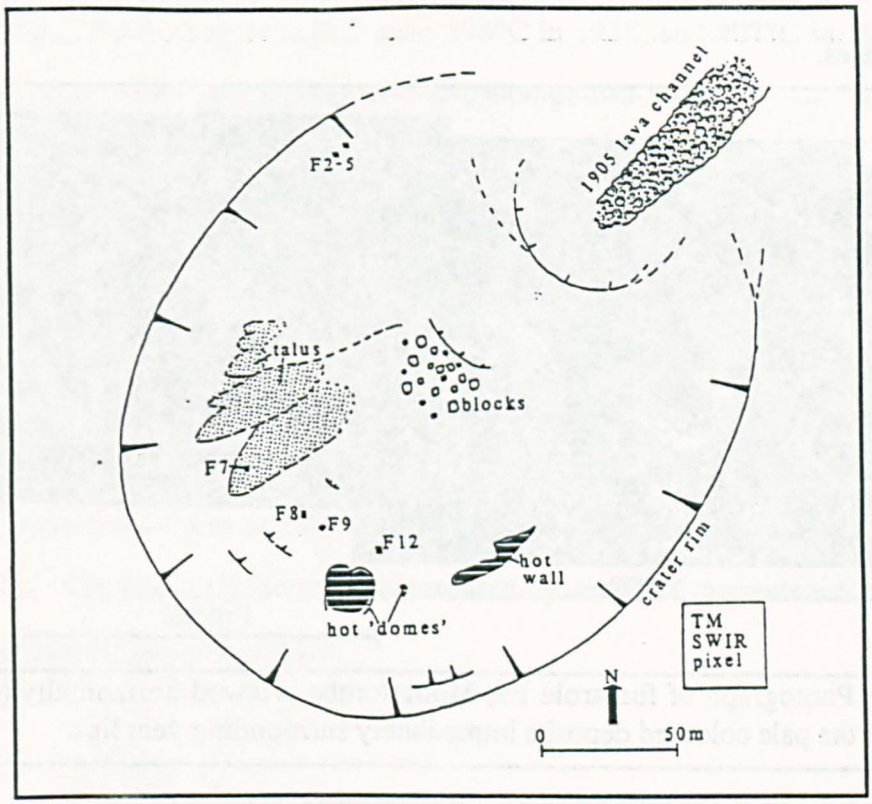

Figure 4.2. Sketch map of the summit crater of Momotombo volcano, showing disposition of high temperature fumaroles. Some incandescent vents, such as F8 and those on the hot 'domes', opened onto steep surfaces and would have been difficult to detect by a vertically pointed radiometer.

Fieldwork for this study was carried out at Momotombo in March - April 1989 and April 1990. Several clusters of hot fumaroles were then present within the summit crater (Figure 4.2), their vent interiors glowing bright orange or red, and pale orange flames of burning gases extending several tens of cm from many vent mouths (Smithsonian Institution, 1989c). There was no visible incandescence beyond vent lips. I recorded a peak gas temperature of 880°C in 1989 (by thermocouple with 25 cm length of probe) at a fumarolic mound referred to as F9 (Figure 4.2), although gas temperatures varied quite widely between individual vents, even those in close proximity (Figures 4.3 and 4.4). The corresponding maximum radiant temperature measured by the SWIR thermometer, viewing the interior of F9, was 888°C. By April 1990, gas temperatures had dropped at many fumaroles, typically by 50-150°C; the highest recorded during this time was 772°C at F9. That gas contact temperatures varied little from radiant temperatures of vent walls implies that, ignoring any effects of atmospheric transmission,

a remotely measured temperature of a vent interior would approximate the temperature of escaping gases.

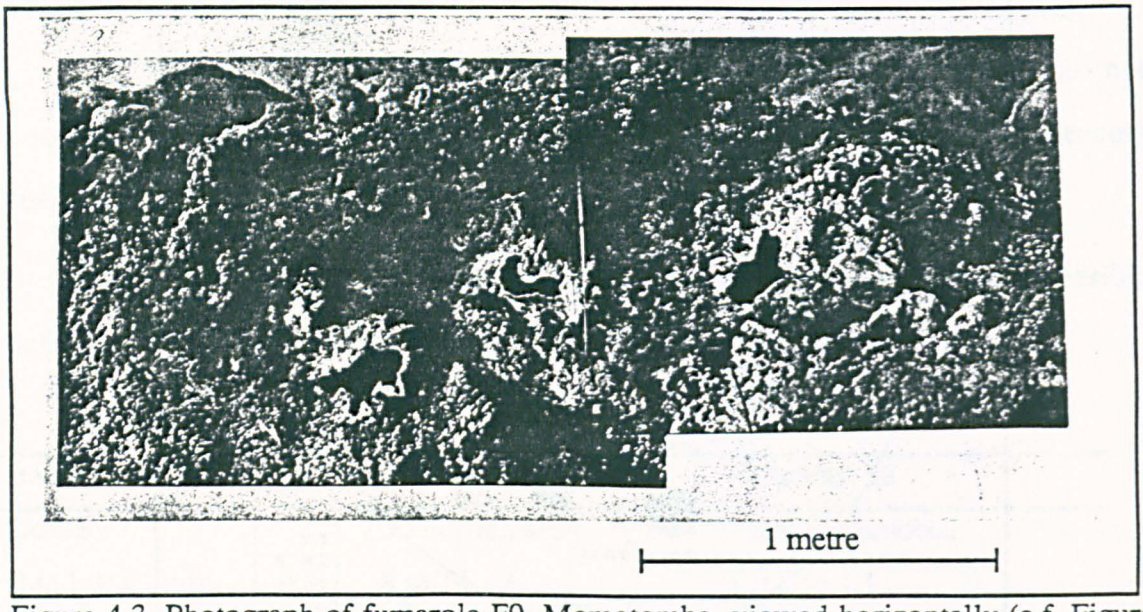

Figure 4.3. Photograph of fumarole F9, Momotombo, viewed horizontally (c.f. Figure 4.2). Note the pale coloured deposits immediately surrounding vent lips.

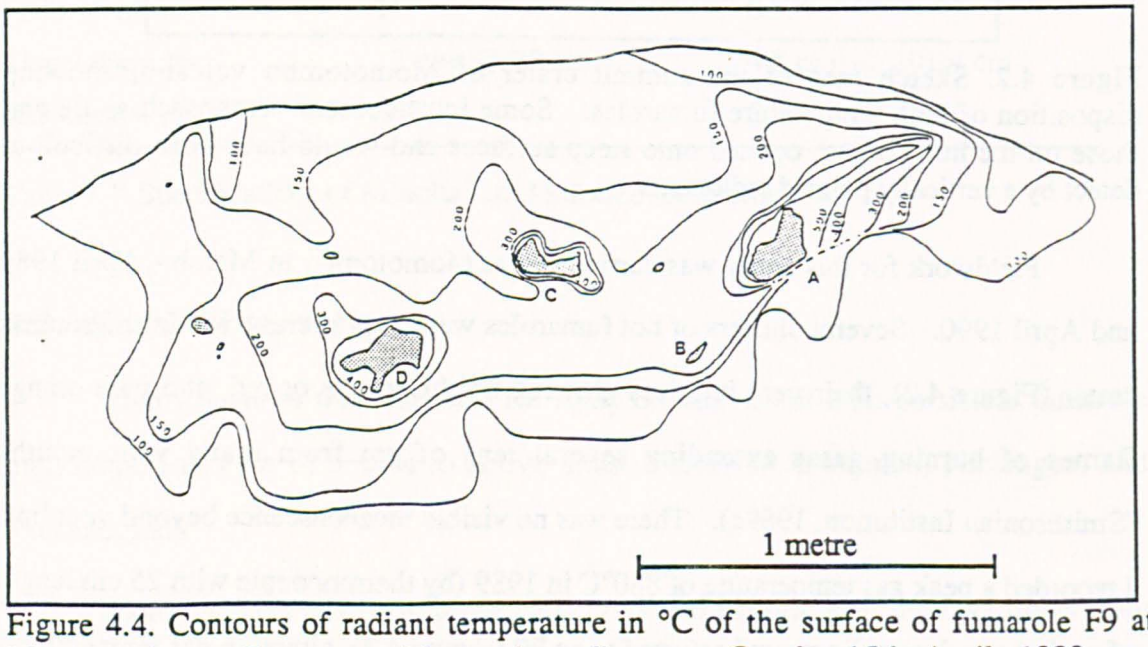

Figure 4.4. Contours of radiant temperature in °C of the surface of fumarole F9 at Momotombo. Compare with previous figure. On the 15th April, 1989, gas temperatures at vents A, B, C and D were 880°C, 870°C, 779°C and 716°C, respectively.

Since its last eruption in 1888-90, Vulcano has experienced often intense fumarolic activity, which is now concentrated on the north rim of the main cone, Gran Cratere (Tedesco *et al.*, 1991). During field investigations in October - November 1988 and September - October 1989, gas temperatures were very stable (Oppenheimer and

Rothery, 1991); the highest recorded were 396°C in 1988, and 407°C in 1989 (at the same vent), though most temperatures were in the range 100-300°C.

4.3.1. Spatial patterns of radiant temperature

Access to F9 at Momotombo was relatively straightforward and it was the site most closely studied there (Figure 4.3). Figure 4.4 shows a map of isotherms on the surface of F9 constructed from the 1989 field data. By measuring the area within each temperature interval, the thermal distribution across a putative 30 x 30 m TM pixel which completely contains F9 but no other high-temperature thermal source, can be obtained (Figure 4.5). Glowing vent orifices, represented by an 800°C component, occupy just 0.054 m^2 within the imaginary pixel.

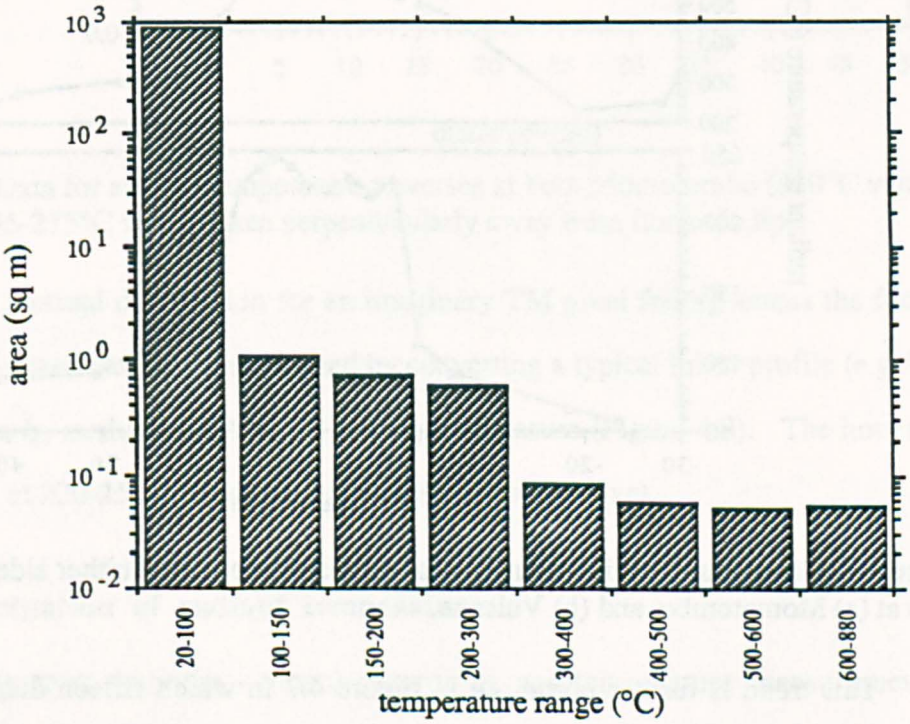

Figure 4.5. Thermal distribution for imaginary 30 x 30 m pixel placed over fumarole F9 at Momotombo. See text.

Attention at Vulcano Island was focussed on a continuous 40 m long fumarole fissure running along the northern rim of the crater. Temperature profiles transverse to the fissure were measured at several points with the 8-14 μm thermometer. These profiles were generally symmetrical about the vent axis, with steep gradients between

about 80°C to 220 °C flanking a plateau of variable width at around 240°C (Oppenheimer and Rothery, 1991). A comparison of field data from Momotombo and Vulcano is shown in Figure 4.6a and b. Although gas temperature was markedly different in each case, the overall shape to the temperature curves is similar at the same spatial scale. There are steep decreases in surface temperature immediately outside the vent lip; at Momotombo, for example, temperatures drop more than 200°C within the 6 mm target circle of the infrared thermometer. 10-50 cm from vents they have fallen to between 125-200°C.

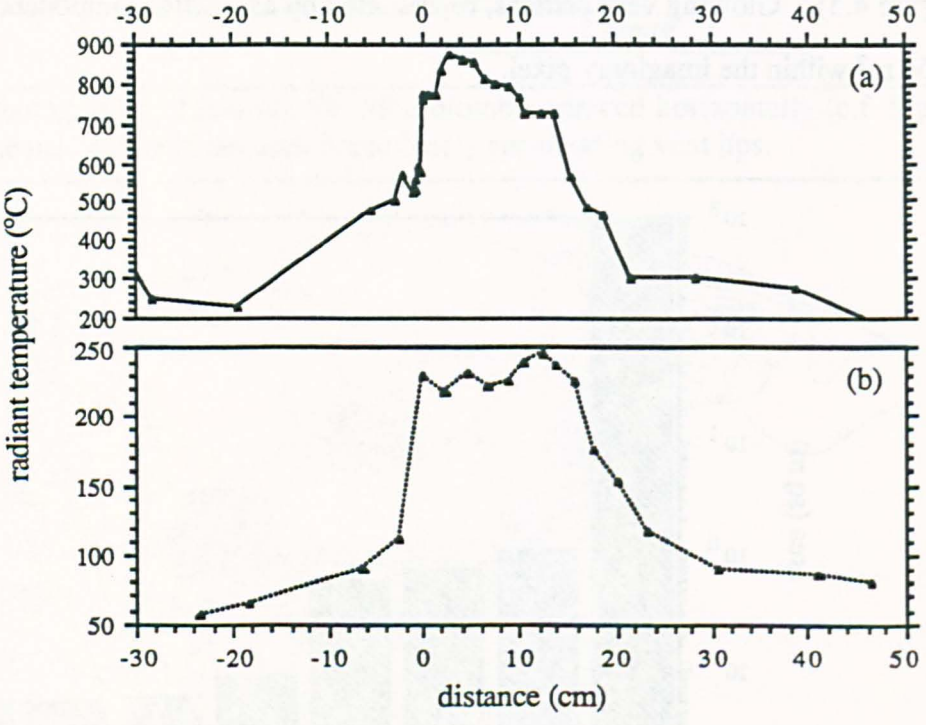

Figure 4.6. Comparison of linear profiles of surface temperature either side of fumarole vents at (a) Momotombo, and (b) Vulcano.

This trend is further borne out in Figure 4.7 in which fifteen thermal profiles measured at Vulcano (gas temperatures between 193 and 275°C), and two at Momotombo (gas temperature of 880°C) are plotted as a function of distance from the vent lip. The temperatures have been normalised by the relation: $(T_x - T_{air}) / (T_{gas} - T_{air})$, where T_x is the measured surface temperature at distance x from the vent lip, T_{air} is the ambient air temperature, and T_{gas} is the gas exit temperature of the fumarole. These dimensionless temperatures are halved within a very few cm of the vent lip. Some of the scatter in the

y-direction can be attributed to wind effects, such as enhanced cooling of the surface on the upwind side of vents (Oppenheimer and Rothery, 1991).

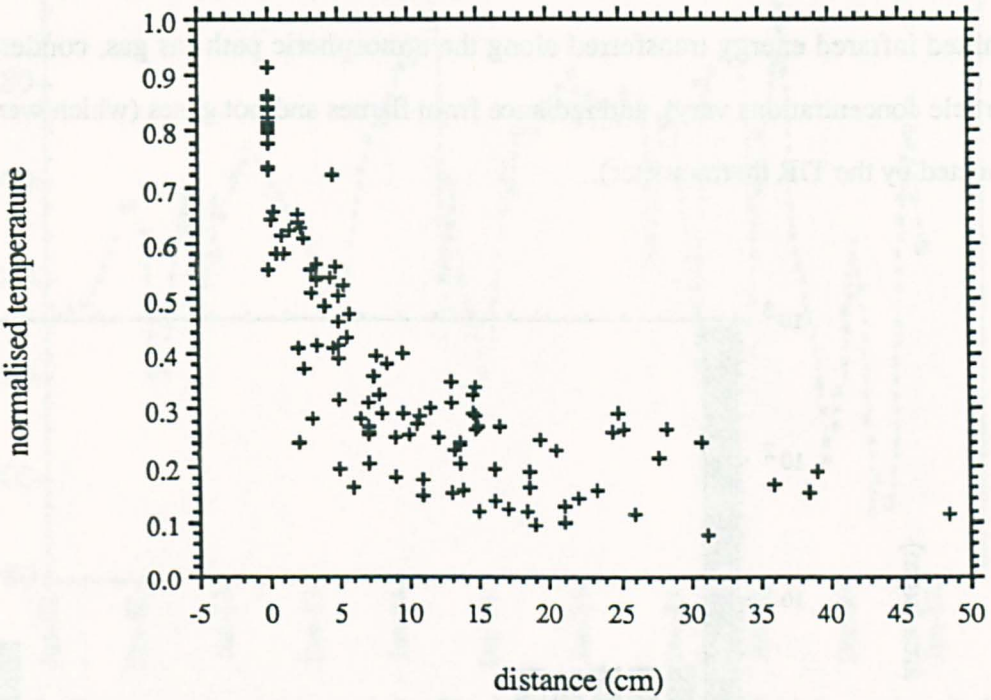

Figure 4.7. Data for several temperature traverses at both Momotombo (880°C vent) and Vulcano (195-275°C vents) taken perpendicularly away from fumarole lips.

The thermal distribution for an imaginary TM pixel falling across the fumarole fissure at Vulcano can be approximated by converting a typical linear profile (e.g. Figure 4.6b) to area by multiplying by a 30 m length of fissure (Figure 4.8). The hottest vent component, at 220-250°C, occupies less than 5 m^2 of the pixel.

4.3.2. Fluctuation of radiant temperatures

Long term (months - years) records of gas temperature measurements are available for many volcanoes. Figure 4.9 shows thermocouple temperatures recorded at F9, Momotombo, between 1983 and 1988 - there is at most about 100°C of variation. But what of radiant temperatures recorded at shorter time intervals ? Continuous infrared measurements of surface radiant temperatures, at the rate of about two per second, were made at both Vulcano and Momotombo. Data at these timescales are shown for close-range measurements (viewing distance of approximately 1 m) of a small region about 2

cm beyond the vent lip of the hottest vent at F9, Momotombo (Figure 4.10). Fluctuation in radiant temperature is slight for the SWIR thermometer but large for the TIR instrument. These variations may result from changes in thermal emission from the target (due to air turbulence either cooling or heating the surface), in the amount of emitted infrared energy transferred along the atmospheric path (as gas, condensate and particle concentrations vary), and radiance from flames and hot gases (which were clearly detected by the TIR thermometer).

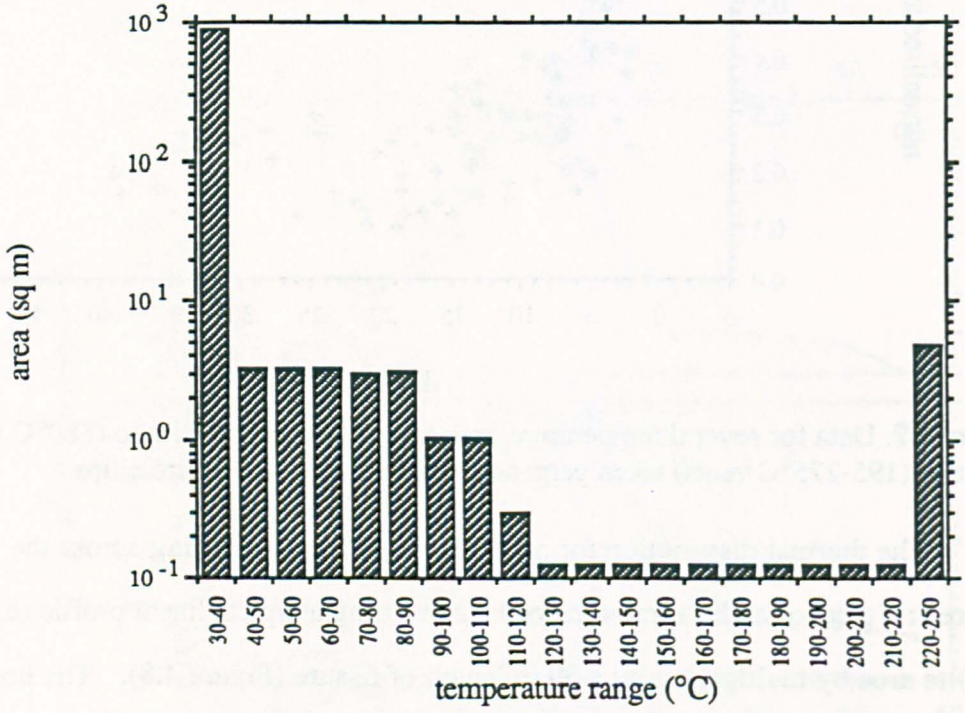

Figure 4.8. Thermal distribution for imaginary 30 x 30 m pixel placed over 30 m length of fumarole fissure at Vulcano. See text.

Considerably smaller variations were observed when the thermometers viewed directly the inner walls of the incandescent vent: over a period of 100 minutes, temperature measured by the SWIR thermometer varied over the remarkably small range of 878-886°C, while during 140 s of rapid readings with the TIR instrument, temperatures varied between limits of 732 and 792°C. Without making measurements across more of the infrared spectrum it is unwise to generalise on the basis of these results without considering specific gas absorption spectra but, given that Momotombo gases are, in common with most fumarole gases, dominated by water vapour (Menyailov

et al., 1986), it is likely that the greater fluctuations observed by the TIR thermometer result from water absorption and scattering phenomena. The 0.8-1.1 μm region is comparatively transparent.

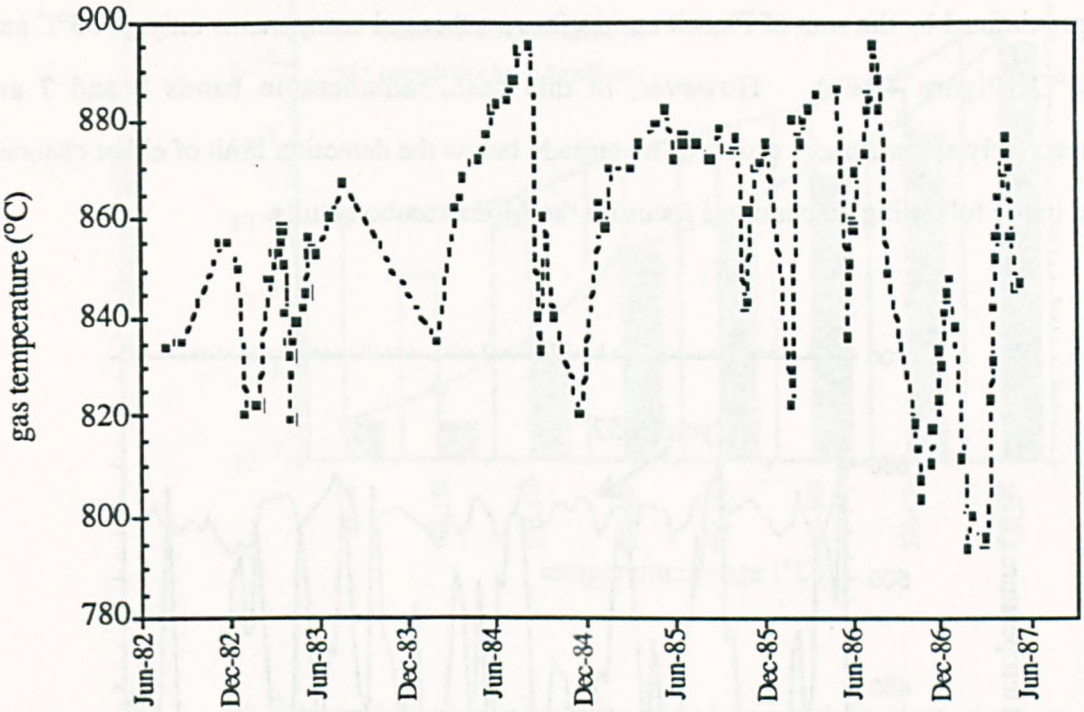

Figure 4.9. Gas temperature record for F9, Momotombo, compiled from data held by INETER.

4.4. Analysis

4.4.1. Thermal components

The spectral radiance corresponding to each of the thermal components displayed in Figures 4.5 and 4.8 can be calculated for any given wavelength using the principles embodied in equations (4.1)-(4.4). It is shown for the central wavelengths of TM SWIR bands 5 and 7 for the Momotombo and Vulcano data, in Figures 4.11a and b respectively. For the Momotombo case, despite their small proportional area, incandescent vent mouths contribute by far the greatest part of the spectral radiance at these wavelengths (over 80 % in band 7 and more than 90 % in band 5). This can also be appreciated in Figure 4.12a which shows the spectral distribution of emitted energy for all wavelengths between 1 and 10 μm. The model spectral radiance distribution is almost

matched by the sum of spectral radiance from just two thermal components, one corresponding to the vent interiors (800°C), the other to ground away from the fumaroles (30°C). For the Vulcano example, the spectral radiance curve is even more closely approximated by the sum of Planck curves for two thermal components only, at 35°C and 225°C (Figure 4.12b). However, in this case, radiances in bands 5 and 7 are respectively about 2 and 1 orders of magnitude below the detection limit of either channel, and in the following discussion I focus on the Momotombo results.

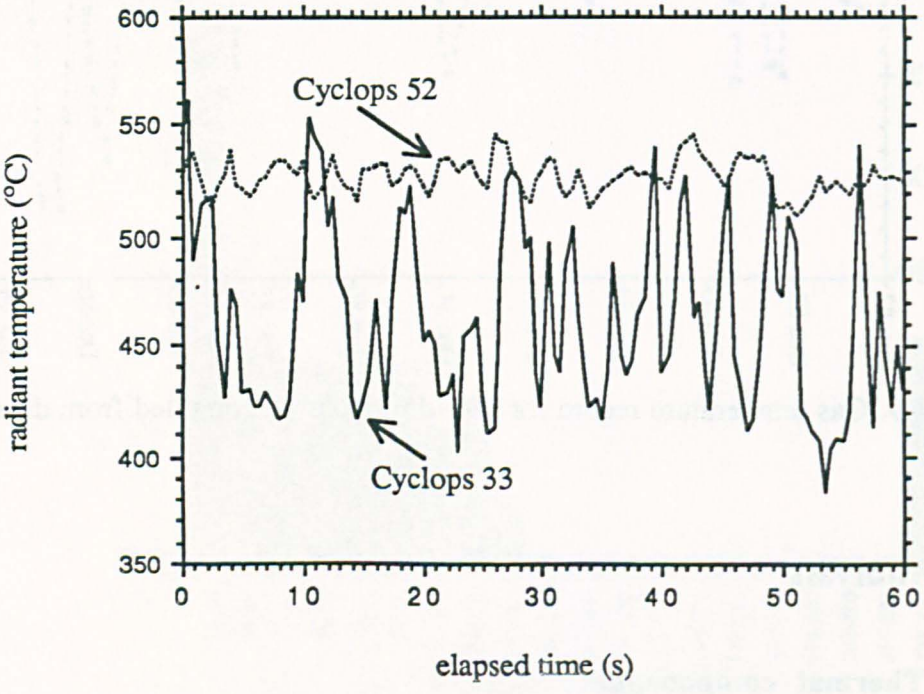

Figure 4.10. Continuous records of radiant temperature of a spot about 2 cm beyond the lip of the hottest vent at F9, Momotombo, on 15 April, 1989. The target area of the Cyclops 33 is nine times that of the SWIR instrument. The two temperature records presented were not taken simultaneously.

The sums of spectral radiance (for all the thermal components at Momotombo F9) at the wavelengths of bands 5 and 7 are 0.019 and 0.039 mW cm^{-2} sr^{-1} μm^{-1} respectively. Using standard calibration data for TM bands 5 and 7 (e.g. Markham and Barker, 1987), and ignoring any atmospheric effects, the corresponding digital numbers (DN) are about 9 and 5 respectively (the TM sensor output is quantised to 8 bits, i.e. each pixel has a value between 0 and 255 for each band). These barely exceed the threshold

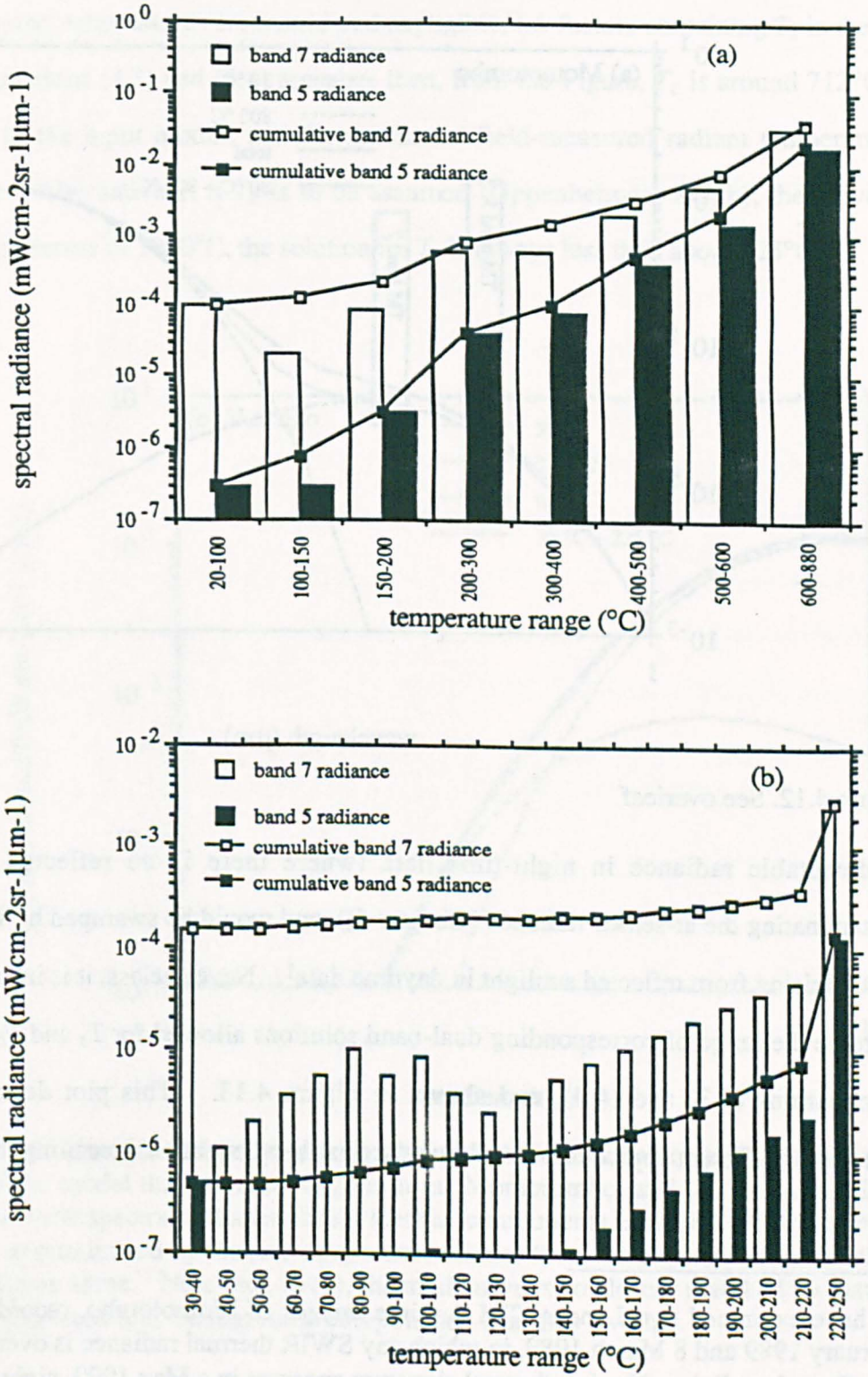

Figure 4.11. Spectral radiance in TM bands 5 and 7 calculated for each thermal component in the model thermal distribution at (a) fumarole F9 at Momotombo, from Figure 4.5, and (b) at Vulcano, from Figure 4.8. In (a) the temperatures used were 30, 125, 175, 250, 350, 450, 550, and 800°C, and in (b) the midpoint of each given range.

the three parameters f, T_s and T_c must be assumed in order to derive the other two. If background temperatures are considered negligible, i.e. factors containing T_s in the dual-band equations (4.3) and (4.4) are zero, then, from the Figure, T_c is around 712°C (c.f. 800°C in the input model, and the maximum field-measured radiant temperature of 880°C). Alternatively, if T_c is to be assumed (Oppenheimer, 1991b), then, even for values in excess of 1000°C, the solution for T_s is always less than about 125°C.

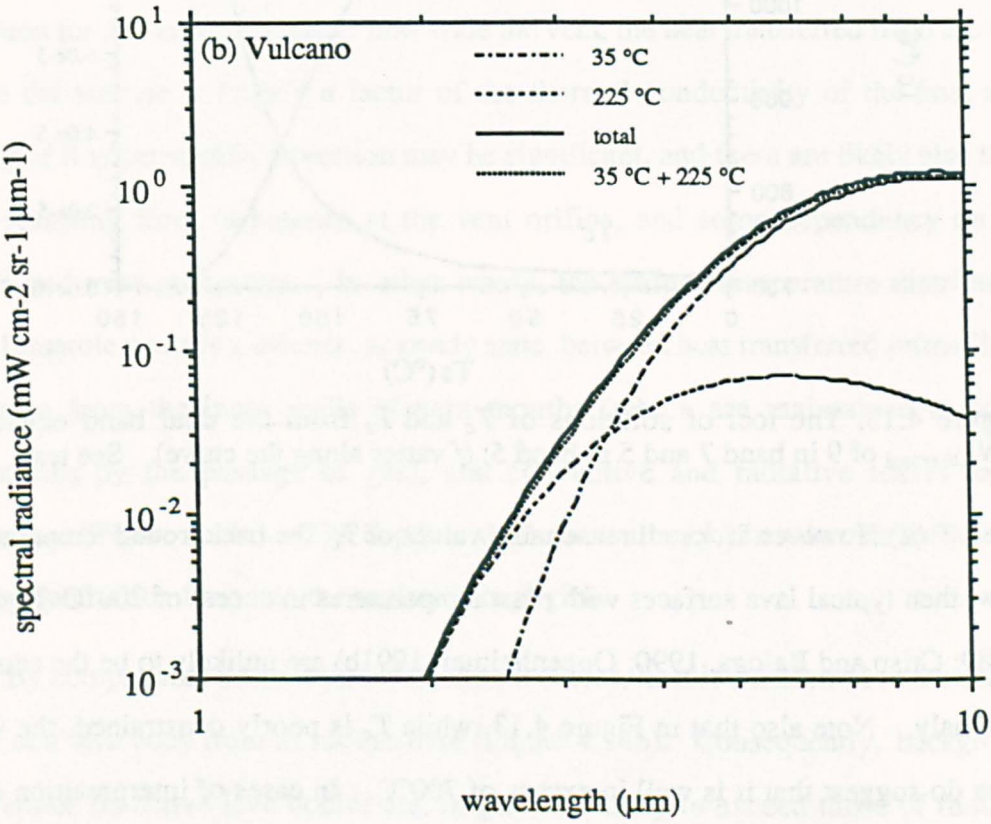

Figure 4.12 (Continued from previous page). Spectral radiance between 1 and 10 µm for each of the model thermal distributions at (a) Momotombo, and (b) Vulcano. In each case, the total spectral radiance for all thermal components is shown. These curves are closely approximated by the sum of spectral radiance from the highest and lowest thermal components alone. Note that, in (b), the total curve is so closely matched by that of the sum of the 'vent' and 'background' components, that they overlap.

This has two implications for potential satellite measurements:

(i) dual-band estimates of fumarole vent interior temperatures are unreliable and should not be taken at face value (e.g. Abrams *et al.*, 1991). If none of the parameters f, T_s and T_c, is predetermined, they are nevertheless mutually dependent (see also Chapter

5). In any case, temperatures of neighbouring fumaroles can vary widely, in which case, estimates of T_c remain at best spectral radiance-weighted averages of several incandescent vents.

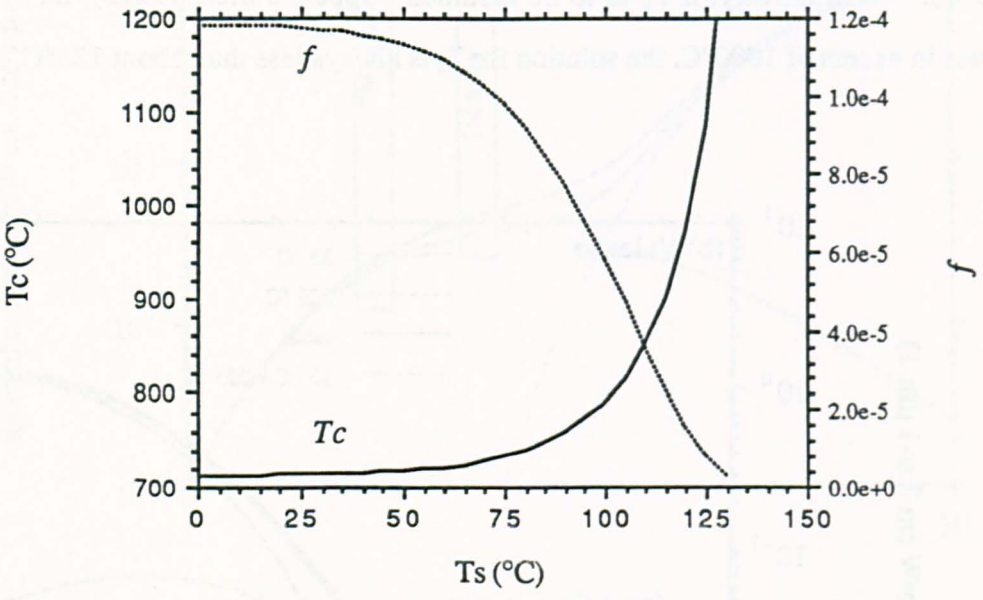

Figure 4.13. The loci of solutions of T_c and T_s from the dual band equations for $DN_{\lambda,thermal}$ of 9 in band 7 and 5 in band 5; (f varies along the curve). See text.

(ii) However, if for all reasonable values of T_c, the background temperature T_s is low, then typical lava surfaces with crust temperatures in excess of 200°C (Flynn *et al.*, 1989; Crisp and Baloga, 1990; Oppenheimer, 1991b) are unlikely to be the cause of the anomaly. Note also that in Figure 4.13, while T_c is poorly constrained, the synthetic data do suggest that it is well in excess of 700°C. In cases of interpretation of small, crater-confined SWIR anomalies, such analysis provides a possible means for distinguishing between fumarole fields and lava bodies.

The reliability of such techniques depends on the size of uncertainties in estimates of the thermally radiant DN, $DN_{\lambda,thermal}$, in each channel. The effect of this on an analysis such as that presented in Figure 4.13 can be gauged by compiling similar plots for a range of DN in bands 5 and 7. For example, if the estimated errors in $DN_{\lambda,thermal}$ for a given pixel are ± 5 in both bands, then graphs could be drawn up for ($DN_{7,thermal}$ + 5) *versus* ($DN_{5,thermal}$ ± 5), and ($DN_{7,thermal}$ - 5) *versus* ($DN_{5,thermal}$ ± 5). In general,

the reliability of estimated $DN_{\lambda,thermal}$ tends to be less for daytime data than for those recorded at night (see Chapter 5). Also, errors are more significant at low DN.

4.4.2. General model of radiant temperature patterns at fumarole fields

Drawing on the foregoing analysis, I propose a general thermal model of fumarolically heated ground as follows. Vent width does not appear to influence the temperature profiles in Figure 4.7, i.e. the distance outwards from a vent lip to a given isotherm is roughly independent of vent size for a given gas temperature. A simple explanation for this is that no matter how wide the vent, the heat transferred from the vent walls to the surface is largely a factor of the thermal conductivity of the host rock (although if it is permeable, advection may be significant, and there are likely also to be effects resulting from turbulence at the vent orifice, and some dependency on gas pressure and vent geometry). In other words, the surface temperature distribution around fumarole vents is a balance, at steady state, between heat transferred primarily by conduction from the inner walls of vent mouths (which are maintained at stable temperatures by the passage of gas), and convective and radiative losses to the environment (Figure 4.14a). The depth to the heat source can be taken as sufficiently great that conduction from it to the surface is negligible.

By comparison, away from incandescent cracks, heat is transferred to the crusted surface of a lava body from its molten core (Figure 4.14b). Consequently, 'background' temperatures on active lava bodies are, in general, likely to exceed those of fumarole fields, although near-magmatic temperatures might prevail over similar fractional areas in each case. Analysis of TM data of a lava flow at Lonquimay volcano, Chile, suggested crust temperatures of between 170-250°C (Oppenheimer, 1991b), and for a lava dome at Láscar volcano, also in Chile, in excess of 200°C (Chapter 5). In reality, a spectrum of phenomena exists, from very active lavas (e.g. lava lakes or ponds sited above degassing magmatic conduits), through substantially cooled lava bodies with low crust temperatures but from which high temperature gases still escape, to fumarole fields where magmatic gases escape from old surfaces that have not been sites of recent eruption of lava. While

different surface temperature patterns may be diagnostic of different volcanic features they need not be unique to them.

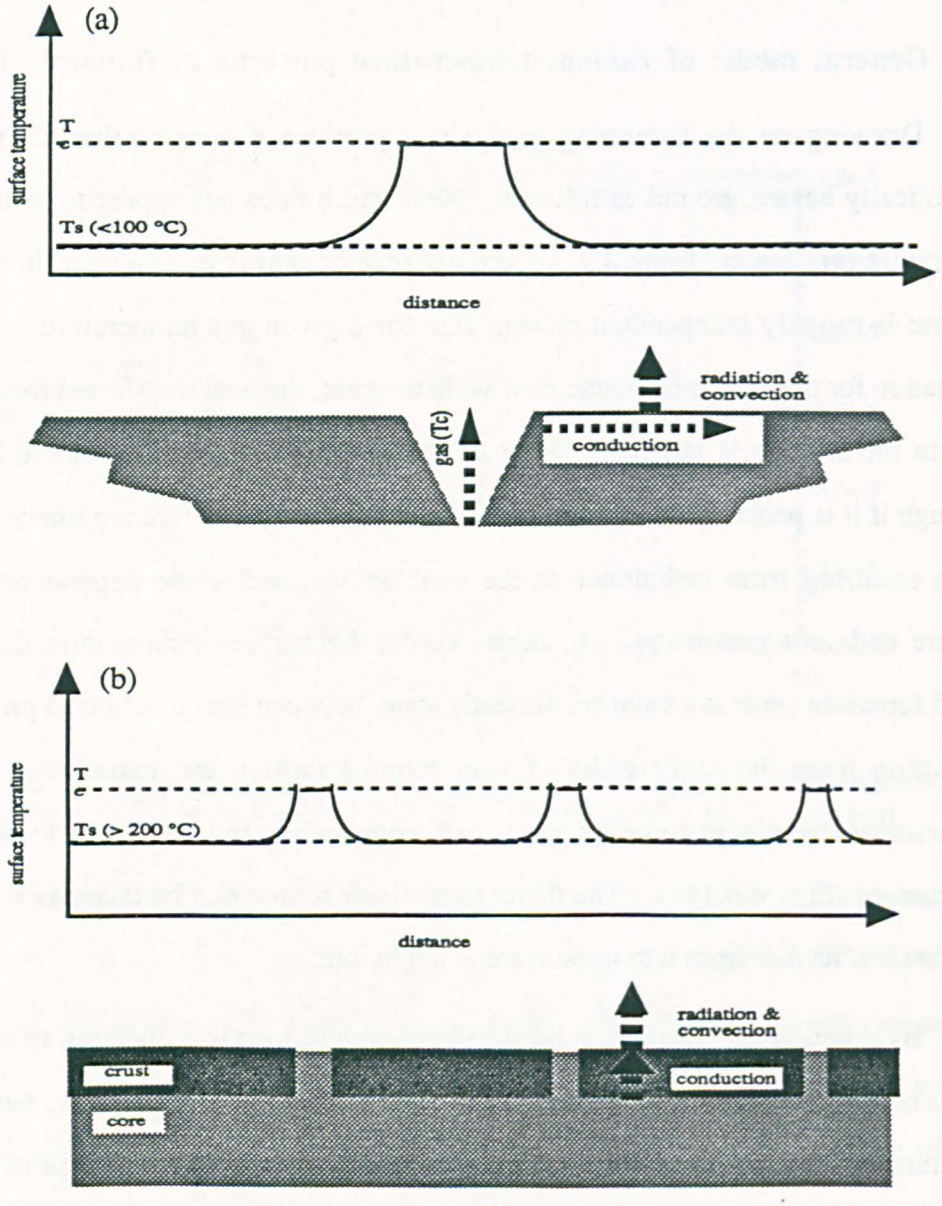

Figure 4.14. Model surface temperature profiles for (a) a fumarole field, and (b) a lava body (see text for discussion).

How representative are the field data collected at Momotombo and Vulcano of fumarole fields in general ? If the theoretical model in Figure 4.14a is accepted, there remains the possibility that variation in the spacing of fumarole vents may influence the distribution of radiance between vent interiors and exteriors. For example, a simple geometrical calculation will show that if total vent area remains fixed but the number of vents increases, so the proportion of SWIR radiance from the outer surfaces will increase

(Figure 4.15). However, following this line of argument, unrealistically large numbers of small vents would be required if regions beyond vent mouths were to contribute substantial radiance in the SWIR. For example, if the annular width, *h*, of hot ground (say >150°C) around fumarole mouths, of diameter 5 cm, is taken as 0.5 m (Figure 4.4), then for the total surface area above this temperature to be equivalent to that of a whole pixel, *n* must be of the order of 1000 vents (Figure 4.15).

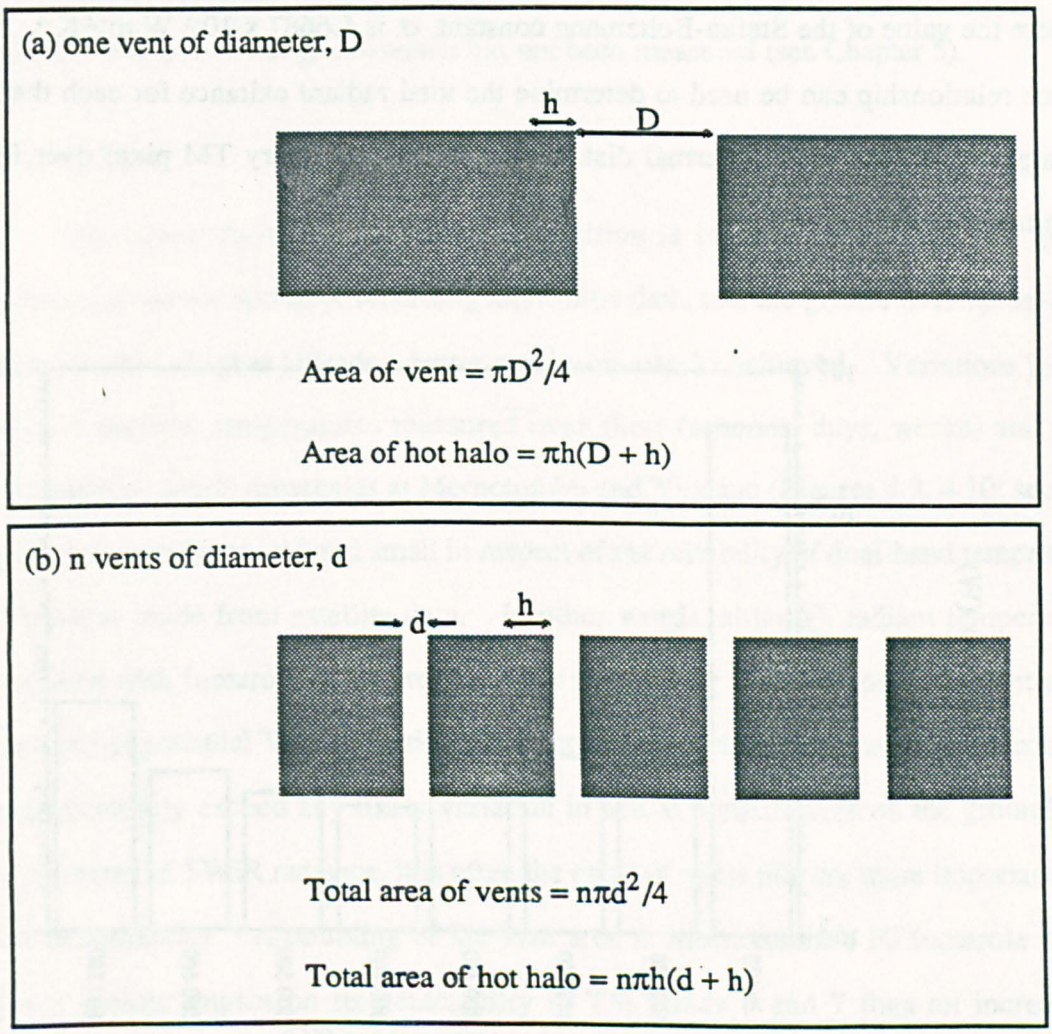

Figure 4.15. Comparison between fumarole fields with few large circular vents and many small circular vents. For a fixed gas temperature, *h*, the distance between the vent lip and a given isotherm is independent of the vent diameter. The total area of ground at temperatures between that at the vent lip and the isotherm chosen increases as the number of vents, *n*, increases. See text for example.

4.4.3. Power output

An important corollary of these results concerns measurements of radiant flux. Temperature estimates obtained from TM data have been used to model radiative heat

outputs (Glaze *et al.* 1989a, Pieri *et al.* 1990, Oppenheimer, 1991b) using Stefan's law (which is derived by integrating equation [4.2] with respect to wavelength). Accordingly, the total radiant exitance, Q_{rad}, from a black-body varies as the fourth power of its absolute temperature:

$$Q_{rad} = \sigma T^4 \qquad (4.5)$$

where the value of the Stefan-Boltzmann constant, σ, is 5.6687×10^{-3} W m^{-2} K^{-4}. The same relationship can be used to determine the total radiant exitance for each thermal component in the model thermal distribution for an imaginary TM pixel over F9 at Momotombo (Figure 4.5).

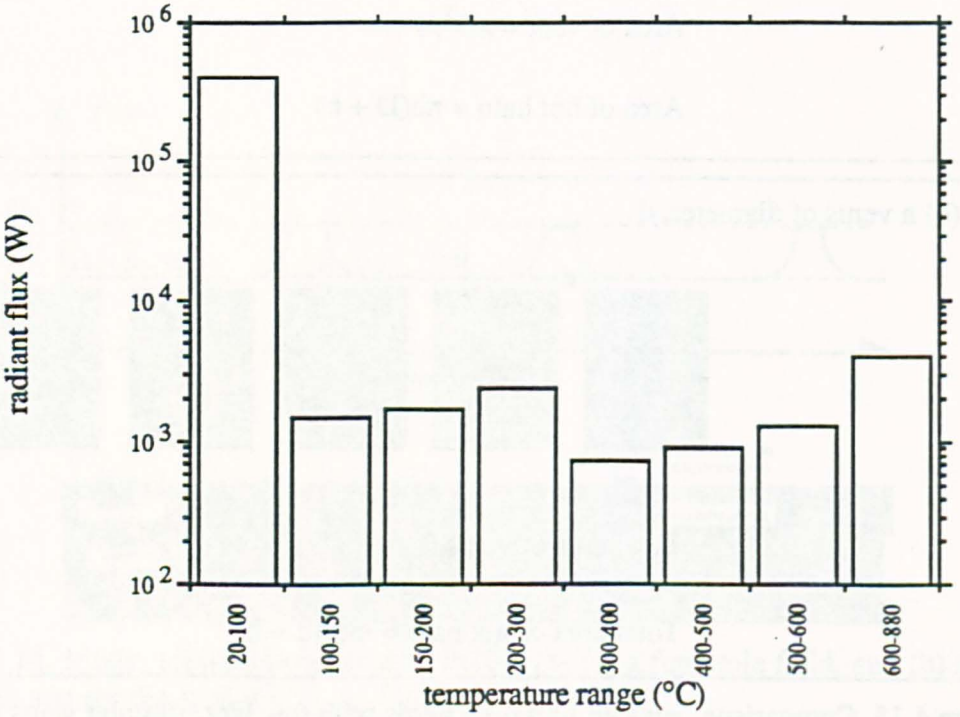

Figure 4.16. Radiant exitance (summed over all wavelengths) calculated for each of the thermal components in the modelled thermal distribution for F9 (Momotombo). Temperatures used in equation (5) were 30, 125, 175, 250, 350, 450, 550, and 800°C. The flux from the background is two orders of magnitude greater than that from the vent interiors.

This is shown in Figure 4.16, from which it can be appreciated that nearly all the whole-spectrum energy comes from the coolest component, and hence belongs to the long wavelength infrared (see also Figure 4.12a). This results, in spite of the fourth

power term for temperature in (4.5), because the fractional areas of the fumarole-heated ground are so small. In other words, for such a thermal distribution, measurements made only in the SWIR cannot adequately constrain the total power output and it would be meaningless to attempt to do so. Instead, it might be more useful (especially for intercomparisons of satellite data acquired on different dates) to simply sum the thermally derived *spectral* radiance where it is measured by a satellite sensor rather than arbitrarily model the flux at wavelengths where it has not been measured (see Chapter 5).

4.4.4. Time

The repeat cycle for TM image acquisition is 16 days for much of the globe. However, given the option of recording night-time data, and the greater overlap between image swaths at higher latitudes, better continuity can be achieved. Variations in gas, and rock surface, temperatures measured over short (seconds, days, weeks) and even long (months, years) timescales at Momotombo and Vulcano (Figures 4.9, 4.10; see also Figure 3.3) may be considered small in respect of the reliability of dual-band temperature estimations made from satellite data. In other words, although radiant temperatures associated with fumarole fields are relatively stable over time periods equivalent to the frequency of potential TM acquisition, the errors in temperatures estimated from such data would generally exceed any likely variation in actual temperatures on the ground. In fact, in terms of SWIR radiance, it is often the areas of vents that are more important than their temperatures. A doubling of the vent area at Momotombo's F9 fumarole would have a greater impact on its detectabilty in TM bands 5 and 7 than an increase in temperature from 800°C to 900°C (Figure 4.17).

4.4.5. TM data of fumarole fields

The earliest study of SWIR anomalies, recognised in TM data of Láscar volcano (Francis and Rothery 1987), has been followed up by Rothery et al. (1988), and Glaze *et al.* (1989a). Integration of field reports and analysis of TM images has suggested that a

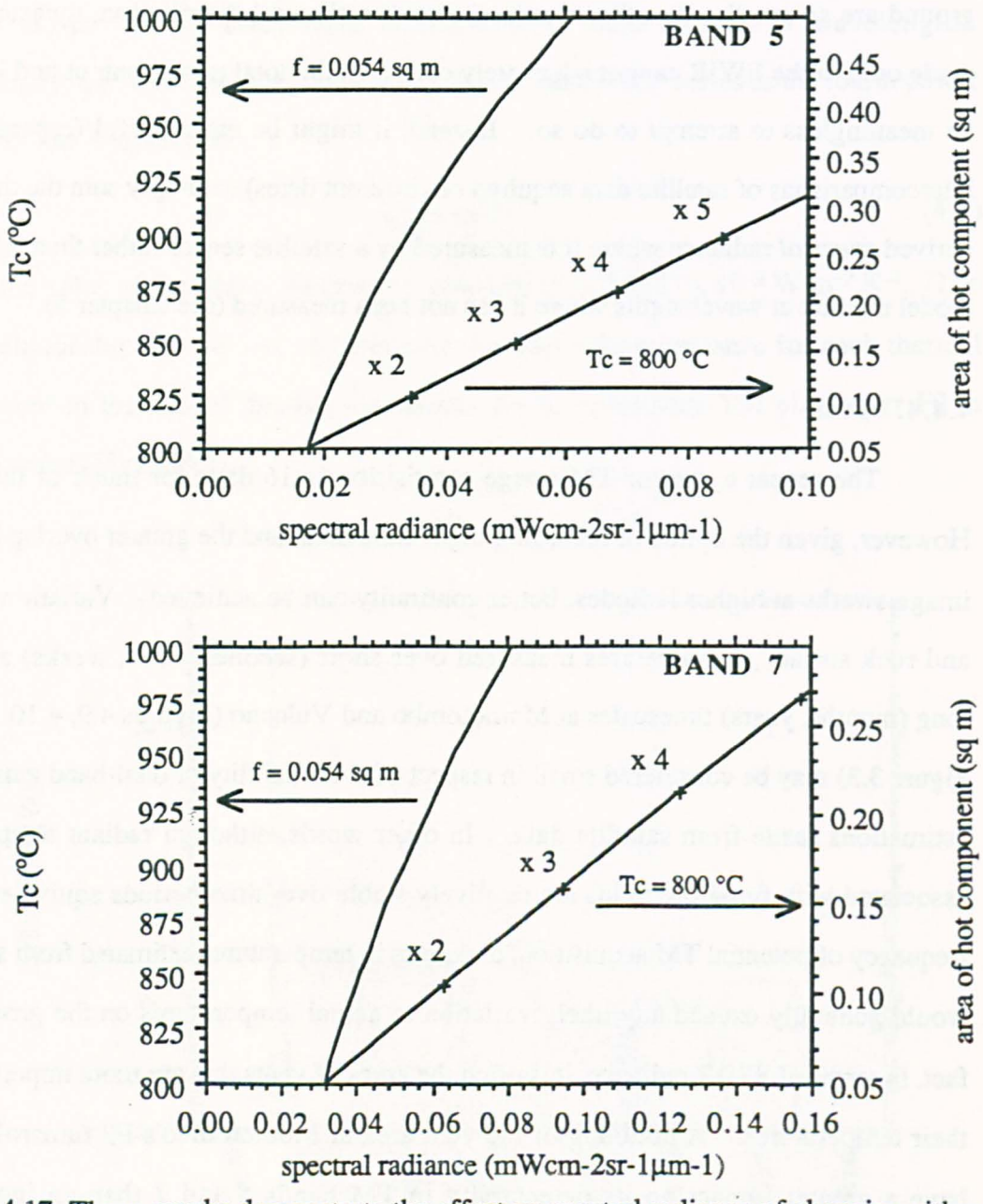

Figure 4.17. These graphs demonstrate the effect on spectral radiance of changing either temperature (curves) of a hot fumarole vent, or its size (straight lines). Crosses on the lines for the case of constant vent temperature indicate integer multiples of vent area. The example chosen is for a vent at 800°C and of 0.054 m^2 area. In band 5 (top), an increase in temperature from 800 to 900°C produces the same increase in spectral radiance as a doubling in area of an 800°C vent. At the longer wavelength of band 7 (bottom), the same doubling of vent area produces about twice as great an increase in spectral radiance than a 100°C jump in vent temperature.

lava dome has occupied the summit crater for much of the period since late 1984, and the activity at Láscar appears to be best explained by cycles of dome building, punctuated by moderate explosive eruptions and dome deflation or destruction (Chapter 5). Some of

the images acquired show small anomalies beyond the main core of 'hot' pixels which correspond to the dome itself. These are almost certainly fumaroles.

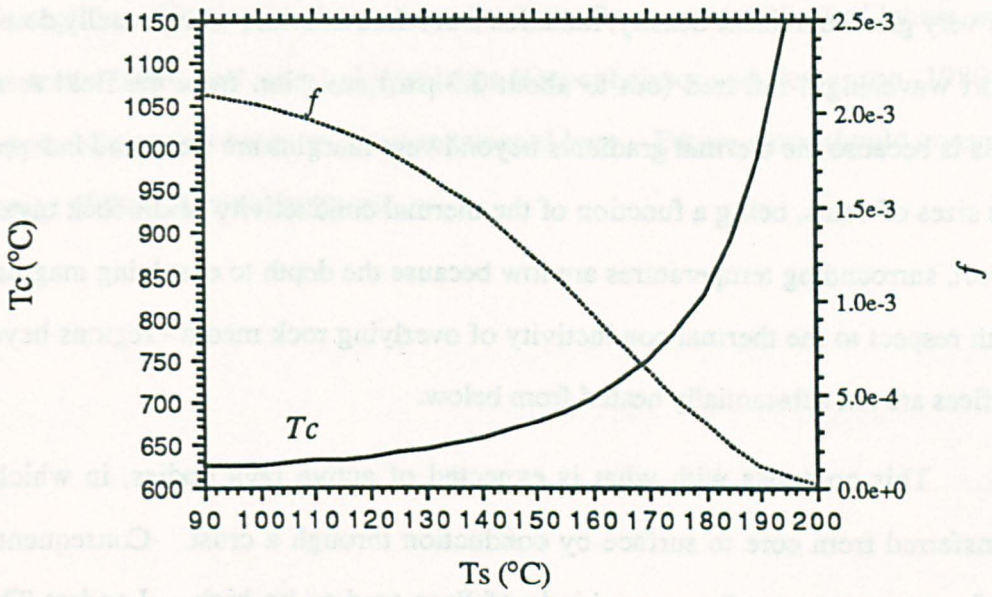

Figure 4.18. Similar plot to Figure 4.13 for $DN_{\lambda,thermal}$ in bands 5 and 7 of 14 and 58 respectively, taken from a single pixel representing a fumarole at Láscar volcano, Chile. Although the data clearly indicate that an incandescent feature has been imaged, they cannot alone tightly constrain either its temperature or that of the cooler background.

The best data for radiometric purposes are provided by a night-time scene recorded on 18 November 1989. Several pixels beyond the margin of the dome there is a pixel with $DN_{\lambda,thermal}$ in bands 5 and 7 of 14 and 58 respectively (following corrections introduced in Chapter 5). The allowable dual-band solutions are shown in Figure 4.18. Band 5 radiance is relatively high compared with that in band 7 and, while the graph does suggest that incandescent material has been detected (all T_c exceed 600°C), the background temperature, T_s, although below 200°C for all possible T_c, is poorly constrained. From spectral information alone, one could not rule out the possibility of cooled lava. More generally, because lava will always cool eventually to ambient temperatures, it is easier to say from such analyses when lava is present than when it is not.

4.5. Conclusions

(i) Provided that high-temperature fumarole vents are neither very small in size, nor very great in number density, radiation from their interiors will generally dominate the short wavelength infrared (out to about 2.3 μm) emission from the field as a whole. This is because the thermal gradients beyond vent margins are steep and independent of the sizes of vents, being a function of the thermal conductivity of the rock material. In effect, surrounding temperatures are low because the depth to exsolving magma is great with respect to the thermal conductivity of overlying rock media - regions beyond vent orifices are not substantially heated from below.

This contrasts with what is expected of active lava bodies, in which heat is transferred from core to surface by conduction through a crust. Consequently, crust surface temperatures for many kinds of flow tend to be high. Landsat TM SWIR sensors are responsive to this dichotomy because band 5 is more sensitive to the cool component, and band 7 is more sensitive to the hot component. Therefore the relative response between bands 5 and 7 indicates the relative importance of hot and cool components, and hence might be suggestive of the nature of volcanic thermal manifestations sensed. Careful comparison of pixel DN in different spectral bands, in consort with appraisals of the shape, size, history and context of thermal anomalies can therefore contribute towards their identification.

(ii) There are too many potential sources of error to determine reliably temperatures of sub-pixel sources by dual-band techniques. Regardless of other uncertainties, one sub-pixel temperature estimate for a region of ground pierced by several fumaroles represents at best a value somewhere between those of the hottest and coolest vents present. Similarly, estimates of the total radiant exitance from measurements made at just two points in SWIR should be viewed with caution. I suggest that the most meaningful approach to volcano *monitoring* with SWIR data is to compare 'raw' measurements made from images, prior to analysis according to necessarily simplistic models. For example, one can very readily assess numbers of

radiant pixels in different bands, numbers of saturated pixels, and total spectral radiance in available channels.

(iii) Lavas and fumaroles are not the only thermal phenomena to be expected in volcanic regions. Fresh pyroclastic deposits (from flows or airfall), 'hot' lahars, warm aqueous crater lakes, and even sulphur lakes (Oppenheimer and Stevenson, 1989) are further possibilities that have not been considered here. Future work should consider a wider range of thermal manifestations.

Chapter 5. Interpretation and comparison of volcanic thermal anomalies in Landsat Thematic Mapper infrared data: Volcán Láscar, Chile, 1984-1991

Paper to be submitted to *Bulletin of Volcanology*.

5.1. Abstract

Fourteen Landsat Thematic Mapper (TM) images of Volcán Láscar (Chile), recorded between December 1984 and January 1991, document the evolution of thermal features within the summit crater. This is probably the best time-series of TM data of its kind; in every image, the two short wavelength infrared bands, 5 and 7, have detected a hot spot on the volcano. The ratio of radiances in each of these spectral channels is shown to depend on the relative contributions from very hot surfaces occupying tiny pixel fractions and broad areas at low to moderate temperatures. Comparison of the response of bands 5 and 7 therefore provides a means for interpreting TM thermal anomalies in the absence of ground observations. Pronounced changes in the configuration and intensity of the anomaly suggest that Láscar has experienced at least two cycles of lava dome

activity between 1984 and 1991. The first of these progressed through a 'cooling' period, possibly reflecting a reduced flux of magmatic volatiles at the surface, and culminated in an explosive eruption on 16 September 1986, which may have completely destroyed the inferred lava dome. The TM data indicate that, by November 1987, a new dome had been emplaced, more than 15 months before it was first discovered by local observers. Láscar's style of silicic volcanism is typical of many volcanoes worldwide and the remote sensing techniques discussed herein could be applied elsewhere.

5.2. Introduction

Satellite remote sensing can fulfil a number of volcanological applications (see Mouginis-Mark *et al.*, 1991), some of which are already semi-operational such as the tracking of ash plumes. A number of preliminary investigations has also been made of the utility of infrared data for observing thermal features on volcanoes (Francis and Rothery, 1987, Rothery *et al.*, 1988, Oppenheimer and Rothery, 1991). Detection of new thermal anomalies, or changes in existing ones, could be of value for hazard evaluation. Such data have also been used to demonstrate thermal properties of lava flows (Pieri *et al.*, 1990; Oppenheimer, 1991b). Although remote sensing satellites offer a continuity of observation difficult to achieve by other means at many volcanoes worldwide (Francis, 1979), previous investigations have tended to concentrate on techniques for analysing individual 'snapshot' TM images. Herein I present an analysis of fourteen TM images recorded on different dates, albeit at irregular intervals, between December 1984 and January 1991 over Volcán Láscar in Chile. In every case, a hot source is revealed by the short wavelength infrared (SWIR) bands of the instrument. This is almost certainly the fullest time series data set of a volcano with a SWIR anomaly.

The aims of this paper are to extend the work of Glaze *et al.* (1989a) on Láscar, and in particular to examine (a) how remotely sensed thermal anomalies of Láscar, or any volcano, can best be interpreted in volcanological terms and (b) how best to compare hot spots in images acquired on different dates (of the same or different volcanoes).

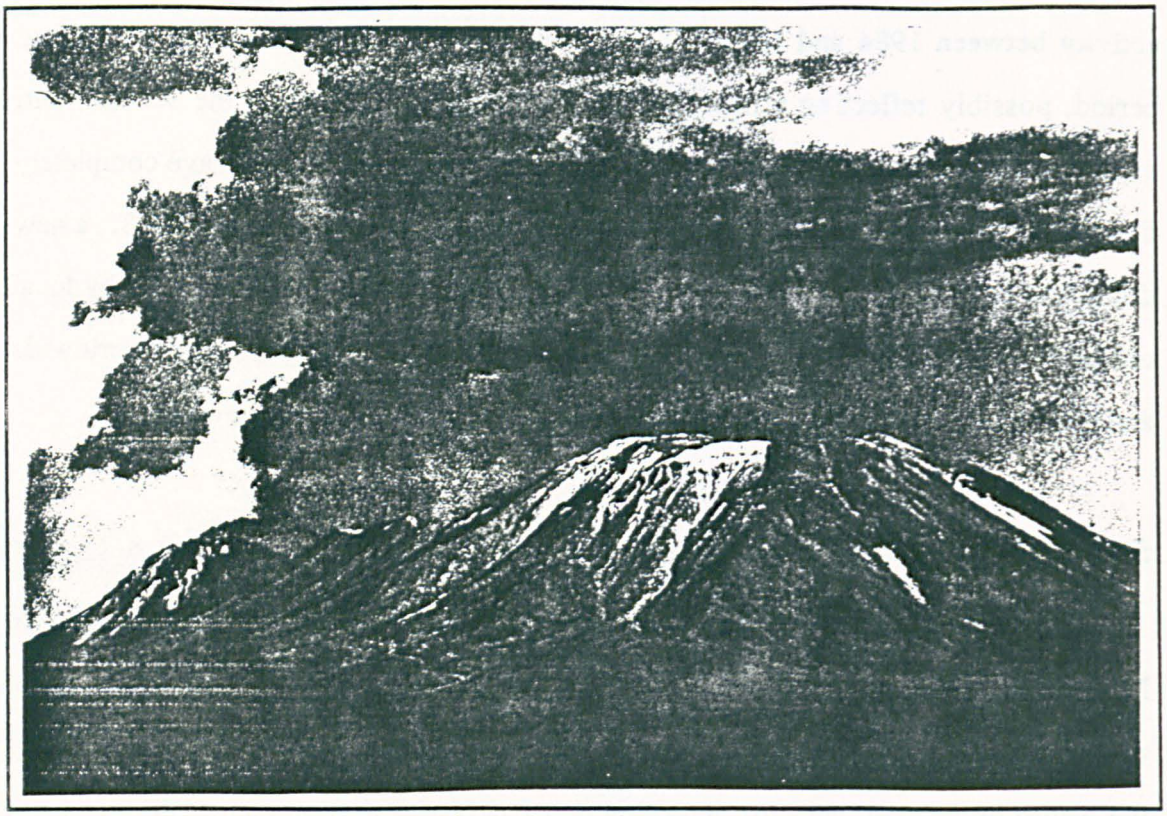

Figure 5.1. Photograph of Láscar from the northwest.

5.2.1. Volcán Láscar

Láscar is the most active volcano of the central Andes of north Chile (Figure 5.1). It is located in Antofagasta region at 23°22' S, 67°44' W, east of the Salar de Atacama and 34 km from the village of Toconao. The rim of the active crater, one of six overlapping summit craters, is about 800 m in diameter and at around 5450 m a.s.l. (Figure 5.2). Because of its location in a sparsely populated region, the historic record of activity at the volcano is meagre (Casertano and Barozzi, 1961). Documentation of its 1986 eruption was prompted only by satellite investigations (Glaze *et al.*, 1989b). However, the oldest inhabitant of the closest settlement, Talabre (11 km west of the summit), Señor Favio Soza Flores, has confirmed that the last few years of persistent fumarolic plume and sporadic explosive eruptions have been typical of the volcano's behaviour throughout his lifetime (Gardeweg *et al.*, 1990). He recalled eruptions in about 1955, 1965 and 1967, and another occasion (he could not remember when) on which incandescent blocks fell at night over the north flank of the volcano (Gardeweg *et al.*, 1990). Explosive eruptions are said to have taken place in March 1960 (Casertano and Barozzi, 1961), and

September 1964 when ash fell over the village of Socaire, 30 km away (Francis and Rothery, 1987).

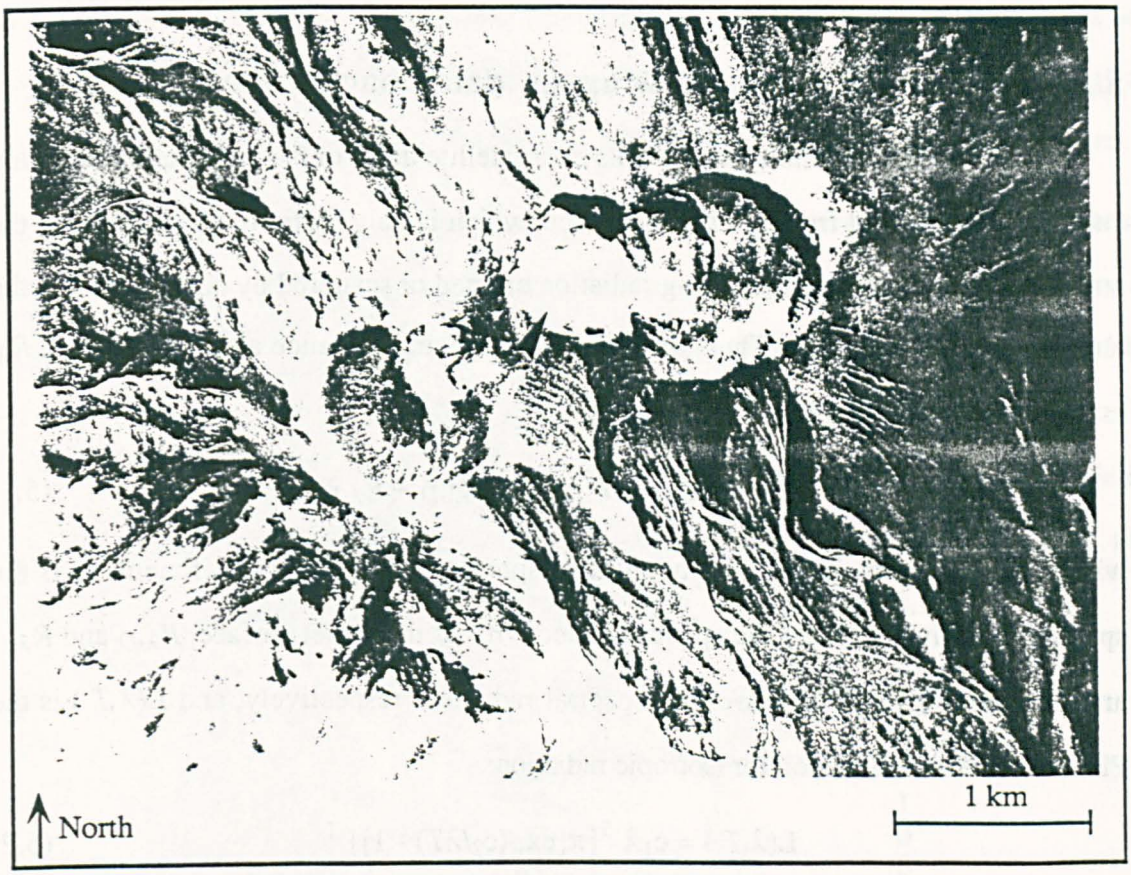

Figure 5.2. Airphotograph of summit complex; the arrow marks the active crater.

Since 1984, intermittent ascents and overflights of Láscar have provided a patchy record of visible activity within the summit crater. Vigorous fumaroles have been observed each time, and, since February 1989, a lava dome has been present (Smithsonian Institution, 1990d, 1991a). Crater glow has been observed from the ground, notably during April 1989 (Smithsonian Institution, 1989g). Moderate explosive eruptions took place in September 1986 (Glaze *et al.*, 1989b) when andesitic ash fell over the town of Salta in Argentina, 285 km ESE of Láscar, the plume climbing 10 km above the summit, and February 1990 when the plume reached an altitude of about 8 km over the volcano (Smithsonian Institution, 1990a,b). Smaller explosions were reported in July 1988 (Smithsonian Institution, 1988), April 1990 (Smithsonian Institution, 1990d) and November 1990 (Smithsonian Institution, 1991a), although the possibility that other sizeable eruptions went unobserved cannot be ruled out, particularly

if they took place by night. In this paper, these and other observations are integrated with interpretations of the TM data to build up a picture of activity at Láscar since 1984.

5.3. Analysis of Thematic Mapper data: background

The infrared radiation which falls on a satellite detector is composed of radiation emitted and reflected from the target surface, which is only partially transmitted by the atmospheric column, and upwelling radiation emitted or scattered by constituents of the atmosphere (Figure 5.3). Thus, the at-satellite spectral radiance at wavelength λ, R_λ, may be expressed as:

$$R_\lambda = \tau_\lambda \varepsilon_\lambda L(\lambda,T) + \tau_\lambda \rho_\lambda R_{\lambda,D} + R_{\lambda,U} \qquad (5.1)$$

where τ_λ is the wavelength-dependent atmospheric transmission coefficient, ε_λ is the spectral emissivity and ρ_λ the spectral reflectivity of the target surface, $R_{\lambda,D}$ and $R_{\lambda,U}$ are the downwelling and upwelling spectral radiances respectively, and $L(\lambda,T)$ is the Planck distribution function for isotropic radiation:

$$L(\lambda,T) = c_1 \lambda^{-5} \{\pi[\exp(c_2/\lambda T) - 1]\}^{-1} \qquad (5.2)$$

in which T is black-body absolute temperature of the target surface, and the constants c_1 and c_2 have the values 3.74127×10^{-16} W m^2 and 1.4388×10^{-2} m K respectively. The at-satellite spectral radiance, R_λ, is found by calibrating the digitized sensor response:

$$R_\lambda = \alpha_\lambda DN_\lambda + \beta_\lambda \qquad (5.3)$$

where α_λ and β_λ are known coefficients and DN_λ is the digital count in spectral band λ for a given pixel. Strictly, here R_λ represents the mean spectral radiance integrated across the sensor's filter function. It is approximately the same as R_λ in (5.1) for the midpoint of the channel.

Data acquired for this study were recorded by the TM instrument carried on board Landsats 4 and 5. The TM acquires data in seven spectral bands during both the forward and reverse sweeps of its scan mirror, building up an image swath 185 km wide composed of 30 x 30 m pixels. Multiple detectors for each spectral band provide 16

lines of data for each mirror sweep. Quantisation of the raw signal to 8 bits dictates the radiometric resolution of TM data (i.e. each pixel for each spectral band has assigned to it a digital number [DN] between 0 and 255), although signal to noise characteristics are also significant. The repeat cycle of each satellite orbit is 16 days but better continuity of coverage may be achieved at high latitudes, and if night-time acquisitions are scheduled.

TM digital data on computer compatible tape (CCT) are available in two basic formats - CCT-P which has been reprocessed to correct for geometric distortions of images, and CCT-A which is 'raw' data. Geometric recoding, which is achieved by cubic convolution (CC) or nearest neighbour (NN) resampling of images to correct for earth rotation, orbital and other parameters, unfortunately reduces the radiometric fidelity of individual pixels. The data set examined here includes CC and NN resampled, and CCT-A format, images, and both day- and night-time scenes (Table 5.1).

Date	CCT-format	day/ night	saturated pixels	
			band 7	band 5
24 Dec 84	CC	day	21	4
14 Mar 85	CC	day	7	1
20 Jul 85	CC	day	1	0
12 Jan 86	NN	day	2	0
8 Aug 86	NN	day	0	0
27 Oct 86	CC	day	1	0
12 Nov 86	A	day	0	0
12 Nov 86	NN	day	0	0
23 Nov 87	NN	day	18	7
23 Nov 87	CC	day	12	3
27 Oct 89	A	day	17	6
17 Nov 89	A	night	12	6
28 Nov 89	A	day	12	6
14 Dec 89	A	day	18	7
25 Mar 90	A	night	3	0
7 Jan 91	A	night	18	3

Table 5.1. TM scenes recorded over Láscar. Data format, time of overpass, and numbers of saturated pixels within the thermal anomaly are reported.

The two TM channels which have proved most useful for monitoring high-temperature volcanic manifestations are the short wavelength infrared bands 5 (1.55-1.75 μm) and 7 (2.08-2.35 μm). This is because their wavelengths closely match those at which most energy is radiated by surfaces at, or near to, magmatic temperatures.

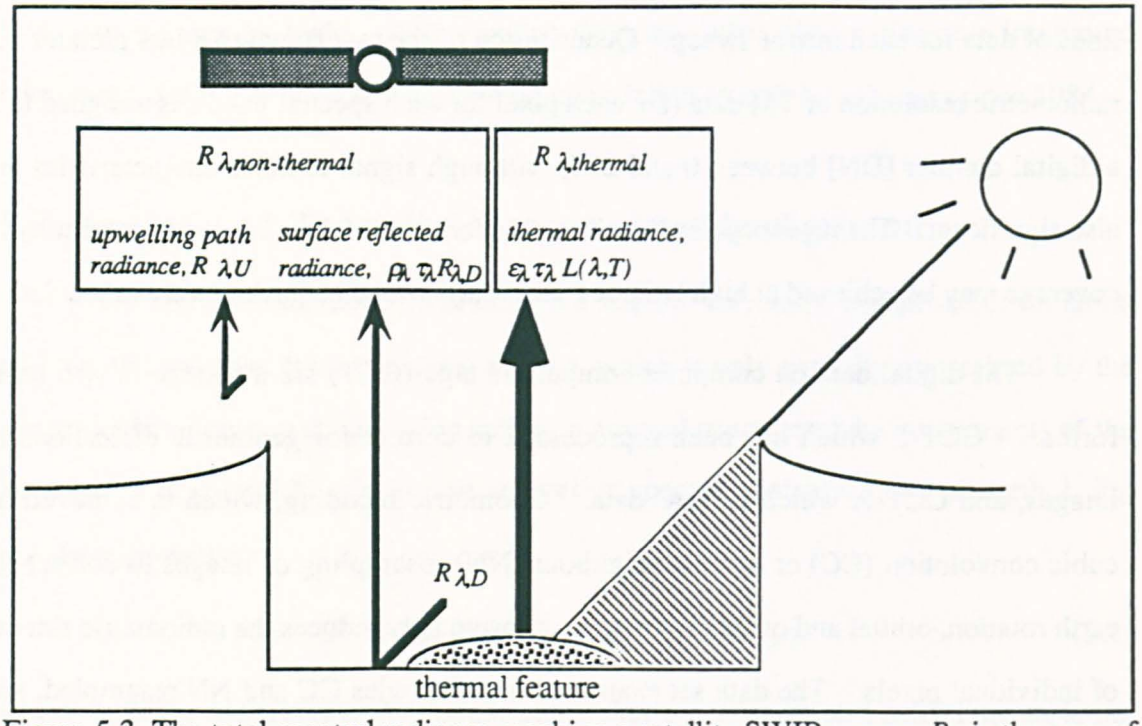

Figure 5.3. The total spectral radiance reaching a satellite SWIR sensor, R_λ,is the sum of $R_{\lambda,U}$ (radiation back-scattered along the atmospheric path), $\tau_\lambda \rho_\lambda R_{\lambda,D}$ (radiation reflected by the ground), and $R_{\lambda,thermal}$ (thermal radiation from the target partially transmitted by the atmosphere).

SWIR data of volcanoes have been examined by Rothery *et al.* (1988), Glaze *et al.* (1989a), Pieri *et al.* (1990), and Oppenheimer and Rothery (1991). In each case, sub-pixel thermal structure was modelled by assuming that individual image pixels sampled areas over which only two surface temperatures were significant, for example a hot component at T_c, corresponding to incandescent sites, and a component at T_s, representing cooler material. If the fraction of the pixel occupied by the hot component is f, then that by the cool component is $1\text{-}f$ (Figure 5.4), and expressions for their combined spectral emission reaching the satellite, $R_{5,thermal}$ and $R_{7,thermal}$, measured in TM spectral bands 5 and 7, may be approximated as follows:

$$R_{5,thermal} = \varepsilon_5 \tau_5 [fL(\lambda_5,T_c) + (1 - f)L(\lambda_5,T_s)] \qquad (5.4)$$

and

$$R_{7,thermal} = \varepsilon_7 \tau_7 [fL(\lambda_7,T_c) + (1 - f)L(\lambda_7,T_s)] \qquad (5.5)$$

where λ_5, λ_7 are centre wavelengths of bands 5 and 7 respectively, ε_5, ε_7 are the emissivities (assumed equal for each thermal component), and τ_5, τ_7 the atmospheric

transmission coefficients in each channel. Any two of the parameters f, T_c and T_s can then be found by graphical or numerical solution of (5.4) and (5.5), if the third is assumed (choosing also appropriate values for τ_λ and ε_λ). Because the value of one of the parameters describing this simple two component thermal model has to be guessed in order to evaluate the other two, the results, and their interpretation, are reliant on the guess. The implications of this dependency are examined shortly.

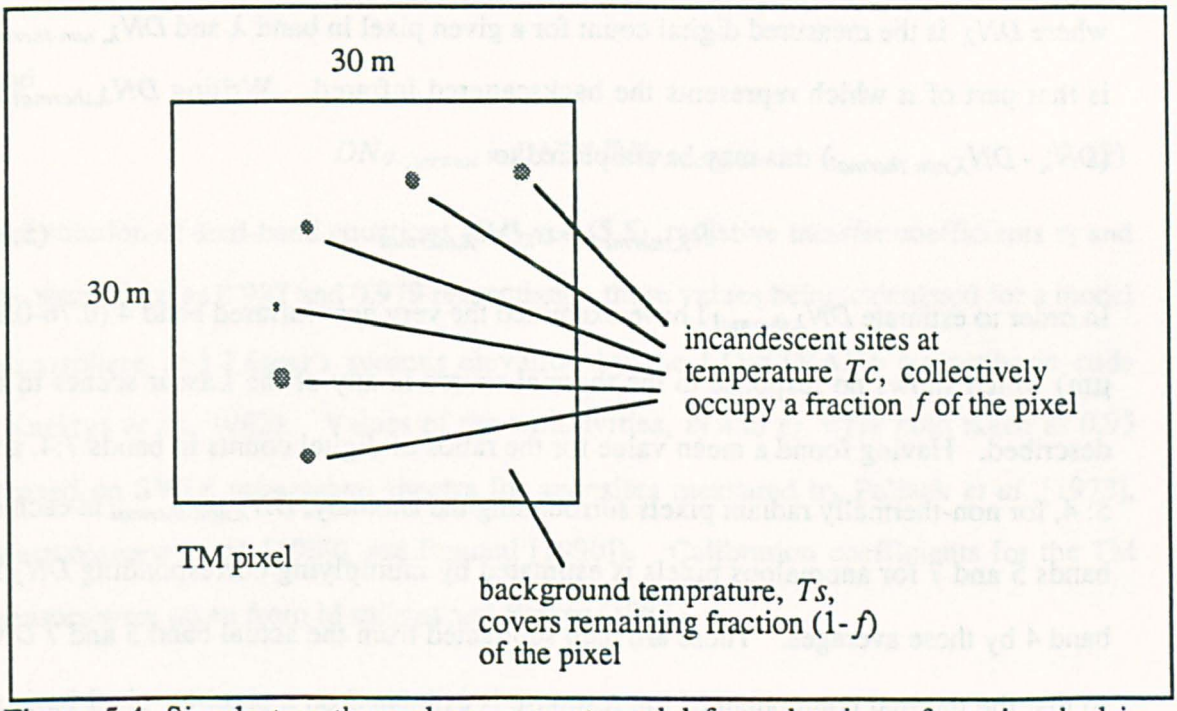

Figure 5.4. Simple two thermal component model for volcanic surfaces invoked in solution of dual-band equations (5.4) and (5.5) in text.

5.3.1. Corrections for reflected solar radiation and other contamination

Before using the TM SWIR data for radiometry, that part of the sensor response which represents thermal radiation from the target, $R_{\lambda,thermal}$ (Figure 5.3), must be isolated. Previous attempts to correct for backscattered light have involved subtracting the digital counts of nearby, non-thermally radiant, pixels from those of "hot" pixels, in each of the two SWIR bands. In the case of anomalies only a few pixels across, this extrapolation can be inaccurate, especially if there are marked differences in illumination where shadow thrown by a crater rim falls across them. I have used a different approach as follows.

Equation (5.1) may be rewritten as

$$R_{\lambda,thermal} = R_{\lambda} - R_{\lambda,non\text{-}thermal} \tag{5.6}$$

where $R_{\lambda,non\text{-}thermal}$ is that part of the signal reaching the satellite not derived from thermal emission from the traget; hence, using (5.3) it follows that

$$R_{\lambda,thermal} = \alpha_{\lambda}(DN_{\lambda} - DN_{\lambda,non\text{-}thermal}) \tag{5.7}$$

where DN_{λ} is the measured digital count for a given pixel in band λ and $DN_{\lambda,\ non\text{-}thermal}$ is that part of it which represents the backscattered infrared. Writing $DN_{\lambda,thermal}$ as $(DN_{\lambda} - DN_{\lambda,non\text{-}thermal})$ this may be simplified to:

$$R_{\lambda,thermal} = \alpha_{\lambda} DN_{\lambda,thermal} \tag{5.8}.$$

In order to estimate $DN_{\lambda,thermal}$ I have examined the very near infrared band 4 (0.76-0.90 μm) which shows no response to the thermal source in any of the Láscar scenes to be described. Having found a mean value for the ratios of digital counts in bands 7:4, and 5: 4, for non-thermally radiant pixels surrounding the anomaly, $DN_{\lambda,non\text{-}thermal}$ in each of bands 5 and 7 for anomalous pixels is estimated by multiplying corresponding DN_{λ} in band 4 by these averages. These are then subtracted from the actual band 5 and 7 DN_{λ} so that the thermal component of the response is estimated on a pixel-by-pixel basis as follows:

$$DN_{5,thermal} = DN_5 - DN_4.\left(\frac{DN_5}{DN_4}\right)_{av.} \tag{5.9}$$

and

$$DN_{7,thermal} = DN_7 - DN_4.\left(\frac{DN_7}{DN_4}\right)_{av.} \tag{5.10}.$$

In practice, the efficacy of this procedure is variable, since the non-thermally-radiant band 7:4 and band 5:4 ratios can have a large spread of values, and sometimes vary systematically across the crater. This most probably arises from differences in illumination, the amount of volcanic fume present, and variable reflectivity of surface materials such as fumarolic incrustations, fresh lava, oxidised lava, and talus deposits.

The use of night-time data is more straightforward, although it is not easy to 'navigate' oneself on such imagery. A more serious concern is that it may not be possible to determine whether or not cloud is present over the target. To correct the night-time scenes for the residual background signal, its average value away from the thermal anomaly, $DN_{\lambda,background}$ was found and subtracted from the anomalous response, i.e.:

$$DN_{5,thermal} = DN_5 - DN_{5,background} \tag{5.11}$$

and

$$DN_{7,thermal} = DN_7 - DN_{7,background} \tag{5.12}.$$

For solution of dual-band equations (5.4) and (5.5), radiative transfer coefficients τ_5 and τ_7 were taken as 0.987 and 0.979 respectively, these values being calculated for a model atmosphere and Láscar's summit elevation by the LOWTRAN6 atmospheric code (Kneizys *et al.*, 1983). Values of the emissivities, ε_5 and ε_7, were both taken as 0.95 (based on SWIR reflectance spectra for andesites measured by Pollack *et al.* [1973], Bartholemew *et al.* [1989] and Pontual [1990]). Calibration coefficients for the TM sensors were taken from Markham and Barker (1987).

5.4. Interpretation of thermal anomalies

Confined lava bodies and high-temperature fumarole fields can have comparable spatial characteristics. 30 x 30 m TM pixels are likely to cover substantial portions of such features and, in both cases, the highest temperature sources contributing to the short wavelength infrared radiance typically occupy only tiny fractions (< 0.01 %) of pixel areas. This partly explains why it has not always been straightforward to identify the nature of TM thermal anomalies in the absence of corresponding ground observations. Of course, a markedly elongate thermal anomaly extending radially from a volcano summit is rather likely to be a lava flow but, in the absence of such obvious spatial clues, interpretation of thermal anomalies has called on background knowledge of the volcano concerned. Previous attempts to ascribe a cause to thermal sources identified in Láscar

TM images concluded with uncertainty as to whether lava bodies or fumaroles had been represented (Rothery *et al.*, 1988). Here, I assess more quantitatively how the spectral and spatial attributes of TM thermal anomalies can allow a broad discrimination between different classes of volcanic thermal manifestation. Such appraisals should have important implications for volcano monitoring efforts which it is hoped will take place when Earth Observing System (EOS) satellite platforms are in orbit (Mouginis-Mark *et al.*, 1991).

5.4.1. Theoretical treatment

For the simple case in which a two-component thermal distribution prevails, as in Figure 5.4, the dual-band equations (5.4) and (5.5) can be used to calculate the background temperature T_S, and f, the fractional area of the hot component, for a given value of T_C, and any pair of allowable digital count values in bands 5 and 7. Figures 5a-e display the results of such analysis in the form of graphs of f against Ts for a range of values of T_C, and for $DN_{7,thermal}$ of 50, 100, 150, 200 and 250. In each case, the steeper curves represent points of equal $DN_{5,thermal}$ whereas the intersecting set mark loci of invariant T_C. The temperature curves are assymptotic towards the pixel-integrated temperature for the given $DN_{7,thermal}$ value. For example, in Figure 5.5b, the family of curves of T_C converge on a T_S of close to 232°C, the uniform temperature that a whole pixel would be at to produce a $DN_{7,thermal}$ of 100. Moving left along these curves, $DN_{5,thermal}$ increases, as does f, while T_S falls; the curves flatten out because the lower end of the dynamic range of band 7 corresponds to a pixel-integrated temperature of about 125°C. In other words, band 7 does not 'see' ground cooler than this. Increase in $DN_{7,thermal}$ shifts the whole set of T_C curves to higher background temperatures, T_S.

Taking a pair of $DN_{7,thermal}$ and $DN_{5,thermal}$, one can readily see the range of permissible values of T_S, T_C and f given by the dual-band solutions. For example, for an individual pixel with a $DN_{7,thermal}$ of 100, and $DN_{5,thermal}$ of 30 (Figure 5.5b), T_S can be anything up to about 200°C. Although T_S is unconstrained in this case, the graph

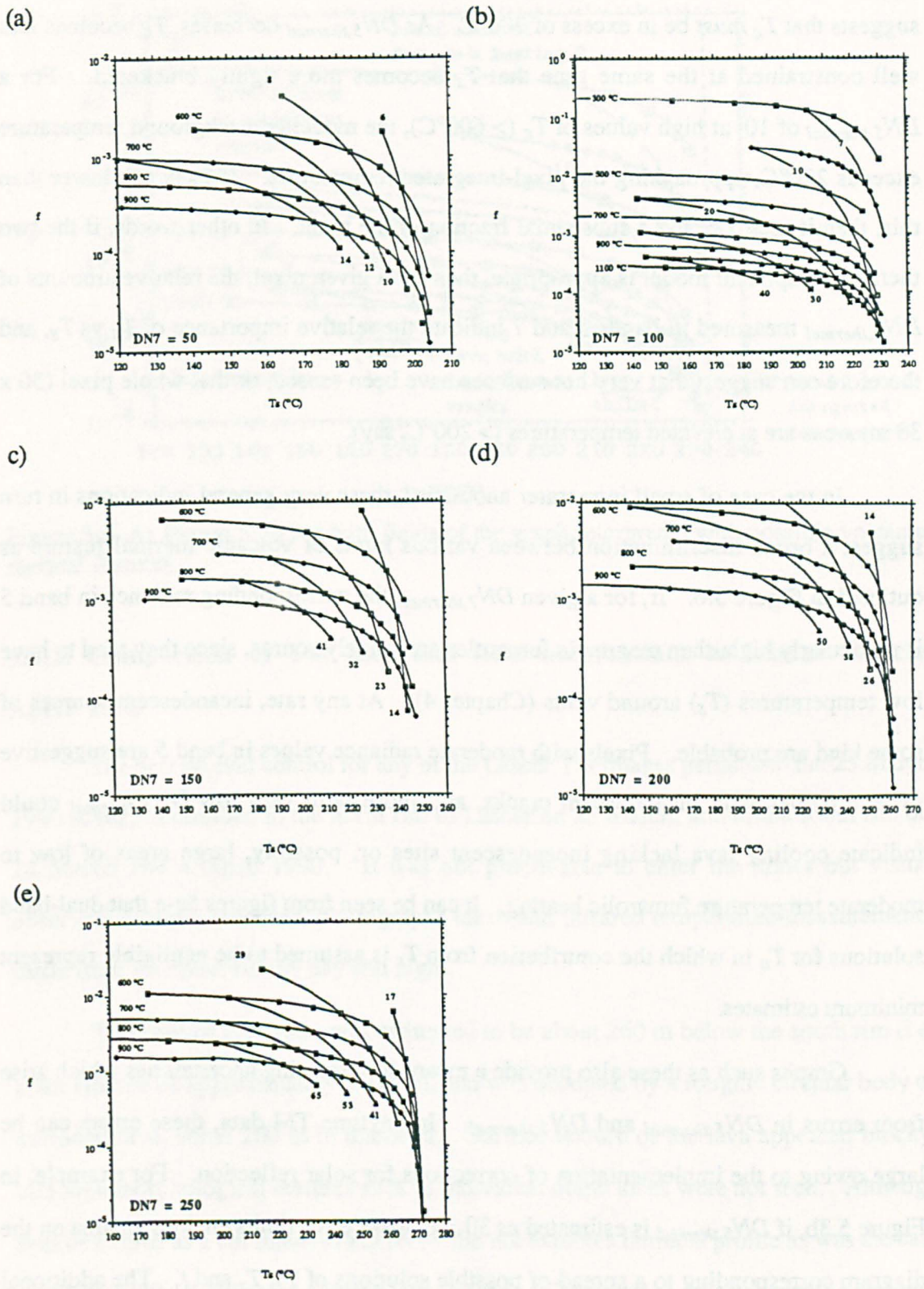

Figure 5.5a-e. Theoretical loci of dual-band solutions for allowable $DN_{5,thermal}$ for $DN_{7,thermal}$ of (a) 50, (b) 100, (c) 150, (d) 200 and (e) 250 respectively. The steeper of the intersecting curves indicate the range of f, T_S and T_C allowed for the given pair of $DN_{5,thermal}$ and $DN_{7,thermal}$. These curves were calculated for spectral emissivities and transmissivities appropriate for Láscar and should be modified accordingly for other conditions of surface material and atmospheric path. See text for full explanation.

suggests that T_C *must* be in excess of 700°C. As $DN_{5,thermal}$ decreases, T_C becomes less well constrained at the same time that T_S becomes more tightly bracketed. For a $DN_{5,thermal}$ of 10, at high values of T_C (> 600°C), the modelled background temperature exceeds 220°C, approaching the pixel-integrated temperature. If T_C is any lower than this, then it must occupy a substantial fraction of the pixel. In other words, if the two thermal component model is appropriate, then for a given pixel, the relative amounts of $DN_{\lambda,thermal}$ measured in bands 5 and 7 indicate the relative importance of T_C vs T_S, and therefore can suggest that very hot surfaces have been sensed, or that whole pixel (30 x 30 m) areas are at elevated temperatures (> 200°C, say).

In the case of small intracrater anomalies, these very general indications in turn suggest a broad discrimination between various kinds of volcanic thermal feature as outlined in Figure 5.6. If, for a given $DN_{7,thermal}$, the corresponding radiance in band 5 is particularly high, then magmatic fumaroles are a likely source, since they tend to have low temperatures (T_S) around vents (Chapter 4). At any rate, incandescent sources of some kind are probable. Pixels with moderate radiance values in band 5 are suggestive of lava bodies with incandescent cracks, and those with very low $DN_{5,thermal}$ could indicate cooling lava lacking incandescent sites or, possibly, large areas of low to moderate temperature fumarolic heating. It can be seen from figures 5a-e that dual-band solutions for T_C in which the contribution from T_S is assumed to be negligible represent minimum estimates.

Graphs such as these also provide a means for assessing uncertainties which arise from errors in $DN_{5,thermal}$ and $DN_{7,thermal}$. In daytime TM data, these errors can be large owing to the implementation of corrections for solar reflection. For example, in Figure 5.3b, if $DN_{5,thermal}$ is estimated as 30 ± 6, these error limits enclose an area on the diagram corresponding to a spread of possible solutions of T_C, T_S and f. The additional effect of errors in $DN_{7,thermal}$ can be imagined as a volume of solutions in f-T_S-$DN_{7,thermal}$ space.

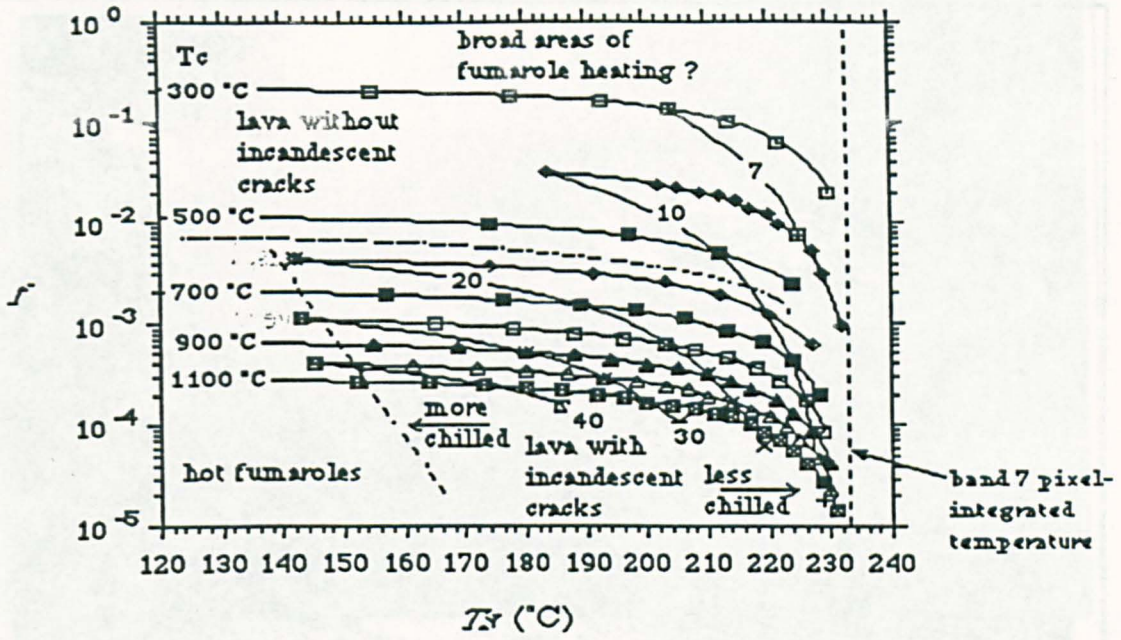

Figure 5.6. As Figure 5.5b but with fields of the graph interpreted with possible volcanic thermal features.

5.4.2. Comparison of TM data and field observations at Láscar March/ April 1990

The best ground control for any of the Láscar TM images pertains to the 25 March 1990 scene. I climbed to the north rim of Láscar on 23 March, and to the south rim on 24 March and 4 April 1990. It was not practicable to enter the crater but visual observations were recorded, photographs taken and infrared temperature measurements made from the crater rim by day and night.

The base of the crater was estimated to be about 260 m below the south rim (i.e. at an altitude of approximately 5200 m), and was occupied by a roughly circular body of extruded lava, some 200 m in diameter. Surface texture of the lava appeared blocky, although morphological features such as individual dome lobes were not seen. Although best described as a confined lava dome, it did not exhibit a domical profile as was the case in April 1989 (Smithsonian Institution, 1989d). Comparison of photographs suggests that the level of the perimeter of the lava body had not changed appreciably since late 1989. To the north and west, the dome abutted a crater terrace, its perimeter marked in places by ring fractures (Figure 5.7).

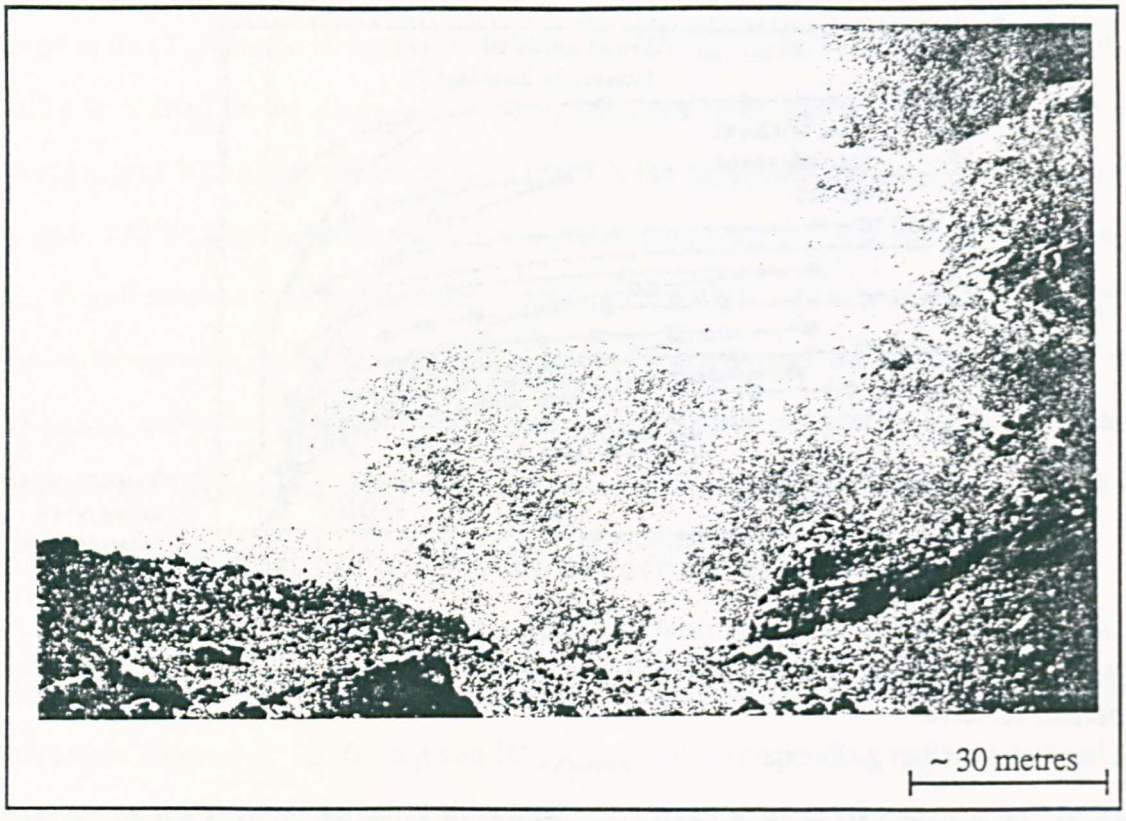

Figure 5.7. Daytime photograph from the south rim taken on 24 March 1990.

By day, vigorous fumaroles, some of which produced a roaring sound, were apparent from their condensed plumes, beyond the margins of the 'dome'; little fume was seen rising from the 'dome' itself, although the whole crater was rather hazy. At night, however, the 'dome' was seen to be peppered with a large number of glowing sites, distributed in arcuate chains and clusters, mostly close to its margins, while the steaming vents that had been visible by day were not incandescent (Figure 5.8a, b). These glowing points did not resemble those associated with crease structures of erupting dome lobes (Anderson and Fink, 1990), and a broad area in the centre of the dome lacked incandescent sites.

Several clusters of red-hot vents were present up to 100 m or more away from the dome edge, probably sited part way up the crater wall. One group was over to the west of the dome, localised in an area of less than about 8 m^2, another, of very small vents aligned tangentially with respect to the 'dome', was close to the adjacent crater to the east of the active crater (Figure 5.2).

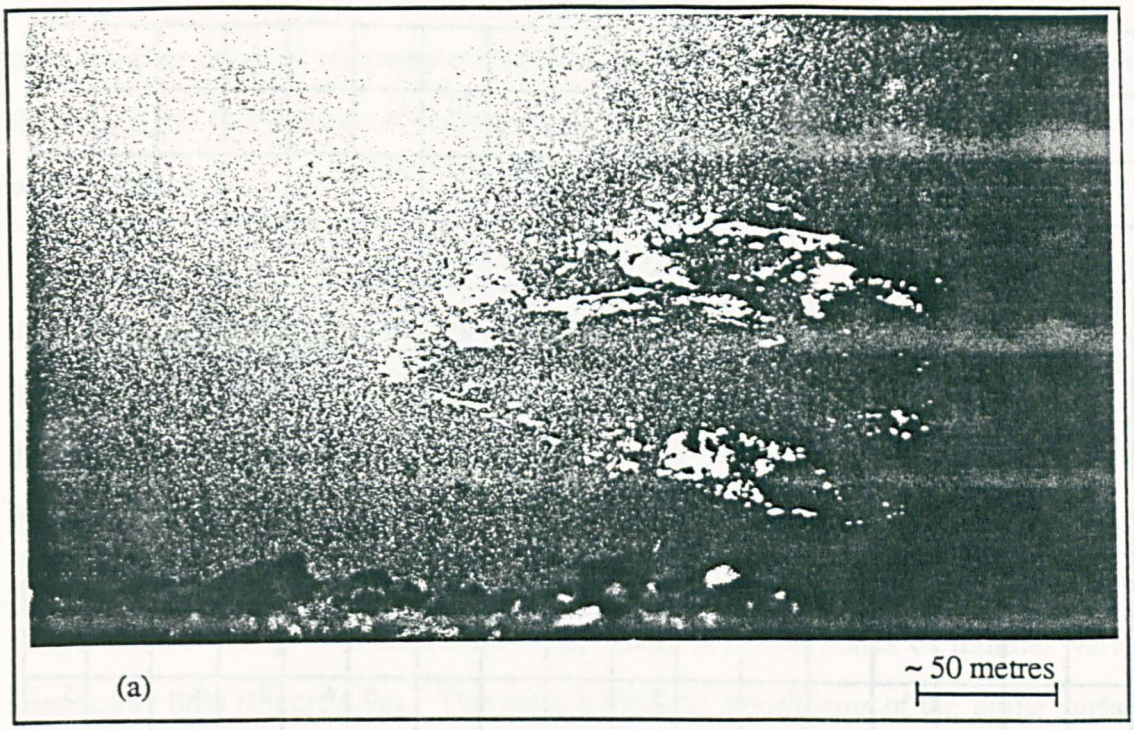

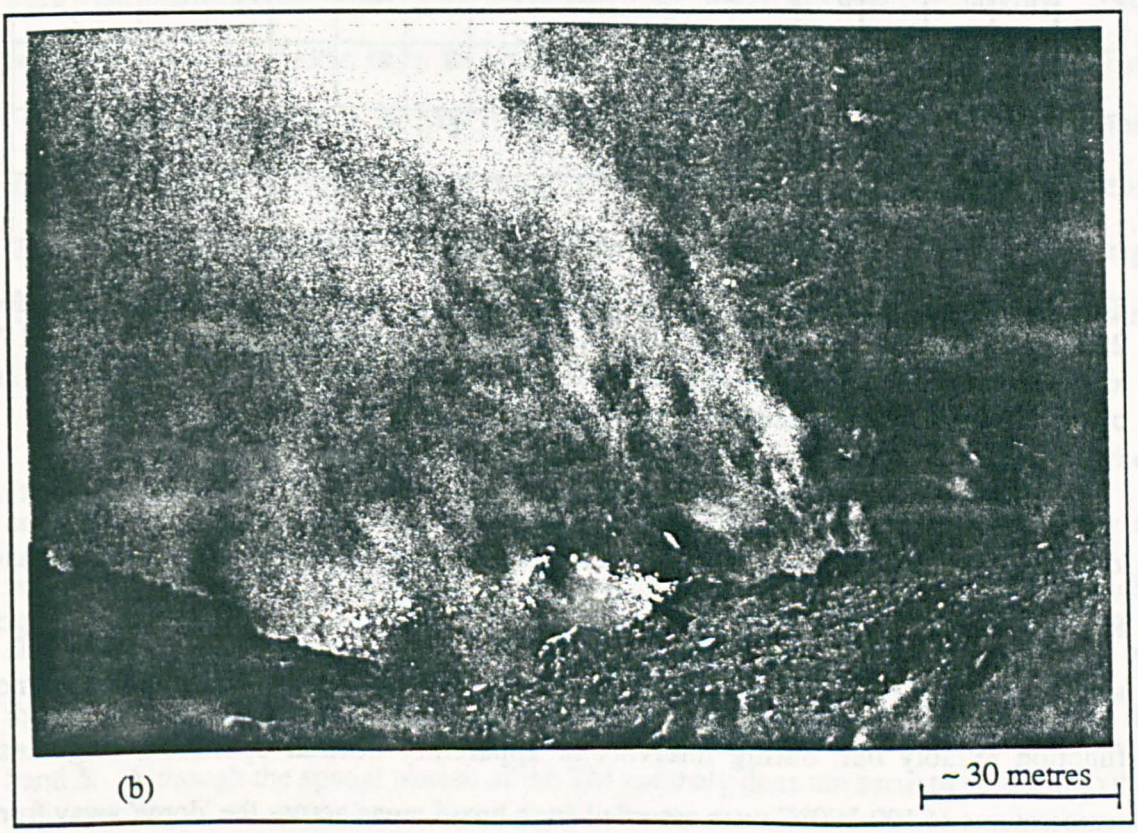

Figure 5.8. Night-time photographs taken from (a) the north rim on 23 March 1990, and (b) the south rim taken on 4 April 1990. The arrow marks the incandescent site whose temperature is recorded in Figure 5.9.

					5	5	5	7								
					5	6	5	8	9	10	11					
			6	5	9	13	16	*18* *6*	*21* *5*	*27* *6*	21	9				
		6	7	12	*18* *7*	*32* *11*	*51* *12*	*44* *9*	*57* *17*	*149* *28*	*97* *18*	*27* *8*	11	5		
	5	7	7	15	26	55	57	47	*92* *6*	*>* *25*	*>* *65*	*31* *18*	*25* *6*	*6* *5*		*
	6		7	7	9	18	20	18	*35* *6*	*150* *25*	*>* *65*	*78* *18*	*18* *6*	*10* *5*		
6	6		6			8	12	8	10	24	*53* *8*	*43* *6*	*29* *6*	*17* *5*	14	
								5		9	11	13	19	*21* *6*	*15* *6*	5
	8	7					6		7		6	7	*15* *7*	16	17	6
										8	6		7	15	12	
					6		5					6	7	8		5
											5		5			5
				5		6		5	5	9	5	7	5	6		
							6	7	7	8	7	9				
								4	7	6	6					
								5								

Table 5.2. DN exceeding 4 after corrections in bands 7 (first row) and 5 (second row) for 25 March 1990 night-time CCT-A data; three pixels, labelled '>' are saturated in band 7, and the line labelled '*' is damaged in band 5. Area represented is 480 x 510 m (30 m pixels). North is approximately up the page.

Temperature measurements were made from the crater rim of regions of the 'dome' using two portable infrared thermometers (described by Oppenheimer and Rothery, 1991). Readings were taken in two parts of the infrared spectrum, 8-14 μm and 0.8-1.1 μm, at a distance of about 500 m. The longer wavelength instrument did not function reliably but, during intervals of apparently normal operation, brightness temperatures of 100-200°C were recorded from broad areas across the 'dome' away from incandescent sites. These are minimum values because this instrument consistently gives low readings arising from absorption of emitted infrared along the atmospheric path (Oppenheimer and Rothery, 1991). The short wavelength infrared thermometer operates

over a higher range of temperatures, and was aimed at sites of incandescence. None filled the 0.33° field of view of the instrument. Even so, temperatures in excess of 780°C were recorded.

The peak temperature measurement was 787°C for an incandescent region occupying approximately one-sixth of the thermometer's field of view. Spot readings immediately away from the glowing region exceeded 500°C. Combining these results in equations similar to (5.4) and (5.2) suggests that the dominant temperature of the incandescent rock was around 940°C. No changes in disposition of incandescent sites on the 'dome' were recognised between or during visits to the summit. Continuous temperature readings of incandescent sites taken over timescales of minutes varied remarkably little (Figure 5.9a). This apparent lack of deformation of the 'dome' surface on short timescales, and the persistence of incandescent areas, suggests that these sites were vent orifices from which high temperature magmatic gas was discharging. The largest of the vents visible from the south rim had an estimated radius of 0.6 m; most vents, however, appeared to be only 10-30 cm across. The estimated rock temperatures may be expected to approximate those of the gas, although it is likely that vent temperatures varied significantly across the crater and even between neighbouring fumaroles on the 'dome'. In the same manner as above, radiant temperatures of 760 and 800°C were estimated for the fumarole vents respectively west and east of the 'dome'.

A TM image was acquired at night on 25 March 1990. Inspection of the corrected digital data shown in Table 5.2 reveals that the anomaly is defined by a rectangular area of approximately 10 x 6 pixels (i.e. about 300 x 180 m) in which $DN_{7,thermal}$ is 10 or more. This must correspond to the 'dome', and possibly some of the fumaroles beyond its margins. Only three pixels are saturated in band 7 and none in band 5. Although the spatial pattern of the TM anomaly does not seem to conform to the lack of incandescent vents in the centre of the 'dome' noted in the field, the central line in the anomaly appears to be damaged in band 5. It is in this channel that a lack of incandescence would be most readily apparent because band 7 would in either case still respond to background temperatures in the region of 150-250°C.

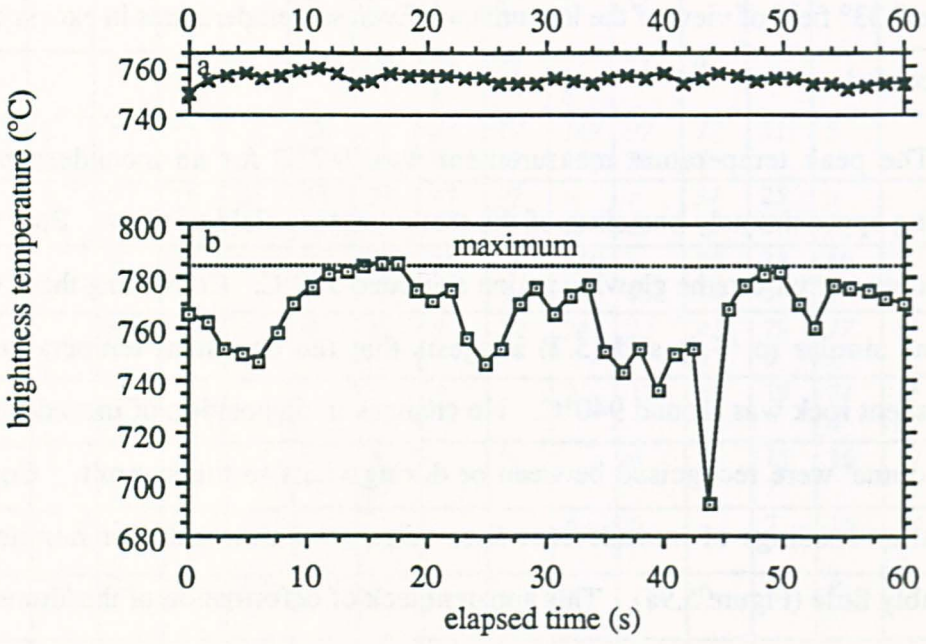

Figure 5.9. Temperatures recorded remotely from the crater rim with the 0.8-1.1 μm infrared thermometer of an incandescent site (see Figure 5.8) which occupied approximately one-sixth of the field of view of the instrument. (a) and (b) record two separate runs between which the thermometer was repositioned slightly. During run (b) more fumes were visible within the crater.

Examination of the paired band 5 and 7 $DN_{\lambda,thermal}$ values for individual pixels in Table 5.2 in conjunction with the curves of Figures 5a-e indicates that band 5 radiances are comparatively large, i.e. that surfaces at high (> 600°C) temperatures are present. However, background temperatures are poorly constrained and the anomaly could not confidently be interpreted as a lava body from the image data alone. It is possible, though, to check for consistency between the TM data and field observations as follows. Ignoring the three pixels saturated in band 7, the next two most radiant pixels have $DN_{\lambda,thermal}$ in band 7 and 5 of 149 and 28, and 150 and 25, respectively. Assuming a temperature of 800°C for the hottest part of these pixels, inspection of Figure 5.5c gives a model temperature for the background of around 220°C, with the hot component occupying about 9×10^{-4} of a pixel. Taking pixel area as 900 m^2, this is equivalent to a single vent of diameter 1 m, ten vents of diameter 32 cm, or fifty vents of diameter 14 cm. If instead, T_c is taken as 900°C, then the corresponding values of T_s and f are around 230 °C and 4.5×10^{-4} respectively, i.e. a single vent of 71 cm diameter, ten of 23

cm diameter or fifty of 10 cm diameter. These estimations are compatible with the background temperatures and sizes of vents estimated from the crater rim. The corroboration of elevated background temperatures supports the existence of a cooling lava body, its crust still warm because of conduction of heat from hotter interior parts.

5.4.3. Other images

For radiometric purposes, CCT-A data are far superior to images resampled for geometric correction. Cubic convolution resampling truncates pixel DN where surrounding pixels have lower DN, and so is particularly unsuitable for investigating features smaller than a pixel in area. In the same way, the DN of saturated pixels at the edges of large anomalies tend to get reduced. The image recorded on 23 November 1987 was acquired as both a cubic convolution and nearest neighbour resampled image, and whereas the numbers of saturated pixels in bands 5 and 7 of the NN image are 7 and 18, respectively, the corresponding numbers of saturated pixels in the CC scene are only 3 and 12 (Table 5.1). If such modified pixel DN were used in dual-band calculations, the results would be misleading. Even nearest neighbour resampled images reveal inconsistencies when compared with 'raw' data. The 12 November 1986 image was acquired in both of these formats. Not only are duplicate 'fill' pixels inserted (Glaze *et al.*, 1989a) but some pixels appear to be mis-registered between bands 5 and 7. For illustration, in the CCT-A image, three adjacent pixels have raw DN (band 7/ band 5) of 134/ 81, 32/ 49, and 34/ 53. In the resampled image, an extra pixel has been inserted in the line in band 7 but not in band 5, hence the DN become 87/ 81, 134/ 48, and 32/ 53. In respect of the 'hottest' of these pixels, this is a serious mis-registration. Note also the far less significant but nevertheless mysterious revaluation in the band 5 DN of one pixel from 49 to 48. Clearly, CCT-A data are preferable for radiometric purposes. In addition, one can be far more confident in analysing night-time data than those recorded by day. For these reasons, in this section, I concentrate on the 6 most recently recorded CCT-A images, in particular the night-time scenes (Table 5.1).

There are some noteworthy aspects of the spatial pattern of the anomalies in these images. The first concerns the identification of distinct and persistent thermal sources beyond the central core of the anomaly, in the four 1989 images. These probably represent high temperature fumaroles beyond the margin of the lava body centred on the crater floor, similar to those that were seen during crater visits in 1990. The night-time image of 17 November 1989 displays this most clearly, there being three groupings of anomalous $DN_{7,thermal}$, one a couple of pixels to the east of the edge of the main anomaly, the others a similar distance to the NW and WSW (Rothery and Oppenheimer, 1991). These same positions are apparent on the remaining 1989 images although this is not the case for the 25 March 1990 image (Table 5.2); the intervening period was marked by the 20 February eruption. Little or no corresponding radiance is apparent in band 5 for any of these anomalies, probably because the vents have only small surface areas.

				7									
					5	8	7	8		5			
			5	7	*21* *6*	*43* *11*	*73* *14*	*81* *16*	*54* *10*	17	8	5	5
			7	25	22	>*71*	>*141*	>*187*	>*143*	*44* *8*	17	6	
			6		*136* *41*	>*96*	>*59*	*214* *40*	>*85*	*131* *20*	15	5	
24 *6*	10		20		>*84*	>*103*	>*125*	>*119*	>*170*	*103* *20*	*20* *5*	6	
	8	6	*17* *10*	19	>*82*	>>	>*156*	>>	>>	*148* *23*	*28* *6*	8	8
		7	8	19	*36* *9*	*182* *37*	>*51*	*210* *43*	*164* *33*	*46* *12*	16		
				5	10	*23* *8*	*39* *8*	*20* *7*	*50* *9*	*17* *6*	6		
			5		9	10	7	10	6	5			
				6		6	7		6	6			

Table 5.3. DN exceeding 4 after corrections in bands 7 (first row) and 5 (second row) for 7 January 1991 night-time CCT-A data; pixels labelled '>' are saturated in the band indicated. Note in particular the structure in the core of the anomaly in band 5. Area represented is 420 x 330 m (30 m pixels). North is approximately up the page.

Nearly all of the images which have saturated pixels show a simple structure to the main anomaly, i.e. a core of saturated pixels surrounded by a halo of lower radiance values. The 7 January 1991 scene is unusual, however, in that there is a very clear zone

of lower radiance at the heart of the anomaly, seen best in band 5 (Table 5.3) because fewer pixels are saturated, although even in band 7 there is a single unsaturated pixel within a ring of saturated ones. If this annular distribution conforms to the distribution of incandescent sites on the ground, then one can envisage the 'dome' with gas discharge concentrated around its margins, possibly along ring fractures. Although this appeared to be the situation within the crater during field visits in 1990, the 25 March 1990 TM scene does not give any hint of such a distribution. Such a disposition of hot sites may indicate a deflating dome, while endogenous or exogenous growth might be marked by a nuclear grouping of 'hot' pixels with DN values decreasing radially outwards.

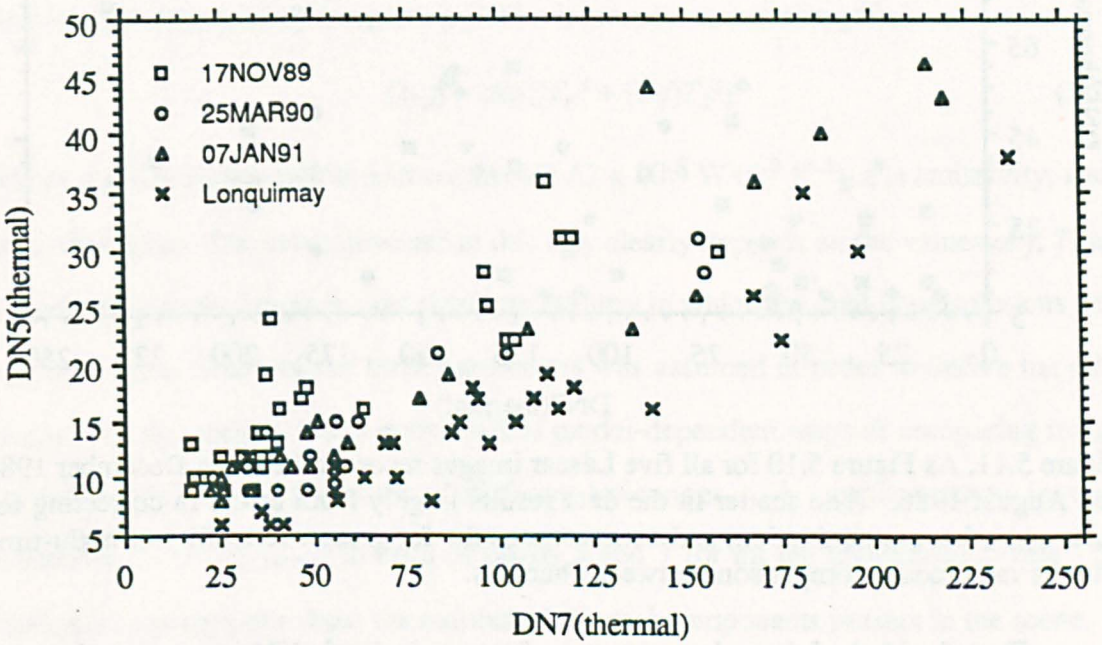

Figure 5.10. Plot of $DN_{5,thermal}$ vs. $DN_{7,thermal}$ for the three night-time Landsat 5 scenes of Láscar, and a daytime Landsat 4 image of a lava flow at Volcán Lonquimay. Pairs of $DN_{\lambda,thermal}$ in which either band was less than 5 were excluded, as were saturated pixels. Differences between the SWIR band radiometric calibration coefficients of the 4 images were negligible; (when this is not the case, digital counts should be compared only after radiometric calibration).

A comparison of the radiometric information contained in the night-time scenes is displayed by the Figure 5.10 which plots the corrected DN in band 5 against that in band 7 for each anomalous pixel, excluding those which were either saturated or had a $DN_{\lambda,thermal}$ less than 5 in either band. Data in the two spectral bands are well correlated,

and broadly overlap for the three scenes, suggestive of a similar thermal make-up to anomalous pixels in each. The 17 November 1989 image does appear to have more pixels with high ratios of band 5 to 7 digital counts and, for these, one can infer with some confidence a preponderance of incandescent sources which were more significant, in terms of emitted SWIR, than their surrounds.

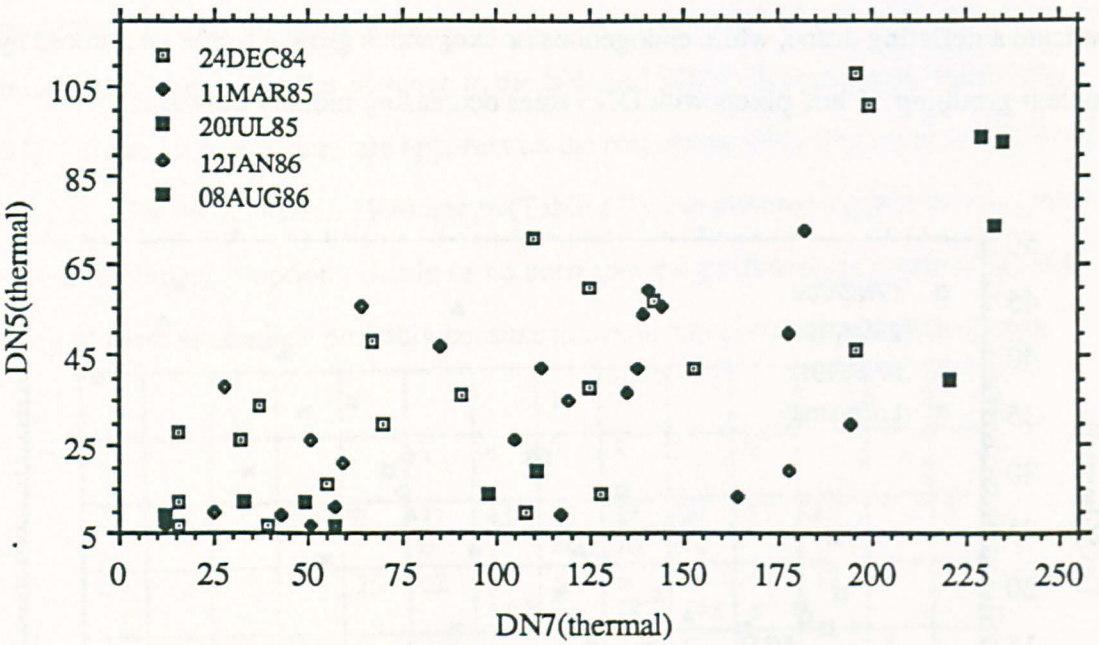

Figure 5.11. As Figure 5.10 for all five Láscar images recorded between December 1984 and August 1986. The scatter in the data results largely from errors in correcting for solar and other contamination, and demonstrates the far greater reliability of night-time data for radiometric comparisons between channels.

Plotted with the Láscar data are results from analysis of a TM image recorded over an active lava flow during the 1989 eruption of Volcán Lonquimay, also in Chile (Oppenheimer, 1991b). Interpretation of these data suggested elevated crust temperatures, in the region of 170-250°C, for the flow top, with incandescent lava occupying only very small fractions of the surface area. The Lonquimay and Láscar data fall into discrete fields of Figure 5.10, the former having consistently lower ratios of $DN_{5,thermal}$ to $DN_{7,thermal}$, indicative of a relatively small SWIR contribution from incandescent regions. This separation demonstrates the potential to discriminate between different kinds of thermal source, and to identify significant changes in long-lived hot

spots. Figure 5.11 shows the same parameters for all the Láscar data recorded between December 1984 and August 1986. The considerable spread in the data, introduced largely by errors in the corrections (5.9) and (5.10), emphasises the importance of using night-time CCT-A data in order to be able to make subtle spectral distinctions.

5.5. Discussion - Volcán Láscar 1984-1991

The next logical step in analysis of such a time-series of image data is to enquire how any apparent changes relate to the progression of activity at the volcano concerned. Glaze *et al.* (1989a) did this for all the Láscar images up to November 1987, modelling the radiant flux (over all wavelengths), Q_{rad}, from the thermal source by application of Stefan's law (obtained by integrating [5.3] with respect to wavelength):

$$Q_{rad} = \sigma\varepsilon S[fT_C^4 + (1-f)T_S^4] \qquad (5.13)$$

where σ is the Stefan-Boltzmann constant (5.67×10^{-8} W m^{-2} K^{-4}), ε is emissivity, and S is surface area. The value obtained in this way clearly depends on the values of f, T_S and T_C inserted into the equation, and therefore the way in which the dual-band solutions were arrived at (i.e. which of the three parameters was assumed in order to derive the other two). For this reason, I now consider less model-dependent ways of comparing images acquired at different times, or of different volcanoes. A simple method involves summing the $DN_{\lambda,thermal}$ in each of bands 5 and 7 for all the anomalous pixels - this makes no assumptions about the number of thermal components present in the scene. In practice it is sensible to choose some threshold below which pixels are ignored because of errors in the corrections applied to the data. A cut-off of 10 was chosen, based on a level appropriate to exclude some pixels which appeared "hot" merely because they had been inadequately corrected for solar and other contamination. Pixels with $DN_{\lambda,thermal}$ below this were not counted for the relevant band - all others were summed in each spectral channel, and the totals converted to spectral radiance using the standard calibration functions of Markham and Barker (1987).

The results are displayed in Figure 5.12. They represent minimum values, especially for band 7, because the $DN_{\lambda,thermal}$ of saturated pixels is effectively unknown. The overall form of the curve up to November 1987 is similar to that drawn up by Glaze *et al.* (1989a), although less has been assumed in order to derive it. A yet more simple intercomparison can be made by summing the saturated pixels in each of bands 5 and 7 [Table 5.1] - this also gives the same shape to the data. Figure 5.12 indicates that the summed radiative output of the whole anomaly in the SWIR has varied significantly through time, suggesting marked changes in surface temperature patterns within the crater. High values of spectral radiance in both bands (20-40 mW cm^{-2} sr^{-1} μm^{-1}) in late 1989 correspond with the presence of the lava dome. Similar values are documented in December 1984, November 1987 and January 1991 images, and one can infer that lava domes were present then also.

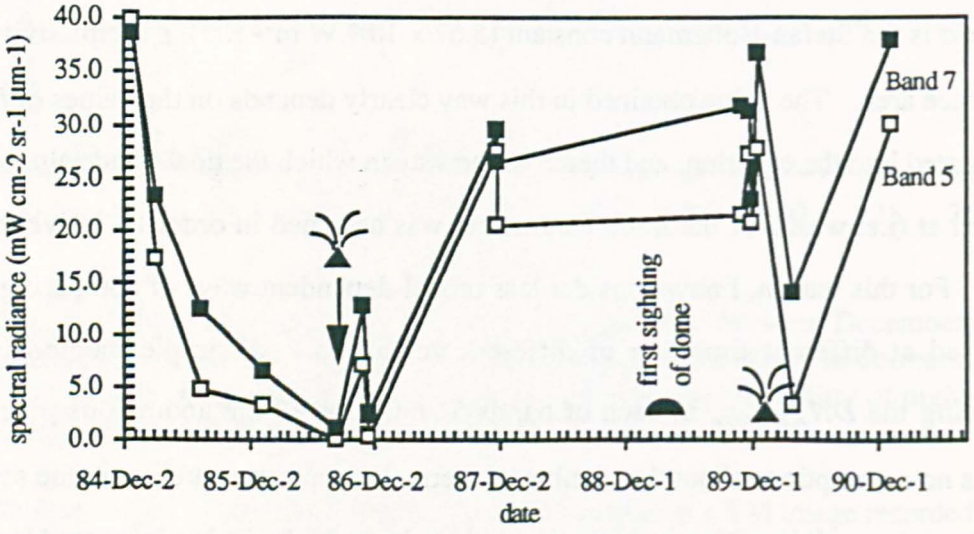

Figure 5.12. Band 5 and 7 spectral radiance through time for each TM image. All $DN_{\lambda,thermal}$ greater than or equal to 10 were summed, except when band 5 anomalies lacked corresponding radiance in band 7, since such pixels had most probably been inadequately corrected for reflected sunlight. Volcano symbols mark 16 September 1986 and 20 February 1990 eruptions.

The TM observation on 23 November 1987 suggests that a dome was present some 15 months before it was first recognised following a climb to the summit (Smithsonian Institution, 1989b). If this is the case, then it must have been emplaced after January 1987 when visual observations from an aircraft confirmed that no lava was present (Peter Francis, personal communication, 1991), or possibly later even than 1

April 1987 when another aerial reconnaissance revealed no magmatic activity (Gardeweg *et al.*, 1990). The TM visible bands 1-3, as well as band 4, were examined to see if there was any evidence of spectral changes which might also indicate the presence or absence of a lava body within the crater. Variable amounts of fume in each image made it impossible to ascertain any spectral shift on the crater floor however, and the thermal data stand alone in providing evidence for the existence of the lava dome. (Nor did the thermal infrared band 6 of the TM images provide any further information, although it sensed the hot source within the crater.)

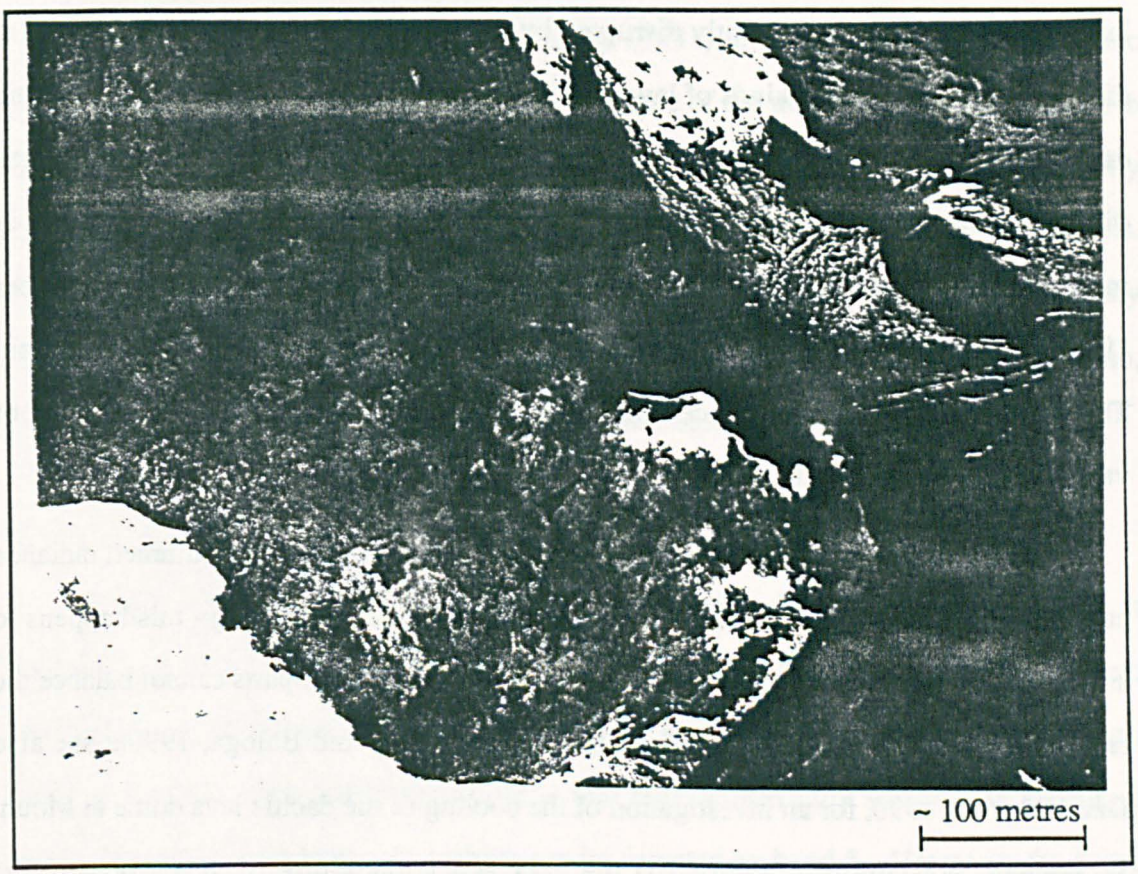

Figure 5.13. Oblique airphotograph taken by Peter Francis in January 1987. The floor of the active crater is clearly visible and shows that no substantial lava body was present at the time. A close comparison with Figure 5.7 and other more recent photographs indicates that the subsequent 'dome' filled the crater to the level indicated by the arrow.

Comparison of photographs taken from the air in January 1987 (Figure 5.13) and from the crater rim since April 1989 (Figure 5.7) indicates the extent to which the crater had been filled by lava in the interim. Very crudely (assuming the confined dome to occupy a conical region with diameter 200 m and depth 90 m), I estimate the volume of

lava emplaced as 9 x 10^5 m^3. A comparable volume seems likely at the time of the 24 December 1984 TM image based on the similarity of the anomaly with those since 1989. It is interesting to note that Glaze *et al.* (1989b) estimated from the extent of ashfall that less than 10^6 m^3 of lava were erupted during the 16 September 1986 eruption.

The consistent decay of the thermal anomaly between December 1984 and August 1986, a little over a month before Láscar erupted, was described by Glaze *et al* (1989a, b). They suggested that the anomaly represented intense fumarolic heating of a cooled lava lake which was subsequently disrupted by the eruption. In reality, there is little to distinguish between some kinds of lava lake and some kinds of lava dome, and semantic debates on the subject would prove somewhat sterile. The same may be said of the distinction between magmatic fumaroles and incandescent cracks in lava carapaces. A more interesting matter is whether or not the decay in the anomaly between December 1984 and August 1986 was symptomatic of the impending September 1986 eruption. This would pertain to circumstances under which infrared monitoring by TM could be of value for eruption forecasts.

In terms of the two-thermal component model, a decrease in the summed radiance can mean the following: (i) background temperatures T_s are decreasing - this happens to any lava body as it cools, because conduction from interior hotter parts cannot balance the radiative and sensible heat fluxes from the surface (Crisp and Baloga, 1990a; see also Dzurisin *et al.*, 1990, for an investigation of the cooling of the dacitic lava dome at Mount St. Helens, Washington), and/or (ii) the area and temperature of very hot surfaces decreases - this could result from a lack of thermal renewal of an active lava surface (i.e. regions exposing core material are not maintained), or a decrease in magmatic gas flux through fumarole vents. If the dataset between December 1984 and August 1986 had been compiled exclusively from night-time CCT-A format images, it might well have been possible to distinguish between such processes. Instead, the uncertainties in the data for this period (Figure 5.11) obscure any subtle spectral trends that might otherwise have been apparent.

Thus it is possible only to conjecture broadly on Láscar's behaviour leading up to the September 1986 eruption; a plausible scenario is as follows. By December 1984, a lava dome occupied the crater. Over the following months no new lava was extruded, and much of the dome carapace cooled. Magmatic volatiles continued to escape at the surface of the cooling dome and possibly the surrounding crater floor, sustaining incandescent fumarole vents. However, solidification of the dome may have impeded degassing from fumaroles, particularly if no endogenous dome growth was taking place; (see Fink *et al.* [1990] for an account of extrusive and intrusive dome growth at Mount St. Helens). According to Jaupart and Allègre (1991), the rate of gas loss from silicic magmas is very sensitive to rise velocity and pressure of the magma; small fluctuations in pressure can trigger explosive eruptions. This may have been the case at Láscar shortly after August 1986 when the TM anomaly had subsided to just a handful of "hot" pixels. Such an alternation of dome growth with explosive episodes has been recognised at many active silicic volcanoes (e.g. Mount St. Helens, 1980-1986 [Swanson and Holcomb, 1990], and Redoubt, Alaska, 1989-1990 [U.S. Geological Survey, 1990]).

5.5.1 Sources of error

Saturation is arguably the most serious problem with TM data because one is forced to use pixels peripheral to the heart of an anomaly for dual-band solutions and other analyses. In all the images studied, there are more thermally-radiant pixels in band 7 than in band 5. This could simply mean that high-temperature sources are absent, or are of a combined area below that which can be detected by band 5. However, the actual area of ground sensed for any 30 x 30 m TM pixel actually exceeds the nominal pixel dimensions, and can be described in a number of ways according to the spatial response of the TM sensors in question (e.g. Markham, 1985). As a result, thermal anomalies tend to be smeared out in TM data (see Oppenheimer, 1991b). TM pixels are known to be slightly mis-registered spatially (see Rothery *et al.*, 1988) but, in addition, if the spatial responses of bands 5 and 7 have significantly different shapes, e.g., band 7 has a broader response than band 5, then, in theory, the thermal response would be mis-registered

between channels, reducing further, in the face of many other uncertainties, the validity of dual-band calculations.

An alternative explanation of the greater spread of band 7 radiance may be that scattering of emitted infrared by volcanic fumes is particularly strong at about 2.08-2.35 μm. Anyone who has looked at magmatic features in a fume-filled crater at night, or seen crater glow from afar, will be familiar with this phenomenon at visible wavelengths. Fumes are also a problem because they can absorb infrared radiation emitted from the ground (Figure 5.9b; Oppenheimer and Rothery, 1991).

One also needs to question the reliability of a time-series of satellite 'snapshots', such as those described here, for making intercomparisons. Clearly, for a dynamic lava body, such as a rapidly overturning lake or active flow, satellite images recorded months weeks or even days apart may indicate at best only the coarsest trends in thermal evolution of the surface (Oppenheimer and Rothery, 1991). Despite some rather large time gaps in the Láscar data set, 'cooling' trends such as that between December 1984 and August 1986, are convincing, and probably reflect a rather gradual development of the volcano's behaviour at the surface during non-eruptive periods.

5.6. Conclusions

The ratio of band 5 to band 7 radiance for a TM thermal anomaly indicates the relative importance of small-size high-temperature sources to broad areas of low to moderate temperatures. If the thermally-derived DN in band 5 is relatively high then it suggests that areas of incandescence are comparatively extensive and/or that background temperatures are low. Such situations might pertain to high-temperature fumarole fields associated with shallow magma bodies. On the other hand, a high proportion of band 7 radiance is suggestive of elevated background temperatures and no, or only small, areas of incandescence, typical of the surfaces of many erupted lavas. Such spectral distinctions can be subtle, and are best made using night-time CCT-A format data. Even then, uncertainties arising from sensor saturation, and the non-uniqueness of solutions to

the 'dual-band' equations, hamper the identification of small intracrater thermal anomalies from remotely-sensed data alone.

Similarities of TM images of Volcán Láscar, acquired at different times suggest that a lava dome had been emplaced by December 1984. Oblique air photographs of the interior of the crater in January 1987 show no lava body whatsoever, implying that it had been entirely removed by the September 1986 eruption. The TM images again suggest that a new dome was extruded sometime before November 1987, although it was not until February 1989, following an ascent by geologists to the summit of Láscar, that the presence of a lava dome was suspected. Photographs of the crater taken since then suggest that the confined dome has a volume of about 10^6 m^3.

Activity at Láscar since 1984 is best characterised by periods of dome growth punctuated by moderate explosive eruptions which produce eruption columns of about 10 km height. Even at a comparatively small scale, the distribution and value of 'hot' pixels in TM anomalies may conform to the disposition of high-temperature features on the ground. Annular anomalies may characterise episodes of dome deflation in which magmatic gas escapes preferentially around the margins; conversely, compact groups of 'hot' pixels may typify periods of dome growth. Several of the TM images show evidence for high-temperature fumaroles beyond the margins of the dome; (this was also observed at Mount St. Helens [Casadevall *et al.*, 1983]).

It is, in some respects, unfortunate that the most intensive remote sensing study of this nature should have focussed on Láscar, perched high on the remote Altiplano of the central Andes, and bereft of routine ground observations or instrumental monitoring. However, it is in large part thanks to the extreme aridity of the prevailing climate and the high summit elevation of Láscar that it has been possible to acquire such a substantial set of cloud-free images of a persistent magmatic/ fumarolic feature. The fact that it has so far proved impossible to obtain a single TM acquisition of Kilauea, Hawaii, because of frequent cloud cover (P. Francis, personal communication, 1991), reinforces this point.

It is planned to continue satellite monitoring of Láscar, and eventually to supplement TM data with images from forthcoming remote sensing platforms, including the Japanese Earth Resources Satellite (JERS-1) scheduled for launch in February 1992. Hopefully, these ongoing investigations, combined with further field observations of this remote volcano in the Chilean Andes, will provide a valuable insight into the dynamics of a widespread style of silicic volcanism.

Chapter 6. Potential of forthcoming spaceborne infrared sensors for measuring thermal emission from volcanoes

---

Physical, biological and chemical processes of the atmosphere, oceans and land surface are interdependent. Because influences such as solar irradiance, volcanic aerosols, trace gases, biomass emission, and land-use change manifest themselves at the global scale, long-term global measurements are needed both to detect the effects and to provide data sets that may parameterise, test, and hence improve predictive models. To these ends, a number of remote sensing satellites are scheduled for launch into Earth orbit over the next decade.

Arguably, the Earth Observing System (EOS), centrepiece of NASA's 'Mission to Planet Earth' initiative (Ormsby and Soffen, 1989), is the most ambitious. Its first multi-sensor, polar orbiting platform is due for deployment in 1998. Later, geostationary satellites promise to provide continuity to many kinds of measurements of the Earth system over a period of fifteen years. The EOS Interdisciplinary Science investigators incorporate a volcanology team whose objectives include documentation of the magnitude, geographic location and frequency of volcanic eruptions, and their effects

on climate (Mouginis-Mark *et al.*, 1991). Other forthcoming orbital remote sensing missions include the European Space Agency's Polar Orbit Earth observation Mission (POEM), and the Japanese Earth Resources Satellites (JERS).

Following a summary of preceding chapters, in this final chapter I examine the potential of several future infrared instruments for measuring thermal radiation from volcanic features. Several topics which could merit future research are mentioned.

6.1. Recapitulation

This thesis has been concerned with both techniques and applications of infrared remote sensing for thermal studies of volcanoes. The foregoing chapters are summarised briefly as follows:

Chapter 1 reviewed applications of remote sensing techniques to volcanological investigations. Frequent global coverage, synoptic perspective and measurements in many regions of the electromagnetic spectrum have permitted several areas of research to be pursued, notably the detection of thermal features. The 'dual-band technique' for estimating temperatures of sub-pixel sized thermal sources using multispectral data was introduced, and the uncertainties of this method outlined.

Chapter 2 presented a new approach to solution of the dual-band equations, and applied it in the analysis of a Landsat TM image of the 1989 eruption of Lonquimay volcano, Chile. The temperature of exposed core material was predetermined in order to calculate surface temperatures of the cooling flow carapace. This demonstrated the downflow cooling of the lava, and enabled estimates of heat losses from the flow surface to be made. These results were consistent with the predictions of theoretical models of lava flow dynamics. Despite the uncertainties which arise in their application, remote sensing techniques provide the only practical means for obtaining a coherent set of measurements for a feature as extensive as a lava flow field. In order, specifically, to appraise the validity of the dual-band assumptions, it was suggested that field

observations be directed at characterising temperature distributions on the surfaces of various kinds of lava.

Chapter 3 introduced preliminary results of such fieldwork. Both the spatial distribution, and temporal variation of temperatures associated with a range of volcanic thermal features were examined. These observations highlighted the significance of the stability in time of thermal patterns, and the attenuation by volcanic fumes of infrared radiation emitted from hot surfaces. For rapidly overturning lava ponds, changes in radiant temperatures, and surface areas of material at given radiant temperatures, can be large and rapid. In such case, comparison of heat loss estimates made from satellite images acquired hours or days apart might not be especially meaningful.

Chapter 4 focussed on the characterisation of surface temperatures associated with fumarole fields. A model for the division of radiant temperatures around fumaroles was put forward which differs from the prevailing description of temperature patterns on the surfaces of active lava flows. Such a difference, it was suggested, might be discernible in Landsat Thematic Mapper images, from the relative response of the two short wavelength infrared bands, and might therefore provide a basis for identification of unknown thermal anomalies. However, caution was advised in taking 'dual-band' derived temperature estimates at face value.

Chapter 5 examined fourteen Thematic Mapper images, recorded between 1984 and 1991, of a persistent hot spot at Láscar volcano in north Chile. This is almost certainly the best dataset of its kind. Spectral information in the two short wavelength infrared bands was used to help interpret the nature of the thermal anomaly and to document its evolution through time. From this analysis, it was evident that Láscar's explosive eruptions (in 1986 and 1990) had been associated with the development of lava domes. Such techniques could provide valuable insight into the dynamics of lava domes.

6.2. Future infrared sensors

A clear limitation of the Landsat TM SWIR sensors, in respect of sub-pixel resolution temperature calculations, is the saturated response arising when as little as 1 % of a pixel's area is occupied by material at magmatic temperatures (Chapters 2 and 5). Even if saturation does not occur, the availability of just two SWIR bands allows the derivation of temperatures only according to very simplistic thermal models for the surfaces under examination. This section looks at the potential of several new instruments to improve such radiometric calculations.

6.2.1. The Optical Sensor of JERS-1

JERS-1 is due to be launched from Japan into a 568 km altitude sun-synchronous polar orbit, in February 1992. The spacecraft will carry a synthetic aperture radar instrument, and the Optical Sensor (OPS), an imaging device with four bands in the visible and very near infrared regions, and four more in the SWIR. The OPS has a 4096 element CCD sensor for each band, providing a quoted spatial "resolution" of 18.3 x 24.2 m, and a swath width of 75 km (NASDA, 1990). Further specifications of channels 4-8 on the OPS are shown in Table 6.1. In terms of spectral position, OPS channels 4 and 5 overlap with Landsat TM channels 4 and 5, respectively, while the filter of TM band 7 spans the central wavelengths of the finer spectral width OPS channels, both 7 and 8.

With twice as many SWIR channels as Landsat TM, the OPS promises to constrain more effectively the thermal emission from volcanic sources in this part of the spectrum. In addition, its smaller pixel size should facilitate the detection of very small magmatic-temperature thermal features (such as fumaroles not associated with new lava), and the resolution of fine spatial detail of larger anomalies. However, OPS data will be quantised to only 6 bits, a significant reduction in the radiometric precision afforded by the Thematic Mapper. To make a fuller appraisal of the utility of OPS sensors, I consider next their potential response to a selection of model thermal distributions.

I begin with analyses of Gradie *et al.* (1988) based on their field infrared spectrometry of the Kupaianaha lava lake in Hawaii. They identified three states of surface activity of the lake: (1) a slow-moving glassy crust, (2) active rifting, exposing hotter, incandescent material, and (3) rapid rifting and vigorous degassing. Analysis of the spectrometer data suggested that radiant temperature distributions across the lava surface could be represented by two components. The visibly different states of behaviour of the lake corresponded to distinctive patterns of radiant temperatures across it. Table 6.2 shows four examples. These have been used in each case to compute the spectral radiance curves between 0.8 and 2.4 μm (Figure 6.1), ignoring atmospheric effects. The upper dynamic limits of the OPS sensors are superimposed on the graph, indicating that lake activity states 2 and 3 would readily saturate all the SWIR bands of the OPS. Only the two spectral channels, 5 and 6, would be likely to make useful measurements in the case of state 1 activity. In this case, the OPS band 6 does make a contribution by occupying part of the spectral lacuna between Landsat TM bands 5 and 7.

Channel	Central wavelength (μm)	Bandwidth (μm)	Dynamic range (mW cm^{-2} sr^{-1} μm^{-1})
4	0.81	0.1	0-23.9
5	1.655	0.11	0-3.33
6	2.065	0.11	0-1.78
7	2.19	0.13	0-1.37
8	2.335	0.13	0-1.08

Table 6.1. Specifications of the OPS.

The thermal distribution for state 1 (Table 6.2) is not dissimilar to that derived from Landsat TM data for the lava dome at Láscar volcano, Chile (Chapter 5), e.g., T_c = 800°C, T_s = 220°C, and $f = 9 \times 10^{-4}$. The OPS could therefore be expected to make some useful measurements of Láscar-like phenomena, although the common problem of SWIR band saturation encountered on TM images of the volcano is unlikely to be much reduced in OPS images. Four OPS scenes of Láscar, as well as two of Erta 'Ale, Ethiopia, have been requested as part of a JERS-1 "verification programme" administered by the National Space Development Agency of Japan. (These will be analysed in 1992-

3, at the Open University, by David Rothery; OPS data of volcanoes in Kamchatka, Italy and Hawaii have also been requested by David Pieri at JPL). With their finer spatial response, the OPS data may reveal spatial detail of the Láscar anomaly not resolved by TM scenes.

Reference	State	T_S (°C)	T_C (°C)	f
a	1	263	758	8.33×10^{-4}
b	1	324	1029	5.33×10^{-4}
c	2	527	820	2.94×10^{-2}
d	3	647	1181	1.39×10^{-2}

Table 6.2. Thermal components estimated by Gradie *et al.* (1988) from spectrometer measurements at Kupaianaha lava lake, Hawaii. The reference letter denotes the corresponding Planck curve in Figure 6.1. Activity states 1, 2 and 3 are described in the main text.

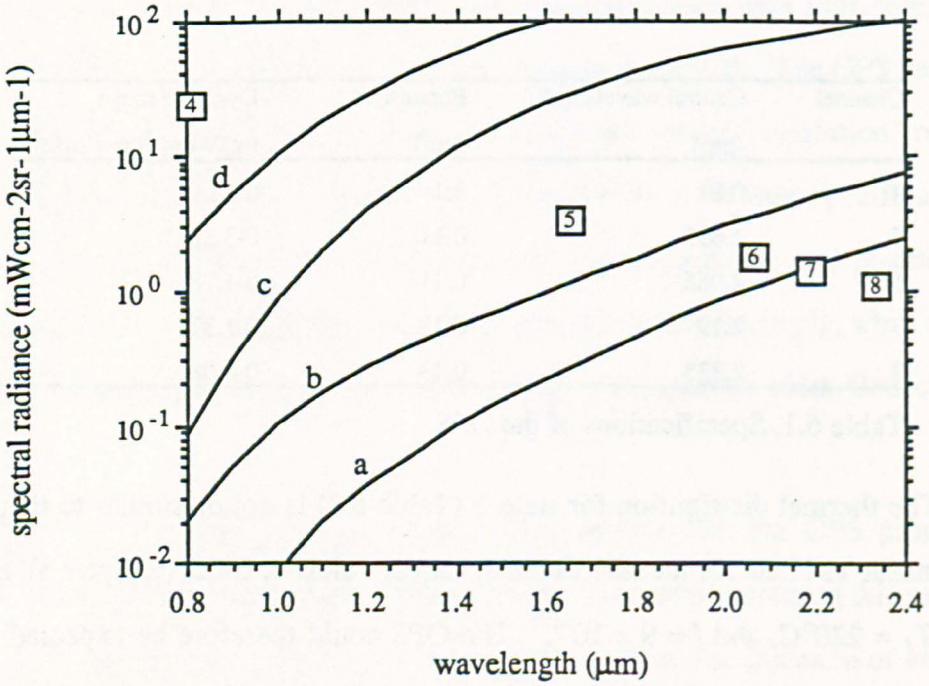

Figure 6.1. Four cases, a-d, of two-temperature component spectral radiance distributions for the Kupaianaha lava lake, Hawaii, as detailed in Table 6.2. The upper limits of the dynamic ranges of OPS sensors 4-8 are superimposed.

In the two-thermal component models examined so far, the cooler 'background' has been sufficiently warm to contribute significant radiance in the SWIR region. Figure 6.2 depicts the spectral radiance distribution in the SWIR region for a hot source at 850°C

occupying a range of areas between 0.01 and 1 m^2, surrounded by ground at just 100°C. Such a distribution could represent a high temperature fumarole field such as at Momotombo volcano (Chapters 3 and 4). In this case, it is the lower sensitivities of the OPS sensors that will determine whether useful measurements can be made. Experience with TM data suggests that the practical lower limit of useful radiance measurements is about 0.01-0.02 mW cm^{-2} sr^{-1} μm^{-1} in the SWIR region. In theory, the OPS should provide at least two spectral measurements for each of the temperature models in Figure 6.2, depending on the atmospheric transmittance. Night-time images would greatly enhance detection of smaller and/or cooler hotspots.

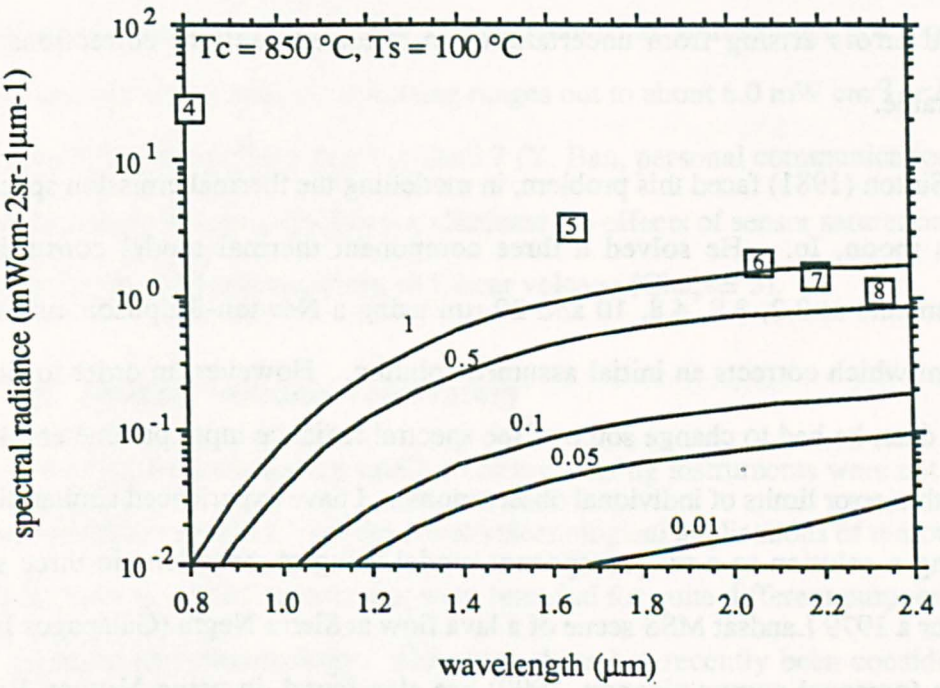

Figure 6.2. Spectral radiance curves for two-temperature-component models with T_c = 850°C occupying areas of 0.01, 0.05, 0.1, 0.5 and 1.0 m^2 within OPS pixels (equivalent to fractional areas, f, of the hot component of 2.3 x 10^{-5}, 1.1 x 10^{-4}, 2.3 x 10^{-4}, 1.1 x 10^{-3} and 2.3 x 10^{-3}), and T_s = 100°C. The upper limits of the dynamic ranges of OPS sensors 4-8 are superimposed.

In cases where there are unsaturated responses in more than two spectral channels, there are possibilities for 'multi-band techniques' to estimate temperatures of sub-pixel sized sources. For n black-body thermal components, T_1, T_2,...., T_n,

occupying corresponding fractional areas $f_1, f_2, \ldots, f_n$, the spectral radiance, R_λ, measured at wavelength λ can be written as follows:

$$R_\lambda = \sum_{i=0}^{n} f_i L(\lambda, T_i) \tag{6.1}$$

where $L(\lambda, T_i)$ is the Planck function (equation 1.3). For example, if measurements were available in three bands, then it might be possible to solve simultaneously f, T_C and T_S for the standard two temperature component model expounded throughout this thesis, without determining *a priori* one of the parameters (equations 1.4 and 1.5). However, even the 'dual-band' equations have no analytical solution. Tackling three or more simultaneous equations of this sort numerically is substantially more difficult than just two, and errors arising from uncertainties in reflected sunlight corrections can be considerable.

Sinton (1981) faced this problem, in modelling the thermal emission spectrum of Jupiter's moon, Io. He solved a three component thermal model constrained by measurements at 2.2, 3.8, 4.8, 10 and 20 μm using a Newton-Ralphson curve-fitting algorithm which corrects an initial assumed solution. However, in order to fit all the spectral data, he had to change some of the spectral radiance input parameters (keeping them within error limits of individual observations). I have experienced similar difficulty in finding a solution to a two-component model using observations in three spectral bands, for a 1979 Landsat MSS scene of a lava flow at Sierra Negra (Galápagos Islands). L. Glaze (personal communication, 1990) has also found, in using Newton-Ralphson algorithms, that solutions are sensitive to the initial guess required by the technique. Further approaches to this problem should be considered in the near future; test material may be provided by Thematic Mapper Simulator (TMS) data recorded during NASA's Multispectral Airborne Campaign in Europe (MAC-Europe 1991). The TMS has three SWIR channels (1.13-1.35, 1.57-1.71 and 2.10-2.38 μm), and was flown over the Italian volcanoes Etna, Stromboli and Vulcano, both by day and by night, in July 1991.

6.2.2. The Enhanced Thematic Mapper (ETM)

The Landsat programme has suffered serious funding setbacks - the replacement for Landsat 5 was due for launch in mid-1991 but now appears to be a year behind schedule. Landsat 6 will carry an improved version of the TM, the Enhanced Thematic Mapper (ETM). To ensure continuity with existing TM products, the ETM will acquire data in the same seven spectral bands, and at the same spatial resolution. In addition, the ETM will be equipped with a 15 m resolution panchromatic sensor. However, the design feature of most interest from our standpoint is the capability to set the gains of the spectral bands from the ground. This will provide for either a high- or low- gain eight-bit setting. The present TM has only a high-gain setting which often results in saturation over strongly-reflective surfaces such as desert sands, as well as over hot spots. The low-gain settings will extend the operating ranges out to about 6.0 mW cm^{-2} sr^{-1} μm^{-1} in band 5, and 3.0 mW cm^{-2} sr^{-1} μm^{-1} in band 7 (Y. Ban, personal communication, 1991). This would reduce though probably not eliminate the effects of sensor saturation, such as encountered in the TM investigations of Láscar volcano (Chapter 5).

6.2.3. An orbiting volcano observatory

Existing and forthcoming satellite remote sensing instruments were not designed with volcanologists in mind. All the novel volcanological applications of remote sensing techniques have exploited sensors that were intended for quite different purposes, such as ozone mapping and meteorology. However, there has recently been consideration of equipping a satellite package dedicated to the surveillance of volcanoes - an orbiting volcano observatory (Pieri and Glaze, 1989). This experimental mission appears likely to receive funding from the Italian Space Agency (D. Pieri, personal communication, 1991). The latest acronym for the project is VEXUVIO (Volcano Experimental Ultraviolet and Infrared Observatory).

Redesign of an existing scanning system to carry 20-30 sensors between 0.25 and 4 μm is underway at the Jet Propulsion Laboratory. Further encouragement for

VEXUVIO came in August 1991, when the European Space Agency approved a proposal to incorporate it on an engineering test platform to be launched into a 28.5° equatorial orbit from the Space Shuttle. In this orbit, many volcanoes would be missed. However, the instrument would be tested, retrieved within six to nine months, and could then be refurbished and launched into polar orbit. An orbiting volcano observatory could be a resource available to the volcanological community within three to five years.

6.2.4. ASTER

The Advanced Spaceborne Thermal Emission and reflection Radiometer (ASTER) has been selected for flight on the first EOS platform, EOS-A1. (It was formerly known as the Intermediate and Thermal Infrared Radiometer [ITIR]). Like the OPS, it is equipped with several channels in both the visible and near infrared (VNIR) and SWIR regions of the spectrum. It has six SWIR sensors, which will produce image data composed of 30 x 30 m pixels. In spectral terms, band 4 of ASTER coincides with band 5 of the OPS, while bands 5-9 of ASTER span approximately the same spectral region as OPS bands 6-8 (Table 6.3). Its pointing capability will mean that any point on the Earth will be accessible at least once every 16 days.

Channel	Bandpass (μm)	Radiometric resolution (%)
4	1.60-1.71	0.5
5	2.02-2.12	0.8
6	2.12-2.19	0.8
7	2.19-2.26	1.0
8	2.29-2.36	1.0
9	2.36-2.43	1.3

Table 6.3. Specifications of ASTER SWIR sensors.

Dynamic ranges of ASTER have not been confirmed yet, although they are certain to span approximately the same regions as equivalent OPS sensors. Finer spectral width of the sensors will reduce errors which arise in Planck calculations where bandpasses are approximated by the midpoints of their spectral response. Nevertheless, on these considerations alone, ASTER does not appear to offer any significant advantages over the

OPS for SWIR volcano monitoring. More important are factors which remain to be verified, such as the spatial registration between spectral bands of each instrument.

A feasible method for such an appraisal might be to record images over a test site where various thermal targets can be arranged. The spatial response of TM sensors has been measured by recording images of arrangements of high contrast targets positioned on the ground (e.g. Schowengerdt *et al.*, 1985). For such purposes, the targets need to be very large (several tens of metres). Because SWIR detectors are so sensitive to thermal radiation from hot surfaces (around 1000°C), thermal targets, capable of maintaining a uniform temperature, would only have to be about a metre square. A number of such hot plates could then be thoughtfully distributed at a suitable test site under the path of the recording instrument to be investigated. This would be a simple experiment - but if realised, it could furnish the means for a much-needed appraisal of the accuracy of remotely-sensed thermal measurements of small hot sources.

6.2.5. Imaging spectrometers

Imaging spectrometry is the simultaneous acquisition of images in many fine-width, contiguous spectral bands. Although designed for facilitating identification of surface materials from diagnostic features of their reflectance spectra, several instruments - some operative, others under construction - have sensors through the SWIR region, and are therefore potentially useful for study of hot volcanic features. The field spectrometer data collected by Gradie *et al.* (1988) and Flynn *et al.* (1989) at the Kupaianaha lava pond, Hawaii (Section 6.2.1) indicate what might be achieved with imaging spectrometers. Ignoring measurements in atmospheric absorption bands, they found least-squares fits of Planck curves for the remaining data points, which suggested in several cases that the lava surface was dominated by two temperature components (Table 6.2). Slight scatter in these data was attributed to small changes in both radiant temperatures and areas (at a given temperature) in the evolving surface of the lava over the time it took the instrument to scan its thousand or so spectral channels (> 60 s).

Because imaging spectrometers make near-instantaneous measurements in all spectral channels for each pixel, this kind of error should be eliminated. In July 1991, the Airborne Visible/ Infrared Imaging Spectrometer (AVIRIS) was operated over the Italian volcanoes as part of the NASA MAC-Europe deployment. Images recorded above Mount Etna and Stromboli may well show evidence of Planck radiation from magma-filled vents, thereby providing test-material for evaluating temperature distributions. The Simplex algorithm (Caceci and Cacheris, 1984) may be appropriate for fitting Planck curves to such data. This dataset should be examined at The Open University and the Jet Propulsion Laboratory during 1992.

A derivative of AVIRIS is HIRIS (High-Resolution Imaging Spectrometer), tentatively ear-marked for inclusion in missions EOS-A2 and -A3 to be launched next century. HIRIS spans the 0.4-2.45 μm wavelength region in 192 spectral bands with 10 nm spectral sampling and 30 m pixel size. The instrument is designed to be pointable, enabling sampling of any point on the Earth's surface a minimum of every 2 days. Although the atmosphere is markedly opaque to portions of the SWIR region, imaging spectrometer data will bridge the gap in the coverage of Landsat TM, OPS and ASTER sensors between the VNIR and SWIR regions. Data acquired in the atmospheric window at about 1.2 μm could be especially significant for radiometry of lava bodies (Figure 6.1).

The narrow spectral width of spectrometer channels might also permit estimation of the concentrations of volcanic gas species which have absorption features within the regions of the spectrum covered. This could allow the estimation of atmospheric transmittance functions and the reconstruction of Planck radiation profiles (Oppenheimer and Rothery, 1991). An investigation is underway to use data from the airborne Thermal Infrared Multispectral Scanner (TIMS) recorded over Mount Etna to quantify amounts of sulphur dioxide in the atmospheric path (D. Pieri, personal communication, 1991). TIMS has six channels in the thermal infrared, one of which coincides with a line absorption of sulphur dioxide at 8.69 μm.

6.3. Related applications

Infrared spectrophotometry of distant planetary bodies, and satellite observations of fires on Earth, can also exploit multispectral techniques to extract temperatures and sizes of sub-pixel resolution. In this section, I briefly discuss some further applications of infrared remote sensing techniques to thermal studies.

6.3.1. Io

Active volcanism is not restricted to Earth. Even before the Voyager spacecraft reached Jupiter's satellite, Io, Peale *et al.* (1979) had predicted the existence of active volcanoes on the moon's surface, arising from tidal heating of its interior. The images recorded by Voyagers 1 and 2 left no doubt that this was the case (Carr *et al.*, 1979), and this discovery stimulated tremendous interest in the nature of volcanic materials on Io. In particular, debate centred on whether or not eruptions of liquid sulphur, to form lakes and flows, had taken place. The Voyager images and broadband infrared observations from Earth provided two lines of argument - reflectance spectra and thermal spectra. Sagan (1979) and Pieri *et al.* (1984) matched the reflectance of flow-like features with that expected of sulphur quenched from different temperatures. However, others have suggested that silicate lavas, and UV irradiated sulphur dioxide frost (Hapke, 1989), or ferrous compounds (Young, 1984) better account for the reflectance of Io's volcanic features.

From our viewpoint, the thermal calculations are more interesting. As discussed in section 6.1.2., Sinton (1981) constrained the temperature and areal extent of volcanically active regions using groundbased infrared observations. He identified both $\approx$ 600 K and $\approx$ 300 K sources. By similar methods, but using Voyager infrared interferometer spectrometer (IRIS) data, Pearl and Sinton (1982) estimated temperatures up to $\approx$ 650 K at the source of the Pele eruption plume. These temperatures are substantially lower than those of silicate melts, and on this basis McEwen *et al.* (1985) suggested that molten sulphur was the primary liquid on the surface of volcanic regions

of Io. However, Gradie *et al.* (1988) countered this argument, pointing out that radiative skin temperatures of lava bodies are likely to be substantially below temperatures of the melt. In addition to their own spectrophotometric observations at Kilauea, they quoted the temperature estimates made by Francis and Rothery (1987) from TM data of Láscar volcano in support of their argument.

More recently, techniques have been established that make possible routine ground-based infrared observations of the locations, temperatures and sizes of volcanic sites on Io (Spencer *et al.*, 1990). Observations are made during Jupiter eclipse with the Infrared Telescope Facility on Hawaii, at 1.6 and 2.2 μm. Láscar is the only terrestrial volcano with a record of thermal emission observations similar to that for Io, and the TM data from bands 5 and 7 (at 1.65 and 2.22 μm respectively) are compatible with the new Io observations. Preliminary calculations of the ratios of heat radiated at these two wavelengths for Io and Láscar show that the high-temperature Io measurements overlap with those for Láscar, suggesting the former are at least consistent with silicate volcanism (Spencer *et al.* 1991).

Looking further ahead, by late 1995 the Galileo spacecraft will have reached the jovian system. Infrared observations of Io will be made at higher spatial and spectral resolution and with greater radiometric precision than ever before, enabling more detailed thermal measurements to be made of volcanic regions of the moon, using multi-wavelength techniques.

6.3.2. Fire

Infrared images recorded by satellites can also detect fires. The early work of Matson and Dozier (1981) on two-wavelength algorithms for estimating subpixel temperatures documented the sensitivity of the 3.8 μm channel of the AVHRR to various industrial sources, including steel mills. Muirhead and Cracknell (1984) identified gas flares in the North Sea with similar data. Rothery (1989) applied the dual-band technique to interpret Landsat TM SWIR data of the Chernobyl fires. This kind of work

has obvious strategic implications. For example, AVHRR thermal images were used during the 1991 Persian Gulf war to monitor destruction of oil facilities in Kuwait.

Similar data have also been shown capable of detecting heat from land clearance fires (Matson and Holben, 1987) and agricultural burning (Muirhead and Cracknell, 1985; Matson *et al.*, 1987). Such surveillance could inspire agreement on the need for, and enable verification of, appropriate environmental protection measures. Crutzen *et al.* (1979) implicated biomass burning as a major source of aerosols and some trace gases in the atmosphere. As such, improving the evaluation of global fire emissions is an important goal, and infrared remote sensing from space is seen as a potential means of achieving it (Matson *et al.*, 1987; Robinson, 1991). The use of multi-wavelength techniques for examining volcanic hotspots might profitably be applied to fire monitoring, for assessing flame temperatures, and thereby deducing the nature of burning fuels.

6.4. Conclusions and overview

The main conclusions of this thesis are synthesised as follows:

(i) Multispectral SWIR data recorded from satellites provide an unique means for estimating heat losses from features as extensive as lava flows. Such techniques can give a valuable insight into the dynamics of widespread styles of effusive volcanism.

(ii) However, because satellite measurements have hitherto spanned only limited parts of the infrared spectrum, modelling of the whole spectrum emission requires a number of assumptions to be made. The results of such extrapolations are therefore only as reliable as the applied models are realistic. Temperature determinations made using dual-band techniques should not be considered accurate or dependable. They can, however, illustrate qualitative trends.

(iii) Measurements at different parts of the SWIR spectrum do reflect the relative proportions of hot and cool surfaces, and can therefore provide clues as to the identity of thermal anomalies known from satellite data alone.

(iv) While the Landsat TM can provide excellent opportunities for studying thermal emission from volcanic features, analysis is constrained by the availability of just two SWIR spectral bands. Several remote sensing instruments to be deployed over the next decade will carry greater numbers of finer spectral width SWIR channels and promise significantly to improve capabilities for thermal measurements.

In contrast to the strictly scientific goals of recent missions to distant members of the solar system, data from EOS and other Earth observation missions could have direct societal implications. For example, infrared sensors might detect a previously unknown thermal feature on a volcano in a populated region. In such circumstances, the volcanic hazards community will expect, and demand, the availability of straightforward algorithms to assist in interpretation of the data.

One of the goals of the EOS Volcanology Investigation team is to monitor volcanoes. It plans to conduct (i) long-term monitoring of some 200 volcanoes, once each during a year, (ii) short-term monitoring of about 50 sites, once each every 16 days, and (iii) continuous surveillance for eruption detection worldwide (Mouginis-Mark *et al.*, 1991). In practice, data rates, instrument duty cycles, conflicts with other EOS investigations, and limited funds will probably restrict the scope of such a monitoring programme. Data archive and distribution will doubtless prove to be a huge undertaking for the EOS Data and Information System (EOSDIS).

One of the most severe difficulties likely to be encountered, however, is that of cloud cover. The gravity of this elementary problem is best illustrated by an example: to date, it has not been possible to obtain a single cloud-free TM image of Kilauea volcano in Hawaii (P. Francis, personal communication, 1991). Many other volcanoes in wide-ranging climatic belts are similarly affected. Unfortunately, the implication of this is that visible and infrared remote sensing techniques cannot be relied on to provide regular monitoring of most volcanoes. At best, they present valuable complements to other techniques, notably spaceborne imaging radar, and conventional ground surveys.

For applications other than volcano *monitoring*, there is not the same urgency for data distribution. Volcanologists will have access to a vast amount of remotely sensed data from new instruments operating in many parts of the electromagnetic spectrum. The wealth of expected data will undoubtedly spawn many investigations of volcanoes in ways impossible by conventional techniques on the ground, promising to advance the understanding of the emplacement of volcanic materials, and their effects on the atmosphere. An era of volcanology from space will blossom soon.

References

Abrams, M., Glaze, L., and Sheridan, M., 1991. Monitoring Colima volcano, Mexico using Satellite data. *Bull. Volcanol.*, 53, 571-574.

Allard, P., and Sabroux, J.C., 1980. Actividad volcanica del Momotombo, Nicaragua. Informe preliminar 4 Agosto 1980. Unpublished report, INETER, Managua.

Allard, P., Carbonnelle, J., Dajlevic, D., Le Bronec, J., Morel, P., Robe, M.C., Maurenas, J.M., Faivre-Pierret, R., Martin, D., Sabroux, J.C., and Zettwoog, P., 1991. Eruptive and diffusive emissions of CO_2 from Mount Etna. *Nature*, 351, 387-391.

Anderson, S.W., and Fink, J.H., 1990. The development and distribution of surface textures at the Mount St. Helens dome. In Lava flows and domes: emplacement mechanisms and hazard implications, J. Fink (ed.), IAVCEI Proceedings in volcanology 2, Springer-Verlag, Berlin, 25-46.

Andres, R.J., Rose, W.I., Kyle, P.R., deSilva, S., Francis, P., Gardeweg, M., and Moreno Roa, H., 1991. Excessive sulfur dioxide emissions from Chilean volcanoes. *J. Volcanol. Geotherm. Res.*, 46, 323-329.

Archambault, C., and Tanguy, J.C., 1976. Comparative temperature measurements on Mount Etna lavas: problems and techniques. *J. Volcanol. Geotherm. Res.*, 1, 113-125.

Bartholemew, M.J., Kahle, A.B., and Hoover, G., 1989. Infrared spectroscopy (2.3 - 20 μm) for the geological interpretation of remotely-sensed multispectral thermal infrared data. *Int. J. Remote Sens.*, 10, 529-544.

Benhamou, G., Allard, P., Sabroux, J.C., Vitter, G., Dajvelic, D., and Creusot, A., 1988. Oxygen fugacity of gases and rocks from Momotombo volcano, Nicaragua: application to volcanological monitoring. *J. Geophys. Res.*, 93, 14872-14880.

Bianchi, R., Casacchia, R., Coradini, A., Duncan, A.M., Guest, J.E., Kahle, A., Lanciano, P., Pieri, D.C., and Poscolieri, M., 1990. Remote sensing of Italian volacnos. *Eos, Trans. Am. Geophys. Union*, 71(46), 1789-1791.

Birnie, R.W., 1973. Infra-red radiation thermometry of Guatemalan volcanoes. *Bull. Volcanol.*, 37, 1-36.

Bonneville, A., and Kerr, Y., 1987. A thermal forerunner of the 28th March 1983 Mt Etna eruption from satellite thermal infrared data. *J. Geodynam.*, 7, 1-31.

Bonneville, A., Vasseur, G., and Kerr, Y.,1985. Satellite thermal infrared observations of Mt Etna after the 17th March 1981 eruption. *J. Volcanol. Geotherm. Res.*, 24, 293-313.

Caceci, M.S., and Cacheris, W.P., 1984. Fitting curves to data: the Simplex algorithm is the answer. *Byte*, May issue, 340-362.

Carr, M.H., 1981. The surface of Mars. Yale University Press, New Haven, 232 pp.

Carr, M.H., Masursky, H., Strom, R.G., and Terrile, R.J., 1979, Volcanic features of Io, *Nature*, 280, 729-733.

Casadevall, T., Rose, W., Gerlach, T., Greenland, L.P., Ewert, J., Wunderman, R., and Symonds, R., 1983. Gas emissions and the eruptions of Mount St. Helens through 1982, *Science*, 221, 1383-1385.

Casadevall, T.J., Rose, W.I., Fuller, W.H., Hunt, W.H., Hart, M.A., Moyers, J.L., Woods, D.C., Chuan, R.L. and Friend, J.P., 1984. Sulfur dioxide and particles in quiescent volcanic plumes from Poás, Arenal and Colima volcanoes, Costa Rica and Mexico. *J. Geophys. Res.*, 89, 9633-9641.

Casertano, L., and Barozzi, R., 1961. Informe sobre el sistema volcanica del Láscar, Santiago, Univ. de Chile, Faculdad de Ciencias Fisicas y Matematicas, Instituto de Geología Publ., 23, 304-315.

Crisp J., and Baloga, S., 1990a. A model for lava flows with two thermal components, *J. Geophys. Res.*, 95,1255-1270.

Crisp, J., and Baloga, S., 1990b. A method for estimating eruption rates of planetary lava flows, *Icarus*, 85, 512-515.

Crutzen, P.J., Heidt, L.E., Krasnec, J.P., Pollock, W.H., and Seiler, W., 1979. Biomass burning as a source of atmospheric gases CO, H_2, N_2O, NO, CH_3Cl, and COS. *Nature*, 282, 253-256.

Daneš, Z.F., 1972. Dynamics of lava flows. *J. Geophys. Res.*, 77, 1430-1432.

de Silva, S.L., and Francis, P.W., 1990. Potentially active volcanoes of Peru - Observations using Landsat Thematic Mapper and Space Shuttle imagery. *Bull. Volcanol.*, 52, 286-301.

de Silva, S.L., and Francis, P.W., 1991. Volcanoes of the Central Andes, Springer-Verlag, Berlin, 216pp.

Dozier, J., 1981. A method for satellite identification of surface temperature fields of subpixel resolution. *Remote Sens. Environ.*, 11, 221-229.

Dozier, J., and Goetz, A.F.H., 1989. HIRIS - EOS instrument with high spectral and spatial resolution. *Photogrammetria*, 43 (3/4), 167-180.

Dragoni, M., 1989. A dynamical model of lava flows cooling by radiation. *Bull. Volcanol.*, 51, 88-95.

Dragoni, M., Bonafede, M., and Boshi, E. 1986. Downslope flow models of a Bingham fluid: implications for lava flows. *J. Volcanol. Geotherm. Res.*, 30, 305-325.

Dzurisin, D., Denlinger, R.P., Rosenbaum, J.G., 1990. Cooling rate and thermal structure determined from progressive magnetization of the Dacite dome at Mount St. Helens, Washington. *J. Geophys. Res.*, 95, 2763-2780.

Eos, 1989. Satellite images monitor volcanoes. *Eos, Trans. Am. Geophys. Union*, 70, 74-75.

Eos, 1991. New EOS payload proposed. *Eos, Trans. Am. Geophys. Union*, 72, 417-418.

Fink, J.H., Malin, M.C., and Anderson, S.W., 1990. Intrusive and extrusive growth of the Mount St Helens lava dome. *Nature*, 348, 435-437.

Fischer, W.A., Moxham, R.M., Polcyn, F., and Landis, G.H., 1964. Infrared surveys of Hawaiian volcanoes. *Science*, 146, 733-742.

Flynn, L.P., Mouginis-Mark, P.J., and Gradie, J.C., 1989. Radiative temperature measurements at Kilauea Volcano, Hawaii. Abstract, IAVCEI General Assembly, Santa Fe, June 25-July 1, 1989, *Bull. New Mexico Bureau Mines Mineral. Resources*, 131, 94.

Francis, P.W., 1979. Infra-red techniques for volcano monitoring and prediction - a review. *J. Geol. Soc. Lond.*, 136, 355-359.

Francis, P.W., and Rothery, D.A., 1987. Using the Landsat Thematic Mapper to detect and monitor active volcanoes: an example from Lascar volcano, northern Chile. *Geology*, 15, 614-617.

Francis, P.W., and Wells, G.L., 1988. Landsat Thematic Mapper observations of debris avalanche deposits in the Central Andes. *Bull. Volcanol.* 50, 258-278.

Francis, P.W., and de Silva, S.L., 1989. Application of the Landsat Thematic Mapper to the identification of potentially active volcanoes in the Central Andes. *Remote Sens. Environ.*, 28, 245-255.

Francis, P.W., Kretschmar, G., O'Callaghan, L., Thorpe, R.S., Sparks, R.S.J., Page, R., de Barrio, R.E., Guillou, G., and Gonzalez, O., 1983. The Cerro Galan ignimbrite. *Nature*, 310, 51-53.

Gaddis, L.R., Mouginis-Mark, P.J., and Hayashi, J.N., 1990. Lava flow surface textures: SIR-B radar image texture, field observations, and terrain measurements. *Photogramm. Eng. Remote Sens.*, 56(2), 211-224.

Gardeweg, M.C., Foot, S., Matthews, S., Oppenheimer, C., Sparks S., and Stasiuk, M.V., 1990. II informe sobre el comportamiento del volcán Láscar: Marzo 1990, Servicio Nacional de Geología y Minería, Santiago, Chile, 31 pp.

Glaze L., Francis, P.W., and Rothery, D.A., 1989a. Measuring thermal budgets of active volcanoes by satellite remote sensing. *Nature*, 338, 144-146.

Glaze, L.S., Francis, P.W., Self, S., and Rothery, D.A., 1989b. The 16 September 1986 eruption of Lascar volcano, north Chile: satellite investigations. *Bull. Volcanol.* 51, 149-160.

Glaze, L.S., and Self, S., 1991. Ashfall dispersal for the 16 September 1986 eruption of Lascar, Chile, calculated by a turbulent diffusion model. *Geophys. Res. Lett.*, 18(7), 1237-1240.

Goetz, A. F. H., and Herring, M. 1989. The High Resolution Imaging Spectrometer (HIRIS) for Eos. *IEEE Trans. Geosci. and Remote Sens.*, 27, 136-144.

Gradie, J., Mouginis-Mark, P., Hayashi, J., and Flynn, L., 1988. Surface temperature and variability of an active lava lake: lessons to be applied to Io. Lunar and Planetary Science Conference XIX, 407-8.

Hapke, B., 1989. The surface of Io: a new model. *Icarus*, 79, 56-74.

Head, J.W., and Wilson, L., 1986. Volcanic processes and landforms on Venus: theory, predictions, and observations. *J. Geophys. Res.*, 91, 9407-9446.

Head, J.W., and Crumpler, L.S., 1990. Venus geology and tectonics: hotspot and crustal spreading models and questions for the Magellan mission. *Nature*, 346, 525-533.

Holasek, R.E., and Rose, W.I., 1991. Anatomy of 1986 Augustine volcano eruption as recorded by multispectral image processing of digital AVHRR weather satellite data. *Bull. Volcanol.*, 53, 420-435.

Holman, J.P., 1972. Heat Transfer. McGraw-Hill, New York, 462 pp.

Hulme, G., and Fielder, G., 1977. Effusion rates and rheology of lunar lavas. *Phil. Trans. Roy. Soc. Lond.*, A285, 227-234.

IAVCEI, 1990. Reducing volcanic disasters in the 1990's. *Bull. Volcanol. Soc. Jap.* 2,35(1), 80-95.

Jaupart, C., and Allègre, C.J., 1991. Gas content, eruption rate and instabilities of eruption regime in silicic volcanoes. *Earth Planet. Sci. Lett.*, 102, 413-429.

Jones, A.C., Wilson, L., and Pinkerton, H., 1990. Surface temperature measurements of active Hawaiian lava flows. IAVCEI International Volcanological Congress, Mainz, Germany, 3-8 September 1990, abstract volume.

Kays, W.M., and Crawford, M.E., 1980. Convective heat and mass transfer. McGraw-Hill, New York, 420pp.

Kieffer, H.H., Frank, D., and Friedman, J.D., 1980. Thermal infrared surveys at Mount St Helens - observations prior to the eruption of May 18. In The 1980 eruptions of Mount St Helens, Washington, Ed. P.W. Lipman and D.R. Mullineaux, *U.S. Geol. Surv. Prof. Pap.*, 1250, 257-277.

Kienle, J., and Shaw, G.E., 1979. Plume dynamics, thermal energy, and long distance transport of vulcanian eruption clouds from Augustine Volcano, Alaska. *J. Volcanol. Geotherm. Res.*, 6, 179-194.

Kienle, J., Dean, K.G., Garbeil, H., and Rose, W.I., 1990. Satellite surveillance of volcanic ash plumes, applications to aircraft safety. *Eos, Trans. Am. Geophys.. Union*, 71, 266.

Kneizys, F.X., Shettle, E.P., Gallery, W.O., Chetwynd, J.H. Jr., Abreu, L.W., Selby, J.E.A., Clough, S.A., and Fenn, R.W., 1983. Atmospheric transmittance/ radiance: computer code LOWTRAN 6. Air Force Geophysics Laboratory, Environmental Research Paper 846, Hanscom AFB, Massachusetts.

Kneizys, F.X., Shettle, E.P., Abreu, L.W., Chetwynd, J.H., Anderson, G.P., Gallery, W.O., Selby, J.E.A., and Clough, S.A., 1988. Users' guide to LOWTRAN 7. Air Force Geophysics Laboratory Environmental Research Paper 1010, Hanscom AFB, Massachusetts, 137pp.

Krueger, A.J., 1983. Sighting of El Chichón sulfur dioxide clouds with the Nimbus 7 Total Ozone Mapping Spectrometer. *Science*, 220, 1377-1379.

Krueger, A.J., Walter, L.S., Schnetzler, C.C., and Doiron, S.D., 1990. TOMS measurement of the sulfur dioxide emitted during the 1985 Nevado del Ruiz eruptions. *J. Volcanol. Geotherm. Res.*, 41, 7-15.

Lathrop, R.G., and Lillesand, T.M., 1986. Use of Thematic Mapper data to assess water quality in Green Bay and Central Lake Michigan. *Photogramm. Eng. Remote Sens.*, 52(5), 671-680.

Le Guern, F., 1987. Mechanism of energy transfer in the lava lake of Niragongo (Zaire), 1959-1977. *J. Volcanol. Geotherm. Res.*, 31, 17-31.

Le Guern, F., Carbonnelle, J., and Tazieff, H., 1979. Erta 'Ale lava lake: heat and gas transfer to the atmosphere. *J. Volcanol. Geotherm. Res.*, 6, 27-48.

Malingreau, J.P., and Kaswanda., 1986. Monitoring volcanic eruptions in Indonesia using weather satellite data: the Colo eruption of July 28, 1983. *J. Volcanol. Geotherm. Res.*, 27, 179-194.

Markham, B.L., 1985. The Landsat sensors' spatial responses. *IEEE Trans. Geosci. Remote Sens.*, GE-23(6), 864-875.

Markham, B.L., and Barker, J.L. 1987. Thematic Mapper bandpass solar exoatmospheric irradiances. *Int. J. Remote Sens.*, 8(3), 517-523.

Matson, M., and Dozier J., 1981. Identification of subresolution high temperature sources using a thermal IR sensor. *Photogramm. Eng. Remote Sens.*, 47(9), 1311-1318.

Matson, M., and Holben, B., 1987. Satellite detection of tropical fire burning in Brazil. *Int. J. Remote Sens.*, 8(3), 509-516.

Matson, M., Stephens, G., and Robinson, J., 1987. Fire detection using satellite data. *Int. J. Remote Sens.*, 8, 961-967.

McClain, E.P., Pichel, W.G., and Walton, C.C., 1985. Comparative performance of AVHRR-based multichannel sea surface temperatures. *J. Geophys. Res.*, 90 (C6), 11587-11601.

McEwen, A.S., Johnson, T.V., Matson, D.L., and Soderblom, L.A., 1985. Volcanic hot spots on Io: correlation with low-albedo calderas. *J. Geophys. Res.*, 90, 12345-12379.

Menyailov, I.A., Nikitina, L.P., Sharpar, V.N., and Pilipenko, V.P., 1986. Temperature increases and chemical change of fumarolic gases at Momotombo volcano, Nicaragua, in 1982-1985: are these indicators of a possible eruption ? *J. Geophys. Res.*, 91, 12199-12214.

Moreno, H., and Gardeweg, M.C., 1989. La erupción reciente en el Complejo Volcánico Lonquimay (Diciembre de 1988-), Andes del Sur. *Rev. Geol. Chile*, 16(1), 93-117.

Mouginis-Mark, P.J., Pieri, D.C., Francis P.W., Wilson, L., Self, S., Rose, W.I., and Wood, C.A., 1989. Remote sensing of volcanos and volcanic terrains. *Eos, Trans. Am. Geophys. Union*, 70(52), 1567-1575.

Mouginis-Mark, P., Rowland, S., Francis, P., Friedman, T., Garbeil, H., Gradie, J., Self, S., Wilson, L., Crisp, J., Glaze, L., Jones, K., Kahle, A., Pieri,D., Zebker, H., Krueger, A., L., Wood, C., Rose,W., Adams, J., and Wolff, R., 1991. Analysis of active volcanoes from the Earth Observing System. *Remote Sens. Environ.*, 36, 1-12.

Mouginis-Mark, P.J., and Francis, P.W., *sub judice*. Satellite observations of active volcanoes: prospects for the 1990s. Submitted to *Episodes*.

Moxham, R.M., 1970. Thermal features at volcanoes in the Cascades Range, as observed by aerial infrared surveys. *Bull. Volcanol.* 34(1), 77-106.

Moxham, R.M., 1971. Thermal surveillance of volcanic activity. UNESCO, Paris, 103-124.

Muirhead, K., and Cracknell, A.P., 1984. Identification of gas flares in the North Sea using satellite data. *Int. J. Remote Sens.*, 5, 199-212.

Muirhead, K., and Cracknell, A.P., 1985. Straw burning over Great Britain detected by AVHRR. *Int. J. Remote Sens.*, 5, 827-833.

Munro, D.C., and Mouginis-Mark, P.J., 1990. Eruptive patterns and structure of Isla Fernandina, Galapagos Islands, from SPOT-1 HRV and large format camera images. *Int. J. Remote Sens.*, 11(8),1501-1509.

NASDA, 1990. Outline of the JERS-1 system. Ministry of International Trade and Industry report, Japan, 31pp.

Naughton, J.J., Derby, J.V., and Glover, R.B., 1969. Infrared measurements on volcanic gas and fume: Kilauea eruption, 1968. *J. Geophys. Res.*, 74(12), 3273-3277.

Oppenheimer, C.M.M., 1989. AVHRR volcano hotspot monitoring. Procs. 4th AVHRR data users' meeting, Rothenburg, FRG, 3-5th September, 1989, 335-338. Appendix A5 - this thesis.

Oppenheimer, C., 1991a. Sulphur eruptions at Volcán Poás, Costa Rica. *J. Volcanol. Geotherm. Res.*, in press. Appendix A7 - this thesis.

Oppenheimer, C., 1991b. Lava flow cooling estimated from Landsat Thematic Mapper data: the Lonquimay eruption, Chile, 1989. *J. Geophys. Res.*, in press. Chapter 2 - this thesis.

Oppenheimer, C.M.M., and Rothery, D.A., 1991. Infrared monitoring of volcanoes by satellite. *J. Geol. Soc. Lond.*, 148, 563-569. Chapter 3 - this thesis.

Oppenheimer, C., and Stevenson, D., 1989. Liquid sulphur lakes at Poás volcano. *Nature*, 342, 790-793. Appendix A6 - this thesis.

Ormsby, J.P., and Soffen, G.A., 1989. Foreword to special volume on the Earth Observing System. *IEEE Trans. Geosci. Remote Sens.*, 27, 107-108.

Otto, G.P, and Chau, T.K.W., 1989. Region-growing algorithms for matching of terrain images. *Image Vision Comput.*, 7(2), 83-94.

Park, S., and Iversen, J.D., 1984. Dynamics of lava flow: thickness growth characteristics of steady two-dimensional flow. *Geophys. Res. Lett.*, 11, 641-644.

Peale, S.J., Cassen,P., and Reynolds, R.T., 1979. Melting of Io by tidal dissipation. *Science*, 203, 892-894.

Pearl, J.C., and Sinton, W. M., 1982. Hot spots of Io. In Satellites of Jupiter (D. Morrison, Ed.), Univ. Arizona Press, Tucson, 724-755.

Pieri, D.C., and Baloga, S.M., 1986. Eruption rate, area and length relationships for some Hawaiian lava flows. *J. Volcanol. Geotherm. Res.*, 30, 29-45.

Pieri, D.C., and Glaze, L.S., 1989. Orbiting Volcano Observatory (OVO): a new "small mission" ? *Eos, Trans. Am. Geophys. Union*, 70(43), 1410.

Pieri, D.C., Baloga, S., Nelson, R. and Sagan, C., 1984. Sulfur flows of Ra Patera, Io. *Icarus*, 60, 685-700.

Pieri, D.C, Glaze, L.S., and Abrams, M.J., 1990. Thermal radiance observations of an active lava flow during the June 1984 eruption of Mount Etna. *Geology*, 18, 1018-1022.

Pieri, D.C., Gillespie, A.R., Kahle, A.B., Kahle, J., and Baloga, S.M., 1985. Thermal infrared observations of lava flows during the 1984 Mauna Loa eruption. In Reports of Planetary Geology and Geophysics Program; 1984, NASA Technical Memorandum, 87563, 251-255.

Pollack, J.B., Toon, O.B., and Khare, B.N., 1973. Optical properties of some terrestrial rocks and glasses. *Icarus*, 19, 372-389.

Pontual, A., 1990. Lithological information in remotely sensed images and surface weathering in arid regions, unpublished PhD thesis, The Open University, UK, 421pp.

Prata, A.J., 1989. Observations of volcanic ash clouds in the 10-12 μm window using AVHRR/2 data. *Int. J. Remote Sens.*, 10(4 & 5) 751-761.

Prata, A.J.F., Cechet, R.P., Barton, I.J., and Llewellyn-Jones, D.T., 1990. The Along Track Scanning Radiometer for ERS-1 - Scan geometry and data simulation. *IEEE Trans. Geosci. Remote Sens.*, 28(1), 3-13.

Rampino, M.R., Self, S., and Stothers, R.B., 1988. Volcanic Winters. *Ann. Rev. Earth Planet. Sci.*, 16, 73-99.

Robinson, J.M., 1991, Fire from space: global fire evaluation using infrared remote sensing. *Int. J. remote. Sens.*, 12(1), 3-24.

Robock, A., and Matson, M., 1983. Circumglobal transport of the el Chichón volcanic dust cloud. *Science*, 221, 195-197.

Rothery, D.A., 1989. A re-interpretation of Landsat TM data on Chernobyl. *Int. J. Remote Sens.*, 10(8), 1423-1427.

Rothery, D.A., and Oppenheimer, C., 1991. Monitoring volcanoes using short wavelength infrared images, Procs. 5th Int. Coll. Physical Measurements and Signatures in Remote Sensing, Courchevel, France, 14-18 January 1991, ESA SP-319, 513-516.

Rothery, D.A., and Oppenheimer, C., in press. Monitoring Mount Erebus by satellite. Antarctic Research Series, American Geophysical Union, Washington DC.

Rothery, D.A., Francis, P.W., and Wood, C.A.., 1988. Volcano monitoring using short wavelength infrared data from satellites. *J. Geophys. Res.* 93, 7993- 8008.

Rothery, D.A., Oppenheimer, C.M.M., Borgia, A., Glaze, L.S., and Pieri, D.C., 1990. Short wavelength infrared observations of an active blocky lava flow, Volcán Arenal, Costa Rica. IAVCEI International Volcanological Congress, Mainz, Germany, 3-8 September 1990, abstract volume.

Rowland, S.K., and Walker, G.P.L., 1990. Pahoehoe and aa in Hawaii: volumetric flow rate controls the lava structure. *Bull. Volcanol.*, 52, 615-628.

Sabroux, J.C., Villevieille, A., Dubois, E., Doyotte, C., Halbwachs, M., and Vandemeulebrouck, J., 1990. Satellite monitoring of the vertical temperature profile of Lake Nyos, Cameroon. *J. Volcanol. Geotherm. Res.*, 42, 381-384.

Sagan, C., 1979. Sulphur flows on Io. *Nature*, 280, 750-753.

Salomonson, V. V., Barnes, W. L., Maymon, P. W., Montgomery, H. E., and Ostrow, H., 1989. MODIS: Advanced facility instrument for studies of the Earth as a system. *IEEE Trans. Geosci. Remote Sens.*, 27, 145-153.

Sawada, Y., 1983. Analysis of eruption clouds by the 1981 eruptions of Alaid and Pagan volcanoes with GOES images. *Pap. Meteorol. Geophys.*, 34, 307-324.

Schowengerdt, R.A., Archwamety, C., and Wrigley, R.C., 1985. Landsat Thematic Mapper image-derived MTF. *Photogramm. Eng. Remote Sens.*, 51(9), 1395-1406.

Scorer, R.S., 1986. Etna: the eruption of Christmas 1985 as seen by meteorological satellite. *Weather*, 41(12), 378-385.

Singh, S.M., 1988. Brightness temperature algorithms for Landsat Thematic Mapper data. *Remote Sens. Environ.*, 24, 509-512.

Sinton, W.M., 1981. The thermal emission spectrum of Io and a determination of the heat flux from its hot spots. *J. Geophys. Res.*, 86, 3122-3128.

Smithsonian Institution, 1988. Lascar. *Scientific Event Alert Network Bull.*, 13(8), 9.

Smithsonian Institution, 1989a. Lonquimay Volcano. *Scientific Event Alert Network Bull.*, 14(2), 12-15.

Smithsonian Institution, 1989b. Lascar. *Scientific Event Alert Network Bull.*, 14(3), 12.

Smithsonian Institution, 1989c. Momotombo. *Scientific Event Alert Network Bull.*,14(4), 11.

Smithsonian Institution, 1989d. Lascar. *Scientific Event Alert Network Bull.*, 14(6), 13.

Smithsonian Institution, 1989e. Lonquimay Volcano. *Scientific Event Alert Network Bull.*, 14(9), 6-8.

Smithsonian Institution, 1989f. Lonquimay Volcano. *Scientific Event Alert Network Bull.*, 14(12), 14-15.

Smithsonian Institution, 1989g. Lascar. *Scientific Event Alert Network Bull.*, 14(11), 14-16.

Smithsonian Institution, 1990a. Lascar. *Bull. Global Volcanism Network*, 15(2), 7-8.

Smithsonian Institution, 1990b. Lascar. *Bull. Global Volcanism Network*, 15(3), 15.

Smithsonian Institution, 1990c. Lonquimay. *Bull. Global Volcanism Network*, 15(3), 15-16.

Smithsonian Institution, 1990d. Lascar. *Bull. Global Volcanism Network*, 15(4), 11-12.

Smithsonian Institution, 1991a. Lascar. *Bull. Global Volcanism Network*, 16(1), 3.

Smithsonian Institution, 1991b. Pinatubo. *Bull. Global Volcanism Network*, 16(5), 2-8.

Sparks, R.S.J., Moore, J.G., and Rice, C.J., 1986. The initial giant umbrella cloud of the May 18th, 1980, explosive eruption of Mount St. Helens. *J. Volcanol. Geotherm. Res.*, 28, 257-274.

Spencer, J.R., Shure, M.A., Ressier, M.E., Goguen, J.D., Sinton, W.M., Toomey, D.W., Denault, A., and Westfall, J., 1990. Discovery of hotspots on Io using disk-resolved infrared imaging. *Nature*, 348, 618-621.

Spencer, J.R., Sinton, W., Oppenheimer, C., and Kaminski, C., 1991. High-temperature volcanic thermal emission: from Io to the Andes. 23rd Ann. Meeting of the Division for Planetary Sciences of the American Astronomical Society, Palo Alto, California, 4-8 November, 1991, abstract volume, in press.

Swanson, D.A., and Holcomb, R.T., 1990. Regularities in growth of the Mount St. Helens dacite dome, 1980-1986. In *The Emplacement of Silicic Domes and Lava Flows, IAVCEI Proceedings in Volcanology*, vol. 2, edited by J.H. Fink, p. 3-24, Springer-Verlag, New York, 1990.

Tabbagh, A., Tabbagh, J., and Dechambenoy, C., 1987. Mapping of the surface temperature of Mount Etna and Vulcano Island using an airborne scanner radiometer. *J. Volcanol. Geotherm. Res.*, 34, 79-88.

Taylor, G.A.M., 1983, The 1951 eruption of Mt. Lamington, Papua. Bull. Bur. Min. Res. Geol. Geophys, 38, Canberra, 129 pp.

Tedesco, D., Toutain, J.P., Allard, P., and Losno, R., 1991. Chemical variations in fumarolic gases at Vulcano Island (Southern Italy): seasonal and volcanic effects. *J. Volcanol. Geotherm. Res.*, 45, 325-334.

Tilling R.I., 1989. Volcanic hazards and their mitigation: progress and problems. *Rev. Geophys.*, 27(2), 237-269.

Tucker, C.J., and Matson, M., 1985. Determination of volcanic ash deposition from El Chichón using ground and satellite data. *Int. J. Remote Sens.*, 6(5), 619-627.

U.S. Geological Survey., 1990. The eruption of Redoubt volcano, Alaska, December 14, 1989 - August 31, 1990. Ed. S.R. Brantley, U.S. Geol Survey Circular, 1061, Washington 1990, 33pp.

Walter, L.S., and Salisbury, J.W., 1989. Spectral characterization of igneous rocks in the 8- to 12-μm region. *J. Geophys. Res.*, 94, 9203-9213.

Wan, Z., and Dozier, J., 1989. Land-surface temperature measurement from space: physical principles and inverse modelling. *IEEE Trans. Geosci. Remote Sens.*, 27(3), 268-277.

Wiesnet, D.R., and D'Aguanno, J., 1982. Thermal imagery of Mount Erebus from the NOAA-6 satellite. *Antarctic J. U.S.*, 17, 32-34.

Williams, R.S. Jr, and Friedman, J.D., 1970. Satellite observation of effusive volcanism. *J. Brit. Interplan. Soc.*, 23, 441-450.

Wilson, L., Sparks, R.S.J., Huang, T.C., and Watkins, N.D., 1978. The control of volcanic column heights by eruption energetics and dynamics. *J. Geophys. Res.*, 83, 1829-1836.

Young, A.T., 1984. No sulfur flows on Io. *Icarus*, 58, 197-226.

Young, P., and Wadge, G., 1990. Flowfront: simulation of a lava flow. *Computers Geosci.*, 16(8), 1171-1191.

Appendix A1. Acronyms and Abbreviations

AMRIR	Advanced Medium Resolution Imaging Radiometer
ASTER	Advanced Spaceborne Thermal Emission and reflection Radiometer
ATSR	Along Track Scanning Radiometer
AVHRR	Advanced Very High Resolution Radiometer
AVIRIS	Airborne Visible Infrared Imaging Spectrometer
CC	Cubic Convolution
CCD	Charged Coupled Device
CCT	Computer Compatible Tape
COSPEC	Correlation Spectrometer
DEM	Digital Elevation Model
DN	Digital Number
EOS	Earth Observing System
EOSAT	Earth Observation Satellite Company
EOSDIS	EOS Data and Information System
ERS-1	European Remote Sensing Satellite-1
ESA	European Space Agency
ETM	Enhanced Thematic Mapper
HIRIS	High Resolution Imaging Spectrometer

HRPT	High Resolution Picture Transmission
HRV	High Resolution Vidicon
IAVCEI	International Association of Volcanology and Chemistry of the Earth's Interior
IDNDR	International Decade for Natural Disaster Reduction
IFOV	Instantaneous Field Of View
INETER	Instituto Nicaraguense de Estudios Territoriales (Nicaragua)
IRIS	Infrared Interferometer Spectrometer (Voyager)
ITIR	Intermediate Thermal Infrared Radiometer
JERS-1	Japanese Earth Resources Satellite-1
JPL	Jet Propulsion Laboratory (US)
Landsat	Land Remote Sensing Satellite
LFC	Large Format Camera
LOWTRAN	LOWTRAN atmospheric transmittance computer code
MAC	Multispectral Airborne Campaign
MODIS	Moderate resolution Imaging Spectrometer
MSS	Multi Spectral Scanner
NASA	National Aeronautics and Space Administration (US)
NASDA	National Space Development Agency of Japan
NERC	Natural Environment Research Council (UK)
NN	Nearest Neighbour
NOAA	National Oceanic and Atmospheric Administration (US)
OPS	Optical Sensor
OVO	Orbiting Volcano Observatory
POEM	Polar Orbit Earth observation Mission
SPOT	Systeme pour l'Observation de la Terre
SWIR	Short Wavelength Infrared
TIR	Thermal Infrared
TM	Thematic Mapper
TMS	Thematic Mapper Simulator (NS001)
TOMS	Total Ozone Mapping Spectrometer

UN	United Nations
UV	Ultraviolet
VEXUVIO	Volcano Experimental Ultraviolet and Infrared Observatory
VNIR	Visible and Near Infrared

Appendix A2. Notation

Symbol	Quantity	Value / SI units
α	cubic expansivity	K^{-1}
α_λ	sensor gain in band λ	$W\ m^{-3}\ sr^{-1}\ DN^{-1}$
b	Wien's constant	2.89782×10^{-3} m K
β_λ	sensor offset in band λ	$W\ m^{-3}\ sr^{-1}$
c	speed of light	2.99×10^{8} m s^{-1}
c_1	first radiation constant	3.74127×10^{-16} W m^2
c_2	second radiation constant	1.4388×10^{-2} m K
c_p	specific heat capacity	J kg^{-1} K^{-1}
$\delta(x)$	thickness of boundary layer	m
DN_λ	digital count in band λ	DN
$DN_{\lambda,non\text{-}thermal}$	digital count of non-thermal radiance	DN
$DN_{\lambda,thermal}$	digital count of thermal radiance	DN
ΔT	temperature excess	K
ε_λ	spectral emissivity in band λ	------
f	fractional surface area of thermal component	------
g	acceleration of freefall	9.80 m s^{-2}
Gr	Grashof number	------

Symbol	Quantity	Value / SI units
η	dynamic viscosity	N s m^{-2}
h	Planck's constant	6.62 x 10^{-34} J s
$H(\lambda,T)$	spectral radiant emittance	------
k	Boltzmann constant	1.38 x 10^{-23} J K^{-1}
k	thermal conductivity	W m^{-1} K^{-1}
L	length scale	m
$L(\lambda,T)$	spectral radiance (spectral radiant emittance)	W m^{-3} sr^{-1}
λ	wavelength	m
λ_{max}	wavelength of peak spectral radiance	m
Nu	Nusselt number	------
Pr	Prandtl number	------
Q_{cond}	conductive heat flux	W
Q_{conv}	convective heat flux	W
Q_{rad}	radiant heat flux (total radiant exitance)	W
ρ	density	kg m^{-3}
ρ_λ	spectral reflectivity in band λ	------
R_λ	at-sensor spectral radiance in band λ	W m^{-3} sr^{-1}
$R_{\lambda,D}$	downwelling spectral radiance	W m^{-3} sr^{-1}
$R_{\lambda,non\text{-}thermal}$	spectral radiance of non-thermal origin	W m^{-3} sr^{-1}
$R_{\lambda,thermal}$	spectral radiance of thermal origin	W m^{-3} sr^{-1}
$R_{\lambda,U}$	upwelling spectral radiance	W m^{-3} sr^{-1}
S	surface area	m^2
σ	Stefan-Boltzmann constant	5.67 x 10^{-3} W m^{-2} K^{-4}
T	thermodynamic temperature	K
T_b	temperature of background component	K
T_c	temperature of hotter component	K
T_e	effective radiation temperature	K
T_s	temperature of cooler component	K
τ_λ	spectral transmissivity in band λ	------

Appendix A3. BASIC programmes to calculate sub-pixel temperatures from Landsat TM data

---

The following programmes were written on a Macintosh computer in Microsoft BASIC Binary Version 2.00. In each case, the algorithms require DN, corrected for reflected sunlight and any other contamination, in Landsat TM bands 5 and 7 for each pixel to be analysed. The first programme calculates T_c and f by solution of the dual-band equations 1.7 and 1.8 (Chapter 1). This is achieved by incrementing or decrementing f until the determined value of T_c is approximately equal for each band. The second calculates the coexisting value of f and T_s, given a predetermined value for T_c, using a slightly different algorithm. In both cases, an error message appears if the temperatures in each spectral band do not converge.

A3.1. Programme to determine T_c

```
0 REM          **********TM.Tc**********
5 REM Programme calculates pixel integrated and dual band temperatures
10 REM for Landsat TM bands 5 and 7 assuming a value for Tc.  CMMO Dec 1988.

15 REM Set up constants and variables

20 REM Emissivities
25 E5=.95
30 E7=.95

35 REM Transmission coefficients
40 TORR5=.987
```

```
45 TORR7=.979

50 REM Constants in Planck's law
55 C1=3.74127E-16
60 C2=.014388

65 REM Central wavelengths (m) in TM bands 5 & 7
70 LAMBDA5=1.65E-06
75 LAMBDA7=2.22E-06

80 REM Variables in iteration process; other constants
85 F=1
90 P=0.01
95 PI=3.1415927

115 REM Get corrected DN in each band
120 INPUT "What is DN in band 5";DN5
125 INPUT "What is DN in band 7";DN7

130 PRINT "DN in band 5 is ";DN5;", and DN in band 7 is ";DN7
135 PRINT "Emissivities are ";E5;" in band 5, and ";E7;" in band 7"
140 PRINT "Transmissivities are ";TORR5;" in band 5, and ";TORR7;" in band 7"
145 PRINT "Temperature of hot source, Tc = ";TC-273.15;"°C"

150 REM Calculate at-sensor radiance using calibration data (Markham & Barker, 1987)
155 R5=(DN5/255)*2.756-.037
160 R7=(DN7/255)*1.452-.014

165 REM Check that DN sufficiently high
170 IF R5<=0 THEN PRINT "DN in band 5 too low": GOTO 235
175 IF R7<=0 THEN PRINT "DN in band 7 too low": GOTO 235

180 REM Inverse Planck function
185 T5=C2/(LAMBDA5*LOG(1+((C1*F*LAMBDA5^-
5)/(PI*1E+07*R5/(TORR5*E5)))))
190 T7=C2/(LAMBDA7*LOG(1+((C1*F*LAMBDA7^-
5)/(PI*1E+07*R7/(TORR7*E7)))))

195 REM  PRINT PIXEL INTEGRATED TEMPS
200 IF F=1 THEN PRINT "Pixel integrated temperatures are ";(INT(10*(T5-
273.15)))/10;"°C  in band 5, and ";(INT(10*(T7-273.15)))/10;"°C in band 7"

205 REM Iteration to find dual band solution
210 IF ABS(T5-T7)<.00001 THEN 230
215 IF T7>T5 THEN F=F+P: P=P/10: GOTO 185
220 F=F-P: IF F<=0 THEN PRINT "Solution does not converge": GOTO 235
225 GOTO 185

230 PRINT"Dual-band temperature, Tc = ";(INT(10*((T5+T7)/2-273)))/10;"°C, for
fraction ";F;"of pixel"

235 END
```

A3.2. Programme to determine T_s

```
0 REM          **********TM.Ts**********
5 REM Programme calculates pixel integrated and dual band temperatures
10 REM for Landsat TM bands 5 and 7 assuming a value for Tc.  CMMO March 1991.
```

```
15 REM Set up constants and variables

20 REM Emissivities
25 E5=.95
30 E7=.95

35 REM Transmission coefficients
40 TORR5=.987
45 TORR7=.979

50 REM Constants in Planck's law
55 C1=3.74127E-16
60 C2=.014388

65 REM Central wavelengths (m) in TM bands 5 & 7
70 LAMBDA5=1.65E-06
75 LAMBDA7=2.22E-06

80 REM Variables in iteration process; other constants
85 FMAX=1
90 FMIN=0
95 PI=3.1415927

100 REM Get temperature of hot source, Tc, (K)
105 INPUT"What is chosen Tc (°C)";TC
110 TC=TC+273.15

115 REM Get corrected DN in each band
120 INPUT "What is DN in band 5";DN5
125 INPUT "What is DN in band 7";DN7

130 PRINT "DN in band 5 is ";DN5;", and DN in band 7 is ";DN7
135 PRINT "Emissivities are ";E5;" in band 5, and ";E7;" in band 7"
140 PRINT "Transmissivities are ";TORR5;" in band 5, and ";TORR7;" in band 7"
145 PRINT "Temperature of hot source, Tc = ";TC-273.15;"°C"

150 REM Calculate at-sensor radiance using calibration data (Markham & Barker, 1987)
155 R5=(DN5/255)*2.756-.037
160 R7=(DN7/255)*1.452-.014

165 REM Check that DN sufficiently high
170 IF R5<=0 THEN PRINT "DN in band 5 too low": END
175 IF R7<=0 THEN PRINT "DN in band 7 too low": END

180 REM Calculate pixel-integrated temperatures
185 TINT5=C2/(LOG(1+C1*LAMBDA5^-
5/(PI*1E+07*R5/(TORR5*E5)))*LAMBDA5)
190 TINT7=C2/(LOG(1+C1*LAMBDA7^-
5/(PI*1E+07*R7/(TORR7*E7)))*LAMBDA7)
195 IF TINT7>TINT5 THEN GOTO 300

200 REM Begin iteration

205 F=.5*(FMAX+FMIN)
210 L5=1+(1-F)*C1*LAMBDA5^-5/((PI*1E+07*R5/(TORR5*E5))-
F*C1*LAMBDA5^-5/(EXP(C2/(LAMBDA5*TC))-1))
215 L7=1+(1-F)*C1*LAMBDA7^-5/((PI*1E+07*R7/(TORR5*E7))-
F*C1*LAMBDA7^-5/(EXP(C2/(LAMBDA7*TC))-1))
220 IF L5<=0 THEN FMAX=.5*(FMAX+FMIN): GOTO 205
225  IF L7<=0 THEN FMAX=.5*(FMAX+FMIN): GOTO 205
```

```
230 REM Calculate Ts in each band
235 T5=C2/(LOG(L5)*LAMBDA5)
240 T7=C2/(LOG(L7)*LAMBDA7)

245 REM Are temperatures in each band approximately equal ?
250 IF ABS(T5-T7)<.001 THEN GOTO 280

255 IF ABS(FMIN-FMAX)<.000000001# THEN GOTO 320
260 IF F<.0000001 THEN GOTO 320
265 IF F> .999999 THEN GOTO 320
270 IF T7>T5 THEN FMAX=F: GOTO 205
275 FMIN=F: GOTO 205

280 REM Print solution of Ts
285 PRINT"Background temperature, Ts = ";(INT(10*((T5+T7)/2-273.15)))/10;"°C"
290 PRINT"when the hot component, Tc, occupies a fraction ";INT(1E+07*F)/1E+07;"
of the pixel"
295 GOTO 325

300 PRINT"Pixel integrated temp in band 7 exceeds that in band 5. If substantial"
305 PRINT"difference, check if correction to band 5 overestimated."
310 PRINT"Pixel integrated temperatures are ";TINT5-273.15;" °C in band 5, and
";TINT7-273.15;" °C in band 7"
315 GOTO 325

320 PRINT "Solution does not converge"


325 END
```

Appendix A4. Láscar pixel maps

Landsat TM images have been recorded over volcán Láscar, Chile, on fourteen dates between December 1984 and January 1991 (Chapter 5). The raw pixel data (no corrections applied) are presented below for each. For each image, pixel DN are given in blocks representing bands 7, 5 and 4 (in that order), excepting night-time scenes for which only DN in bands 7 and 5 are given (again, in that order). Rows and columns are as on the original images, i.e. north is approximately up the page in each case unless indicated otherwise. The title for each set of files provides the local recording date of that image, the 10-digit scene identification number, and the CCT format (CC, NN or A). The first digit of the scene ID indicates either Landsat 4 or Landsat 5.

A4.1. December 24, 1984 (5029814010, CC)

63	61	53	58	64	69	66	54	51	45	47	37
62	60	57	76	126	164	122	78	53	49	55	51
64	62	70	107	205	255	255	255	118	66	50	46
69	63	89	177	255	255	255	255	250	70	52	52
254	253	252	251	255	255	255	255	255	107	47	46
92	88	137	249	255	255	255	255	255	93	46	51
52	61	83	163	255	255	255	255	180	78	41	36
54	68	68	119	193	177	144	125	77	54	38	37
54	62	68	84	90	78	56	45	46	38	32	34
52	52	56	57	52	49	41	40	43	33	35	30

92	90	67	64	72	67	58	49	48	53	63	55
99	90	75	76	85	92	83	61	38	54	67	64
105	92	91	93	119	209	255	209	26	57	60	64
101	87	111	136	120	196	255	237	125	29	47	64
89	87	119	178	228	251	255	232	107	37	43	60
87	84	102	186	233	251	255	233	128	41	39	56
92	91	106	149	167	174	239	254	91	44	44	49
79	84	105	125	132	114	114	111	61	56	48	46
79	81	89	102	101	74	53	47	57	53	49	49
77	80	78	82	80	66	53	53	56	47	47	44
72	73	73	75	76	75	74	74	71	70	71	73
72	73	74	74	75	75	76	77	77	76	75	75
70	71	71	70	70	71	74	74	76	77	76	75
69	70	70	69	69	69	70	71	72	73	73	72
69	70	70	70	69	70	69	68	68	68	69	70
70	70	70	71	70	70	70	68	67	68	69	70
71	71	70	71	70	70	70	72	70	71	73	74
70	70	70	70	68	69	71	74	75	75	75	77
70	70	70	69	68	69	73	75	78	76	74	73
70	69	69	68	69	69	73	74	72	70	69	69

A4.2. March 14, 1985 (5037814011, CC)

51	40	40	41	31	27	23	20	27	36
52	47	48	50	68	51	12	10	24	32
52	54	52	67	92	169	154	52	12	24
59	60	81	110	173	255	255	121	14	15
74	84	134	196	255	255	255	163	36	9
84	93	129	240	246	255	255	167	35	14
70	77	88	159	167	220	231	120	32	17
68	72	70	79	81	98	105	68	37	28
66	70	70	82	76	54	40	44	44	35
64	67	64	66	68	54	43	46	39	30
83	68	60	62	50	46	37	34	42	58
92	77	73	76	68	46	15	17	28	50
98	86	85	86	80	91	78	24	19	31
101	102	102	101	99	190	180	57	11	17
102	123	134	135	115	255	231	86	16	12
111	123	140	149	113	224	248	101	25	17
109	119	128	129	126	104	152	103	37	26
108	121	130	121	109	93	80	67	57	44
103	104	117	120	103	82	69	72	67	60
104	107	101	112	106	86	67	73	63	50
74	62	53	53	49	40	29	27	37	46
80	71	64	64	51	38	22	16	25	39
82	77	71	69	64	45	20	12	21	33
84	91	87	78	74	55	24	12	11	15
84	96	102	77	65	52	39	25	12	16
90	98	111	82	69	65	53	35	17	18
88	99	116	103	83	75	65	46	28	22
77	97	110	100	86	75	64	55	52	43
82	81	90	94	89	70	59	63	58	49
79	83	82	88	86	72	57	54	52	42

A4.3. July 20, 1985 (5050614004, CC)

		6	7	7	8	6	6	
7	3	9	30	55	35	7	8	10
7	4	18	0	117	227	57	0	8
1	19	38	109	241	235	73	14	8
7	22	61	131	255	241	57	9	7
41	40	59	79	109	123	70	8	12
56	57	66	68	42	46	60	30	27
53	54	64	67	50	38	39	40	28

		6	7	10	10	9	10	
8	9	8	13	14	10	10	9	13
9	5	9	1	30	51	25	6	13
11	9	20	16	103	105	15	10	12
19	6	19	23	97	87	14	9	9
76	60	63	63	66	56	29	11	15
101	113	115	97	73	64	56	49	47
88	95	110	108	89	73	69	70	53
		9	9	9	10	11	11	
7	9	9	9	9	9	11	11	15
7	9	10	9	9	9	11	11	11
8	7	7	8	8	9	10	11	11
26	9	13	19	20	11	9	11	10
70	51	55	59	54	35	18	19	19
92	111	105	80	68	64	52	51	48
70	83	96	94	81	67	62	62	61

A4.4. January 12, 1986 (5068213581, NN)

89	93	100	121	64	25	28
93	142	73	251	255	56	24
90	125	78	89	255	110	19
126	134	62	187	128	47	23
132	142	128	89	47	47	38
170	170	131	135	162	82	39
169	135	114	114	145	128	39
168	114	114	143	130	80	41
94	91	92	72	39	36	49
111	112	103	90	71	34	32
123	114	106	87	82	56	27
127	114	127	84	85	64	29

A4.5. August 8, 1986 (5089013524, NN)

22	6	5	4	5	4	4	5	8	11
17	5	22	10	4	4	8	8	8	5
22	11	8	9	11	14	20	20	21	5
34	14	10	36	30	28	28	55	42	0
39	31	25	53	42	30	53	53	29	3
48	13	10	11	7	10	9	10	9	14
43	21	6	11	15	25	22	13	11	12
66	40	10	44	65	43	44	29	7	12
71	63	45	83	87	51	61	40	11	14
77	89	77	90	75	69	63	42	28	27
35	7	11	11	11	11	11	11	13	15
34	11	11	12	12	15	15	13	12	13
43	12	12	23	43	43	43	16	12	12
62	27	40	76	62	48	48	39	17	12
73	62	69	74	62	62	65	58	21	13

A4.6. October 27, 1986 (5097013500, CC)

			53	59	54	54	44	45	29	20	34	40	37	30
						46	40	36	80	95	44	29	35	33
			54	54	51	78	80	14	168	244	114	8	33	33
			54	52	60	119	120	55	167	195	9	5	30	
				54	73	105	100	131	103	38	17	17	21	
				56	71	70	78	183	161	81	36	18	17	
		45	52	63	66	92	80	203	255	151	41	20	16	
			48	53	60	85	65	46	135	115	39	24	37	.
			56	45	48	68	67	50	41	44	45	33		
	55	55	80	59	52	63	64	54	46	41				
		56	53	57	59	59	56							
60	56	52	78	91	49	49	45							
	58	54	59	63	42	39	38							
		51	52	48	45									
			80	83	79	75	70	62	60	54	57	56	59	47
						74	69	59	55	43	39	51	54	52
			88	85	80	83	79	61	82	165	65	37	49	54
			90	86	89	102	101	77	99	186	69	22	46	
				88	98	106	106	90	74	48	36	25	29	
				92	103	94	97	103	100	77	61	38	18	
		77	81	94	101	106	110	127	152	86	67	44	25	
			85	91	99	119	101	81	89	81	64	44	39	
			86	78	88	115	106	79	74	83	71	57		
	84	89	97	85	87	109	103	86	79	75				
		84	82	81	91	101	97							
90	86	83	96	113	88	86	80							
	88	82	86	90	76	68	68							
		78	76	75	73									
			63	66	61	58	55	53	51	49	48	48	49	44
						61	56	51	47	41	42	45	48	48
			78	77	69	69	64	56	45	28	29	45	51	50
			87	78	76	73	77	73	59	31	18	29	54	
				81	84	87	85	74	67	58	31	20	38	
				84	87	85	89	70	60	61	49	24	21	
		80	79	84	84	79	86	74	61	58	59	41	21	
			90	91	88	92	84	78	69	65	58	40	30	
			89	77	90	103	82	71	71	70	60	51		
	70	72	81	71	82	92	85	81	72	66				
		68	78	92	81	83	86							
64	63	63	73	91	83	78	75							
	64	62	64	67	70	71	71							
		61	59	57	58									
61	59	57	58											

A4.7. November 12, 1986 (5098613492, A)

	36	34	37	34	30	28
42	44	32	87	134	32	34
60	56	51	58	46	30	29
50	48	50	47	41	32	27
51	61	112	131	38	36	29
54	51	50	70	48	30	30
	58	53	52	50	50	50
66	66	60	61	81	49	53
71	78	71	63	58	48	48
80	77	73	68	66	53	45
80	81	82	81	68	58	49
84	80	74	69	62	56	47

	79	78	78	75	82	98
80	76	72	69	66	68	73
85	85	81	73	62	64	71
90	90	87	81	73	63	65
88	91	82	76	76	67	61
85	91	82	78	73	69	64

A4.8. November 12, 1986 (5098613492, NN)

36	34	37	34	30	30
44	32	87	87	134	32
55	55	51	58	46	30
48	50	47	47	41	32
51	61	113	131	38	36
54	51	50	70	48	30

58	53	52	50	50	50
66	60	61	81	48	53
78	71	63	58	48	48
77	73	68	66	53	45
81	82	82	81	61	58
80	74	74	69	62	56

79	79	78	78	75	82
76	76	72	69	66	68
85	85	81	73	62	64
85	85	81	73	62	64
90	90	86	81	73	63
88	91	82	76	76	67

A4.9. November 23, 1987 (4195613522, CC)

46	79	130	136	130	130	64	28	30
55	133	255	255	255	245	124	41	30
89	180	255	255	255	255	223	104	39
120	210	255	255	255	255	203	134	71
107	140	238	241	251	255	161	96	52
78	85	98	127	204	239	153	54	25

100	86	100	90	83	73	52	46	55
95	117	180	169	167	130	66	34	43
122	157	179	196	226	198	129	64	40
154	174	205	255	255	255	156	83	46
147	153	199	214	247	250	146	79	48
120	120	125	135	158	163	129	69	44

100	95	90	79	79	62	28	38	60
103	112	115	104	92	86	62	37	43
115	124	120	107	88	84	85	55	39
129	128	108	107	108	94	87	71	39
117	116	107	108	117	106	88	71	42
98	114	111	96	105	98	86	53	53

A4.10. November 23, 1987 (4195613522, NN)

64	53	63	75	73	67	84	84	49	31	35
68	51	130	255	255	255	255	173	49	35	33
62	67	145	255	255	255	255	255	174	56	34
75	113	219	255	255	255	255	255	171	107	53
71	106	129	255	255	255	255	144	144	92	49
70	81	89	109	148	148	226	226	109	39	31
70	60	69	83	84	80	83	60	60	47	39

```
100 104  80  75  75  67  64  61  53  56  59
111  94 115 175 175 144 138  89  39  41  53
107 110 146 175 182 208 208 155  93  47  47
105 143 170 200 255 255 255 255 114  73  41
114 145 150 200 221 255 255 255 113  72  43
113 120 120 126 134 157 155 112 112  55  47
113 120 120 126 134 157 155 112 112  55  47

 87 103  87  71  65  57  55  46  52  59  54
102 108  92  88  74  70  66  30  37  61  63
113 103 103 109 104  92  90  62  38  43  76
101 103 118 120 114  93  82  87  56  41  48
 97 117 133 114 107 108  94  88  70  38  48
105 114 117 111 105 117 109  91  72  41  53
112  97 106 117  97 104 109  91  72  41  53
```

A4.11. October 27, 1989 (4266014040, A)

```
 59  74 129  72  59  56  64

        67  61  80 102  86  69  61
    59  73  69 103 113 255 255 120  79  70  57
    64  83  76 171 255 255 255 255 255 132  74
 65  81  82  89 249 255 255 255 255 178 161  90
 68  76  73  97 158 255 255 255 165 102  86  54
134 132  68  93 144 255 255 255 110  92  65  54
 81 108  67  72 101  95 101 104  78  49  39
 65  68  60  55  65  61  59  65  59  49

 84  95  95  85  76  77  87

        83  79  82  96  92  82  79
    92  99  82  95 104 219 171  87  80  95  82
  - 98 107  97 124 255 255 210 119 130 110 101
 93 117 107 100 141 255 255 249 163 104 112  95
 89 112 111 112 131 255 255 138 121  99  93  79
102 109  99 122 131 152 150 137 106 101  81  84
 90  97  95 114 124 108 110 109  82  66  65
 90  96  86  87 108  87  78  91  86  68

 69  66  64  63  59  67  74

        61  64  74  69  66  66  69
    77  69  67  78  74  71  67  69  72  89  76
    78  77  73  72  77  72  69  70  74  86  79
 74  78  74  75  83  82  78  77  79  67  82  77
 67  75  78  84  87  85  89  84  88  78  78  87
 62  75  86  98  95  92  91  82  81  71  88  96
 56  73  92 103  95  83  86  84  66  62  75
 65  68  60  55  65  61  59  65  59  49
```

A4.12. November 17, 1989 (4268202312, A, night-time, north is down)

```
                    11   6   8
            10   6   6   6  10   9   9   9
                11  10  10  15   5  10  12
            12   9  11  12  13  13  12  11
                12  19  23  22  18  15  14  11  10
        10  16  19  22  40  35  36  36  17  12
 8  21   7  14  51  49 168 255 106 121  36  25  10  17  24
 8  21  13  21  34 102 255 255 255 255 113  48  25  26  63
        11  15  34 159 255 255 255 255  59  39  17  15  16
            10  37  96 255 255 255 104  41  23  14  13
                    21  47 120 117  97  39  18  12   9
            9   9  15  31  27  24  22  14  11   9
                9   9   9  12  19  19  14  13   8           8
                    8  10   8  11  12  63  17
                               13  30
```

					5	3	5							
			5	4	5	5	4	6	5	5				
				5	6	5	5	5	5	5				
			4	5	7	5	7	6	7	6				
				6	7	6	7	9	7	5	5	5		
		6	6	6	8	13	14	12	11	9	5			
4	5	6	6	6	8	13	14	12	11	9	5	7	5	5
3	7	5	7	9	22	255	255	255	93	36	18	12	9	16
		5	6	8	30	255	255	255	106	29	24	13	2	8
			7	19	28	173	224	58	22	16	7	7	5	
					10	17	31	31	25	12	10	4	7	
			4	6	7	12	10	10	8	7	6	5		
				5	4	5	7	7	7	5	5	6		6
					5	4	6	5	5	14	6			
									6	7				

A4.13. November 28, 1989 (4269214035, A)

	55	56												
51	72	73	56	52	57	62								
	58	65	61	59	58	60	69	66	59	52	47	48	43	47
	59	58	59	65	73	77	98	68	61	62	59	46	61	59
	59	62	64	67	110	255	255	110	70	61	55	46		
	59	59	68	98	255	255	255	255	108	84	73	58	59	
	65	68	69	92	255	255	255	255	41	102	69	49	56	
	61	62	70	87	191	255	255	214	87	73	62	48	42	
66	79	60	66	77	89	116	145	93	77	52	44	45	37	
60	75	60	59	72	74	83	78	66	64	54	50			
60	61	61	59	59	62	56	68	65	55					
	81	80												
79	84	87	81	74	79	78								
	82	83	82	79	73	73	81	78	78	72	65	66	63	63
	87	84	79	79	80	81	86	78	73	75	77	62	92	89
	89	85	80	78	93	145	174	87	75	74	79	67		
	86	80	85	88	144	255	255	136	81	80	86	74	72	
	93	90	89	88	255	255	255	255	82	90	83	71	71	
	88	94	88	88	109	215	176	113	86	81	78	68	60	
86	88	87	89	92	87	92	102	89	84	72	69	72	60	
82	88	82	83	83	89	92	91	83	80	70	72			
87	84	82	81	81	81	77	84	81	74					
	70	66												
68	68	68	59	58	65	59								
	68	65	62	57	59	62	60	56	64	63	53	53	50	52
	72	66	59	63	67	62	57	52	58	71	58	58	78	70
	70	67	61	67	66	60	53	48	54	71	65	65		
	76	73	68	68	61	54	52	52	60	72	65	64	54	
	79	72	68	62	61	58	56	59	62	66	63	59	51	
	78	73	73	67	62	62	62	65	62	62	62	54	48	
68	70	71	75	71	68	69	67	66	63	67	67	54	48	
66	66	68	72	68	67	71	67	65	62	62	64			
66	68	68	71	69	65	66	65	64	57					

A4.14. December 14, 1989 (4270814035, A)

	57	65	124	70	65	72	74				
	54	67	83	68	65	60	73	79	78	62	49
			49	40	70	149	133	98	80	64	61
	61	62	57	53	74	98	255	255	168	93	72
60	57	56	69	77	149	255	255	255	255	137	111
61	54	67	69	84	131	255	255	255	255	116	148
62	65	77	74	81	113	255	255	255	255	92	118
59	99	99	57	74	113	167	255	255	255	124	88
64	112	141	55	70	98	91	161	255	137	80	59
65	68	73	60	53	63	70	74	94	71	60	53

	82	87	105	90	87	89	94				
	82	87	105	90	87	89	94	89	87	78	69
			80	74	88	97	99	96	89	82	83
	99	94	84	72	86	94	141	149	104	79	87
85	80	85	85	85	97	164	255	255	150	103	98
78	77	99	91	89	99	255	255	255	182	95	104
83	79	100	94	88	91	136	255	227	152	98	99
75	90	94	82	92	106	106	171	255	147	102	93
81	89	101	76	90	102	96	112	125	109	87	82
88	88	87	77	74	81	81	83	99	89	76	71

	71	75	68	65	62	69	73				
	72	65	57	60	60	65	72	72	72	73	66
			53	58	66	70	68	69	64	71	78
	71	64	55	59	66	67	68	71	69	71	78
56	66	65	62	60	66	67	67	70	72	73	92
51	65	68	63	63	63	64	67	68	72	73	75
50	61	67	63	65	66	68	73	74	74	74	75
48	53	59	62	69	67	71	74	73	73	74	77
50	52	56	63	65	66	67	72	72	71	73	74
51	56	60	59	62	65	62	67	68	70	70	70

A4.15. March 25, 1990 (4281002295, A, night-time)

					10	10													
					9	10	10	10	12	9									
						10	11	10	13	14	15	16	6	9					
		9	9	11	10	14	18	21	23	26	32	26	14	9					
		9	11	12	17	23	37	56	49	62	154	102	32	16					
		10	12	12	20	31	60	62	52	97	255	255	36	30					
		11	9	12	12	14	23	25	23	40	155	255	83	23					
	11	11	8	11	7	9	13	17	13	15	29	58	48	34	8				
		9	7	7	7	6	9	7	10	9	14	16	18	24	10				
8	6	13	12	4	7	9	7	11	7	12	9	11	12	20	11	8			
							8	5	8	7	13	11	8	12	15	7			
						11	6	10	7	7	9	9	11	12	22	19			
							9	7	7	7	7	10	7	10	26	20			
					10	6	11	7	10	10	14	10	12	10	21	22	7		
								11	12	12	13	12	14	7	20	17	10	6	6
									9	12	11	11	11		13	7	11	7	6
						8	6	6	10	9	8	9	9	7	9	8	8	7	
												8			11		10		
															8		10		

					6	5													
					5	6	6	4	6	5									
						5	7	5	6	5	6	5	3	5					
		5	5	4	4	6	7	7	9	8	9	6	7	4					
		4	5	5	6	10	14	15	12	15	31	21	11	6					
		4	5	3	5	5	7	5	5	9	28	68	21	9					
		4	5	3	5	5	7	5	5	9	28	68	21	9					
	4	4	4	6	4	3	5	5	5	5	7	11	9	9	4				
		6	5	4	3	6	2	5	3	3	6	6	5	6	5				
4	4	4	5	4	5	3	5	4	4	5	4	7	3	10	8	5			
							4	5	4	4	4	5	4	6	8	5			
						3	5	3	4	4	3	5	6	5	8	5			
							4	6	2	5	2	5	5	5	9	9			
					4	5	4	5	4	5	5	5	3	5	6	6	4		
								6	4	5	4	5	5	5	5	7	4	3	5
									5	5	5	3	6		6	3	6	5	4
						3	5	4	5	5	5	5	4	4	6	4	4	5	
												6			3		6		
															5		6		

A4.16. January 7, 1991 (4309802225, A, night-time, north is down)

1	4	3	2	4	3	4	4	6	2	8	6	7	7	6	7	4	3	2	3
2	4	5	4	6	9	7	11	11	8	12	11	9	11	5	2	4	2	4	2
1	5	2	5	2	7	7	10	11	15	12	15	14	7	10	5	5	2	2	4
5	5	5	5	7	9	11	22	55	25	44	28	15	10	7	6	5	2	2	2
3	5	5	6	5	9	21	51	169	215	255	187	41	24	13	12	8	5	4	3
5	5	7	7	13	13	33	153	255	255	255	255	255	24	22	11	13	8	9	6
5	5	4	6	6	11	25	108	255	255	255	255	255	6	25	9	15	29	3	5
7	5	6	7	9	10	20	136	255	219	255	255	141	6	11	3	6	7	3	3
4	4	5	5	8	11	22	49	255	255	255	255	27	30	12	8	9	3	5	3
4	4	6	5	10	10	13	22	59	86	78	48	26	12	10	2	2	2	4	2
3	3	5	6	6	9	9	10	9	13	12	13	10	8	7	5	5	3	3	5
3	5	4	3	4	7	5	8	10	7	7	8	6	12	6	4	4	5	2	3
5	3	5	6	7	6	6	7	6	9	7	6	7	8	6	1	5	3	3	3
4	2	3	5	6	5	6	5	6	6	4	5	7	5	6	5	3	4	3	3
4	6	3	5	5	6	7	5	6	6	5	6	6	3	5	3	6	5	3	3
5	4	3	5	3	4	3	4	3	4	4	4	5	5	3	5	4	5	5	4
2	4	5	5	5	6	3	6	5	5	4	5	5	5	3	5	3	5	3	4
4	5	3	6	4	4	6	5	6	5	4	6	6	5	6	4	4	5	4	3
4	3	4	4	5	6	4	9	12	10	11	11	6	6	5	3	4	5	3	4
4	3	5	5	3	5	7	15	36	46	54	40	12	7	5	5	5	4	4	4
3	4	4	3	6	5	9	26	255	255	159	255	85	6	13	5	6	5	3	6
4	5	5	4	4	5	8	23	173	122	128	106	87	5	7	4	6	9	5	5
3	5	4	4	5	6	6	23	88	43	62	99	44	4	6	6	5	3	5	3
4	3	5	3	4	6	7	11	146	190	144	74	5	7	5	5	4	5	3	5
4	3	5	3	4	5	6	6	13	19	17	14	9	6	5	6	4	4	5	5
3	4	3	3	4	5	5	5	7	7	7	6	3	4	7	2	4	5	4	4
5	5	5	2	5	3	5	6	3	5	6	5	5	5	3	5	5	3	5	3
5	3	4	3	3	6	4	4	4	5	6	4	4	5	5	4	3	4	3	2
4	4	3	3	3	5	4	5	4	5	3	6	4	5	3	3	4	3	5	5
4	4	3	3	3	5	4	5	4	5	3	6	4	5	3	3	4	3	5	5
4	3	4	5	3	5	4	3	5	3	5	4	6	3	4	4	3	4	3	4

Appendix A5. AVHRR for volcano hotspot monitoring

Paper published in Proceedings of the 4th AVHRR Data Users' Meeting, Rothenburg, Germany, 3-5 September 1989, EUMETSAT, 335-338.

A5.1. Abstract

AVHRR thermal infrared channels are sensitive to greatly sub-pixel sized hotspots such as lava lakes or flows. A technique used to derive the temperature and area of sub-pixel resolution hot sources is examined in the context of such volcanic phenomena. Fieldwork at Stromboli and Vulcano (Italy) has emphasised the general point that, depending on the style of activity, it is not always meaningful to monitor the thermal budget of a volcano from satellite 'snapshots'. Additional restrictions on the quantitative value of AVHRR for infrared volcano monitoring arise from the channel bandpasses and pixel geometry.

A5.2. Introduction

It is logistically impossible to monitor at ground level all the world's active and potentially active volcanoes and it is clear that orbital remote sensing will play several roles in their surveillance. Earlier work has demonstrated the sensitivity of AVHRR channel 3 to sub-pixel sized high-temperature sources such as gas flares, forest fires and lava lakes (Matson and Dozier, 1981; Matson and Holben, 1987; Wiesnet and D'Aguanno, 1982). This is because the 3.55-3.93 μm bandpass corresponds to the peak of the Planck function for a black body temperature around 500°C.

Studies using Landsat TM short wavelength infrared bands 5 and 7 have shown potential for measuring the temperature, radiant flux and emittance of volcano hotspots (Rothery *et al.*, 1988; Glaze *et al.*, 1989a). I discuss here the applicability of AVHRR to a similar quantitative role.

A5.3. AVHRR and the dual band method

The use of AVHRR infrared channels in the derivation of sea and land surface temperatures is well known. Pixel-integrated brightness temperatures may be obtained for each of channels 3, 4 and 5 by utilising the inverse of the Planck function; a variety of techniques being available to correct for the effects of the atmospheric path. Consider next a pixel including a lava lake with surface temperature T_h surrounded by ground at temperature T_b. The channel 3 and 4 pixel-integrated temperatures should lie between T_b and T_h but differ because of the wavelength dependence of the Planck function. From them, both T_h and p, the hot fraction of the pixel, can be calculated, if we can assume T_b. This dual band method has been used with AVHRR data to estimate the temperatures and dimensions of various sub-pixel sized industrial hot sources (Matson and Dozier, 1981). Unfortunately, there are problems with this approach, particularly in volcanic situations:

(i) A two-component surface temperature field is unrealistic with such large pixels. A c.1 km sided AVHRR pixel straddling a volcano will sample ground of a

range of altitudes, aspects and surface cover, so selection of a background temperature is not trivial. It is also unreasonable to model the hot volcanic surface (e.g. lava body or fumarole-field) by a single temperature. The simplest thermal model of lava surfaces comprises two temperatures: those of glowing cracks and cooler crust.

(ii) Even if we are happy to accept a two-component temperature distribution, it is readily seen in Figure A5.1 that uncertainty in T_b is magnified greatly in deriving the dual-band target temperature. A very small, very hot source may not produce a resolvable anomaly in channel 4, in which case the dual band calculation is invalid.

(iii) The AVHRR instantaneous field of view is not well constrained; generally pixels are 'blurred' both across and along scan lines (eg. Figure 3 in Wiesnet and D'Aguanno, 1982). The amount of blur is partly a function of the scan angle for a given pixel (Prata *et al.*, 1990). It is important to account for this in calculations that involve areas and in summation of radiant flux for two or more pixels. This is particularly relevant when comparison of multi-temporal data sets is undertaken.

A5.4. Fieldwork on Italian volcanoes

For the general purpose of better understanding the remotely sensed data, I have taken portable infrared thermometers to several volcanoes in Italy and Central America to obtain ground truth (Oppenheimer and Rothery, 1991). Radiant temperatures of a variety of hot surfaces were measured with 8-14 μm and 0.8-1.1 μm bandpass infrared thermometers.

Stromboli is one of the world's most active volcanoes. During the study-period in October-November 1988, incandescent scoria were frequently erupted from intracrater boccas, some of which were filled with lava. Radiant temperatures of these vents (measured from crater rims at 'safe' distances of about 50 m) fluctuated rapidly due to the activity of lava inside, and the amount of volcanogenic fumes in the field of view. Such temporal variation brings into question the quantitative value of an isolated satellite 'snapshot' of strombolian activity.

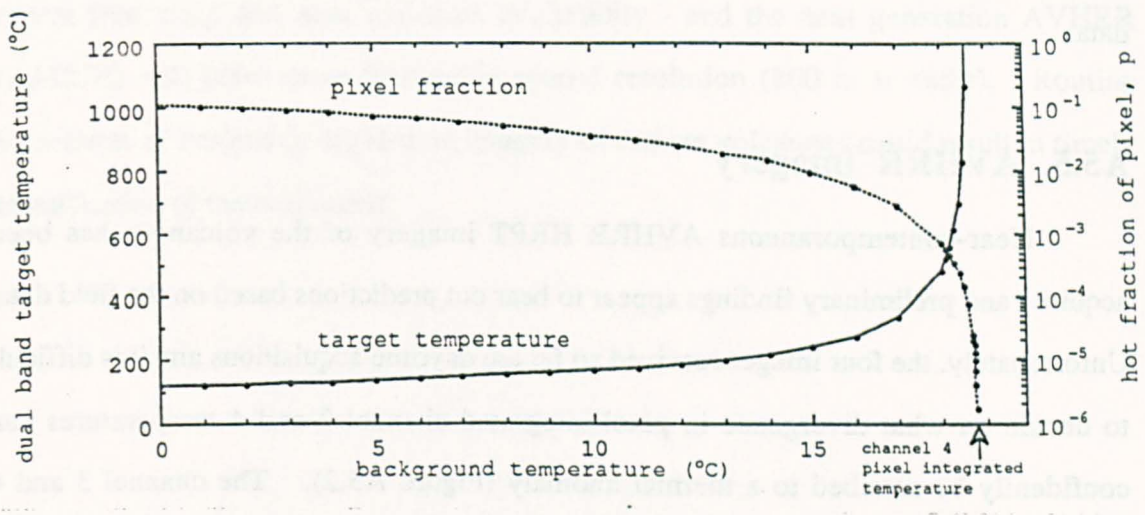

Figure A5.1. Dual band target temperature, T_h, and fraction of pixel calculated for various values of T_b. Channel 3 and 4 pixel-integrated temperatures were 48.3°C and 18.9°C respectively (real example from image of Mount Etna, Italy).

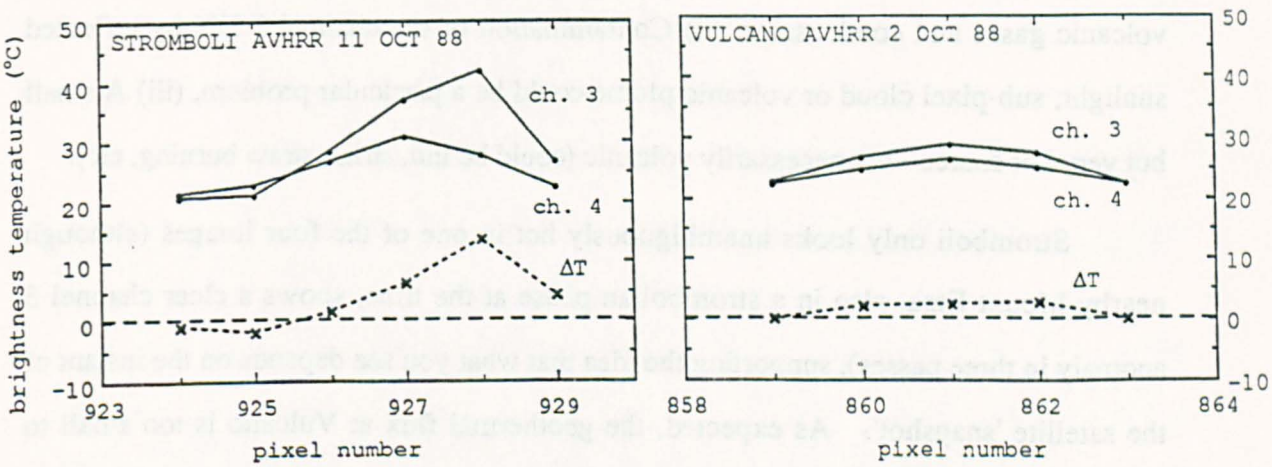

Figure A5.2. Pixel-integrated brightness temperatures across the summit craters of Stromboli and Vulcano derived from AVHRR images. The divergence in channel 3 and 4 temperatures (ΔT) on Stromboli indicates channel 3 sensitivity to the lava bodies whereas at Vulcano the slight discrepancy over land is probably due to contamination of channel 3 by reflected sunlight.

Since its last eruption during 1888-90, Vulcano has been in a state of variably intense fumarolic activity which is now concentrated on the north rim of the main cone. During an 18 day period in the field in October-November, 1988, gas temperatures were very stable; the highest recorded was a moderate 396°C. Radiant temperatures of rock and sublimate surfaces around gas vents reflected this stability, suggesting that thermal

monitoring of sufficiently hot and/or extensive fumarole fields might provide meaningful data.

A5.5. AVHRR imagery

Near-contemporaneous AVHRR HRPT imagery of the volcanoes has been acquired and preliminary findings appear to bear out predictions based on the field data. Unfortunately, the four images received so far are daytime acquisitions and it is difficult to decide on what divergence in pixel-integrated channel 3 and 4 temperatures can confidently be ascribed to a thermal anomaly (Figure A5.2). The channel 3 and 4 brightness temperatures are typically very close over the sea and diverge on land, channel 3 giving the higher values. Several factors may be responsible: (i) Differential atmospheric attenuation in the two channels, exacerbated by the absorption effects due to volcanic gases and condensates. (ii) Contamination of the channel 3 DN by reflected sunlight; sub-pixel cloud or volcanic plume could be a particular problem. (iii) A small but very hot source - not necessarily volcanic (could be industrial, straw burning, etc).

Stromboli only looks unambiguously hot in one of the four images (although nearby Mount Etna, also in a strombolian phase at the time, shows a clear channel 3 anomaly in three passes), supporting the idea that what you see depends on the instant of the satellite 'snapshot'. As expected, the geothermal flux at Vulcano is too small to detect (Oppenheimer and Rothery, 1991).

A5.6. Conclusions

AVHRR is clearly not an ideal tool for thermal monitoring of volcanoes. Conditions of the volcanic source, atmospheric path and uncertainties in pixel resolution restrict the potential for meaningful quantitative measurements. AVHRR could even 'miss' a hotspot hidden by fumes or sub-pixel cloud. On the other hand care must be taken in ascribing a channel 3 anomaly in daytime imagery to a hot source: reflected sunlight could be the cause.

It is important, however, to stress the strengths of AVHRR - low cost, high repeat frequency and near real-time availability - and the next generation AVHRR (AMRIR) will offer more favourable spatial resolution (800 m at nadir). Routine inspection of preferably night-time imagery of remote volcanoes *could* result in timely identification of thermal unrest.

Appendix A6. Liquid sulphur lakes at Poás volcano

Clive Oppenheimer and David Stevenson

Published in *Nature*, 342, 790-793, 1989.

A6.1. Abstract

The level of the hot, acid crater lake at Volcán Poás, Costa Rica, dropped progressively over a two-year period up to April 1989, when only scattered boiling mudpools remained[1-3]. After the last of the water disappeared, part of the former lake-bottom was occupied by ponds of molten sulphur. This is the first reported occurrence of terrestrial sulphur lakes, and we suggest their formation was a response to removal of the overlying water, which allowed sediment temperatures to rise above the liquidus of elemental sulphur deposits they contained. The sulphur ponds circulated vigorously and were kept molten at a temperature of ~ 116 °C by the passage of hot gases. The low viscosity of sulphur at this temperature is likely to have been critical in enabling its migration through the lake sediments to collect at fumarole vents. Aspects of the origin

of the sulphur lakes at Poás may be analagous to the formation of putative sulphur bodies on the Jovian moon, Io[4,5].

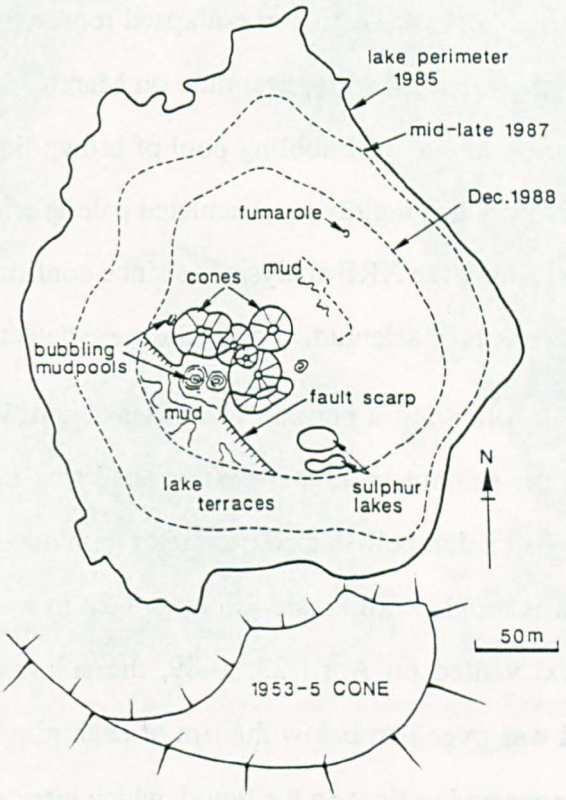

Figure A6.1. Sketch map of the Poás intracrater on 23rd April, 1989, with former lake levels shown for comparison.

Poás is a composite volcano of the Cordillera Central in Costa Rica, rising 1300 m above its base at 1400 m. Historically it has been in a state of near-continuous mild activity, characterised since an episode of explosive/effusive eruptions in 1953-5 by intense fumarole emissions and intermittent phreatic eruptions usually through a shallow crater lake. The lake plays an important role in the hydrothermal system of the volcano, typically condensing ~ 100 kgs^{-1} of steam from lake-floor fumaroles while transferring heat by evaporation, radiation and conduction at the water surface[6,7]. A shallow injection of magma beneath the lake between 1987-1988, inferred from microgravity increases[3], may be responsible for its recent dessication (Figures 1,2).

Between early 1987 and March 1989, the water level dropped by about 32 m[1], falling the last 6 m in less than 2 months, and revealing a muddy floor scattered with boiling mud pools. Two of these pools located towards the southeast part of the crater

subsequently dried up and became the site of several 1-3 m high yellow cones composed of fragmental sulphur and lithic particles (Figure A6.3a). Occasionally, 1 m high chimneys developed at their apices. The cones collapsed repeatedly, forming pits that continued to emit gases. Seen by us for the first time on March 16, 1989, one of these pits, about 2 m in diameter, contained a bubbling pool of brown liquid (Figure A6.3b). A sample taken in a bottle quenched rapidly to vesiculated pale-green sulphur with minor admixed lake sediment. Qualitative XRF analysis has since confirmed the purity of the sulphur, though significant traces of selenium and arsenic were detected.

By April 19, 1989, following a period of continual modification of the cones (Figure A6.3c-e), two larger sulphur lakes were established side by side within steep-sided collapse pits. One had a dumbell-shaped perimeter with maximum dimensions ~ 24 m x 11 m; the other was roughly elliptical with axes ~ 28 m x 15 m (Figure A6.2). When the crater was next visited on April 23, 1989, the sulphur pond surface had dropped about 0.5 m and was over 1 m below the rim of each pit. Blocks of sediment calved from the pit walls appeared to float on the liquid, which was dark brown in colour, visibly translucent and remarkably fluid, bubbling vigorously over most of its surface. The temperature of the molten sulphur, measured by thermocouple, was 116 °C (J. Barquero, pers comm), well below the boiling point of sulphur, (~ 444 °C). There was no crust on the surface although a terrace of pale yellow solid sulphur had formed around the edge, and the pit walls and rims were coated in bright yellow sulphur sublimates. Condensates could be seen rising above the liquid surface and the smell of SO_2 was strong. These observations are important as they indicate that the sulphur was kept molten and uncrusted by the passage of hot gases, (presumably at a temperature close to 116 °C). Meanwhile, 50-100 m away, spectacular phreatic emissions of non-juvenile ash and blocks were building a cluster of at least six ~ 10 m high cones[2] (Figures 1,2). Some of the plumes were dark and cypressoid; others were yellow-coloured, presumably by elemental sulphur.

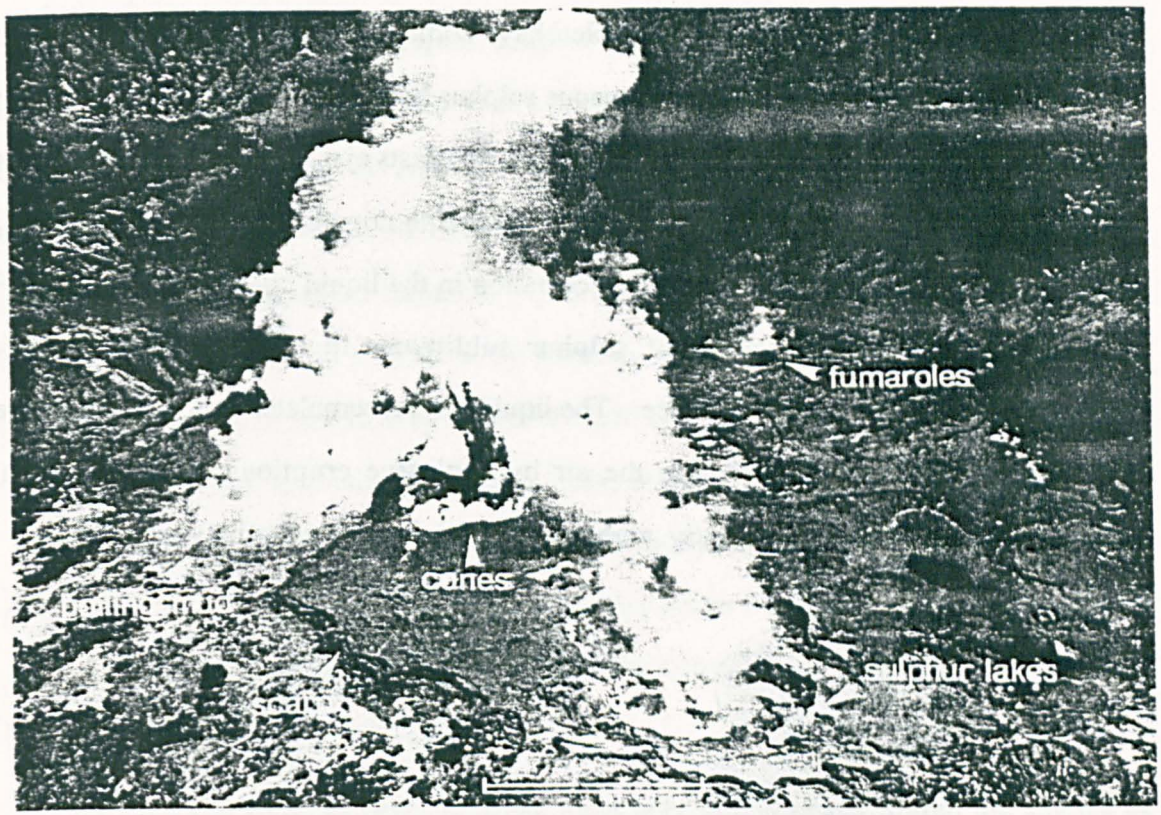

Figure A6.2. Photograph of dessicated lake-floor taken from eastern end of the 1953-5 cone, looking approximately NW. Scale bar is about 25m.

To our knowledge, terrestrial sulphur lakes have never before been documented. 'Steaming pits' and 'niches' containing liquid sulphur were reported at Ebeko volcano (Kuriles, USSR)[8] in 1952 but unfortunately, their dimensions are not recorded. It is possible that these features were no more unusual than the driblets of molten sulphur commonly found at fumarole fields and solfataras. However, Ebeko did reportedly produce a sulphur flow in 1934[9] and similar flows have also been recorded at Siretoko-Iôsan (Japan)[10], Volcan Azufre (Galapagos Islands)[11], Mauna Loa (Hawaii)[12,13] and Lastarria (Chile)[14]. These rare occurrences of flows of molten sulphur have been attributed to melting and mobilisation of sulphur deposits of fumarolic origin[14,15].

Although sulphur lakes were hitherto unknown, their existence beneath aqueous crater lakes has previously been inferred from observations of floating sulphur 'spherules' found at the volcanoes Kusatsu-Shirane (Japan)[16] and Ruapehu (New Zealand)[17]. Ohashi[16] proposed that the hollow spherules formed by the upwards passage of gas bubbles through liquid sulphur, and manufactured similar morphologies

by laboratory experiment. Sulphur 'bubbles' have commonly been observed floating on the lake-water at Poás[18] but here, subaqueous sulphur lakes were postulated on different grounds, following recovery of greenish sulphur pyroclasts ejected by phreatic emissions through the crater lake during the 1970's[19]. The morphology of the sulphur ejecta[19,20], as in the case of the spherules, indicated formation in the liquid phase. Francis *et al.*[20] suggested that at Poás, melting of sulphur sublimates in large volumes of rock surrounding fumaroles had taken place. The liquid then accumulated in fissures and pore spaces prior to being sprayed into the air by explosive eruptions, for example, in September 1978 (when significantly, perhaps, the lake-floor was partially exposed[20]).

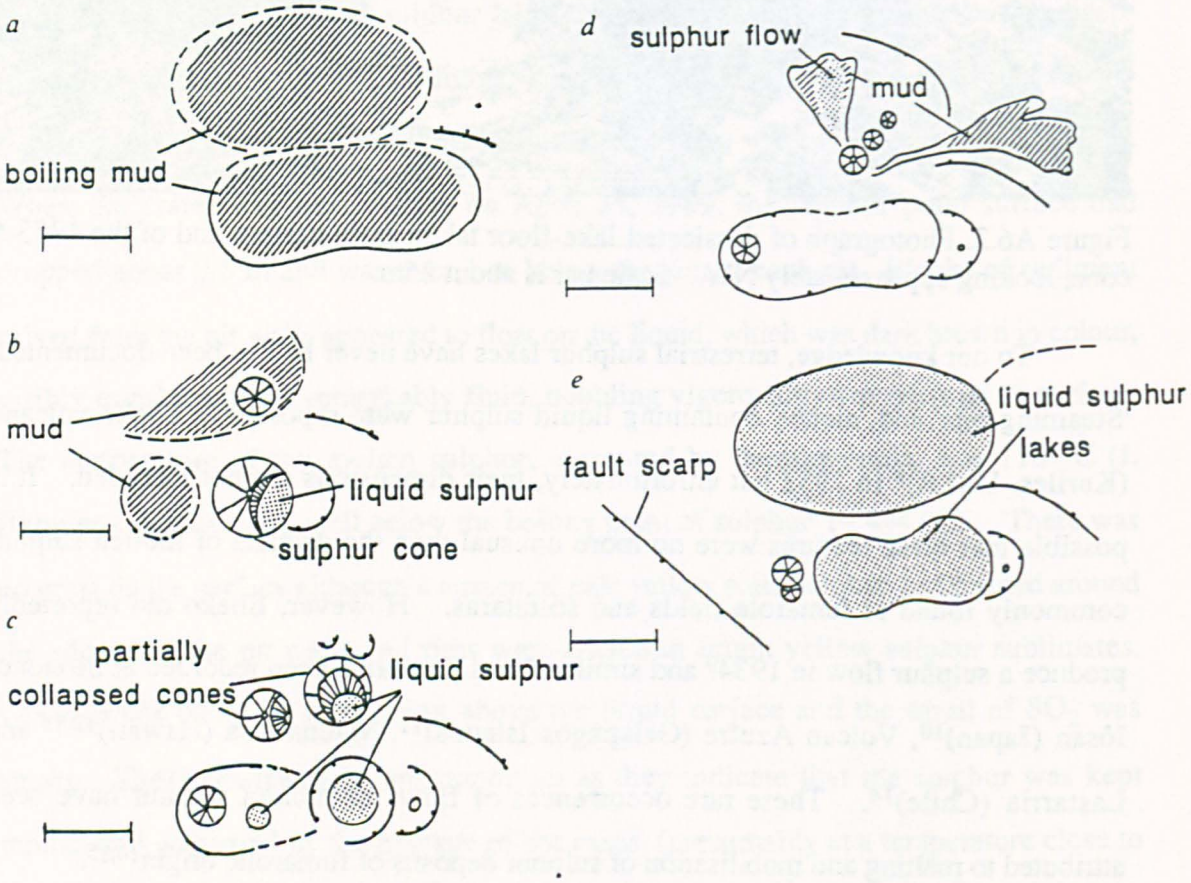

FigureA6.3. Evolution of sulphur ponds: (a) 3rd March, 1989, site initially occupied by bubbling mud pools, (b) 16th March, 1989, ~ 2m high cones of pyroclastic sulphur develop rapidly - partial collapse of one cone exposes molten sulphur pond, (c) 31st March, 1989, continued cone construction and destruction - several sulphur ponds, (d) 10th April, 1989, small flow of separated mud and, probably, sulphur from new cone but ponds temporarily absent, possibly due to quenching by rainfall, (e) 23rd April, 1989, sulphur lakes re-established. Scale bar is approximately 10m.

We suppose that the liquid sulphur ponds at Poás were also supplied by remobilised fumarolic deposits, (although a primary melt separated from silicate magma at depth is feasible[21,22]), on the grounds that secondary sulphur deposits are abundant at Poás. They occur within the lacustrine sediments[23,24], as disseminated sulphur particles, and sulphur-filled fumarole pipes and tubes. An eruption in January 1988 threw out lake mud with ~ 5-10 % by volume of sulphur particles (G. Brown, pers comm). The oxidation of H_2S by SO_2 in the acid aqueous conditions of the crater lake[17] may be responsible for their formation. The reaction rapidly precipitates elemental sulphur which would settle on the lake-bed. Both H_2S and SO_2 have been identified at Poás: gas analyses[9] of fumaroles on the near-dry crater floor in February 1989 showed 5.0 mole % H_2S, and the SO_2 flux, measured by correlation spectrometer in February 1982, was around 700 tonnes/day[21].

The presence or absence of water must play an important role in the change of state of sulphur. Although there may be localised pockets of molten sulphur where gas temperatures exceed the sulphur liquidus, widespread melting will be inhibited when the aqueous lake is present because the water-saturated sediments remain below the local boiling point of water. Loss of water removes this temperature buffering system so that temperatures of sediment fluxed by hot gases can increase above the sulphur liquidus, generating much greater volumes of melt. The Poás sulphur ponds did not appear until all the water in the vicinity had been driven off, and then, following a period of sulphur-cone construction and destruction. The collapse of the cones into molten sulphur pools suggests that chambers of the liquid may have developed at very shallow levels beneath the lake-bed.

Concentration of the molten sulphur at these specific sites is more difficult to explain. There is no obvious topographic cause as appeared to be the case of the Mauna Loa sulphur flow[13]. However, in the absence of data on the volume of the sulphur lakes at Poás, or of the proportion of sulphur contained in the sediments, it is not possible to estimate the region over which sulphur has migrated. Clearly, proximity to fumarolic vents is important as indicated by the gas flux through the sulphur lakes but also highly

significant is the pond temperature of 116 °C. Between its melting point, ~ 113 °C, and ~ 159 °C, where cyclic octatomic sulphur begins to polymerise, the viscosity of liquid sulphur is of the order of only 10 cp[14,15], (about ten times that of liquid water at room temperature[4]). Such low viscosity is likely to have been a critical factor enabling the molten sulphur to move towards fumarole sites through fractures in the lacustrine sediments, or pores created by melting of the originally disseminated sulphur.

Terrestrial sulphur flows received renewed attention following recognition of the importance of sulphur volcanism on Io, from the images of the Voyager spacecraft. For example, Greeley *et al.*[13] re-examined the Mauna Loa sulphur flow in the field to gain insight on possible processes taking place on Io. Unfortunately, the evidence for liquid sulphur bodies on Io is inconclusive: (1) Ground-based and Voyager observations in the infrared identified ~ 130-430 °C hotspots - temperatures that were argued to be too low for silicate magma[25,26]. However, it is well known that lava bodies are typically composed of cool crust as well as glowing cracks and indeed temperatures of terrestrial lava surfaces derived from single channel satellite data fall in the same range[27]. (We measured a peak radiant temperature of 97.0 °C for the surface of the Poás sulphur ponds with an 8-14 μm bandpass radiometer, the low value probably due to attenuation of emitted infrared by fumes). (2) The reflectance spectra of volcanic regions of Io have been related to those of elemental sulphur, whose colour variations with temperature change are well known[13,28]. More recently, however, Hapke[29] argues that the only unambiguously identified species is SO_2, and that all the observed spectra can be modelled by combination of SO_2 condensates and basalt.

In the light of such controversy, we make only tentative implications regarding Io from our observations at Poás. The most interesting and instructive parallel concerns the role of water. Unlike the other Galilean satellites, Io has lost its water, which is why S_n and SO_2 are likely to be the dominant volcanic volatiles[4] - sulphur volcanism on Io takes place in the absence of water. The appearance of sulphur lakes at Poás following dessication of the aqueous crater lake may therefore mimic to some extent the evolution of sulphur volcanism on Io. We also re-emphasise that low viscosity, as observed at Poás,

is likely to be a significant factor in coalescing large volumes of molten sulphur within a solid matrix.

A6.2. Acknowledgements

CO and DS are both supported by NERC studentships. We thank Jorge Barquero, Steve Hallinan, Gerardo Soto and Ben Van Wyk de Vries for assistance in Costa Rica, John Watson for XRF analyses, John Taylor for artwork, Eilene Theilig for a helpful review of the manuscript, and Geoff Brown, Peter Francis, Dave Rothery and Hazel Rymer for advice and encouragement.

A6.3. References

1 Scientific Event Alert Network Bull. 14(3), 4-6 (1989)

2 Scientific Event Alert Network Bull. 14(4), 7-10 (1989)

3 Rymer, H. & Brown, G. Nature 342, 902-905 (1989)

4 Sagan, C. Nature 280, 750-753 (1979)

5 Carr, M.H., Masursky, H., Strom, R.G. & Terrile, R.J. Nature 280, 729-733 (1979)

6 Brown, G. *et al.* Nature 339, 370-373 (1989)

7 Brown, G.C., Rymer, H. & Stevenson, D.S. J. Geol. Soc. London 148, 585-593 (1991)

8 Gorshkov, G.S. Volcanism and the Upper Mantle (1970)

9 Scientific Event Alert Network Bull. 14(5), 9-10 (1989)

10 Watanabe, T. Japanese J. of Geology and Geography 17, 289-310 (1940)

11 Colony, W.E. & Nordlie, B.E. Economic Geology 68, 371-380 (1973)

12 Skinner, B.J. Pacific Science 24, 144-145 (1970)

13 Greeley, R., Theilig, E. & Christensen, P. Icarus 60, 189-199 (1984)

14 Naranjo, J.A. Nature 313, 778-780 (1985)

15 Theilig, E. A primer on Sulfur for the Planetary Geologist. NASA Contr. Rep. 3594 (1982)

16 Ohashi, R. J. Akita Mining College 1, 1-10 (1919)

17 Giggenbach, W. New Zealand J. of Science 17, 33-45 (1974)

18 Smithsonian Institution Scientific Event Alert Network. Global Volcanism 1975-1985 (1989)

19 Bennett, F.D. & Raccichini, S.M. Nature 271, 342-344 (1978)

20 Francis, P.W., Thorpe, R.S., Brown, G.C. & Glasscock, J. Nature 283, 754-756 (1980)

21 Casadevall, T.J. *et al.* J. Geophys. Res. 89, 9633-9641 (1984)

22 Whitney, J.A. & Stormer, J.C. Geology 11, 99-102 (1983)

23 Prosser, J.T. & Carr, M.J. J. Volcan. Geotherm Res. 33, 131-146 (1987)

24 Brantley, S.L., Borgia, A., Rowe, G., Fernadez, J.F. & Reynolds, J.R. Nature 330, 470-472 (1987)

25 Sinton, W.M. J. Geophys. Res. 86, 3122-3128 (1981)

26 Pearl, J.C. & Sinton, W.M. in Satellites of Jupiter, ed. Morrison, D. Uni. Ariz. Press (1982)

27 Rothery, D.A., Francis, P.W. & Wood, C.A. J. Geophys. Res. 93, 7993-8008 (1988)

28 McEwen, A.S. & Soderblom, L.A. Icarus 55, 191-217 (1983)

29 Hapke, B. Icarus 79, 56-74 (1989)

Appendix A7. Sulphur eruptions at Volcán Poás, Costa Rica

Paper in press for *Journal of Volcanology and Geothermal Research*, 49, 1992.

A7.1. Abstract

Since the recent desiccation of the crater lake at Volcán Poás, Costa Rica, vigorous fumarolic activity on the exposed lake-bed has been associated with the manifestation of miniature sulphur volcanoes, sulphur flows and sulphur pools. In this paper, observations of 2-3 m high, active sulphur volcanoes are reported, and mechanisms for their formation proposed and discussed. Their ejecta, composed of milled particles, crystals and accretionary lapilli of sulphur, are unlike previously described pyroclastic sulphur deposits, and probably form from a spray of crystallised sulphur forced to the surface by fumarolic gases passing upwards through shallow bodies of liquid sulphur. While much of the erupted material is recycled, the reservoir of molten sulphur can also be replenished by influxing magmatic-hydrothermal fluids. $\delta^{34}S$ isotope ratios of several samples of native sulphur collected at Poás range between -9.4 and -12.3 ‰ (CDT). These are among the isotopically lightest volcanic deposits of

elemental sulphur reported, although this pronounced depletion is readily explained by the likely formation of the sulphur under the acidic conditions of the aqueous lake and hydrothermal system. The total amount of native sulphur deposits contained within lake sediments at Poás, and perhaps at other active volcanoes with crater lakes, is potentially substantial. A large explosive eruption could, by volatilisation and oxidation of this sulphur, inject large volumes of sulphur dioxide into the atmosphere.

The greenish colouration of the sulphur, reminiscent of other documented terrestrial sulphur eruptions, is probably due to impurities. This emphasises the point that interpretation of spectral reflectances of the jovian moon Io, regarding the possible contribution of sulphur, cannot rely on extrapolation of laboratory data for pure materials.

A7.2. Introduction

Sulphur is a remarkable substance. Its unusual physical properties, not least the 2000-fold increase in viscosity of the liquid as the molecules polymerise at around 159 °C, and the complexity of its chemistry are well-known. The wide range of melting points encountered reflects the different molecular forms, which can coexist. For example, by slightly changing the temperature in the system S_x, values for x between 1 and about 10^6 are possible (Schmidt and Siebert, 1973). Sulphur and its compounds are important components of volcanic processes, and have been implicated in acid precipitation in the vicinities of many volcanoes worldwide (Casadevall *et al.*, 1984b), and climatic effects resulting from large explosive or effusive eruptions (Rampino *et al.*, 1988). Irrespective of their magnitude, some plinian events appear to have been much more sulphur-rich than others, for example the 1982 eruption of El Chichón in Mexico (Hoffmann and Rosen, 1983; Hoffmann *et al.*, 1987). Sulphur fluxes in quiescent plumes also vary widely, apparently exceeding, in some cases, amounts that could be sustained by estimated volumes of magma present (Andres *et al.*, 1991). Diverse potential reservoirs of sulphur have been considered to account for these discrepancies (e.g., Williams *et al.*, 1990), among them fumarolic sulphur deposits. Albeit on a comparatively small scale, remobilisation of fumarolic sulphur has been recognised at a

number of volcanoes. Recent investigations of such phenomena have sought to draw implications for the possible roles of sulphur in volcanism of Jupiter's moon, Io.

A7.2.1. Volcanic liquid sulphur

Few active terrestrial volcanoes lack the bright yellow incrustations of elemental sulphur deposited around fumarole vents. It is generally believed to be precipitated by redox reactions involving hydrogen sulphide and sulphur dioxide (Banfield, 1954; Colony and Nordlie, 1973; Giggenbach and Matsuo, 1991). Sulphate deposits (e.g., thenardite, anhydrite, gypsum) are also common (Stoiber and Rose, 1974). Despite the abundance of solid native sulphur, and fumarole temperatures which often exceed the sulphur liquidus, only a few cases of large bodies of molten sulphur have been reported. Arguably the most spectacular of these was the effusion of a 1400 m long sulphur flow at Siretoko-Iôsan volcano, Japan, in 1936. Watanabe (1940) witnessed active flows there and described them as follows: "Without any precursory roaring, molten sulphur, having a chocolate brown colour, began to spout and flow from a smaller tunnel-like hole... The enormous volume of liquid fell with a thundering roar in a brown cascade from the top of the steep cliff of the Kakono-Sawa (valley)... bushes and trees near the course of the river were also covered by the spray of sulphur". Smaller fossil sulphur flows have been documented at Volcán Azufre, Galapagos Is. (Colony and Nordlie, 1973), Mauna Loa, Hawaii (Skinner, 1970; Greeley *et al.*, 1984), Lastarria, Chile (Naranjo, 1985) and Momotombo, Nicaragua (Smithsonian Institution, 1990a). In all cases, formation of the sulphur liquid was attributed to the melting and remobilisation of fumarolic deposits.

It has been suggested that liquid sulphur is present in large quantities beneath some aqueous crater lakes, including those at Mount Ruapehu, New Zealand (Giggenbach, 1974; Hurst *et al.*, 1991), Poás, Costa Rica (Bennett and Raccichini, 1978) and Kusatsu-Shirane, Japan (Ohashi, 1919; Takano and Watanuki, 1990), on the basis of sulphur spherules which form slicks seen floating on the lakes, or from pyroclastic sulphur deposits that have been erupted subaqueously. Spherules of liquid sulphur were ejected from a shallow borehole sunk into the crater floor at White Island, New Zealand,

in 1928 (Grange, 1959); a hot lake was often present within the crater. However, it was at Poás, in March - April 1989, subsequent to desiccation of the warm crater lake, and growth of 1-3 m high sulphur volcanoes, that ponds of molten sulphur (Figure A7.1) were discovered close to the periphery of the exposed lake-bed (Smithsonian Institution, 1989a; Oppenheimer and Stevenson, 1989).

Figure A7.1. Photograph of sulphur ponds taken looking north from the 'dome' in April 1989. The dimensions of the nearer pond are 24 x 11 m and those of that behind it 28 x 15 m.

A7.2.2. Volcán Poás

Poás rises about 1300 m above its base at 1400 m in the Cordillera Central of Costa Rica, and is a composite volcano of basaltic to andesitic composition (Prosser and Carr, 1987). Since explosive eruptions in 1953-5, its activity has been characterised by intense fumarolic discharge and intermittent phreatic eruptions, generally through the lake which filled the central crater from 1965. The interaction between the lake - thermally and chemically well-mixed acid-sulphate-chloride waters of extremely low pH (Brantley *et al.*, 1987; Neshyba et al., 1988) - and the magmatic-hydrothermal system of the

volcano has been investigated by Brown *et al.* (1989; 1991) and Rowe *et al.* (1991a). According to Rymer and Brown (1989), a shallow injection of magma beneath the lake between 1987-1988, inferred from microgravity increases, may have exceeded the summit hydrothermal system's capacity to buffer the volcano's heat output, resulting in a progressive 32 m decrease in lake level between early 1987 and March 1989 (Smithsonian Institution, 1989a). Rowe *et al.* (1991a) suggested that low rainfall contributed to the lake's disappearance, and that the estimated increase in heatflow between 1987-1988 resulted from release of magmatic gases following rupture of the chilled margin of an existing magma body, with little or no ascent of new magma.

Sulphur eruptions ensued shortly after loss of the aqueous lake in early 1989; the main conclusions from observations of the sulphur ponds (Oppenheimer and Stevenson, 1989) were that (a) the liquid sulphur derived from melting of fumarolic deposits contained in the lake sediment, (b) loss of the overlying water *may* have significantly encouraged this, since it removed a temperature buffering system which would otherwise maintain sediment interface temperatures below the sulphur liquidus, (c) the low viscosity corresponding to the temperature (116 °C) of the molten sulphur would have greatly facilitated its migration and coalescence within the sediment, and (d) the vigorous gas flow through the ponds maintained their temperature and inhibited growth of a crust.

Sulphur eruptions have been reported intermittently at Poás since that time (e.g., Smithsonian Institution, 1989c, d; 1990a, c). That the cones appear to predominate during the dry season (late December to April) is hardly surprising, or necessarily significant, since with the aqueous lake recharged during heavy rains (usually during May to November), it is no longer easy to see what activity occurs on the submerged crater floor. It is noteworthy that active mud/sulphur cones *have* been observed within the lake (Smithsonian Institution, 1990d). This paper sets out to document the evolution of the miniature sulphur volcanoes, concentrating on the nature of their tephra, and the evidence which bears on their eruptive mechanism, in the wider context of the importance of sulphur-bearing species in terrestrial and planetary volcanism.

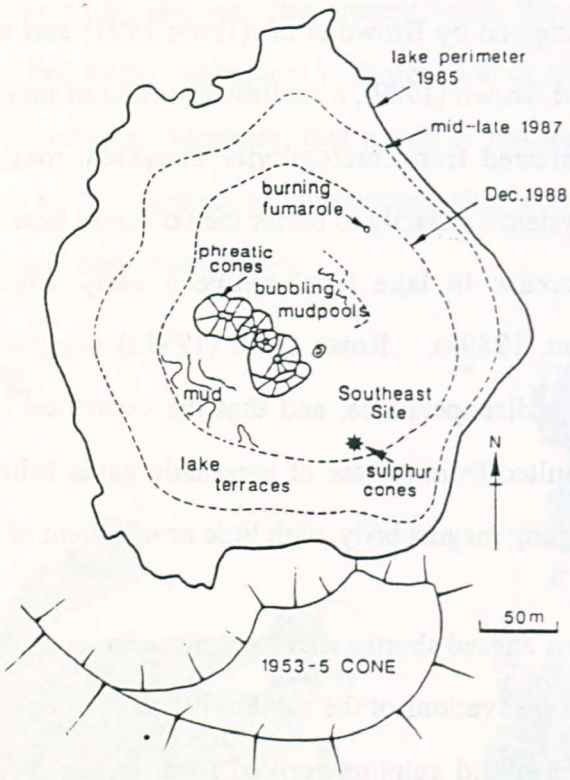

Figure A7.2. Sketch map of Poás crater, April 1990.

A7.3. Observations of sulphur volcanoes at Poás, April 1990

To illustrate the activity at Poás, the following description presents a life-cycle of a sulphur volcano which formed during April 12-13, 1990. All times are local, 6 hours behind UT. This is representative of the activity that, since early 1989, has been manifest at the same southeast portion of the lake-floor of Poás, hereafter the Southeast Site, when it has been exposed (Figure A7.2). Development of the sulphur cones which reached eventual heights of about 3 m above their bases, typically took place over a few, or a few tens of hours, and involved several stages:

A7.3.1. Mud/sulphur "geysers"

The crater floor was visited from 1045 to 1200 hours on the 12th April, 1990. Most of the lake-bed was exposed; a few bubbling pools of mud remained, particularly

towards the centre of the crater. Numerous fumaroles discharged turbulent plumes of gases, some of them burning intermittently with pink-orange flames. At the Southeast Site (which had been occupied by the sulphur ponds in 1989), vigorous gas pulses, at a rate of about one every two seconds, were rupturing an apparently muddy surface. These bursts sprayed mud and coagulated sulphur particles to heights of up to 5 m, developing a concentric rampart of ejecta a few metres from the vent. This activity was similar to that observed in early 1989 (Smithsonian Institution, 1989b)

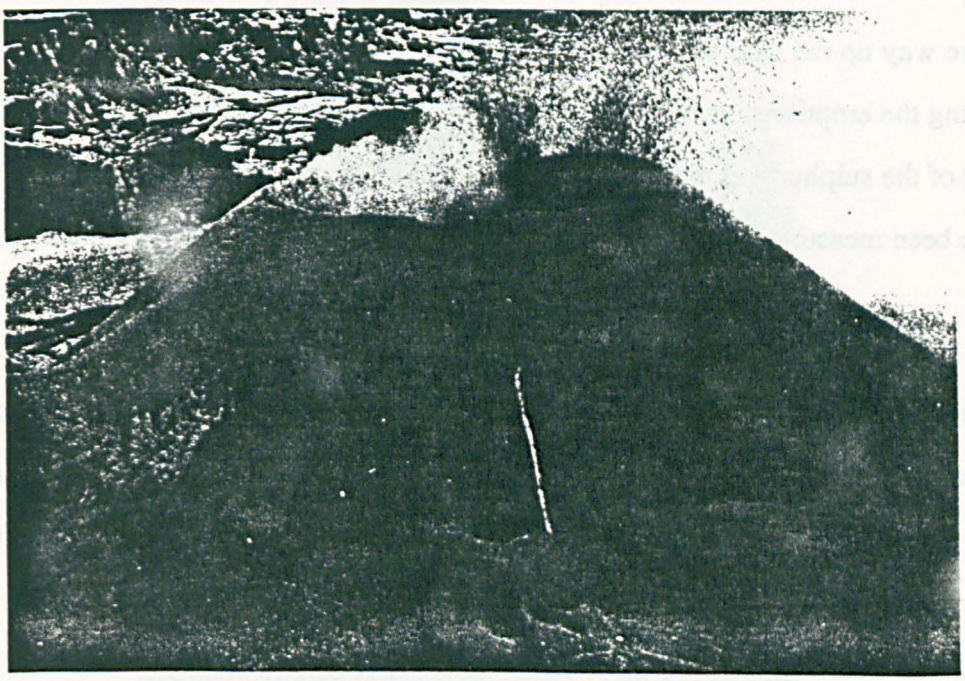

Figure A7.3. Active sulphur cone-with-crater, at Southeast Site on 13th April, 1990. The stick is 1.15 m in length; (the depressions to its left are footprints).

A7.3.2. Cone-with-crater.

When the crater bottom was next visited, less than 24 hours later, on the 13th April at 0900 hours, a 1.8 m high cone of pale greenish-yellow sulphur tephra had been established at the site of the earlier mud/sulphur "geysers" (Figure A7.3). Eruptions continued at the rate of about one per second, projecting sulphur tephra up to 3 m above a 2.7 m diameter crater lip. Much of the tephra fell within this crater. During an approximately 2 hour period, gas pulses varied in frequency and intensity, although little

new material was added to the cone. The ejecta appeared to be substantially finer grained than during the previous day's activity when more mud may have been incorporated. At this stage, the cone had a basal diameter of about 7 m and sides at an angle of almost 40 ° from the horizontal, and its surface layers were composed of loose, unwelded sulphur tephra. Small-scale mass-wasting of material down the slopes of the cone was frequent. The relatively low temperature of the ejecta was confirmed by thermocouple readings taken with the probe pushed into the substrate of the cone at various points - a maximum temperature of 96.7 °C was recorded close to the crater lip. Temperatures about a third of the way up the side of the cone were around 55 °C. The exit temperature of the gas driving the eruptions is unlikely to have exceeded the maximum value by much since the bulk of the sulphur was clearly not molten. Gas temperatures in the region of 90-100 °C have been measured at the Southeast Site fumaroles (Smithsonian Institution, 1990b).

The cone was climbed, and video records made of the activity within its funnel-shaped crater. Inner crater walls were steep and parts of them caved in frequently. About 0.75 m below the crater lip, a bed of solid sulphur fragments was maintained in near continuous agitation by the upwards stream of gases. A steady, diffuse white plume of condensed gases emanated from the crater.

A7.3.3. Mature cone

Between 1100 and 1115 hours, the active sulphur volcano filled its crater and built an almost perfect cone, taking its eventual height to about 2.9 m above base (Figure A7.4). During this stage, discharge of gas and sulphur tephra was restricted to a roughly 10 cm diameter vent at the apex of the cone. As a result of this constriction in the vent, a steady stream of gases and particulate sulphur developed, rising 10 m above the vent. Occasionally, discharge was blocked for a few seconds, before being cleared by bursts of gas; otherwise a near-vertical plume was sustained for about one hour, depositing a carpet of sulphur up to at least 15 m downwind from the cone. Sulphur tephra still did not weld to the sides of the cone, although a 10-20 cm high chimney-like structure developed

at the vent apex. Some liquid, possibly molten sulphur or condensates, appeared to be adhering to the lips of the vent as the gas rushed through. Shortly after 1200 hours, emission from the cone subsided to intermittent pulses of gas and sulphur particles. Although the total volume of tephra erupted was not estimated, that of the cone was approximately 40 m^3.

Figure A7.4. Active mature cone at Southeast Site on 13th April, 1990. The height of the cone is about 2.9 m above base.

A7.3.4. Destruction

After their short, active lives, the sulphur cones were destroyed. Although this was not observed in progress, remnants of destroyed cones were sometimes seen less than a day after their construction. The first sulphur pool observed in 1989 was contained within the remains of a cone from which a large sector had been lost

(Oppenheimer and Stevenson, 1989). However, not all the edifices were destroyed in this way: some, particularly at the periphery of the active site, remained dormant and intact for periods of days, subject to water erosion, and deposition from the quiescent gas plume which emerged from the centre of the crater. Possible mechanisms for destruction of cones are discussed later.

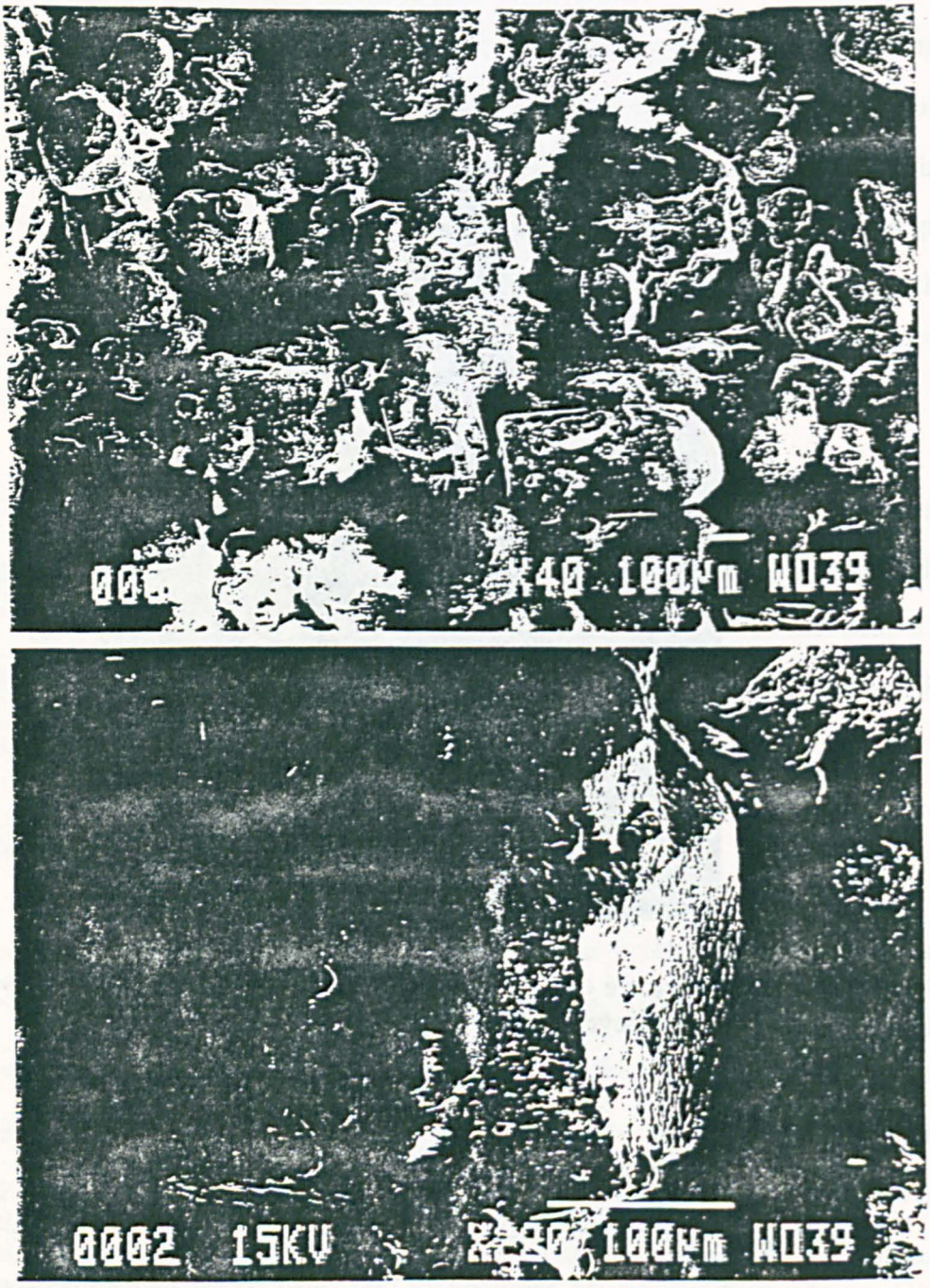

Figure A7.5. Scanning electron micrographs of a sample of sulphur tephra erupted at Poás on 13th April 1990. Many sulphur grains show well-developed crystal faces.

A7.4. Sulphur tephra

The nature of sulphur deposits erupted during construction of the miniature cones at Poás raises interesting questions concerning their modes of formation. Microscopic inspections (SEM and ordinary light) reveal the following components:

(a) Individual subhedral to euhedral, equant crystals of sulphur, apparently orthorhombic, and generally less than 500 μm across (Figure A7.5). Crystal surfaces appear smooth or show parallel ridges with flake-like protrusions under the SEM.

(b) Well-rounded, equant sulphur grains up to about 1 mm in diameter, some showing remnants of crystal faces.

(c) Cemented aggregates of crystals and rounded grains of sulphur which exceed about 850 μm in diameter and dominate size fractions > 1.4 mm (Figure A7.6). These include small particles adhering to single, larger grains, aggregates of equidimensional grains which have fused together to varying extents, and accretionary lapilli up to 5 cm across (Figure A7.7).

(d) Accidental lithics, probably clays derived from the lake sediment (concentrated proportionaly in the smaller size fractions).

(e) Chemical, possibly vapour phase, precipitates on the surfaces of other particles, visible at low magnification under ordinary light microscope. A white flaky mineral adheres to the exterior of sulphur grains, and cavities in the accretionary lapilli have coatings of fine white crystals. Qualitative EDS analysis, and crystal morphologies seen under the SEM suggest this may be gypsum which, along with amorphous silica, is one of the principal chemical sediments at Poás (Brantley *et al.*, 1987).

Although the sulphur is not markedly vesiculated, bulk densities of tephra samples, measured in the laboratory, are relatively low - in the region of 1240 kg m^{-3} (cf. density of pure sulphur about 2000 kg m^{-3}). Granulometry of the tephra deposits is displayed by the graphs in Figure A7.8. These deposits are, however, quite unlike the pyroclastic sulphur ejected by phreatic bursts through the crater lake during the 1970's (Figure A7.9). This material was highly vesicular, and the morphological and grain size similarities to basaltic scoria led Francis *et al.* (1980) to suggest that temperatures had been sufficiently elevated (up to 200 °C) to take the melt into the high viscosity field. In addition, they differ from a further distinct kind of sulphur ejecta commonly found within the inner crater, which is un-vesiculated, yellow in colour (Munsell 7.5 Y 8.5/ 6), and has grain-shapes reminiscent of basaltic achneliths (Figure A7.10). Ohashi (1919) also noted sulphur "grains" at Kusatsu-Shirane volcano, which he suggested might be fragments of sulphur which were still liquid when they burst in the air having travelled through the crater lake.

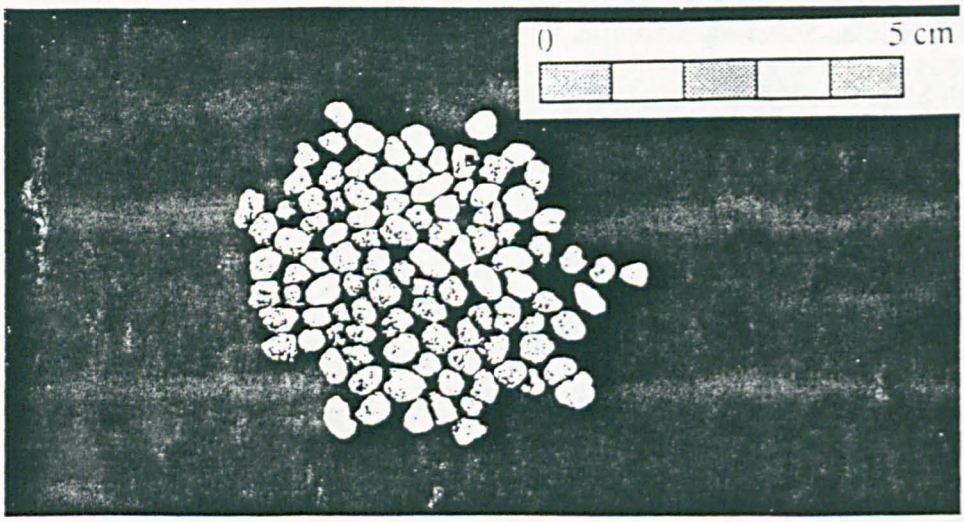

Figure A7.6. Photograph of tephra in 2.8-4 mm size fraction, collected at Poás on 13th April, 1990. These are aggregates of small sulphur particles.

A7.4.1. Accretionary lapilli

Accretionary sulphur lapilli up to 5 cm in diameter were collected during the

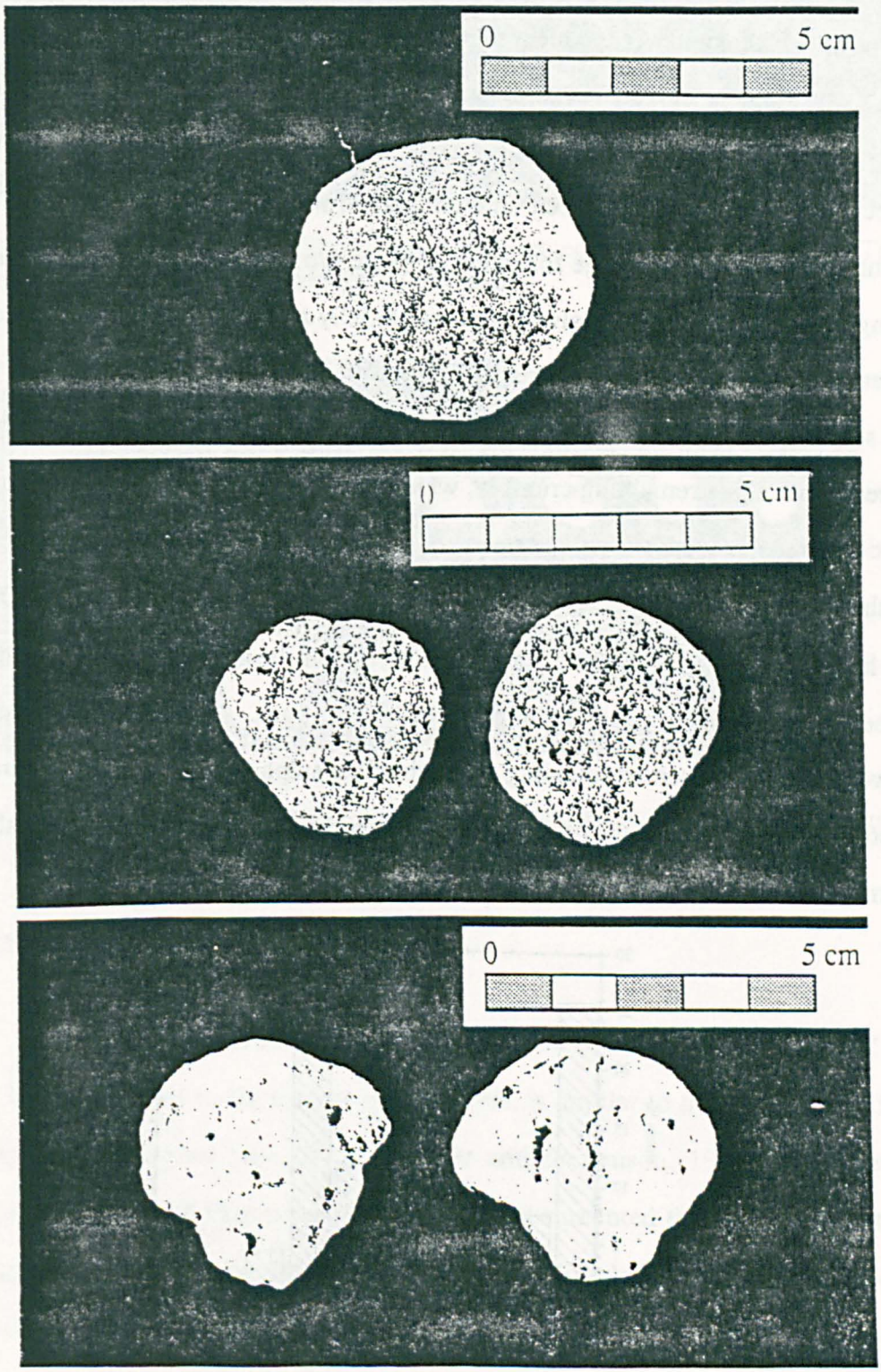

Figure A7.7. Photographs of accretionary sulphur lapilli erupted at Poás on 13th April, 1990 (one whole and two sectioned).

activity described above. Most are quite spherical and display a weak concentric layering (Figure A7.7) but some are more tabular and irregularly shaped. Bulk densities range between 900-1500 kg m^{-3} (equivalent to porosities of 25-55 %); the largest has a mass of about 50 g. While accretionary lapilli in silicate ash deposits owe their binding forces to either capillary attraction of fluid bridges of condensed vapour phases between particles, or electrostatic attraction between smaller grains, the individual components of the sulphur accretions are too large for either of these processes to be likely. Alternative binding mechanisms might involve fusion of partially remelted grains, introduction of a separate molten sulphur phase, or possibly crystallisation of a vapour phase. The first of these seems most likely since a gradation in the fusion of individual particles in lapilli is apparent, with some remaining crumbly, while others, whose constituent sulphur grains can still be recognised, are well consolidated (Figure A7.7). Inspection under the SEM also shows some fluidal contacts (Figure A7.11). Agglomeration of the sulphur particles must have taken place within the conduit and crater of the active cones, where material was being turned over almost continuously by bursts of gas. This agitation is also likely to have caused the observed rounding of much of the sulphur tephra. The appearance of accretionary lapilli around the mud/sulphur geysers may indicate that they were also able to form in water-filled fumarole vents.

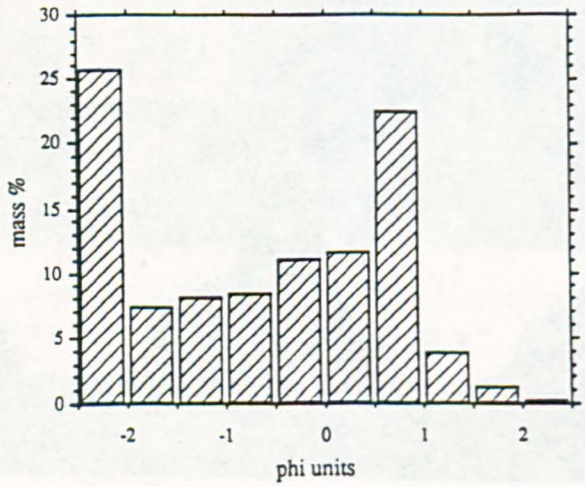

Figure A7.8. Grain-size frequency curve of sulphur tephra erupted at Poás on 13th April, 1990. The sample was collected from the side of a cone, about 1 m from the vent.

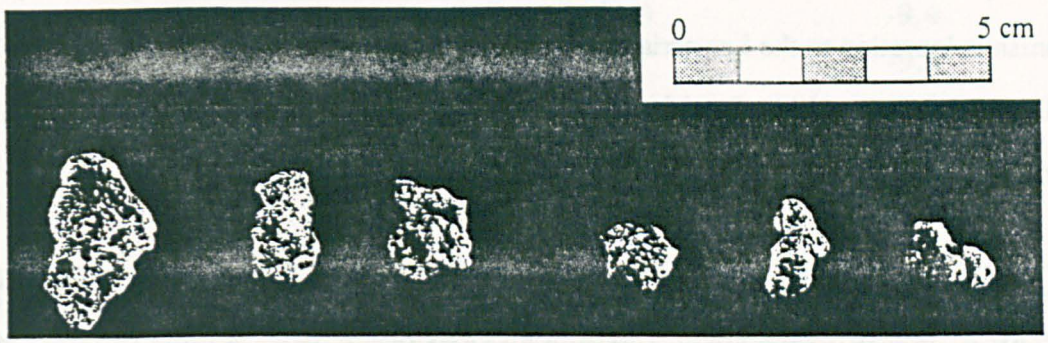

Figure A7.9. Photograph of pyroclastic sulphur collected at Poás in 1979, by R. Thorpe. The tephra is dark coloured and markedly vesicular.

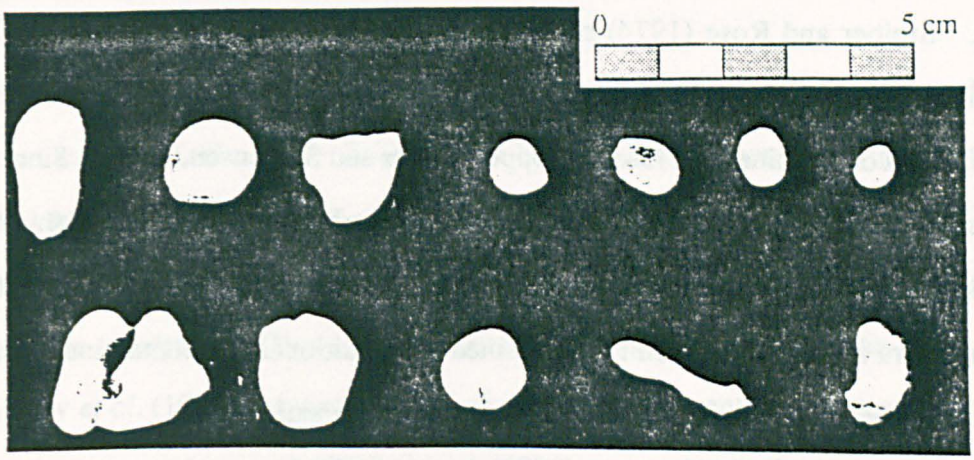

Figure A7.10. Yellow, non-vesicular sulphur pyroclasts collected close to the Southeast Site in 1989 and 1990.

A7.4.2. Colouration

The greenish colouration of the sulphur tephra (close to Munsell 2.5 GY 7/ 4), which is not confined to the surface of fragments, is similar to that observed in frozen samples of the sulphur lakes (Oppenheimer and Stevenson, 1989). Bennett and Raccichini (1978) and Francis *et al.* (1980) also documented the green colouration of pyroclastic sulphur deposits collected at Poás. Interestingly, shades of green have been reported for some other volcanic sulphur deposits known to have passed through the liquid phase: Watanabe (1940) noted a "light green to yellowish green color" of some of the sulphur erupted at Siretoko-Iôsan; Ohashi (1919) observed colours of spherules collected from the crater lake of Kusatsu-Shirane ranging from "dirty greenish-yellow to

sulphur-yellow", most being of the former colour; and Naranjo (1985) reported a pale-greenish colouration to the Lastarria flows at source. The captain of the second recorded landing party to visit White Island, in 1854, remarked on crystalline sulphur carpeting the crater floor as resembling a "meadow of gorgeous green" (Luke, 1959).

The colours of pure quenched sulphur depend on the allotropes present and hence the temperatures of formation and cooling histories of the melt. Colour differences in sulphur collected at Poás might therefore reflect different melt temperatures, and/or the effects of subaqueous versus subaerial quenching. In addition, impurities may impart colour. Stoiber and Rose (1974) reported abnormally seleniferous, orange-coloured sulphur collected at Poás. Frozen sulphur pool samples collected in 1989 also showed trace amounts of selenium and arsenic (Oppenheimer and Stevenson, 1989). Since much of the sulphur recently erupted at Poás is likely to have been recycled a number of times by remelting and remobilisation at fumarolic sites, it seems likely that the colouration of sulphur tephra at Poás is the result of combined compositional and contamination effects (particularly, perhaps, by incorporation of grey lake sediment).

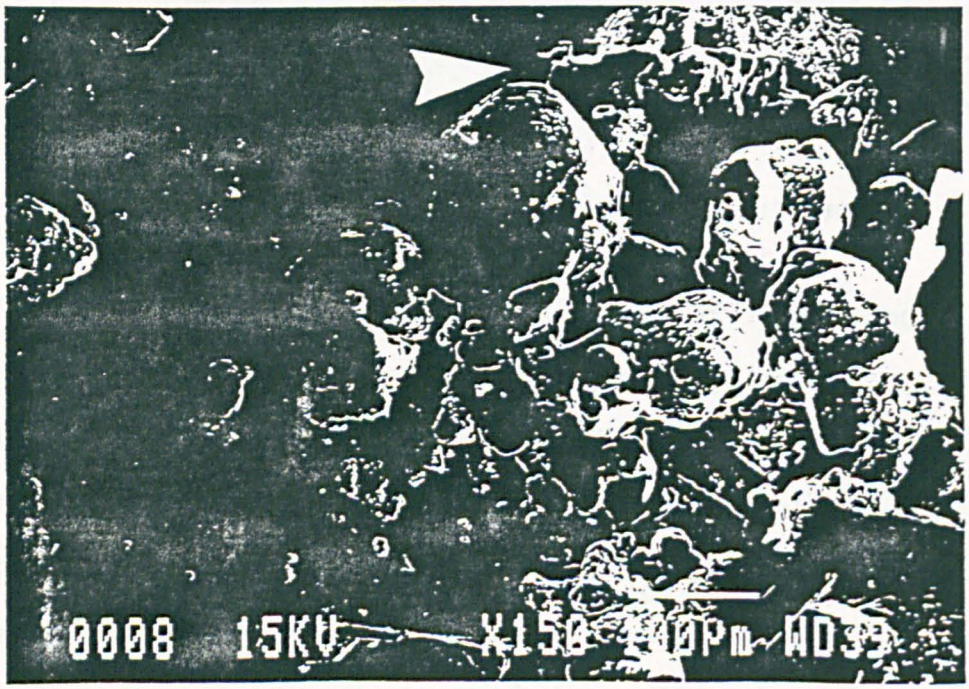

Figure A7.11. Scanning electron micrograph of sulphur tephra showing filamentous contact between two individual grains (arrow). Other grains appear to be fused together.

Sample number	Type of native sulphur	$\delta^{34}S$ (‰ relative to CDT)
POA 79/1	pyroclastic sulphur (collected 1979)	-9.4
POA 90/P	yellow "achnelith" (collected 1990)	-9.8
POA 90/1/2	sulphur tephra erupted on 13 April 1990	-10.2
POA 89/1/1	active sulphur pond (21 April 1989)	-11.8
POA 90/F	yellow, crystalline block in lake sediment (collected 1990)	-12.3

Table A7.1. Sulphur isotope variation in elemental sulphur samples collected at Poás. Analyses performed by J. Maynard at the Open University using a 602E mass spectrometer. Accuracy approximately ± 0.2 ‰.

A7.4.3. Isotope data

Sulphur isotope measurements of tephra and other elemental sulphur deposits collected at Poás (Table A7.1) show them to be among the isotopically lightest reported volcanic native sulphur deposits, with $\delta^{34}S$ values ranging between -12.3 ‰ and -9.4 ‰ relative to CDT. For comparison, the $\delta^{34}S$ of 140 native sulphur samples collected from 44 volcanic localities in Japan ranged between -9 ‰ and +7 ‰ (Ueda *et al.*, 1979), Menyailov *et al.* (1986) measured a $\delta^{34}S$ of -3.8 ‰ for elemental sulphur collected in the crater of Momotombo, and Williams *et al.* (1990) reported a single measurement of -2.4 ‰ at Nevado del Ruiz, Colombia. All of these are more enriched in ^{34}S than the Poás samples. However, recent sampling at White Island (Giggenbach and Matsuo, 1991; Giggenbach, written commun. 1991) has revealed $\delta^{34}S$ content down to -15 ‰ in both H_2S and elemental sulphur in low temperature (111 °C) vapour discharges, closely comparable with the Poás data.

A7.5. Discussion

A7.5.1. Origin of sulphur at Poás

Oppenheimer and Stevenson (1989) considered that melting and remobilisation of fumarolic deposits contained in the lake sediments provided the sulphur in the active

ponds. Much of the sulphur almost certainly originated from subaqueous reactions of fumarolic gases, notably disproportionation of SO_2 (Giggenbach, 1987):

$$3SO_2\ (g) + 2H_2O\ (g/l) = 2H_2SO_4\ (aq) + \tfrac{1}{x}S_x\ (l/s) \qquad (A7.1),$$

or indirectly:

$$4SO_2\ (g) + 4H_2O\ (g/l) = 3H_2SO_4\ (aq) + H_2S\ (g) \qquad (A7.2),$$

followed by:

$$H_2SO_4\ (aq) + 3H_2S\ (g) = \tfrac{4}{x}S_x\ (l/s) + 4H_2O\ (g/l) \qquad (A7.3).$$

In acid aqueous environments, the SO_2 disproportionates almost quantitatively. Any H_2S present can be oxidised to elemental sulphur by a variety of agents including SO_2, O_2, H_2O, H_2SO_4 and Fe^{3+} (Giggenbach, 1987; Giggenbach and Matsuo, 1991), e.g.:

$$2H_2S\ (g) + SO_2\ (g) = 2H_2O\ (g) + \tfrac{3}{x}S_x\ (l/s) \qquad (A7.4),$$

and:

$$2H_2S\ (g) + O_2\ (g) = 2H_2O\ (g) + \tfrac{2}{x}S_x\ (l/s) \qquad (A7.5).$$

Native sulphur may also have been deposited in the aqueous lake via hydrolysis of intermediate polythionate ions (Takano and Watanuki, 1990), e.g.:

$$3S_3O_6^{2-}\ (aq) + 2H_2O\ (g) = \tfrac{4}{x}S_x\ (l/s) + 5SO_4^{2-}\ (aq) + 4H^+\ (aq) \qquad (A7.6).$$

Rowe *et al.* (1991b) have reported polythionate ion concentrations ($[H_2S_xO_6]$, $4 \leq x \leq 6$) exceeding 4000 ppm in lake water at Poás, and suggested that such enrichment reflected low ratios of SO_2/H_2S in the subaqueous fumaroles.

Suspended sulphur is a common occurrence in active crater lakes and has been documented at several volcanoes, including El Chichón, Mexico, where nearly a quarter of collected suspended solids was elemental sulphur (Casadevall *et al.*, 1984a).

Disseminated sulphur, and sulphur pipes, veins and tubes, are present within the lake sediments at Poás (Prosser and Carr, 1987); bulk analyses of several lake sediment samples collected mainly from exposed terraces on the southern and eastern lakeshores at Poás revealed an average elemental sulphur content of 4.5 ± 1.0 % (Rowe *et al.*, in prep.), although the proportions of native sulphur deposited may well be significantly greater closer to sites of contemporaneous subaqueous fumarolic discharge. At White Island, shallow boreholes sunk into the desiccated crater lake bed in 1885 penetrated two 1 m thick seams of sulphur (Luke, 1959) which may well have been fossil analogues of the liquid sulphur bodies at Poás. Since 1989, sulphur ponds have been observed intermittently at Poás; it is likely that they would crust over during heavy rainfall which would also carry mud into the pits. Although little of the tephra was dispersed far beyond the field of cones, and much of the sulphur remained available for recycling, volatilisation is likely to have removed some from the reservoir. However, the liquid bodies could also have been replenished by condensation of any sulphur vapour present in the fumarolic gases that pass through, and by continued reaction of H_2S and SO_2 (A7.4).

The isotopic ratio of native sulphur deposited from fumarolic gases reflects the isotopic equilibrium achieved between sulphur species present, and the reaction path by which the sulphur is deposited. A number of factors are influential, including temperature, pressure, oxygen fugacity, and the ratio of total sulphur species to water (Ueda *et al.* 1979). Fractionation between hydrogen sulphide and sulphur dioxide which takes place by the following reaction:

$$H_2{}^{34}S + {}^{32}SO_2 = H_2{}^{32}S + {}^{34}SO_2 \qquad \text{(A7.7)}$$

is said to account for much of the spread in isotopic ratios found in subaerially precipitated fumarolic sulphur. Thode *et al.* (1971) demonstrated the dependence of the equilibrium constant for (A7.7) on temperature - at lower temperatures, the hydrogen sulphide is more depleted in ^{34}S relative to sulphur dioxide. Sakai and Nagasawa (1958)

observed this fractionation in gases collected at Showashinzan volcano, Japan, as did Menyailov *et al.* (1986) in 105-790 °C fumarole gases collected at Volcán Momotombo, Nicaragua. A further consideration is a kinetic isotopic effect which occurs in the deposition of native sulphur by (A7.4). In laboratory experiments at 25, 200 and 280 °C, Grinenko and Thode (1970) found that $^{32}SO_2$ reacted around 1.6 % faster than $^{34}SO_2$.

However, the unusually low values of $\delta^{34}S$ measured for Poás sulphur (Table A7.1) are most readily understood if it is accepted that most of the sulphur formed in the low-temperature, acid aqueous environment of the lake (equations A7.1-A7.3). Oana and Ishikawa (1966) presented experimental results showing a 20 ‰ fractionation between ^{34}S in sulphuric acid and elemental sulphur produced by the disproportionation of sulphur dioxide in aqueous solution (A7.1), at temperatures between 150 and 300 °C. The $\delta^{34}S$ of the precipitated sulphur ranged between -8.1 and -13.5 ‰ (with respect to the starting sulphur dioxide which was assumed to have a $\delta^{34}S$ of 0 ‰). This matches closely the spread of $\delta^{34}S$ values, -9.4 to -12.3 ‰, measured for Poás samples (and similarly low $\delta^{34}S$ values measured in elemental sulphur vapour discharges at White Island [Giggenbach and Matsuo, 1991]). The phenomenon of volcanic native sulphur that is markedly depleted in ^{34}S may be prevalent wherever it is formed in aqueous solution, i.e. in crater lakes and deep brines of hydrothermal systems.

A7.5.2. Mechanisms of sulphur eruptions at Poás

What eruptive mechanism was behind the formation of the sulphur volcanoes at Poás ? They are wholly unlike 0.5 m high "sulphur cones" at Volcán Azufre, Galapagos Islands, reported by Colony and Nordlie (1973). These were "delicate" and formed of a "loosely-packed crystalline mass of bright yellow sulphur" produced at slow rates by precipitation from fumarole gases (Colony and Nordlie, 1973). However, 3 m high cones of crystalline sulphur with "steam jets" observed within the crater of White Island in 1870 (Luke, 1959) may well have been similar to the recent phenomenon at Poás,

given that they, too, formed within an active crater that intermittently contained a hot aqueous lake. Unfortunately, it appears that no other details of these features have been recorded.

Destruction of sulphur cones at Poás has revealed pits of bubbling, molten sulphur, and it is reasonable therefore to suppose that, when active, they are underlain by bodies of liquid sulphur which extend over fumarolic conduits. The 28 x 15 m and 24 x 11 m dimensions of the sulphur ponds observed in April 1989 (Oppenheimer and Stevenson, 1989) indicate that such molten sulphur chambers may well be more laterally extensive than the small size (< 8 m basal diameter) of individual cones might suggest. Indeed, a single such body could underlie several cones.

The most plausible eruptive mechanism for the sulphur cones is, then, an expulsion of a liquid or partly crystallised spray from a molten sulphur chamber. Such a process is analogous, in some respects, to the mechanism of strombolian eruptions (Wilson, 1980) except that the driving volatiles are not exsolving from the melt itself but are fumarolic gases of the magmatic-hydrothermal system beneath the crater. (Analysis of a gas sample collected near the Southeast Site in November 1990 by W. Giggenbach suggested that it was not a primary volcanic-magmatic fluid but a mixture of re-evaporated lake water and fumarolic sulphur [W. Giggenbach, written commun., 1991]). Only a comparatively small volume of liquid needs to be carried off to account for the volume of a cone: for example, a typical cone of 40 m^3 of sulphur at bulk density 1240 kg m^{-3} corresponds to only 27 m^3 of liquid sulphur of density 1800 kg m^{-3} (although this is, of course, an underestimate since material dispersed beyond the cone is not included). In addition, the discontinuous eruption rate could be interpreted as a result of spasmodic release of pressure and foaming of liquid sulphur out of the chamber.

Temperatures in the molten sulphur reservoir at the Southeast Site were probably close to the 116 °C measured in the ponds in 1989, and almost certainly did not exceed

159 °C since there was no evidence for plastic sulphur that had been polymerised[1]. The temperatures measured close to the eruptive vents were little below 100 °C suggesting that there was only a slight thermal gradient in the whole system. The fusion of sulphur particles within the conduit to form accretionary lapilli also suggests that temperatures were close to the liquidus. This may explain the well-developed crystals of sulphur in the tephra; as the molten spray ascended within the vent prior to eruption, it was quenched at temperatures only slightly below the liquidus (Figure A7.12). In practice, the freezing point of sulphur depends on a number of factors, including the pressure and temperature history of the melt, and impurities it contains. Cooling of molten sulphur can involve different reaction paths with the result that different metastable mixtures of allotropes can be produced (Meyer, 1976). In the laboratory, the measured freezing point of remelted samples of Poás sulphur tephra varied between 100-105 °C when there was no agitation, and between 109-111 °C when the liquid was stirred.

---

[1] However, Gary Rowe and Jorge Barquero recorded a temperature of 159 °C in a 6 x 3 m pit of greyish-green liquid sulphur located at the northeast periphery of the lakeshore ("burning fumarole" site of Figure A7.2) in March 1990 (Smithsonian Institution, 1990a). Their observations (written commun., 1991) follow: "Adjacent to the sulphur pool was an approximately 2.5 metre high cone with a 1.0 m wide vent which periodically ejected dark green globs of liquid sulphur several metres above the lip of the cone... most material landing on the sides of the cone where it quickly solidified. Temperature of a freshly ejected glob was measured at 135 °C prior to solidification. The liquid sulphur pool which fed this activity was about a metre below the base of the cone and also displayed a temperature of 159 °C. The globs were flattened and possessed irregular shapes with maximum dimensions of about 20 cm and maximum thicknesses of 2-3 cm. Similar activity had formed two other cones of similar size and form near the lake's edge..... The whole area surrounding these cones was composed of a hardened floor of the cooled sulphur/ sediment mixture (about 100 m^2)". Rowe (written commun., 1991) likens this eruptive style to that associated with formation of basaltic spatter cones, and suggests that the significantly higher fumarole temperatures result in the differences from activity at the Southeast Site.

An alternative eruption mechanism could involve the formation of solid sulphur by direct deposition from fumarolic gases, possibly by reactions (A7.4) or (A7.5). Low temperature volcanic vapours may contain a significant proportion of their total sulphur in elementary form (Giggenbach, 1991), and Poás fumarole emissions do contain particulate sulphur (G. Brown, oral commun., 1991). Colony and Nordlie (1973) suggested that reaction (A7.5), taking place at temperatures below 130 °C, was the main mechanism for precipitation of sulphur at fumarole vents of Volcán Azufre, Galapagos Islands, and estimated sulphur deposition rates of 2.55×10^{-6} kg m^{-2} s^{-1}. Such slow rates are orders of magnitude less than cone-building rates at Poás. Certainly, when the sulphur ponds were exposed at the surface, although some precipitation of bright yellow sulphur took place around their rims, there was clearly no 'snow' of sulphur crystals falling from the emerging gas plume sufficient to build a cone. Moreover, the estimated mass fluxes of sulphur erupted to form cones could not be supported by realistic gas fluxes: assuming a value of $x = 8$ in equation (A7.5), for every mole of sulphur precipitated, 8 moles of H_2S are required. The most rapid phase of cone growth was observed during infilling of the 'cone-with-crater' to produce a near-perfect cone, adding a volume of at least 4 m^3 in 15 minutes This corresponds to a mass eruption rate of 5.5 kg s^{-1} (density = 1240 kg m^{-3}) of sulphur tephra, or 22 mol s^{-1} (RMM of S_8 = 0.2568 kg). If equation (A7.5) is assumed to go completely to the right hand side (Colony and Nordlie, 1973), then a corresponding flux of 170 mol s^{-1} of H_2S are required, or 3.9 m^3 s^{-1} at STP. The material was being ejected from a narrow pipe of about 5 cm radius, which would indicate that even if the gas expelled were pure H_2S (and gas analyses on the near-dry crater floor in February 1989 revealed only 0.36 vol% H_2S [Rowe *et al.*, 1991a]), then ridiculously high velocities of the order of 500 m s^{-1} would be necessary to sustain the flux. Precipitation of sulphur from vapour may well, however, be responsible for the 'chimneys' which often surmounted sulphur cones at Poás.

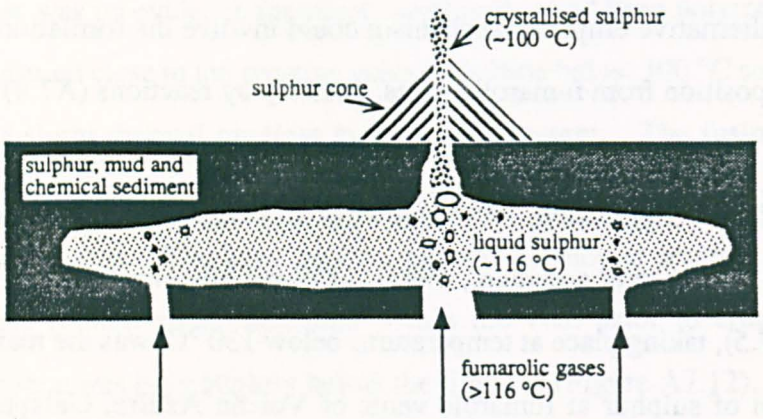

Figure A7.12 Schematic diagram of the postulated mechanism of sulphur eruptions at Poás.

Further evidence for the sulphur tephra being a crystallised spray of liquid rather than a directly precipitated 'snow', is its green colour. Gas-precipitated sulphur observed at Poás was bright yellow, for example around the margins of the active sulphur ponds and at the apices of inactive cones from which gases escaped weakly. Sulphur quenched from the ponds froze to a similar pale green colour as the tephra, indicating that the tephra was most probably derived from an equivalent melt.

A7.5.3. Destruction of sulphur cones

The sulphur cones had relatively short life-spans (a few tens of hours to a few days), though cone sectors sometimes remained after partial destruction. They could have been destroyed (a) explosively, and/or, (b) by collapse. Clogging of fumarole vents, resulting from increased viscosity of the sulphur melt, due to either temperatures exceeding 159 °C or mixture with greater proportions of lake sediments, might have caused evisceration of cones through increases in gas pressure. Hurst *et al.* (1991) suggested that temperature increases in a layer of liquid sulphur beneath the aqueous lake at Mount Ruapehu, such that it passed into and then out of the polymerisation phase, were responsible for phreatic eruptions there. However, there was no evidence for quenched plastic sulphur erupted from the Southeast Site cones at Poás and it is unlikely

that such elevated temperatures were ever reached there, although this may well have been the case at hotter fumarole vents elsewhere. A more reasonable hypothesis for destruction of the cones is that melting within the edifices, or water saturation, caused them to founder under their own weight. In a comparable manner, sulphur cones at Volcán Azufre, Galapagos Islands, toppled occasionally; upper portions of the cones which collapsed inwards melted, clogging the vent and resulting in the ejection of "balls of spatter" (Colony and Nordlie, 1973).

A7.5.4. Major sulphur-rich explosive eruptions at Poás ?

Volcanoes are the primary natural source of sulphur dioxide, and can influence the physical behaviour of the atmosphere (Rampino *et al.*, 1988). Several volcanoes have high non-eruptive SO_2 fluxes, including Mount Etna, Italy (Allard *et al.*, 1991), Nevado del Ruiz, Colombia (Williams *et al.*, 1990) and Masaya, Nicaragua (Stoiber *et al.*, 1986) of the order of 1000's of t d^{-1}, as estimated by Correlation Spectrometer (COSPEC). A flux of 700 t d^{-1} of SO_2 was estimated at Poás by this method in 1982 (Casadevall *et al.*, 1984b). At several volcanoes, the observed SO_2 fluxes appear greatly to exceed the amount that could be sustained by exsolution from known or inferred volumes of magma (Williams *et al.*, 1990, Andres *et al.*, 1991). Various possible causes for this discrepancy have been considered, including degassing from large, deep magma bodies (Giggenbach *et al.*, 1990; Williams *et al.*, 1990), a sulphur-rich gas phase from an underplating basaltic magma (Fournelle, 1990), assimilation of sulphide-bearing wall rock, evaporites or fumarolic sulphur deposits (Williams *et al.*, 1990), and the potential for a separate free volatile phase existing in the magma prior to eruption (Sigurdsson *et al.*, 1990).

The sulphur content of magmas discharged in plinian eruptions also seems to be an important factor in their potential climatic effects (Rampino and Self, 1984; Jakosky, 1986; Hoffmann, 1987; Hoffmann *et al.*, 1987). A minor eruption at Poás in April 1989 produced a convecting plume, coloured yellow and orange (D. Stevenson, oral

commun., 1989), presumably by elemental sulphur scavenged from fumarolic deposits. Analysis of ashfall at the northwest and west rims of the crater at Poás revealed 19 % by weight of native sulphur (G. Soto, written commun., 1991). Could a large explosive eruption at Poás be unusually sulphur-rich ?

Aqueous lakes filling active craters appear to provide an efficient way to produce and concentrate native sulphur deposits in a short time, reactions (A7.1)-(A7.3). A 'back of the envelope' estimation of the amount of sulphur that could be deposited at Poás in the roughly twenty year period since the aqueous lake has been present can be made as follows. The input of steam which condenses within the hydrothermal system is about 70 kg s^{-1} based on energy and mass balance considerations of Brown *et al.* (1991), equivalent to a flux of approximately 4000 mol s^{-1}. Proportions of SO_2 in high temperature fumarole vapours at Poás, reported by Rowe *et al.* (1991a), range between about 2 and 7 mol%. Even at the lower end of this spread, the SO_2 flux corresponds to some 80 mol s^{-1}; (note that this is about one-tenth the daily flux from subaerial fumaroles estimated using COSPEC in 1982 [Casadevall *et al.*, 1984b]). If all this produced elemental sulphur by reaction (A7.1), then $\frac{1}{24}$ times as much S_8, ie. 3.2 mol s^{-1} or approximately 0.8 kg s^{-1}, would be precipitated. In twenty years, this amounts to over 5 x 10^8 kg. Every mole of S_8 volatilised and oxidised would provide 8 moles of SO_2 (RMM = 0.064 kg).

Just twenty years' worth of elemental sulphur could, therefore, yield about 10^9 kg of SO_2. This is a significant amount, although the potential atmospheric effects of an explosive release of this much SO_2 would depend on many other factors. It is roughly one-and-a-half times the Total Ozone Mapping Spectrometer (TOMS) derived estimate of 6.6 x 10^8 kg of sulphur dioxide released by the November 1985 Nevado del Ruiz eruptions (Krueger *et al.*, 1990), about 10 % of that estimated for the 1982 El Chichón eruption by air sampling (Hoffmann and Rosen, 1983), and 5-7 % of the estimated annual total global, eruptive and non-eruptive, volcanic SO_2 output (Berresheim and Jaescke, 1983; Stoiber *et al.*, 1987). While this calculation is distinctly speculative,

particularly because of the uncertainty in the flux of sulphur bearing gases (the 'magmatic' composition being chosen as most likely to reflect the *net* input of sulphur), a similar sulphur deposition rate of 0.26 kg s^{-1} was estimated by Rowe *et al.* (1991a). They suggested that much of this native sulphur might be deposited in voids left after dissolution of rock by the extremely corrosive hydrothermal brines.

A7.5.5. Implications for Io

The extent to which sulphur participates in volcanism of the jovian moon, Io, has been the subject of hot debate ever since the Voyager mission imaged its active surface (e.g., Sagan, 1979; Young, 1984). Identification of thermal anomalies on the surface, and the spectral characteristics of flow-like features extending from calderas, were taken by some workers to indicate eruptions of liquid sulphur, forming lakes (Pearl and Sinton, 1982; Lunine and Stevenson, 1985) and flows (Sagan, 1979; Pieri *et al.*, 1984). However, others have disputed the evidence and suggested instead that silicate volcanism and UV irradiation of sulphur dioxide frost (Hapke, 1989) or ferrous compounds (Young, 1984) could better account for spectral signatures of the surface. The argument swings from camp to camp - in a recent paper, Nelson *et al.* (1990) stated that elemental sulphur and sulphur dioxide *can* explain the whole UV and visible spectral albedo of Io. Whatever the truth concerning Io (and we shall hopefully have a much clearer picture, both in terms of spatial and spectral resolution, once the Galileo mission approaches the jovian system) the controversy sparked renewed interest in industrial sulphur flows (Greeley *et al.*, 1990) as well as the rare occurrences of terrestrial sulphur eruptions (e.g., Theilig, 1982; Greeley *et al.*, 1984).

The essential aspect of the sulphur volcanism at Poás is that it is gas-driven: the initial formation of sulphur deposits results from reaction of the fumarolic gases which then appear to have been responsible for melting and remobilising the precipitated sulphur, and ultimately, for maintaining temperatures within liquid sulphur bodies, replenishing them, and driving the frequent, cone-building sulphur eruptions.

Analogous processes could be taking place on Io albeit on a vastly greater scale. Remelting of fumarolic sulphur deposits could result from heat transferred from hot gases or proximal silicate lava bodies. Accumulation and mobilisation of liquid sulphur would be greatly facilitated if the melt had a low viscosity, as was the case at Poás, which would bracket likely temperatures. Liquid sulphur bodies could be maintained for long periods as a result of the passage of fumarolic gases, which can inhibit the growth of crusts and replenish evaporative losses by condensation of fresh sulphur.

As Greeley *et al.* (1990) emphasised, one should be cautious in interpreting the nature of the ionian surface by comparing its albedo with spectral measurements of pure laboratory materials. Their observations of industrial sulphur flows showed that standard tables of the physical properties of sulphur did not predict the actual colouration, freezing point and rheology of flows. Similarly, the yellow-green colouration of tephra at Poás suggests that impurities in the melt can be responsible for producing spectral characteristics different from that of pure sulphur. It is self-evident that one must exercise caution in drawing analogies between these terrestrial phenomena of a few 10's of metres scale, with features, many kilometres in dimensions, postulated to exist on Io. Nevertheless, students of ionian volcanism may note further implications that I have failed to recognise.

A7.6. Concluding remarks

The observations of active sulphur volcanoes at Poás are best explained by eruptions of a crystallised spray of sulphur from shallow chambers of the liquid, expelled by the passage of fumarolic gases. There is an interesting analogy to draw here with the Frasch process by which strata-bound elemental sulphur deposits have been worked in parts of Mexico and the USA (Shearon and Pollard, 1950). In this method, the sulphur is first melted by injection of steam, at 165 °C and 16 atm pressure, into the sulphur-bearing horizon through the outer pipe of a concentric three part array. The resulting liquid is then forced to the surface by injection of compressed air at 20 atm down the

central pipe. The sulphur emerges as a liquid foam from which the air is separated. At Poás, injection of fumarolic gases into the base of a body of liquid sulphur may be able to pressurise the melt such that, episodically, liquid sulphur is carried upwards, is crystallised, and is then erupted to build cones. During quiescent periods, the bursts of escaping, hot gas (close to the sulphur liquidus) have the effect of fluidising the bed of sulphur particles within the vent, and create appropriate conditions for partial annealing of sulphur crystals to form accretionary lapilli, and rolling to produce rounded grains.

It is important to recognise that this is largely a gas-driven system; changes in gas temperature, as well as the extent to which rainfall recharges the lake or carries sediment over the active region, will affect the nature of sulphur manifestations. The proportion of lake sediments mixed with the sulphur is also likely to influence the rheology of the material.

Crater lakes at active volcanoes can provide a favourable environment for the rapid concentration of large deposits of native sulphur; observations at several such volcanoes worldwide support this notion. Where this is the case, major explosive eruptions could result in considerable SO_2 release to the atmosphere.

A7.7. Acknowledgements

My thanks go to Jon Maynard for isotopic analyses and thoughts on their significance, Liz Harper and Naomi Williams for assistance with the SEM, Stuart Boyd, Geoff Brown, Peter Francis, Ron Greeley, Charles Harding, David Rothery, Hazel Rymer, Gerardo Soto and David Stevenson for discussions, Richard Thorpe for providing sample POA79/1, David Stevenson, Steve Hallinan and Ben van Wyk de Vries for sample POA 89/1/1, and José Badilla and Zaida Solis for friendly hospitality at the Parque Nacional del Volcán Poás. I am especially grateful to Gary Rowe for suggesting many improvements to the manuscript, and for furnishing me with preprints and his unpublished data, and Werner Giggenbach who enlightened me in aspects of aqueous

geochemistry. Fieldwork was funded by the Natural Environment Research Council of the United Kingdom.

A7.8. References

Allard, P., Carbonnelle, J., Dajlevic, D., Le Bronec, J., Morel, P., Robe, M.C., Maurenas, J.M., Faivre-Pierret, R., Martin, D., Sabroux, J.C. and Zettwoog, P., 1991. Eruptive and diffuse emissions of CO2 from Mount Etna. Nature 351: 387-391.

Andres, R.J., Rose, W.I., Kyle, P.R., deSilva, S., Francis, P., Gardeweg, M. and Moreno Roa, H., 1991. Excessive sulfur dioxide emissions from Chilean volcanoes. J. Volcanol. Geotherm. Res., 46: 323-329.

Banfield, A.F., 1954. Volcanic deposits of elemental sulphur. Canadian Mining Metallurgical Bull. 47; 769-775.

Bennett, F.D. and Raccichini, S.M., 1978. Subaqueous sulphur lake in Volcán Poás. Nature 271: 342-344.

Berresheim, H. and Jaescke, W., 1983. The contribution of volcanoes to the global atmospheric sulfur budget. J. Geophys. Res. 88: 3732-3740.

Brantley, S.L., Borgia, A., Rowe, G., Fernandez, J.F. and Reynolds, J.R., 1987. Poás volcano crater lake acts as a condenser for acid metal-rich brine. Nature 330: 470-472.

Brown, G., Rymer, H., Dowden, J., Kapadia, P., Stevenson, D., Barquero, J. and Morales, L.D., 1989. Energy budget analysis for Poás crater lake: implications for predicting volcanic activity. Nature 339: 370-373.

Brown, G.C., Rymer, H.R. and Stevenson, D.S., 1991. Volcano monitoring by microgravity and energy budget analysis. J. Geol. Soc. Lond. 148: 585-593.

Casadevall, T.J., de la Cruz-Reyna, S., Rose, W.I., Bagley, S., Finnegan, D.L. and Zoller, W.H., 1984a. Crater lake and post-eruption hydrothermal activity, El Chichón volcano, Mexico. J. Volcanol. Geotherm. Res. 23: 169-191.

Casadevall, T.J., Rose, W.I., Fuller, W.H., Hunt, W.H., Hart, M.A., Moyers, J.L., Woods, D.C., Chuan, R.L. and Friend, J.P., 1984b. Sulfur dioxide and particles in quiescent volcanic plumes from Poás, Arenal and Colima volcanoes, Costa Rica and Mexico. J. Geophys. Res. 89: 9633-9641.

Colony, W.E. and Nordlie, B.E., 1973. Liquid sulfur at Volcán Azufre, Galapagos Islands. Econ. Geol. 68: 371-380.

Fournelle, J., 1990. Anhydrite in Nevado del Ruiz November 1985 pumice: relevance to the sulfur problem. J. Volcanol. Geotherm. Res. 42: 189-201.

Francis, P.W., Thorpe, R.S., Brown, G.C. and Glasscock, J., 1980. Pyroclastic sulphur eruption at Poás volcano, Costa Rica. Nature 283: 754-756.

Giggenbach, W., 1974. The chemistry of Crater Lake, Mt Ruapehu (New Zealand) during and after the 1971 active period. New Zealand J. Sci. 17: 33-45.

Giggenbach, W.F., 1987. Redox processes governing the chemistry of fumarolic gas discharges from White Island, New Zealand. Appl. Geochem. 2: 143-161.

Giggenbach, W.F., Garcia P., N., Londoño C., A., Rodriguez V., L., Rojas G., N. and Calvache V., M.L., 1990. The chemistry of fumarolic vapor and thermal-spring discharges from the Nevado del Ruiz volcanic-magmatic-hydrothermal system, Colombia. J. Volcanol. Geotherm. Res. 42: 13-39.

Giggenbach, W.F. and Matsuo, S., 1991. Evaluation of results from Second and Third IAVCEI Field Workshops on Volcanic Gases, Mt Usu, Japan, and White SIland, New Zealand. Appl. Geochem. 6: 125-141.

Grange, L.I., 1959. In White Island, Ed Hamilton WM and Baumgart IL, NZ Dept. Sci. Ind. Res. Bull. 127: :25-31.

Greeley, R., Theilig, E. and Christensen, P., 1984. The Mauna Loa sulfur flow as an analog to secondary sulfur flows (?) on Io. Icarus 60: 189-199.

Greeley, R., Lee, S.W., Crowm, D.A. and Lancaster, N., 1990. Observations of industrial sulfur flows: implications for Io. Icarus 84: 374-402.

Grinenko, V.A. and Thode, H.G., 1970. Sulfur isotope effects in volcanic gas mixtures. Can. J. Earth Sci. 7; 1402-1409.

Hapke, B., 1989, The surface of Io: a new model. Icarus 79: 56-74.

Hoffmann, D.J., 1987. Perturbations in the global atmosphere associated with the El Chichón volcanic eruption of 1982. Rev. Geophys. 25: 243-259.

Hoffmann, D.J. and Rosen, J.M., 1983. Stratospheric sulphuric acid fraction and mass estimate for the 1982 volcanic eruption of El Chichón. Geophys. Res. Lett. 70: 313-316.

Hoffmann, D.J., Rosen, J.M., Harder, J.W. and Rolf, S.R., 1987. Observations of the decay of the El Chichón stratospheric aerosol cloud in Antarctica. Geophys. Res. Lett. 14: 614-617.

Hurst, A.W., Bibby, H.M., Scott, B.J. and McGuinness, M.J., 1991. The heat source of Ruapehu crater lake; deductions from the energy and mass balances. J. Volcanol. Geotherm. Res. 46: 1-20.

Jakosky, B.M., 1986. Volcanoes, the stratosphere, and climate. J. Volcanol. Geotherm. Res. 28: 247-255.

Krueger, A.J., Walter, L.S., Schnetzler, C.C. and Doiron, S.D., 1990. TOMS measurement of the sulfur dioxide emitted during the 1985 Nevado del Ruiz eruptions. J. Volcanol. Geotherm. Res. 41: 7-15.

Luke, J., 1959. In White Island, Ed Hamilton WM and Baumgart IL, NZ Dept. Sci. Ind. Res. Bull. 127: 14-24.

Lunine, J.I. and Stevenson, D.J., 1985. Physics and chemistry of sulfur lakes on Io. Icarus 64: 345-367.

Menyailov, I.A., Nikitina, L.P., Sharpar, V.N. and Pilipenko, V.P., 1986. Temperature increase and chemical change of fumarolic gases at Momotombo volcano, Nicaragua in 1982-1985: are these indicators of a possible eruption ? J. Geophys. Res. 91: 12199-12214.

Meyer, B., 1976. Elemental sulfur. Chem. Rev. 76: 367-388.

Naranjo, J.A., 1985. Sulphur flows at Lastarria volcano in the North Chilean Andes. Nature 313: 778-780.

Nelson, R.H., Smythe, W.D., Hapke, B.W. and Cohen, A.J., 1990. On the effect of X rays on the color of elemental sulfur: implications for Jupiter's satellite Io. Icarus 85; 326-334.

Neshyba, S., Fernandez, W. and Diaz-Andrade, J., 1988. Temperature profiles from Poás crater lake. Eos, Trans. Am. Geophys. Union 69(19): 588.

Oana, S. and Ishikawa, H., 1966. Sulfur isotope fractionation between sulfur and sulfuric acid in the hydrothermal solution of sulfur dioxide. Geochem. J. 1: 45-50.

Ohashi, R., 1919. On the peculiar sulphur spherules produced in a crater lake of the volcano Shirane, in the province of Kozuke, Central Japan. J. Akita Mining College 1: 1-10.

Oppenheimer, C. and Stevenson, D., 1989. Liquid sulphur lakes at Poás volcano. Nature 342: 790-793.

Pearl, J. and Sinton, W., 1982. Hot spots of Io. In Satellites of Jupiter (D. Morrison, Ed.), pp 724-755. Univ of Arizona Press, Tuscon.

Pieri, D.C., Baloga, S., Nelson, R. and Sagan, C., 1984. Sulfur flows of Ra Patera, Io. Icarus 60: 685-700.

Prosser, J.T. and Carr, M.J., 1987. Poás volcano, Costa Rica: geology of the summit region and spatial and temporal variations among the most recent lavas. J. Volcanol. Geotherm. Res. 33: 131-146.

Rampino, M.R. and Self, S., 1984. Sulphur-rich volcanic eruptions and stratospheric aerosols. Nature 310: 677-679.

Rampino, M.R., Self, S. and Stothers, R.B., 1988. Volcanic winters. Ann. Rev. Earth Planet. Sci. 16: 73-99.

Rowe, G.L., Brantley, S.L., Fernandez, M., Fernandez, J.F., Barquero, J. and Borgia, A., 1991a. Fluid-volcano interaction in an active stratovolcano: the crater lake system of Poás volcano, Costa Rica. J. Volcanol. Geotherm. Res., in press.

Rowe, G.L., Ohsawa, S., Takano, B., Brantley, S.L., Fernadez, J.F. and Barquero, J., 1991b. Using crater lake chemistry to predict volcanic activity at Poás volcano, Costa Rica. Bull. Volcanol.; in press.

Rymer, H. and Brown, G., 1989. Gravity changes as a precursor to volcanic eruptions at Poás volcano, Costa Rica. Nature 342: 902-905.

Sagan, C., 1979. Sulphur flows on Io. Nature 280: 750-753.

Sakai, H. and Nagasawa, H., 1958. Fractionation of sulfur isotopes in volcanic gases. Geochim. Cosmochim. Acta 15; 32-39.

Schmidt, M. and Siebert, W., 1973. Sulphur, in Comprehensive Inorganic Chemistry Vol 2, Eds Bailar JC, Emeléus HJ, Nyholm R, Trotman-Dickenson AF. Pergamon Press, Oxford: 795-933.

Shearon, W.H. and Pollard, J.H., 1950. Modern sulfur mining. A staff -industry collaborative report. Industrial Engineering Chem. 42; 2188-2198.

Sigurdsson, H., Carey, S., Palais, J.M. and Devine, J., 1990. Pre-eruption compositional gradients and mixing of andesite and dacite magma erupted from

Nevado del Ruiz Volcano, Colombia in 1985. J. Volcanol. Geotherm. Res. 41: 127-151.

Skinner, B.J., 1970. A sulfur lava flow on Mauna Loa. Pacific Sci. 24: 144-145.

Smithsonian Institution, 1989a. Scientific Event Alert Network Bull. 14(3): 4-6.

Smithsonian Institution, 1989b. Scientific Event Alert Network Bull. 14(4): 7-10.

Smithsonian Institution, 1989c. Scientific Event Alert Network Bull. 14(7): 19-20.

Smithsonian Institution, 1989d. Scientific Event Alert Network Bull. 14(10):12-13.

Smithsonian Institution, 1990a. Bull. Global Volcanism Network 15(4): 6-8.

Smithsonian Institution, 1990b. Bull. Global Volcanism Network 15(5): 7-8.

Smithsonian Institution, 1990c. Bull. Global Volcanism Network 15(7): 4.

Smithsonian Institution, 1990d. Bull. Global Volcanism Network 15(11): 6.

Stoiber, R.E. and Rose, W.I., 1974. Fumarole incrustations at active Central American volcanoes. Geochim. Cosmochim. Acta 38: 495-516.

Stoiber, R.E., Williams, S.N. and Huebert, B.J., 1986. Sulfur and halogen gases at Masaya Caldera Complex, Nicaragua: total flux and variation with time. J. Geophys. Res. 91: 12215-12231.

Stoiber, R.E., Williams, S.N. and Huebert ,B.J., 1987. Annual contribution of sulphur dioxide to the atmosphere by volcanoes. J. Volcanol. Geotherm. Res. 33: 1-8.

Takano, B. and Watanuki, K., 1990. Monitoring of volcanic eruptions at Yugama crater lake by aqueous sulfur oxyanions. J. Volcanol. Geotherm. Res. 40: 71-87.

Theilig, E., 1982. A primer on sulfur for the planetary geologist. NASA Contr. Rep. 3594, NASA, Washington DC: 34pp.

Thode, H.G., Cragg, C.B., Hulston, J.R. and Rees, C.E., 1971. Sulfur isotope exchange between sulfur dioxide and hydrogen sulfide. Geochim. Cosmochim. Acta 35; 35-46.

Ueda, A., Sakai, H. and Sasaki, A., 1979. Isotopic composition of volcanic native sulfur from Japan. Geochem. J. 13; 269-275.

Watanabe, T., 1940. Eruptions of molten sulphur from the Siretoko-Iôsan volcano, Hokkaidô, Japan. Jap. J. Geol .Geogr. 17: 289-310.

Williams, S.N., Sturchio, N.C., Calvache V., M.L., Mendez F., R., Londoño C., A. and García P., N., 1990. Sulfur dioxide from Nevado del Ruiz volcano, Colombia: total flux and isotopic constraints on its origin. J. Volcanol. Geotherm. Res. 42: 53-68.

Wilson, L., 1980. Relationships between pressure, volatile content and ejecta velocity in three types of volcanic explosion. J. Volcanol. Geotherm. Res. 8: 297-313.

Young, A.T., 1984. No sulfur flows on Io. Icarus 58: 197-226.

Room for your own notes